Synthesis of Novel Integrated Actuators Powered by Shape Memory Alloys

THIS IS A TEMPORARY TITLE PAGE
It will be replaced for the final print by a version
provided by the registrar's office.

Thèse n. 1234 2021
présentée le 17 novembre 2021
à la Faculté des sciences de base
Integrated Actuators Laboratory
Programme Doctoral en Robotics, Control, and Intelligent Systems
École polytechnique fédérale de Lausanne

pour l'obtention du grade de Docteur ès Sciences
par

Sean Thomas

acceptée sur proposition du jury :

Dr. Denis Gillet, président du jury
Prof. Yves Perriard, directeur de thèse
Prof. Bruno Dehez, expert externe
Dr. Luigi Borelli, expert externe
Prof. Yves Bellouard, expert interne

Lausanne, EPFL, 2021

"**Creativity** is *intelligence* having **fun**"
— Albert Einstein

To my family...

Acknowledgements

I would like to express my deepest gratitude to Prof. Yves Perriard, my thesis director, for welcoming me into his laboratory, supporting my ideas and efforts and guiding me through my doctoral studies. His advice, enthusiasm and excellent leadership has truly inspired me and moulded my professional and personal development.
I would like to express my deepest appreciation to Prof. Bruno Dehez, Dr. Luigi Borelli, and Prof. Yves Bellouard, who graciously accepted to review this thesis, and to Dr. Denis Gillet for being the jury president.
I am also deeply grateful to my advisors Dr. Morgan Almanza and Dr. Thomas Martinez whom I deeply appreciate for giving me their time during our long discussions, their insightful comments and for giving all the valuable advice and ideas that has made my research experience productive and fulfilling.
I am especially grateful to a number of friends and colleagues who has made my PhD life, not just joyful but also truly memorable. I am thankful to Adrien Thabuis for his friendship, his ingenious ideas, advice and for the amazing collaborative efforts we have fostered. Without Paolo Germano and his help on all my prototypes, this thesis would not be a possibility and I would like to express my deepest gratitude. I would also like to thank my colleagues, Dr. Yoan Civet, Camilo Hernandez, Raphael Mottet and Patricio Peralta for their compassion and their willingness to help me no matter what throughout my research. The Integrated Actuators Laboratory has the most friendly, welcoming and dedicated team and I would like to extend my thanks to each and every one of them, especially Sofia Ntella and Pooneh Mohaghegh.
Most of all, I am indebted to my family. My mother, father and sister have also supported me unconditionally and encouraged me in all my endeavours. I am forever grateful for their guidance and without them, none of my successes would matter. I would also like to thank my friends and girlfriend for supporting me along this journey. Their valued support has allowed me to stay motivated and determined during my thesis.

Lausanne, November 17, 2021 S. T.

Abstract

In the modern age of miniaturisation, Smart Materials, a type of material that reacts mechanically to a certain stimulus, have become an integral part of this revolution. Among these materials, Shape Memory Alloys (SMAs), who have the highest volumetric work density, are the ideal candidate in creating lightweight and miniature actuators. These alloys are a type of smart material that are able to revert back to their original shape when deformed as they are exposed to high temperatures. This exotic behaviour has allowed them to be the core active component in a plethora of applications such as grippers, bio-mimetic robots and surgical instruments.

Despite their high work density and their ability to function as artificial muscles, their implementation comes with some challenges. While the Shape Memory Effect (SME), the ability to recover strain when a thermal load is applied, is a remarkable behaviour, it is also a complex and multi-physical one. This complicates their design and makes it difficult to predict their behaviour. Furthermore, these alloys are only able to recover strain when deformed at low temperatures. This implies that a biasing element is required to exploit these materials in reversible actuators. Due to these limitations, the work density of SMAs, when implemented as actuators in robotic systems, are often much lower than their theoretical maximum.

In this thesis, the different types of SMA actuator implementations are studied from various applications to understand the design requirements and subsystems that are required to build an actuator. A holistic approach is, then, used to construct a design methodology to create highly integrated SMA-powered actuators in the hopes to prevent the degradation of the material's work density as is often the case in traditional SMA-based robotic systems. Here, in this work, the various identified subsystems of the SMA-powered actuator is combined to serve as a multi-functional element in the novel integrated SMA actuator.

In this thesis, different strategies are employed to integrate the SMA actuator into the robotic system while also proposing adapted sizing methodologies such that the resulting SMA-powered system can be sized to fit the required specifications to enable lightweight, compact and high bandwidth solutions. The work presents various case studies that utilise the proposed holistic design and sizing methodologies to serve as a proof-of-concept and to validate the methodology.

In this work, compliant and flexure-based mechanisms are exploited to exclude the need for a dedicated biasing element and create lightweight SMA-powered grippers to demonstrate the advantages of the proposed methodology. Additionally, utilising the mechanical behaviour of the SME, a lightweight mechanically-controlled crawling robot is designed and implemented.

Abstract

Furthermore, the work proposes, with the help of topology optimization and kirigami-inspired design, the creation of compliant SMA structures that allow the material to generate multiple outputs while remaining compact and easy to assemble. Lastly, a novel bistable gripper is designed and sized to experimentally validate the design methodologies proposed in this work.
The results in this thesis, reveal the extraordinary value of SMAs in creating lightweight robotic systems and presents various strategies to allow the further integration of the alloy within the system. The different areas in which the degradation of the work density are present in traditional SMA-powered systems and proposes design methodologies accompanied with sizing strategies to create lightweight, high bandwidth and integrated SMA-based robotic systems.

Keywords: Shape Memory Alloys, Artificial Muscles, Compliant Mechanisms, Flexures, Mechanical-Intelligence, Buckled Beam, Topology Optimization, Kirigami, Bistable

Résumé

À l'ère moderne de la miniaturisation, les matériaux intelligents, un type de matériau qui réagit mécaniquement à un certain stimulus, font désormais partie intégrante de cette révolution. Parmi ces matériaux, les alliages à mémoire de forme (AMF), qui présentent la plus forte densité de travail volumétrique, sont le candidat idéal pour créer des actionneurs légers et miniatures. Ces alliages sont un type de matériau intelligent capable de reprendre sa forme initiale lorsqu'il est déformé en étant exposé à des températures élevées. Ce comportement exotique leur a permis de devenir le composant actif principal d'une pléthore d'applications telles que les pinces, les robots bio-mimétiques et les instruments chirurgicaux.

Malgré leur densité de travail élevée et leur capacité à fonctionner comme des muscles artificiels, leur mise en œuvre s'accompagne de certains défis. Si l'effet de mémoire de forme (EMF), c'est-à-dire la capacité à récupérer la déformation lorsqu'une charge thermique est appliquée, est un comportement remarquable, il est également complexe et multi-physique. Cela complique leur conception et rend difficile la prédiction de leur comportement. En outre, ces alliages ne sont capables de récupérer leur déformation que lorsqu'ils sont déformés à basse température. Cela implique qu'un élément de polarisation est nécessaire pour exploiter ces matériaux dans des actionneurs réversibles. En raison de ces limitations, la densité de travail des SMA, lorsqu'ils sont implémentés comme actionneurs dans des systèmes robotiques, est souvent bien inférieure à leur maximum théorique.

Dans cette thèse, les différents types d'implémentations d'actionneurs SMA sont étudiés à partir de diverses applications afin de comprendre les exigences de conception et les sous-systèmes qui sont nécessaires pour construire un actionneur. Une approche holistique est ensuite utilisée pour construire une méthodologie de conception afin de créer des actionneurs hautement intégrés alimentés par le SMA dans l'espoir d'empêcher la dégradation de la densité de travail du matériau, comme c'est souvent le cas dans les systèmes robotiques traditionnels basés sur le SMA. Dans ce travail, les différents sous-systèmes identifiés de l'actionneur alimenté par le SMA sont combinés pour servir d'élément multifonctionnel dans le nouvel actionneur SMA intégré.

Dans cette thèse, différentes stratégies sont employées pour intégrer l'actionneur SMA dans le système robotique tout en proposant des méthodologies de dimensionnement adaptées afin que le système alimenté par le SMA puisse être dimensionné pour répondre aux spécifications requises pour permettre des solutions légères, compactes et à large bande passante. Le travail présente diverses études de cas qui utilisent la conception holistique proposée et les méthodologies de dimensionnement pour servir de preuve de concept et pour valider la

méthodologie.
Dans ce travail, des mécanismes souples et flexibles sont exploités pour exclure le besoin d'un élément de polarisation dédié et créer des pinces légères alimentées par SMA pour démontrer les avantages de la méthodologie proposée. En outre, en utilisant le comportement mécanique du SMA, un robot rampant léger et mécaniquement contrôlé est conçu et mis en œuvre. En outre, le travail propose, à l'aide de l'optimisation de la topologie et de la conception inspirée de Kirigami, la création de structures SMA compliantes qui permettent au matériau de générer des sorties multiples tout en restant compact et facile à assembler. Enfin, un nouveau préhenseur bistable est conçu et dimensionné pour valider expérimentalement les méthodologies de conception proposées dans ce travail.
Les résultats de cette thèse révèlent l'extraordinaire valeur des SMA dans la création de systèmes robotiques légers et présentent diverses stratégies pour permettre l'intégration de l'alliage dans le système. Les différents domaines dans lesquels la dégradation de la densité de travail sont présents dans les systèmes traditionnels alimentés par des SMA et propose des méthodologies de conception accompagnées de stratégies de dimensionnement pour créer des systèmes robotiques légers, à large bande passante et intégrés à base de SMA.

Mots-clés : Alliages à mémoire de forme, Muscles artificiels, Mécanismes compliant, Flexions, Intelligence mécanique, Lame flambée, Optimisation topologique, Kirigami, Bistable.

Contents

List of Figures

List of Tables

Introduction

In the recent decades, there has been a wave of technological progress due to the advancements in miniaturisation. This trend to create smaller and more efficient devices has led to giant leaps in technological advancement. This era of miniaturisation, often referred to as the Second Industrial Revolution, was sparked by the creation of the integrated circuit. The exponential scaling and miniaturisation of silicon transistors has led to computers, filling entire rooms, being transformed into handheld devices that fit in one's pockets. This trend has allowed electronics to have faster performance, lower power consumption and be cheaper than its predecessor which often directly translates to market share. Miniaturisation has also given a competitive edge to technological and commercial products over its competitors. However, this age of miniaturisation has not been restricted to electronics but has also impacted mechanical and optical devices. Motors, sensors and other such devices have all gone through the same trend in reduced footprint and increased performances resulting in a market where miniature actuators and sensors are readily available for relatively low prices.

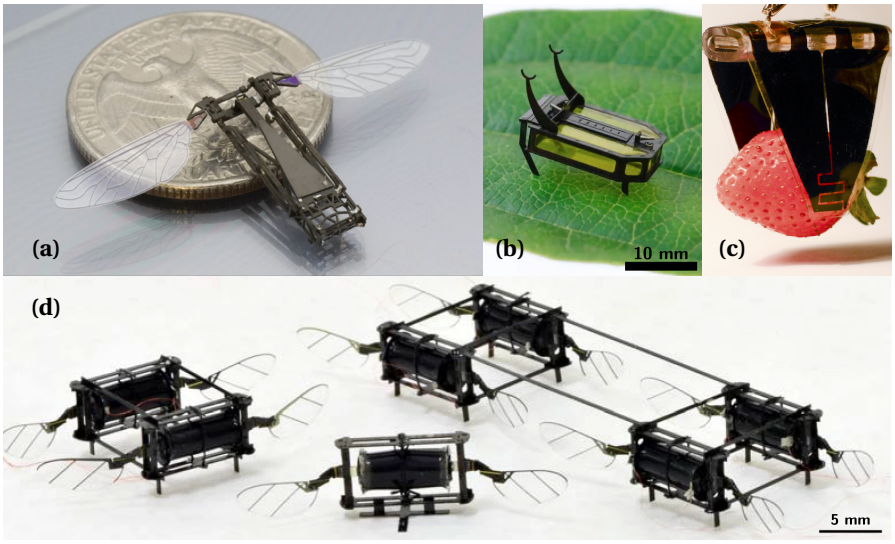

Figure 1: Miniature actuators powered by Smart Materials. (a) A piezo-powered flapping insect robot by Sreetharan et al. (2012) (b) An untethered shape memory alloy-powered beetle robot powered by Yang et al. (2020) (c) A soft gripper based on electrostatic actuation by Shintake et al. (2016) (d) A dielectric elastomer actuator-based flying micro-robot by Chen et al. (2019).

The basic component of any robotic system is the actuator which is responsible for moving and controlling the system. The principle behind creating miniature robotics systems, thus, consists of downsizing actuators. The design and sizing criteria for actuators can not be necessarily applied from the macro scale when downsizing. However, the primary agent for the miniaturization of actuators has been the proliferation of Smart Materials. These materials, often referred to as artificial muscles, are able to provide some form of work as a response to a certain stimulus such as stress, an electric or magnetic field. The active and reactive nature of these materials allow them to be used as actuators or sensors in creating compact and integrated actuators. These materials can be integrated and tailored to fit within a certain use case based on the physical requirements of the application. These applications can range from micro-grippers, biomimetic robots to crawling robots as shown in fig. 1.

The choice of smart material depends on a range of parameters, notably, the activation stimulus, the time response, and its work density. When considering miniaturisation and creating actuators for compact and lightweight systems, the work density is often used as the leading parameter in choosing the smart material. As shown in fig. 2, among most smart materials, the material, that presents with the highest work density and is, thus, the primary candidate for miniature actuators, is the Shape Memory Alloy (SMA). These alloys, often composed of Nickel and Titanium, is a brand of smart material that reacts to temperature. Variants of these alloys that react to a magnetic field are also present. But the thermoelastic variant of the shape memory alloys are more widely used and can be obtained in different shapes and sizes. There are different varieties of the thermally activated SMAs but the alloy that is the most widely available is the Nickel-Titanium alloy, often known as NiTiNOL. The properties of the material can be changed by modifying the atomic percentages of the alloy or by doping the alloy with other metals.

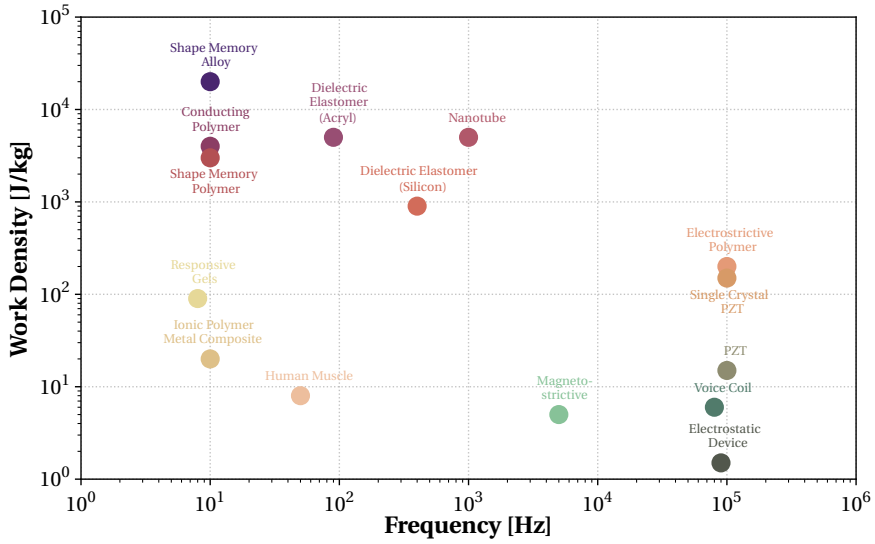

Figure 2: Comparison of different smart materials based on their work density and their time response (from Preumont (2006))

Design Considerations

As stated, due to the high work density of the material, SMAs are generally used in applications where low weight and a compact footprint is required. However, as observed in fig. 2, the requirement to heat the active element, results in SMAs having relatively low time responses. Cooling, when employed passively, results in extended waiting times before the repeated actuation of the SMA actuator. This results in the material being primarily used in systems that do not require high bandwidths. However, when downsizing the actuator, the volume-to-surface area ratio increases, resulting in faster cooling times. Thus, SMAs are often used in applications such as micro-actuators and grippers. Furthermore, due to the bio-compatible nature of the alloy, they have been used in biomedical applications for smart catheters and minimally invasive surgery robots. Recently, there has also been a surge of work done where SMAs are used to create autonomous, walking robots and self-reconfigurable robots. All of these applications require actuators that have high work outputs while remaining light and compact. Thus, SMAs have become an ideal candidate for these use cases.

As the commonality in these application is the limitations in space and weight, the design specification of the required actuators often take into account the final weight and size of the system. These SMAs are able to revert back to their original shape when heated. This behaviour, often referred to as the Shape Memory Effect (SME), is exploited to create these actuators. Only after some deformation alters its shape, will this behaviour allow the active element to perform some work when heated. Thus, these SMA actuators require various transmission stages and sensors when implemented within a certain application. As SMA actuators are required to output more work while staying compact, the implementation of such actuators take into consideration how the final work density is affected by the addition of these external components. Due to the strengths of the SMA with regards to its work density, the main design consideration taken into account is the design of these external components and the minimisation of the extra weight and volume added to the overall actuator.

Implementing SMA actuators into compact system results in noiseless operation and their high force-to-weight ratio and muscle-like actuation make them suitable for soft robotics and biomimetic/bio-inspired robots. However, as previously mentioned, they have small bandwidth and low operating frequencies, primarily due to their large cooling times. As explored in the work by Soother et al. (2020), this poses the principle challenge when designing SMA actuators. Furthermore, the force output of SMAs are relatively low and this is, often, counteracted by using bundles of SMA wires. However, increasing the volume of SMAs also increases the cooling time and further decreases the operating frequency, creating a trade-off between the two parameters. Finally, the shape memory effect and the thermoelastic behaviour of the SMA is highly non-linear and complex. This makes the actuators difficult to control and requires special methods and sensors to control them.

When combined, these factors make the design of SMA actuators and their integration into complex applications difficult and cumbersome. Due to the various trade-offs that exists

when designing the active element, accurate sizing of the actuator is critical to optimize the final footprint and weight of the system. When volume and weight constraints are present, a holistic design approach is required where the entire system and the actuator is considered in the design process. Due to the complex nature of the smart material and the sometimes complex nature of the application, the sizing of the active element becomes difficult and results in a system that is not fully optimised or is oversized. These concessions in the design process results in a degradation of the overall work density of the SMA actuator.

Thesis Statement

In this thesis, the main goal of the work is to explore, develop and demonstrate novel holistic approaches to creating highly integrated SMA-powered actuators. As shape memory alloys are known for their high work density, they are primarily used in applications where lightweight and compact actuators are a necessity. In this work, the traditional SMA design methodology are studied and adapted to improve their work density and allow them to harness the full potential of the smart material. In doing so, this work presents various design strategies and analytical models that enable creating integrated systems in a plethora of different use cases.

In this thesis, the main focus of the work is to explore and respond to the following key research questions:

How can the work density degradation of SMAs be prevented when designing actuators? As miniaturisation becomes critical in the design of actuators and robotic systems, the need for materials with high work density has increased. SMAs are touted to have the highest work density among most smart materials and are thus, primarily used in scenarios where a lightweight or compact design are a necessity. However, the alloy alone cannot be used to create an actuator and various other components must work in tandem with the material for it to function as an actuator. These additional elements such as a biasing element or a kinematic stage, degrade the work density of the overall actuator by introducing passive elements into the system. One of the primary goals of this work is to explore various strategies a designer can employ to prevent this work density degradation. In exploring the question: *what strategies can be employed in the design of SMA actuators that alloy the material to be used to its full potential?*, the work hopes to develop a design methodology that can be implemented in any application such that the resulting actuator maximises the work density resulting in a robotic system that is lightweight and compact. In this work, the proposed design strategies are employed in various case studies so as to validate the methodology and while, creating lightweight robotic systems.

How can the traditional sizing methodology be adapted for integrated SMA actuators? In most implements, SMA-powered actuators are heated by simply passing a current through the material and relying on Joule's losses to raise its temperature. However, when cooling the

material so as to return the alloy back to its original state, most actuators rely simply on the passive thermal exchange with the surrounding air. This often results in a low bandwidth for the final system. When relying solely on passive cooling, the most critical design parameter to consider becomes the geometry and size of the active SMA element. Here, decreasing the diameter or thickness of the SMA wire / sheet can drastically reduce the cooling time and thus, drastically increase the bandwidth of the final system. Thus, when designing SMA-powered actuators, appropriately sizing the SMA is key to creating a fast and responsive actuator. In the traditional SMA design, simplified sizing strategies exist that allow creating the perfect balance between the size and force output of the active element. However, when designing more complex and highly integrated SMA systems, this work aims to adapt the traditional sizing strategies to fit the proposed design methodologies. In this work, the various case studies that validate the novel methodologies implement the proposed sizing strategies such that the resulting robotic system employs the smallest active element and results in a system that can be rapidly cooled using passive means.

Can a generative design approach be used to create and validate compliant SMA structures? Traditionally, the fabrication of parts with complex geometries has been a difficult task and has limited the design of mechanical parts to simple geometries. However, the recent improvements in the field of additive manufacturing has allowed the fabrication of structures with such complex geometries. Furthermore, the additive manufacturing of smart materials, especially Ni-Ti based SMAs, has made strides recently and has enabled the possibility of 3D printing complex SMA structures a real possibility. However, the question arises: *How can one design a complex SMA structure while taking into account the shape memory effect and predict its resulting behaviour?*. The multi-physical and complex nature of the shape memory effect makes is difficult to accurately predict the behaviour of the alloy when heated which in turn makes it difficult to size and design such active structures. Often, generative algorithms have been used in designing structures when a complex actuation with multiple design constraints are required and where an intuitive design strategy is not feasible. However, due to the highly non-linear nature of the SMA, makes algorithmically generated designs computational expensive resulting in low mesh sizes and domain spaces limited to 2D. In this work, the goal of the thesis aims at proposing a strategy to design complex multi-output actuators based on compliant SMA structures so as to harness the potential of the recent advances in additive manufacturing. Furthermore, due to the high computational cost of simulating the shape memory effect, this work aims to present a simple strategy to generate designs while taking abstraction of the shape memory effect that can still feasibly function as a reversible actuator. Furthermore, in this work a qualitative factor is presented and with the help of Finite Element Modelling (FEM) allows the comparison of the various generated designs with regards to their feasibility as an SMA-powered actuator.

Thesis Outline and Contributions

CHAPTER 1: Overview of SMA Actuator Design

This chapter provides an overview of the basic and most commonly used implementations of the SMA-powered actuator. Here, a basic overview of the working principle of each type of actuator is presented and described. The three most common methods of implementing the SMA actuator is detailed so as to give an idea of the requirements of an SMA-based actuator. This chapter also delves into the different fields in which this type of actuator is employed. Various examples of SMA-powered robotic systems are studied in each domain so as to understand the different design considerations and parameters that impact the design of SMA-powered actuators. Furthermore, this study allows establishing the basic building blocks present in SMA actuators and understand the functions of each subsystem. Finally, this chapter enables taking a holistic view of the SMA actuator design and establish the drawbacks of the traditional design and the areas in which work density degradation can be reduced.

CHAPTER 2: Predicting the Shape Memory Effect

Understanding and predicting the behaviour of the SMA when subjected to a thermal load is critical when designing and sizing SMA-based actuators. In this chapter, the Shape Memory Effect (SME) is introduced and described. Furthermore, the main constitutive models that allow the prediction of the shape memory effect is showcased. The different parameters and multi-physical variables that define the effect in the macro-scale is shown in this chapter. These 1D analytical models are presented as they can be simply implemented and used to size SMA actuators that employ the alloy in simple geometries such as wire and sheets. In scenarios, where more complex geometries are to be simulated, the different parameters required to define the material within a commercial finite element method software is also summarised. Furthermore, in this chapter, these constitutive models are adapted such that they can be employed in sizing the standard bias-spring SMA actuator. Lastly, this chapter presents the traditional simplified sizing methodology used in standard SMA actuator design.

CHAPTER 3: Development and Modelling of Biased Kinematic Stages for SMA Actuators

In this chapter, a holistic design approach is presented where the kinematic stage and the biasing element are integrated to further optimize the work density of the final system. Here, the use of flexure-based compliant structures are used to create kinematic stage where the linear motion of the traditional SMA actuator is converted into a more complex desired multi-axial output. The inherent stiffness of the compliant mechanisms, which are generally viewed as a drawback, is harnessed to function as the biasing element for the SMA actuator. In this chapter, this novel design methodology is described and the traditional sizing methodology is adapted such that it can be used for any application. Using simplified pseudo-rigid body

models, a generalised analytical model is presented and described to allow the sizing of the kinematic stage with respect to the mechanical limitations of the chosen SMA element. Finally, the design and sizing strategy, presented in this chapter, is showcased and validated using a case study of a drone-ready SMA-powered gripper.

CHAPTER 4: Mechanical Approach to SMA Actuator Control

As SMAs are compared to biological muscles due to their high work density, this alloy is often used in bio-inspired applications. In this case, the high work density and lightweight requirement of the robotic application is critical in the design of the SMA actuator. Often, the control electronics and sensors are omitted in the estimation of the work density and this subsystem is one of areas in which the work density is most degraded. In this chapter, a mechanically controlled control strategy is proposed that makes use of the thermomechanical effect of the SMA to control itself. In this approach, the mechanically controlled SMA element does not require any sensors or electronics. Here, in this chapter, this control methodology is validated using a lightweight untethered inchworm robot powered by a single helical SMA spring. This chapter describes and models the inchworm robot while also comparing it with other tethered and untethered inchworm robots showcasing the distinct advantages of the proposed design methodology.

CHAPTER 5: Generation of Actuators Powered by Compliant SMA Elements

The advances made in additive manufacturing has allowed the 3D printing of complex geometries fabricated from SMAs. These techniques, while still being expensive and inaccessible has created a need for design tools and strategies for designing complex compliant SMA actuators. In this chapter, the holistic design approach is used to propose a novel design methodology for creating compliant SMA structures that serve as the kinematic stage and as the active element. In this chapter, topology optimization and a simple qualitative comparison factor is presented so as to algorithmically design compliant SMA structures while also being able to determine their feasibility in the context of SMA-powered actuators. A simple prototype is used to validate the factor and with the help of experimental results, it is used to showcase the attractive nature of the algorithmically generated multi-output designs. Furthermore, a kirigami-inspired design approach is also presented that allows creating high force-high stroke actuators that combine the highly stretchable kirigami-inspired meta-materials and SMAs. Here, in this chapter, these actuators are validated using experimental results and a proof-of-concept SMA-based linear actuator.

CHAPTER 6: Validation using a Novel SMA Gripper System

Finally, in this last chapter, the various design principles, methodology and sizing strategies are exploited to create a bistable SMA gripper. This case study is used to validate the design

methodology and sizing strategy proposed in the previous chapters by implementing them in the design of the gripper. Here, the gripper is powered using a pair of antagonistic SMA helical coils and makes use of flexure-based buckled beams and pivots to create a compact and light weight bistable industrial gripper. In this chapter, an analytical model of the flexural gripper is described and present so as to enable the sizing of the SMA elements. In this chapter, the sizing methodology, presented in the previous chapters, enables using the thinnest SMA spring that still enables the snap-through of the buckled beam allowing the gripper to have a short cooling period, thereby, increasing the bandwidth of the industrial gripper. This chapter, along with the various case studies present in this work, gives a concrete application in which the proposed design methodologies can be implemented.

Conclusion and Contributions

Finally, in this chapter, a conclusion showing the different contributions of this work and the answers to the various research questions posed in this work. Furthermore, the outlook and future implications of the design methodology are presented and described.

1 Overview of SMA Actuator Design

1.1 Introduction

In the scope of miniaturisation, creating highly integrated robotic system has become possible with the help of smart materials, notably Shape Memory Alloys (SMA). These alloys, having the highest work density, has made it possible to create miniature artificial muscles that can be integrated into compact and lightweight applications. SMAs have an interesting behaviour which consists of recovering any strain imposed on it when heated above a certain critical temperature threshold, often referred to as the Shape Memory Effect (SME). These alloys exploit the SME to create reversible actuators that are lightweight and compact. This effect is highly non-linear and is dependant on multiple variables, resulting in a highly complex and difficult to model behaviour. Thus, designing and sizing these alloys to create optimised actuators for complex applications is difficult and cumbersome.

In this chapter, an overview of the different implementations of SMA actuators are explored. In the context of different applications, the SMA actuators that are embedded in the different robotic systems are investigated. The traditional design methodology for these actuators are studied and presented in this chapter. The different examples of SMA actuators are used to create a conventional design methodology and the different subsystems of the robotic systems are studied. In this chapter, an in-depth look into the advantages and limitation of the methodology is conducted. In this manner, the conventional design methodology can be adapted into taking a holistic view of the robotic system and create a novel design approach that further promotes the integration of the SMA actuator subsystems into the final robotic system.

1.2 Working Principle of SMA Actuators

Shape Memory Alloys are a subclass of smart materials that react to heat. This special brand of material, with the help of some micro-structural changes, can react mechanically when subjected to an external non-mechanical stimulus, in this case, temperature. The shape

memory effect that occurs in this alloy occurs due to some phase transformation that happens when heated and cooled around a certain transition temperature. At low temperatures, the material exists in its Martensite (M) phase where the material can be deformed easily. These deformations, similar to plastic deformation, result in the material being permanently deformed at these low temperatures. As the alloy is heated up above its transition temperature, the material transforms from the M phase to the Austenite (A) phase, recovering any of the *"permanent"* strain imposed on it at low temperatures. This capacity to recover any strain imposed on it and return back to its original shape is often referred to as the shape memory effect. As the material cools below the transition temperature, the alloy returns back to the M phase, allowing the material to be *"plastically"* deformed once again. The detailed description, along with the analytical and numerical models, is detailed in chapter 2.

The basic idea behind the implementation of the SMA, in the context of an actuator, is to pair the active material with a biasing element. As stated previously, the SMA element requires a deformation at low temperatures to produce any work when heated to its transition temperature. This implies that for the actuator to behave reversibly and create a work cycle, a certain system is required to deform the SMA at low temperature so as to enable the SMA to actuate when heated. A one-directional SMA actuator is also possible where the SMA is stretched and then heated to revert back to its original shape or constrained to generate an increasing stress based on the applied temperature. These actuators can be used for single actuation application such as deployment mechanisms as shown in the work by Mohd Jani et al. (2017). However, in this work, two-directional SMA actuators are explored and studied. These two-directional actuators require a biasing force as the SMA elements can only recover strain in one direction. These linear actuators, thus, require some kind of biasing mechanism that can apply a biasing force in the opposite direction. As shown in the work by Bellouard (2008), the most common mechanisms used to return the SMA back to its neutral position are bias-springs, dead-weights or another SMA element in an antagonistic configuration as illustrated in fig. 1.1.

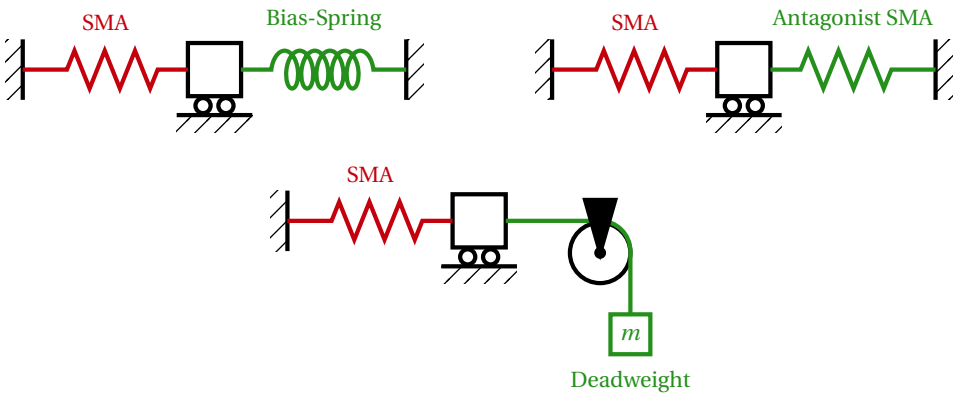

Figure 1.1: A schematic representation of the basic types of linear SMA actuators. In general, a separate kinematic stage is used to transform the linear output into the desired output.

The **Biased-Deadweight SMA Actuator** has the advantage of being quite simple to implement as it consists of simply applying a constant load to the active element irrespective of the temperature. Here, the SMA based on the phase will displace the constant load by a fixed stroke. At low temperatures, the deadweight elongates the SMA element and as the SMA heats up and changes phase, the load will be displaced. As there is always the same constant load, there is a high risk of overheating the SMA and risking reaching stresses above the recommended maximum pull force of the SMA. Thus, to prevent this irreversible damage to the SMA actuator, a constant load that is below the maximum pull force of the SMA is used. This greatly limits the maximum load that can be displaced by the SMA actuator preventing widespread adoption of this method of implementation.

The **Biased-Spring SMA Actuator**, on the other hand, consists of pairing the SMA element with a biasing passive spring. This method of implementation is also quite simple to implement and thus, is the most widely used method for designing SMA actuators. Here, the idea consists of using a passive spring to apply a spring force to the SMA at low temperatures. This allows the SMA to be deformed and activates the SME when the alloy is heated. As the material transforms from the M to the A phase, the spring is deformed while the SMA element returns to its original shape. Here, due to the increasing elongation of the spring, an increasing spring force acts on the SMA as the temperature is increased. This implies that based on the temperature and the rigidity of the spring, the force and stroke of the actuator can be sized. The sizing methodology and analytical models of this type of actuator will be detailed in chapter 2. However, the actuator can only be controlled in one direction during the heating phase, while during the cooling, the SMA actuator returns back to its neutral position uncontrolled.

The **Antagonistic SMA Actuator** consists of pairing the SMA element with an antagonistic biasing SMA element. In this method, the actuator can be actuated in both directions. As the first SMA is heated, the strain recovery cause the antagonistic SMA to be deformed and elongated. When heating the antagonistic SMA, the inverse effect occurs, where the first SMA is deformed and elongated while the antagonistic SMA reverts back to its original shape. Thus, by alternatively heating the SMA pair, the actuator can be made to actuate in both directions. The primary downside to such an implementation is the difficulty in sizing and controlling such an actuator due to the compounding of the highly non-linear nature of each of the SMAs. These SMAs are still widely used in many applications do to the additional degree of freedom present in the actuator. The sizing methodology of these actuators will also be described in chapter 2.

The three methods of implementation represent the majority of the different types of SMA actuators. Using this biasing principle for pre-stretching the SMA element, a reversible and cyclical actuator can be fabricated. It is important to note that the biasing element along with the SMA represent only the subsystems that create the reversible work offered by the active material. However, when creating an SMA actuator, additional structures and elements are required to form a complete actuator for the required application. The implementations of these additional subsystems are often the source of the work-density degradation of the alloy.

1.3 Analysis of SMA Actuators

As stated previously, the primary advantage of actuators powered by SMAs are the fact that, owing to their high work density, these actuators can be designed to be compact and lightweight. However, this is only the case when designing specifically for the required application. Due to the active nature of the material, when the SME is exploited specifically for the requirements of the use case, the resulting actuator can be integrated into the overall robotic application. Thus, when analysing the various methods in which these SMA actuators are designed, it is important to consider the application and its domain. Due to the long cycling time of the SMA elements, SMA actuators are primarily used in systems and domains where low bandwidth but compact actuators are required. Based on the work by Mohd Jani et al. (2014) and Sreekumar et al. (2007), these SMA-based actuators are used in a variety of different fields and applications. Their work show that these actuators have been used in the automotive industry as miniaturised actuators for various subsystems to replace traditional electromagnetic or pneumatic actuators. In aerospace applications, where there are geometric volume constraints, they have been used to create micro-grippers, vibration dampers or deployment mechanisms. Furthermore, due to their bio-compatibility, these SMA actuators have also found its way into the biomedical field where they have been used to create miniature medical and surgical instruments such as endoscopes, medical tweezers and stents among others. Recently, however, there has been wide interest in creating miniature bio-inspired and reconfigurable robots where these SMAs are used as artificial muscles.

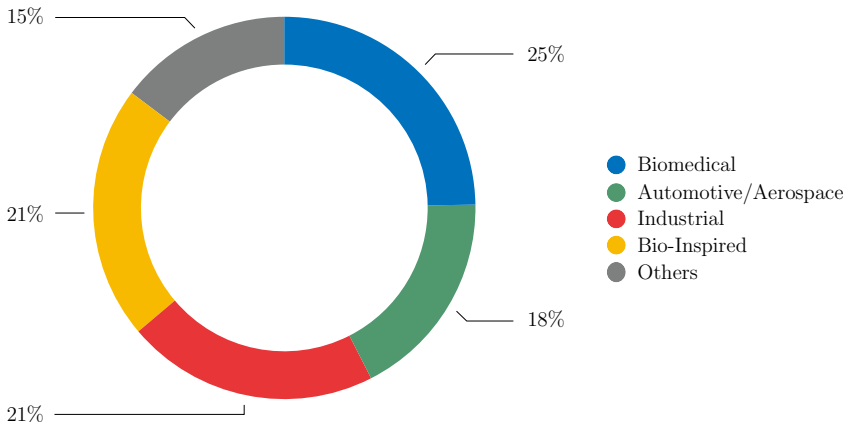

Figure 1.2: A simple SEO-keyword analysis of the different applications of Shape Memory Alloy actuators.

A simple keyword analysis of SMA actuators gives a rough idea of the distribution of the various research interests and domains in which these actuators are employed as shown in fig. 1.2. Thus, in this section, the goal is to explore the different domains in which SMA

actuators are employed and study, using some examples, the various design parameters and choices used to create appropriate actuators for the appropriate application. By doing so, the important and key factors that make up the design of SMA actuators can be established. These factors can, thus, be used to detail the various areas in which these actuators can be improved and optimised such that when designing future SMA actuators, the final systems can be further integrated. By exploring the design choice used in the following examples, a design methodology can be established for creating novel improved SMA actuators that can fully harness the high work density of the alloy.

1.3.1 Biomedical Applications

Due to the tight volume constraints in the biomedical field, actuators that prioritize compact footprints have been favoured. Furthermore, in the medical field, reduced noise, vibration, and contamination are necessary. Additionally, a high time response is not required and slower actuation can be tolerated. This makes it an ideal domain for SMA actuators to flourish. The examples presented in this section are chosen to examine the various types of SMA actuators implemented in the biomedical field so as to extrapolate the different design parameters and choices used in this specific domain.

In the first example, the authors, Liu et al. (2019), have developed a mesoscale actuator used to maintain the visual clarity of the lens in endoscopes during invasive robotic surgeries as shown in fig. 1.3(a). Here the main design criteria were the limitation of contaminants and the extreme volume constraints imposed by the human body. The actuator must fit on the tip of the endoscope which is inserted within the body during surgery. The tight footprint required by the project specifications has created a need for smart materials, specifically shape memory alloys, to be used in this application. The alloy being biocompatible has also played a key role in the choice of smart material. The actuator, proposed in this work, consists of a simple bias-spring SMA actuator where the active element consists of a thin SMA wire and the biasing element consists of a passive tractional spring. Here, the actuator, using a pin as a simple pivot, transforms the linear motion of the SMA actuator into a rotation of the lens cover. This cover, considered the output, is used to clear the surgical camera and maintain visual clarity during surgery.

In the work by Abdul Kadir et al. (2019), the authors have designed and fabricated a multi-segmented SMA-based actuator system for endoscopic applications as shown in fig. 1.3(b). In this second example, the main design criteria were the volume constraints of the actuator, the biocompatibility of the actuator and the high strokes required. As with the previous example, the actuator is used in minimally invasive surgery and thus, requires the actuator to be biocompatible and prevent any unwanted pollution of the body during operation. Furthermore, due to the tight volume constraints of the human body, the actuator makes use of the high volumetric work density of the alloy to create this compact actuator. The actuator proposed in this work consists of multiple bias-spring SMA actuators arranged in

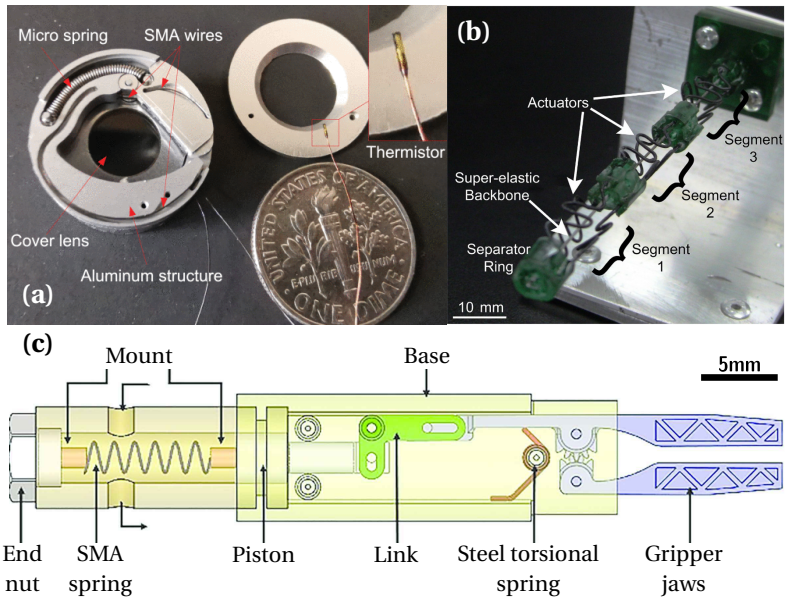

Figure 1.3: Examples of different implementations of SMA actuators in the biomedical field : (a) An SMA powered actuator used for visual clarity in surgical cameras taken from the work by Liu et al. (2019) (b) A multi-segmented SMA endoscope taken from the work by Abdul Kadir et al. (2019) (c) A minimally invasive surgical gripper taken from the work by Roshan et al. (2018)

an antagonistic manner. Here, a flat SMA spring is used to provide the high strokes required and is paired with an elastic backbone that provides the rigidity for the endoscope while also allowing the SMA spring to return back to its original state during cooling. Opposing SMA flat spring are placed surrounding the biasing element to allow the endoscope to actuate in other directions and increase the degrees of freedom of the endoscope.

In this last example, the authors, Roshan et al. (2018), have designed and fabricated a minimally invasive surgical gripper based on an SMA spring actuator. As stated by the authors, in minimally invasive surgeries, manipulations are often performed in confined and tight spaces and thus, the main design criteria were the miniaturisation of the actuator and maintaining the high energy density of the alloy. In this example, the proposed gripper is fabricated using several components including an SMA spring as the active element and a torsional spring as a biasing element as shown in fig. 1.3(c). Furthermore, a pivot linking system is used as a kinematic stage that converts the linear actuation of the SMA spring into a rotational output of the gripper jaws.

In the case of actuators designed for biomedical applications, there is a large focus for compact and work dense actuators. Furthermore, in some cases, the biocompatibility of the SMA plays a large role in the choice of the actuator. The design of the final actuator in this application is largely dependant on the volume constraints imposed by the human body. Here, actuators generally tend to value stroke over force output and thus, SMA springs are generally used as

they come with higher elongations but at the price of lower force outputs. Furthermore, using bias-spring SMA actuators allows the actuator to have a reversible and cyclical actuation. In the presented examples, the bias-spring was chosen over the antagonistic SMA due to the reduced complexity and simplicity in the control. However, the implementation of sensors and control electronics can often result in increased volume requirements and can degrade the work density of the final system.

1.3.2 Automotive and Aerospace Applications

As in the case of SMAs in the biomedical field, the high work density and the ability of SMA actuators to be compact and lightweight has allowed them to be attractive in the automotive and aerospace fields. A common requirement of automotive products are high miniaturisation and integration. The small size and weight of SMA actuators has made them ideal in aerospace applications as well. In this section, some examples have been studied to determine the various design requirements of SMA actuators in these fields. By studying the various types of automotive or aerospace SMA actuators, the various design criteria and limitations can be extracted.

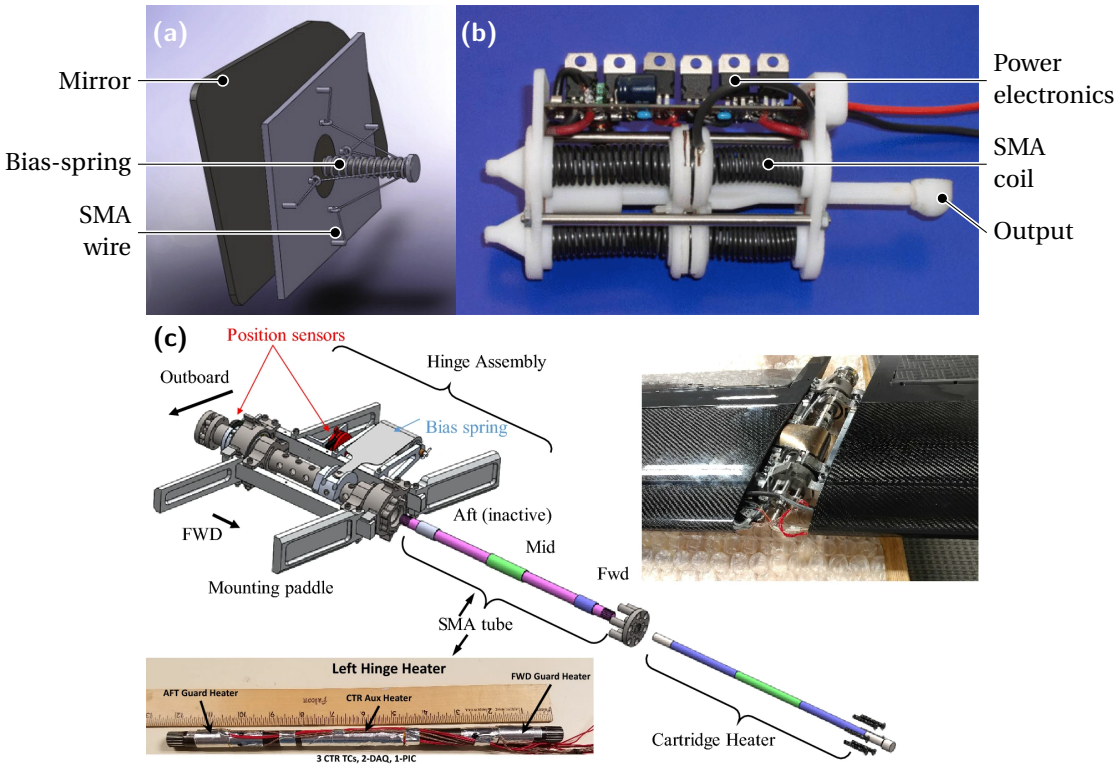

Figure 1.4: Examples of different implementations of SMA actuators in automotive and aerospace applications : (a) An active SMA powered mirror taken from the work by Williams et al. (2010) (b) An automotive tumble flap powered by an SMA actuator taken from the work by Bellini et al. (2009) (c) An active span-wise adaptive wing taken from the work by Bellini et al. (2009)

In the first example, the authors, Williams et al. (2010), have designed and fabricated a lightweight and cost effective active mirror actuator as shown in fig. 1.4(a). The traditional power mirrors that use electromechanical actuators have been commonplace in the automotive industry. The authors have designed an alternative using SMAs to create an active automobile mirror that is lightweight and employs a work dense actuator. In this work, the active mirror consists of a biasing spring surrounded by four SMA wires. The mirror, mounted on a spherical joint, can be actuated in the four cardinal directions. Since a limited stroke length is required, SMA wires have been used to actuate the mirror. Furthermore, a single passive spring has been implemented as a biasing element for each of the SMA wire actuators. The spherical pivot on which the mirror is mounted converts the linear movement of the SMA actuator into the required rotational movement. The SMA wires are actuated using Joule's heating by passing a current across the wires. The control of the actuator is performed by using a variable structure controller. The authors have focused their work to be lightweight and robust and thus, have used the high work density of the alloy to their advantage.

In the second example, the authors, Bellini et al. (2009), have sized and fabricated a binary SMA actuator for automotive tumble flaps. Here, this solid-state actuation system is developed to replace the existing traditional electromagnetic and pneumatic actuators used in the industry. In this work, the authors focused on creating a miniature actuator by harnessing the high work density of the shape memory alloy. The main constraints presented in this work, as stated by the author, are the power to weight ratio, robustness and reliability of the actuators. Furthermore, the clean, silent and smooth operation of the actuator in addition to its self-sensing capabilities added to the attractive nature of the material in this application. In this prototype, the basic concept consists of using SMA coils with an antagonistic SMA coil as the biasing element as shown in fig. 1.4(b). Furthermore, in the work, a thermoelectric module is used to aid in the heat transfer from one SMA coil to the other for increased operation frequency. Here, a pair of SMA coils are used in parallel to increase the overall force output of the actuator.

In this final example, the authors, Benafan et al. (2019), have integrated an SMA actuator within the wing of aircraft to create an active span-wise adaptive wing as shown in fig. 1.4(c). In the aerospace domain, creating lightweight actuators that can reduce the load of the aircraft is the primary constraint that has allowed SMAs to penetrate the industry. The high work density of the materials allows for the creation of lightweight actuators that can still produce the large forces required in this application as displayed in this work. SMA actuators can be utilized to build safer, lighter, and less complicated systems that are compatible with future electric-aircraft concepts. In this work, a bias-spring rotational SMA actuator is created to alter the shape of the wing. A SMA tube is paired with a torsional bias spring to create the rotational actuator. Position sensors and a heating cartridge is integrated into the system to create the full working prototype for the adaptive wing. Due to the low profile of the structure and by using an SMA tube, the entire actuator fits withing the profile of the wing while still delivering high output forces.

As shown in these examples, the high force output and the ability to create lightweight systems has been the primary design criteria that has allowed SMA actuator to proliferate in this engineering domain. In each example, the high work density of the SMA has been exploited to create actuators that can produce large force while remaining compact and lightweight. In each example, discrete systems were used to create the active and biasing elements. A separate conversion mechanism employing hinges or pivots were used in each case to convert the output of the SMA actuator into the required motions showing an area in which some degradation of the work density is present.

1.3.3 Industrial Applications

The primary reason that SMAs have started to be integrated into industrial applications has been the need for lightweight and powerful actuators. The high power and energy densities of the SMA has made it an ideal candidate to save weight and construction space when compared to traditional electric and pneumatic actuators. Furthermore, these SMA industrial actuators operate with reduced noise and emissions with is often overlooked in industrial applications but can be essential in clean-room applications. In this section, various examples of industrial gripper powered by shape memory alloys are presented so as to understand and establish a clearer picture of the various design requirements and constraints present in the domain.

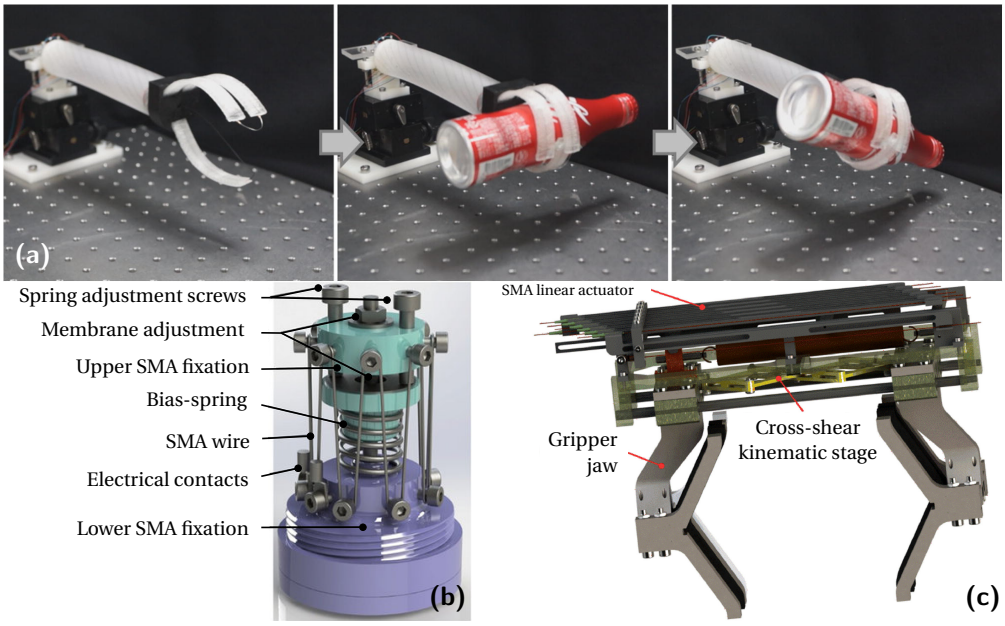

Figure 1.5: Examples of different implementations of SMA actuators in industrial applications : (a) A soft robotic gripper powered by an SMA wire taken from the work by Rodrigue et al. (2017) (b) A bistable vacuum gripper taken from the work by Motzki et al. (2016) (c) A two-prong industrial robotic powered an SMA wire taken from the work by Lu et al. (2019)

In the first example, the authors, Rodrigue et al. (2017), have designed and fabricated a soft robotic gripper powered by an SMA wire. Here, the SMA wire-based soft bending actuator

was designed to exploit the power-to-weight ratio of the material and create a lightweight robotic finger as shown in fig. 1.5(a). In the work, the proposed actuator consists of a curved polydimethylsiloxane (PDMS) matrix with an embedded SMA wire. Here, the wire, acting as the active element, is biased by the PDMS matrix. During the activation, the SMA wire attempts to straighten itself when heated and is reverted back to its curved state with the help of the PDMS matrix during cooling. The high power-to-weight ratio allows three 200 μm SMA wires to exert 1.5 N of gripping force. The use of the biasing PDMS matrix allows the repeated actuation of the actuator. The curved nature of the PDMS matrix and the actuator acts as the kinematic stage that converts the actuation of the SMA into the required gripping motion. In this work, the authors have prioritized creating an actuator that is lightweight and has soft actuation to not damage the grasped object. The use of SMAs in this application has allowed the authors to create a lightweight actuator while still enabling a high grasping force.

In this second case study, the authors, Motzki et al. (2016), have developed an SMA-powered vacuum gripper. The gripper, as shown in fig. 1.5(b), consists of a bias-spring surrounded by a long SMA wire in traction. Here, the SMA wire is wound around multiple screws to create the illusion of multiple independent SMA wires that work in parallel to increase the output forces. Furthermore, a bistable mechanism is used to convert the SMA actuation into a constant holding force that requires no additional energy from the SMA after the initial trigger force. The gripper is actuated using Joule's heating by passing a current across the SMA wire and the authors have implemented a resistance measurement which allows the control of the gripper using self-sensing. In this work, the leading design criteria was the energy efficiency of the bistable mechanism and the high output forces of the SMA wire. The SMA wire system allowed the final vacuum gripper to be lightweight while still offering the required forces to trigger the snap-through of the bistable mechanism.

In the final example, the authors, Lu et al. (2019), have designed and fabricated a robotic gripper which aims to grasp uncooperative objects as shown in fig. 1.5(c). In this work, the authors have chosen to replace traditional hydraulic actuators with an SMA-powered actuator due to their reduced complexity and points of failure. Additionally, their high energy density, low energy consumption and quick response when heated were attractive features for this application. The robotic gripper consists of three major subsystems: the SMA linear actuator, the hinge coupler mechanism and the gripping claws. The SMA linear actuator consists of eight SMA wires fixed on one end and fixed to a sliding shaft on the other end. This allows a stroke amplification of the linear actuator without reducing the output forces. The system offers some redundancy where if one of the wires fails, the other wires allows the continued operation of the SMA gripper. The coupler mechanism makes use of a cross-shear hinge mechanism to convert the linear actuator of the SMA actuator into the required dual parallel motion of the claws. The mechanism also offers a stroke amplification to the overall gripper. The biasing element allows the repeated actuation of the system and is accomplished using a simple passive spring. In this work, the authors have prioritized the high work density of the alloy to create a compact system with higher energy efficiency and higher longevity.

As shown in the presented examples, the key design criteria of SMA actuators in industrial applications are the lightweight and compact nature of the resulting SMA actuators. The use of SMAs and their high power-to-weight ratio has allowed actuators to be created that are lightweight and are, thus, highly attractive as end-effectors for robotic arms. Furthermore, using bistable mechanisms and bias-springs has allowed SMA-powered industrial grippers to be energy efficient by not requiring continuous energy to grasp objects. The biasing elements also allow the repeated actuation of the gripper without introducing any contaminants or complex assemblies. The slow cooling time and the reduce operating frequency has always been a challenge in industrial applications but has been outweighed by the high work density of the alloy.

1.3.4 Bio-inspired Robotic Applications

In the hunt for creating bio-inspired robotic system, there has been a intentional effort in finding smart materials that have similar performances to biological muscles. In this regard, the high volumetric work density of SMAs and its naturally compliant natures has made it comparable to biological muscles and has made it the primary candidate for bio-inspired applications. When creating such bio-inspired robotic systems, the main design constraints are often the weight and volume of the system. SMAs, being the ideal candidate for lightweight systems, allows robotic systems to be highly integrated and make use of the energy density of the material. Implementing traditional electromagnetic and pneumatic systems can be useful in creating tethered systems but when designing untethered systems that have a focus on reduced weight, implementing SMA-powered actuators have become a necessity.

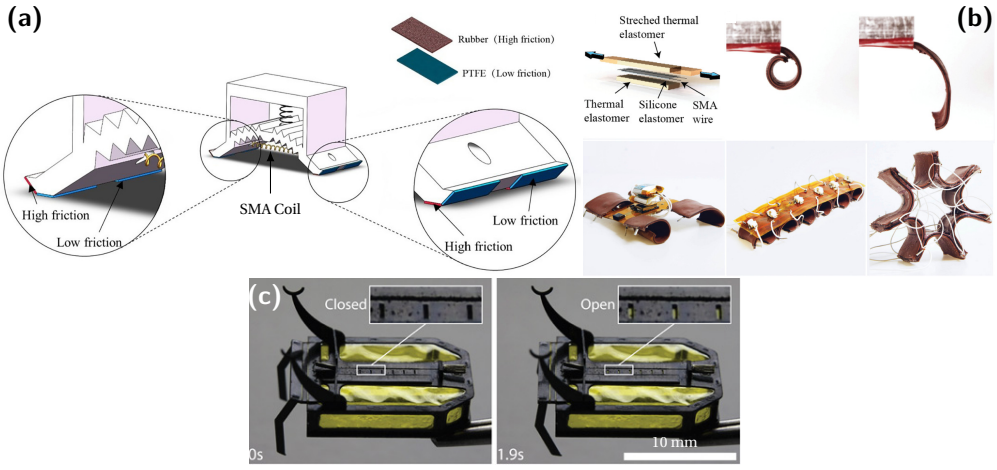

Figure 1.6: Examples of different implementations of SMA actuators in bio-inspired robotic systems : (a) A soft-actuated crawling robot taken from the work by Liang et al. (2020) (b) A highly dynamic mobile robot taken from the work by Huang et al. (2019) (c) A sub-milligram crawling SMA-powered robot taken from the work by Yang et al. (2020)

In this first example, the authors, Liang et al. (2020), have designed an SMA-actuated soft crawling robot. In this work, the authors have focused on creating a lightweight actuator

that is able to propel itself across a surface with a gait similar to an inchworm as shown in fig. 1.6(a). Due to the tight volume and weight constrains of the application, the authors have incorporated the elastic nature of the robot body as the biasing element to the SMA coil. However, the robot requires a passive spring as an auxiliary biasing element to accelerate the robot recovery and improve the gait coordination of the insect robot. The slow cooling of the SMA coil results in a slow gait for the insect robot but reducing the diameter of the coil can drastically increase the robot speed. However, the control of the robot and the electronics have not been integrated into the system. This tethered crawling robot has exploited the high energy density of the SMA to create a small lightweight robot.

In the second example, the work by Huang et al. (2019), presents a highly dynamic SMA-powered moving robot. Here, as shown in fig. 1.6(b), the authors exploit the naturally compliant nature and the high work density of the alloy to create the actuator that powered the moving robot. In this work, the SMA actuator consists of a single SMA wire encased in a biasing silicone elastomer. Furthermore, a thermally conductive elastomer is used to dissipate the heat from the SMA, acting as a heat sink, to increase the time response of the robot. Miniaturised power electronics has been added to the robot to allow the robot to move untethered. The flexural response of the SMA wire is used to actuate the robot and is also used as the crawling motion. The authors, by creating a highly integrated system, has allowed them to fully exploit the high work density of the smart material.

In the last example, the authors, Yang et al. (2020), have developed an ultra-lightweight crawling robot that is powered by a shape memory alloy wire. This autonomous sub-gram micro-robot, as shown in fig. 1.6(c), makes use a thin SMA wire attached to a small hinge that allows the actuation of the legs when the SMA is heated. The biasing element in this case is composed of a thin leaf spring that is used to create the two-way activation of the SMA actuator. The authors have achieved such a lightweight SMA-powered robot by avoiding the use of any senors or electronics and instead using a chemical heating element. A reservoir of methanol is used to heat the SMA wire using vents that are opened and closed based on the position of the robot legs. This mechanical control has allowed the authors to fully harness the high work density of the SMA wire and create an ultra-lightweight robot. In this case, the primary design principle that motivated the design of the robot was the final weight and energy density of the system.

When considering the different examples of bio-inspired robotic system, the common design criteria considered by the different authors has been to reduce the overall weight and complexity of the system. When creating such miniature and lightweight systems, designing monolithic parts with reduced complexity and assembly has been critical in harnessing the work density of the SMA actuator. In these examples, the SMA actuator has been integrated into the body of the robot as opposed to separating the actuator and robot body into discrete subsystems.

1.4 Design Criteria

The various actuators shown in the previous section display the diversity and variety of designs that exist to create an SMA actuator. When exploring the different domains in which SMAs are used, it shows that these alloys have become an attraction option to replace traditional pneumatic and electromagnetic actuators. Furthermore, it is evident that the domain in which the SMA is used has a large impact on the design and implementation of the actuator. This implies that when designing SMA-powered actuators, a holistic approach must be taken where the application and the entire system is considered in the design process.

In the case of biomedical applications, the SMA actuators are implemented based on the design constraints imposed by the human body. The various examples of biomedical applications are summarised in table 1.1. In this domain, the fact that SMA actuators have smooth operation and do not introduce any particulate matter as opposed to pneumatic or hydraulic systems, makes them an attraction alternative. Furthermore, when dealing with the tight volume constraints imposed by the human body, the high work density of the material becomes a crucial detail in the choice of the active material. Furthermore, as the SMA can be heated rapidly, using Joule's heating which involves simply passing a current across the SMA, a rapid actuation can be obtained which is highly attractive in this domain. As shown in the examples, small and powerful SMA wires and springs are used to create the actuators while passive micro-springs are employed to enable two-way actuation.

Table 1.1: A summary of the various implementations of the biomedical SMA actuators.

	Active Element	Biasing Element	Kinematic Stage	Heating Strategy	Sensor
Liu et al. (2019)	Wire	Micro-spring	Pin Pivot	Joule's heating	Thermistor
Abdul Kadir et al. (2019)	Flat springs	Elastic backbone	Rigid link / Backbone	Joule's heating	External Camera
Roshan et al. (2018)	Spring	Torsional spring	Pins and gears	Heated water	Thermocouple

When it comes to SMA actuators designed for automotive and aerospace applications, they are often conceived with high force outputs as a priority. Since the shape memory effect is scalable, these alloys can be used in micro and macro applications. Here, traditionally actuators used in this field at this scale tend to be bulky and heavy. The high work density of the alloy allows creating powerful actuators with large force outputs that are still lightweight when compared to similar traditional actuators. Furthermore, the rapid actuation and the low bandwidth required in these application has also allowed SMAs to penetrate the market. The fact that, often, SMA-powered actuators have a simple design and reduced complexity allows these actuators to be used in this domain that values longer lifespan and reduced failure points. In table 1.2, the implementation summary of the different examples are shown.

However in industrial applications, the higher operating bandwidth requirement has often

Table 1.2: A summary of the various implementations of the aerospace and automotive SMA actuators from the different examples.

	Active Element	Biasing Element	Kinematic Stage	Heating Strategy	Sensor
Williams et al. (2010)	Wires (in parallel)	Spring	Pivot	Joule's heating	External position sensor
Bellini et al. (2009)	Springs (in parallel)	Antagonistic SMA springs	Linear guide	Thermo-electric module	None
Benafan et al. (2019)	Tube	Torsional spring	Bearing and hinges	Heater catridge	Thermocouple

limited the use of SMAs. In cases where a soft gripper or a gripper that is lightweight, the natural compliance and the work density of the material has allowed it to adapt to the requirements of the industry. In some cases, the absence of contaminant as in the case of pneumatic grippers can be an attractive characteristic that force the adoption of SMA-based grippers. In this domain, the weight and force outputs of the actuator are the primary design constraints when considering the choice of active material. When designing SMA-powered grippers for industrial application, the weight if often factored into the design process. Furthermore, as the primary challenge of SMA actuators is the low operating bandwidth due to the cooling requirements, adequate sizing must be considered when designing the active SMA element for the use case scenario. In table 1.3, a summary of the different implementation strategies are shown when creating such SMA-based industrial grippers.

Table 1.3: A summary of the various implementations of the industrial SMA actuators.

	Active Element	Biasing Element	Kinematic Stage	Heating Strategy	Sensor
Rodrigue et al. (2017)	Wire	PDMS matrix	Shape setting	Joule's heating	None
Motzki et al. (2016)	Wire	Spring	Bistable mechanism	Joule's heating	None
Lu et al. (2019)	Wires (in series)	Spring	Cross-shear coupler	Joule's heating	External position sensor

In the last major domain in which SMAs are often employed, they are favoured due to their resemblance to human muscles with respect to their volumetric work density. In the case of bio-inspired actuators, the goal has always been to create the smallest and lightest actuator such that the system can remain in the mesoscale. This often imposed a strict weight and volume constraint for the actuator when dealing with bio-inspired robotic systems. SMAs, whose speciality is creating lightweight actuators, have often been the first choice for such systems. In table 1.4, the different implementations are displayed for the previously presented examples. Often, these robotic systems have been designed around the material rather than the other way around. This holistic approach, often used in this domain, is rarely exploited

in the other applications. The tight weight and volume constraints have force the authors to create highly integrated systems.

Table 1.4: A summary of the various implementations of the bio-inspired SMA-powered systems.

	Active Element	Biasing Element	Kinematic Stage	Heating Strategy	Sensor
Liang et al. (2020)	Spring	Elastic body and bias spring	Elastic body geometry	Joule's heating	None
Huang et al. (2019)	Wire	Silcome elastomer matrix	Elastomer shape setting	Joule's heating (Heatsink)	Thermistor
Yang et al. (2020)	Wire	Leaf spring	Flexural hinge	Chemical heating	Mechanical vents

As observed with the various examples, the constraints of the application plays a major role in the implementation and design of the SMA actuator. When studying the different applications, the major design constraints that are considered when designing these SMA-powered actuators, include :

- a weight constraint
- a volume constraint
- a high force or stroke output requirement
- a reduced contaminants or biocompatibility requirement
- a rapid actuation requirement
- or a two-way actuation requirement

Using these design constraints, the sizing and design choices can be made to create an SMA-powered actuator that is more suited for the desired application. In this work, these constraints and lessons learned from the various examples in the different applications are exploited and translated to other situations.

1.5 Traditional Design Elements of an SMA-based System

Using the various examples of SMA actuators, that were explored in the previous section, a holistic approach to SMA actuator design can be taken. In each case, the primary goal of the actuator was to exploit the high work density of the smart material to create a lightweight or compact actuator. Often, sub-optimal solutions were employed when compared with the implementations present in other domains. In the case of bio-inspired systems, the SMA actuators had a large focus on the work density and the final weight of the system, however, in

other domains such as industrial applications, these techniques could be employed to further improve the performances of the grippers. By translating lessons learned from one domain to another, the hope is to allow the entire robotic system to fully harness the high work density of the SMAs.

With the goal of improving the work density of the final system, the different SMA-powered examples can be studied to establish the areas in which a more integrated approach can be taken. As shown in the previous section, there are common subsystems that exist when designing the SMA-based robotic system. By establishing a commonality between the different types of actuators, the strategies employed in one domain can be easily translated to another. As shown in fig. 1.7, the SMA actuator can be divided in to four basic building blocks. These subsystems each have a specific role and allows the SMA actuator to perform the required output when actuated using a thermal load.

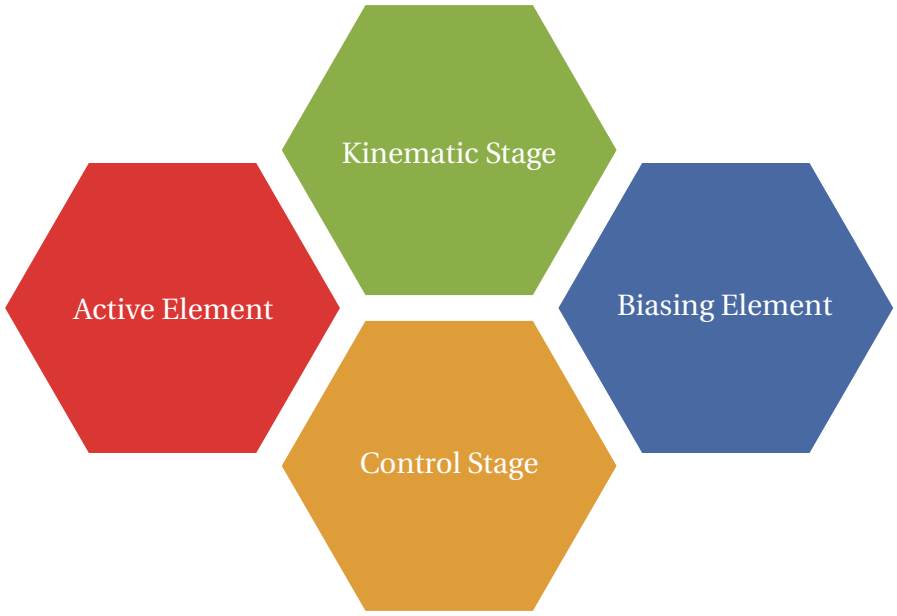

Figure 1.7: A visual representation of the different subsystems that exist in traditional SMA-based systems.

1.5.1 Building Blocks of an SMA Actuator

Often, these different subsystems exists as discrete building blocks in the SMA-based robotic system. These subsystems each fulfil a different role in the operation of the SMA actuator.

The **Active Element** is the SMA element that is present within the system and is responsible to providing the work for actuation. The SMA, as shown in the examples, can be fabricated in various shapes. Often, they are used as wires when space is limited, low strokes and high force outputs are required. When higher strokes are required, SMA coils are used as they are able to elongate over 100% of their length with a trade-off in force output. In certain cases,

thin SMA sheets are used for higher force output. In most cases, however, as passive cooling is employed, the geometry of the SMA element plays a major role in the operating frequency of the actuator. Here, thinner and smaller SMA sheets or wires allow for faster time responses.

In applications where two-way or repeatable activation is required, the **Biasing Element** is added to the actuator. The role of the biasing element consists of deforming the SMA at low temperatures so that the shape memory effect can occur when the active element is heated. As mentioned previously, the most simple forms of biasing elements consist of a deadweight, a passive spring or an antagonistic SMA. These elements allow the actuator to be actuated repeatedly or in both directions. The dependence of the SMA actuator for such a biasing subsystem greatly degrades the work density of the SMA actuator when considered as a whole. Often, in the case of SMA actuators, these passive elements allow the repeated actuation of the active element without providing any additional work.

As the traditional SMA-based actuator is often a linear actuator, some kind of **Kinematic Stage** is present to convert the linear movement of the actuator into the required output motion. In most cases, such as grippers, the simple linear motion of the SMA actuator is not sufficient. In such cases, the kinematic stage is employed using pins, hinges, gears and bearings, to convert the linear motion of the actuator into a more complex motion. In certain cases, this stage is used to amplify the stroke or output forces of the actuator. In the most simple applications, a hinge or lever arm is used to convert the linear movement of the actuator into a rotational one. The kinematic stage is, often, a critical subsystem when designing an SMA-powered robotics system.

The last subsystem, the **Control Stage**, consists of the electronics, sensors or heating mechanism used to activate and control the shape memory effect. In the case of SMAs, a thermal load must be applied to the active material to activate the shape memory effect and initiate the strain recovery of the alloy. In most cases, the simplest solution consists of harnessing the internal resistance of the SMA and heat the alloy using Joule's heating. Here, a current is passed across the SMA to allow Joule's losses to heat the material above its transition temperature and produce the required stroke. In such a case, considerable care must be taken to not overheat the material which will results in permanent shape setting of the SMA or destruction of the SMA wire or coil. In such cases, a temperature sensor, position sensor or even sensorless control is employed to control the heating process of the active element. This additional stage consisting of sensors or control electronics is not considered in the work density of the actuator and often degrades this density and efficiency. In cases where space or weight is limited, the control stage is an expensive addition to the actuator.

1.6 Summary and Conclusion

In this chapter, the working principle of the traditional SMA-powered actuator and the various examples of different implementations of SMA actuators in literature is presented. In the case of SMAs, the material requires a biasing element when requiring two-way activation. Only

when the alloy is pre-stressed above a critical stress will the material show any strain recovery when heated. Thus, in this chapter, the most common types of SMA actuator implementations are presented, detailing the ways in which the alloy can be pre-stressed as shown in the work by Bellouard (2008). Using passive springs or an antagonistic SMA as the biasing element is often the simplest and more efficient solution to creating a two-way SMA actuator.

In an effort to understand the different design considerations that exists when conceiving and fabricating SMA-based robotic systems, this chapter explores the major domains in which SMA-powered actuators thrive. Due to the high work density of the alloy, this material is often found in applications where weight and space constraints exist such as the biomedical, aerospace or automotive, industrial and bio-inspired applications. By studying various examples in each case, the dependence of the domain on the design constraints and implementations was made evident. Each major domain has a set of their own constraints which heavily affect the design of the actuator.

By studying these examples, a set of design considerations and constraints can be extracted so as to create a primary design principle when designing SMA-powered actuators. In most cases, the work density of the alloy is the main reason that compels the authors to integrate the SMA into their robotic system. When considering the various applications, taking a holistic design approach where the entire robotic system including the constraints are considered, can result in a considerable optimization of the work density. By exploring the strategies employed in certain domains and translating them to other domains can result in novel actuators.

Furthermore, in this chapter, studying the robotic systems from the various major fields has been used to establish the different subsystems that exists in a traditional SMA-powered actuators. The four subsystems are shown to have their respective functions and constraints. They are often designed independent of each other and are implemented without the consideration of the other subsystems. These building blocks of the SMA actuator, being discrete systems, show a considerable area in which these designs can be improved. Having discrete subsystems, that do not take into account the other subsystems, degrade the work density of the final system. In this work, a novel holistic approach to designing integrated SMA-powered actuators will be presented.

When designing such systems, sizing the SMA element based on the surrounding components is essential. The interactions between the different subsystems is often a balancing act that requires careful consideration of their respective mechanical properties. In the following chapter, the different SMA models are detailed and presented so as to adequately size the SMA element for the required stroke and force output of the actuator. The shape memory effect of the alloy is a multi-physical behaviour that is non-linear. The following chapter will present a simplified model and sizing methodology to create an adapted SMA-powered actuator.

2 Predicting the Shape Memory Effect

2.1 Introduction

Shape Memory Alloys (SMA) are a type of smart material that are known to exhibit some form of strain recovery. This exotic behaviour to revert back to its original shape comes from their ability to change their microscopic crystalline structures when subjected to some kind of non-mechanical external stimulus. Some types of SMAs are able to recover their original structure when exposed to a magnetic field and thus, they are often referred to as magnetic shape memory alloys as shown in the work by Faran and Shilo (2016). However, the most commonly used type of SMAs have the ability to recover large amounts of strain when exposed to a thermal load and is also the smart material used in this work.

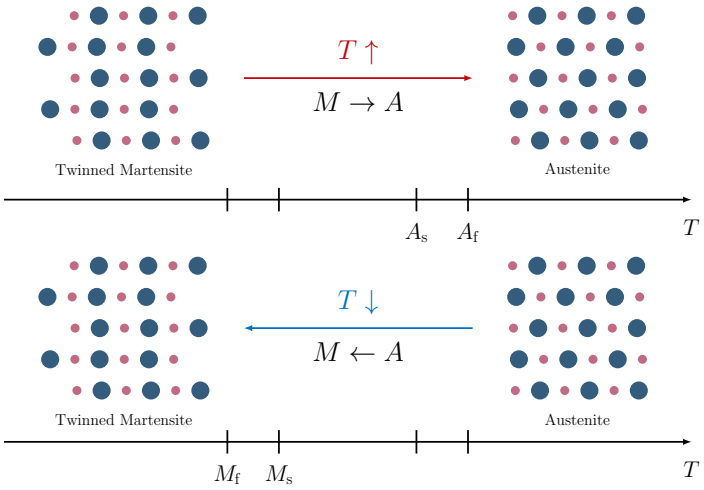

Figure 2.1: A visual representation of the phase transformations that occur during Shape Memory Effect (SME) under no load adapted from the work by Rao et al. (2015).

As shown in fig. 2.1, these alloys exist in two main phases : a stable low temperature Martensitic (M) phase and a stable high temperature Austenitic (A) phase. The transition between

these phases due to the realignment of the micro-structures is responsible for the interesting phenomenons observed in these alloys. A rise in temperature, above a certain temperature threshold, causes the recovery of residual misalignment of the crystalline structures during mechanical loading and unloading. Macroscopically, this realignment is observed as a recovery of any earlier strain imposed on the alloy and this is often referred to as the Shape Memory Effect (SME).

Table 2.1: The material properties of Ni-Ti taken from the work by Duerig and Pelton (1994) and Rao et al. (2015)

Material Property	Value
Density [g/m^3]	6.4-6.5
Specific Heat [J/kg °C]	450-620
Thermal Conductivity [W/m K]	8.6-18
Latent Heat [kJ/kg]	19-32
Electrical resistivity [10^{-6} Ω m]	0.5-1.1
Thermal expansion coefficient [10^{-6} K^{-1}]	6.6-11

The SME was first reported in the work by Chang and Read (1951) in the 1950s. However, since then, there exists several different alloys that demonstrate the same interesting behaviour as shown in the work by Wayman and Duerig (1990). The most commonly used alloy among these is the Ni-Ti alloy that was discovered at the US Naval Ordnance Laboratory in 1963 as thus, the alloy is often referred to as *NiTiNOL*. In this work, the almost equiatomic Ni-Ti based SMA alloy is used due to its commercial availability in various different geometries and its excellent mechanical properties as shown in table 2.1. Furthermore, various additives and changes in atomic ratios can be used to change the transition temperatures threshold. The change in phase occurs over a range of temperature and thus, as shown in fig. 2.1, when transitioning from the M to the A phase, the starting and finishing transition temperature are represented as A_s and A_f while the starting and finishing M phase transition temperature thresholds are represented as M_s and M_f, respectively.

In fig. 2.2, the entire SME cycle can be observed along with the various changes in the phase and crystalline structures. At low temperature, the alloy exists in the twinned M phase. When subjected to a certain critical stress threshold, there are some shear lattice distortions that allow the material to be highly deformed (~ 8%) and retain this strain. This effect is often referred to as detwinning and transforms the alloy to the detwinned M state. At high temperatures, above a certain threshold, the alloy transforms into the A phase and the crystalline structures are restructured such that the material reverts back to its original shape before the mechanical loading. If the material is mechanically loaded while in the A phase or by decreasing the transition temperature below the ambient temperature, any deformations imposed on the material is immediately recovered. This effect is known as Superelasticity or Pseudoelasticity

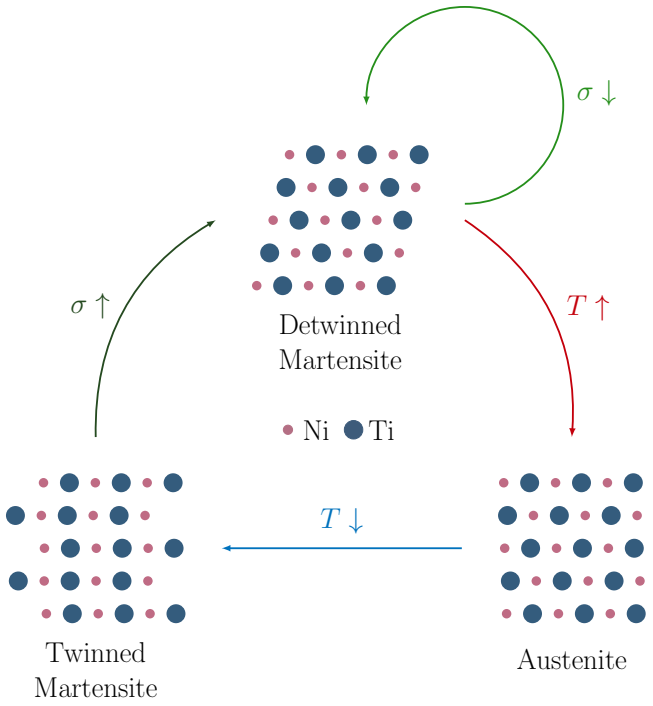

Figure 2.2: A schematic representation of the Shape Memory Effect (SME) showing the different phase transformations and crystalline structures where σ and T represent the applied mechanical and thermal load, respectively.

(SE) as shown in the work by Otsuka and Shimizu (1986). However, if the material is allowed to cool below the transition temperature, the alloy reverts back to the M phase where it can be deformed and retain its shape once again. This entire cycle is known as the SME and can be exploited to create highly compact and energy dense actuators. In fig. 2.3, the required latent heat of transformation can be observed during the forward and backward transformations between the M and A phases. Often, as shown in the work by He and Rong (2004) and represented in fig. 2.3, differential scanning calorimetry (DSC) can be used to accurately measure these transition temperature thresholds.

As shown in the previous chapter, the main design criteria for SMA-based actuators is having a small footprint or being lightweight. Thus, when designing actuators, the active element and the biasing elements have to be perfectly balanced so that neither subsystems are oversized which results in wasted space or weight. Furthermore, as the cooling is often passive in SMA-powered actuators, employing larger SMA elements can exponentially decrease the bandwidth of the resulting actuator. The accurate sizing of the SMA element and biasing elements are, thus, critical in designing a compact and dynamic SMA actuator. In this chapter, various analytical and finite element method (FEM) models are presented so as to accurately predict the SME. Furthermore, using the developed models, various complex and simplified sizing methodology are described and presented such that the SMA can be adequately sized for any

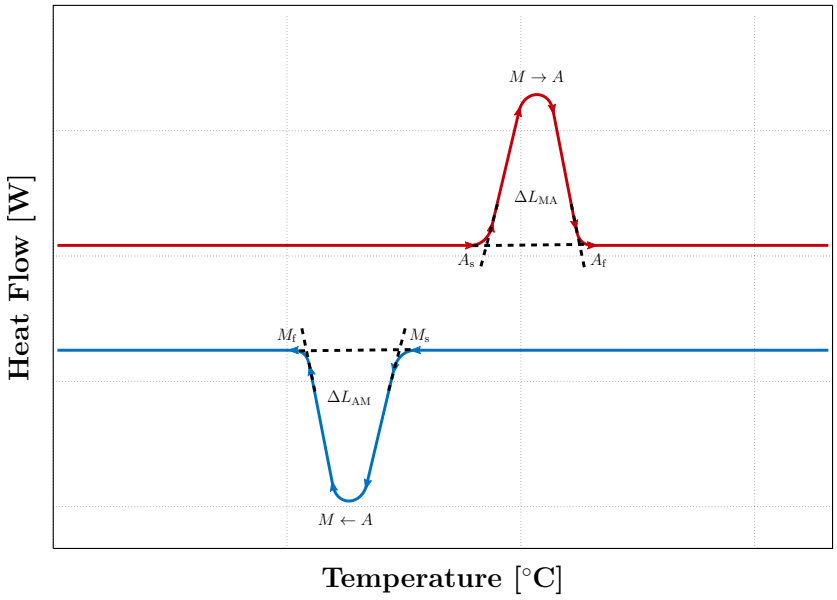

Figure 2.3: Schematic representation of a differential scanning calorimetry (DSC) graph showing the energy required during the SME where ΔL represents the latent heat of transformation between the two phases.

given application resulting in an energy dense actuator.

2.2 Analytical Modelling of the SME

The Shape Memory Effect (SME) is a difficult process to model analytically due to the different phase transformations and interdependent variables. In the work by Liang (1990), the authors presented a set of constitutive equations to describe a unified one-dimensional phenomenological model that incorporates the multi-physical nature of the SME and its internal variables. This model takes into account the phase transformations from the M and the A phases. The basic constitutive model presented by Liang (1990) is as follows,

$$d\sigma = \frac{\delta\sigma}{\delta\varepsilon}d\varepsilon + \frac{\delta\sigma}{\delta\xi}d\xi + \frac{\delta\sigma}{\delta T}dT \tag{2.1}$$

$$d\sigma = Ed\varepsilon + \Omega d\xi + \Theta dT \tag{2.2}$$

which can be further simplified using constant material functions as

$$\sigma - \sigma_0 = E(\varepsilon - \varepsilon_0) + \Omega(\xi - \xi_0) + \Theta(T - T_0) \tag{2.3}$$

where $E(\varepsilon,\xi,T)$ represents the Young's modulus of the SMA material, $\Omega(\varepsilon,\xi,T)$ represents the transformation tensor and $\Theta(\varepsilon,\xi,T)$ is the thermal coefficient of expansion of the SMA. Here, σ represents the stress, ε represents the strain, T represents the temperature and ξ

represents the martensite fraction of the material. Here, the subscript 0 indicates the initial conditions before the current phase transformation. Based on experimental evidence, as stated in the work by Liang (1990), the Young's Modulus, E, of the SMA is directly proportional to the martensite fraction of the material. Thus, the following assumption is made to estimate the Young's modulus :

$$E(\varepsilon, \xi, T) = E(\xi) = E_A + \xi(E_M - E_A) \tag{2.4}$$

where, E_A and E_M represent the Young's modulus of the SMA when it is entirely in the Austenite phase or the Martensite phase, respectively. Subsequently, the subscript M and A represent whether the material is currently in the Martensite or Austenite phases, respectively. Furthermore, in the case of SMAs, a material limit must be imposed such that the maximum residual strain, ε_L of the SME is incorporated into the model. This imposition creates a relationship between the Young's modulus and the transformation tensor :

$$\Omega = -\varepsilon_L E \tag{2.5}$$

In SMAs, the driving force that transforms the material from the A and M phases is the chemical free energy as a function of temperature and stress. In order to depict the martensite fraction as a function of stress and temperature during transformation, Liang (1990) developed an experimentally based cosine model, which fits well with experimental observations. The constitutive equations for the transformation from the A phase to the M phase, for $C_M(T - M_\mathrm{s}) < \sigma < C_M(T - M_\mathrm{f})$, are described as follows:

$$\xi = \frac{1-\xi_0}{2} cos\left[a_M\left(T - M_\mathrm{f} - \frac{\sigma}{C_M}\right)\right] + \frac{1+\xi_0}{2} \tag{2.6}$$

while the reverse transformation, with $C_A(T - A_\mathrm{f}) < \sigma < C_A(T - A_\mathrm{s})$, from the M phase to the A phase is described as follows:

$$\xi = \frac{\xi_0}{2} cos\left[a_A\left(T - A_\mathrm{s} - \frac{\sigma}{C_A}\right)\right] + \frac{\xi_0}{2} \tag{2.7}$$

where ξ_0 represents the initial martensite fraction prior to the current transformation, σ and T is the current applied stress and temperature on the material, and a_M and a_A are expressed as follows:

$$a_M = \frac{\pi}{M_\mathrm{s} - M_\mathrm{f}},\ a_A = \frac{\pi}{A_\mathrm{f} - A_\mathrm{s}} \tag{2.8}$$

The material property C_M and C_A, as shown in fig. 2.4, represent relationship between the critical stresses and transformation temperatures of the SMA. These constants are experimentally deduced and are considered linear as shown in the work by Yoo et al. (2015). These constants determine the critical stresses, σ_cr required to induce transformation or the determine the critical transformation temperatures at a certain imposed stress. The evolution of the martensite fraction based on the constitutive equations are shown in fig. 2.5.

The Liang (1990) model is effective at modelling the transformations from the martensite to the austenite phase and vice versa. This model is quite accurate when sizing actuators

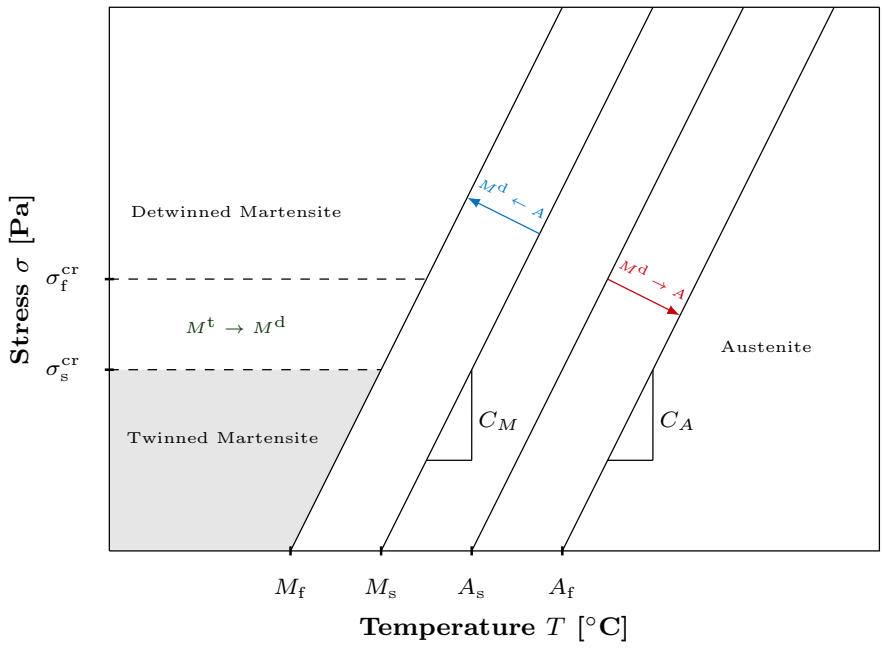

Figure 2.4: Graphical representation of the phase transformations showing the thermal and mechanical properties of the material. This graph presents the change in the transformation temperature based on the imposed stress on the SMA adapted from the work by Ricciardi and Antonucci (2021)

that have higher strokes where the material has always reached its maximum residual strain. However, the model does not take into account the crystal structure changes that exist in the M phase at lower temperatures. This crystal structure change, referred to as detwinning, as shown in fig. 2.2, occurs entirely within the M phase and results in a highly non-linear behaviour when a critical stress is imposed on the material.

The current model has described the internal state variable, ξ, to represent only the percentage of the material that has been changed into the M phase and does not consider the detwinning process. However, in the work by Brinson (1993), the authors have separated the internal state variable into two parts, the temperature-induced M phase ξ_T and the stress-induced M phase ξ_S as described by the following relationship:

$$\xi = \xi_S + \xi_T \tag{2.9}$$

This distinction allows the modelling of the shape memory effect starting from the M phase and the material's superelasticity. This division of the martensite fraction appropriately captures the microscopic activity of the material in the M phase. When the material is in the M phase at lower temperatures, ξ_T accounts for the temperature-induced crystal structure. Once sufficient stress is imposed on the material, the detwinning process converts the crystal structure to increase the value of ξ_S.

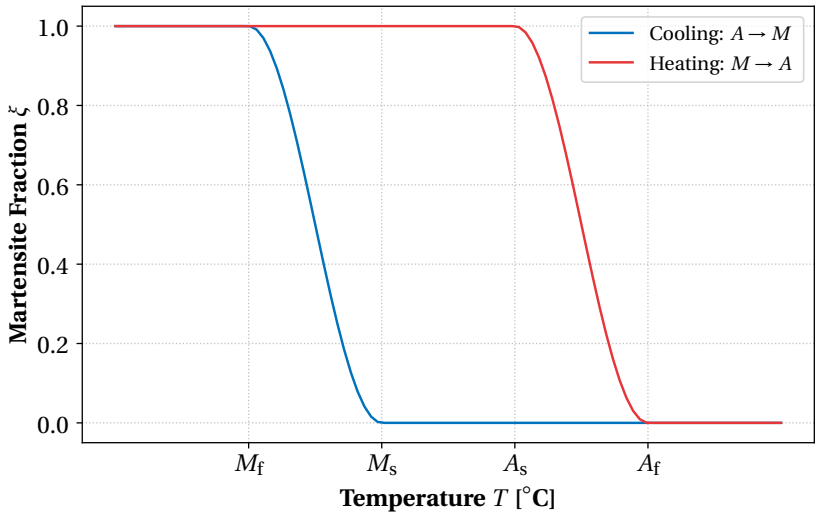

Figure 2.5: The relationship between the temperature and the martensitic fraction based on the Brinson (1993) constitutive equations. The strain recovery of the SMA is directly proportional to the martensite fraction.

Now, based on the changes made using the Brinson model, the original constitutive equations eq. (2.3), are adapted as follows:

$$d\sigma = \frac{\delta\sigma}{\delta\varepsilon}d\varepsilon + \frac{\delta\sigma}{\delta\xi_S}d\xi_S + \frac{\delta\sigma}{\delta\xi_T}d\xi_T + \frac{\delta\sigma}{\delta T}dT \tag{2.10}$$

which can be further simplified using constant material functions as

$$d\sigma = Ed\varepsilon + \Omega_S d\xi_S + \Omega_T d\xi_T + \Theta dT \tag{2.11}$$

$$\sigma - \sigma_0 = E(\varepsilon - \varepsilon_0) + \Omega_S(\xi_S - \xi_{S0}) + \Omega_T(\xi_T - \xi_{T0}) + \Theta(T - T_0) \tag{2.12}$$

where the subscript 0 indicates the initial conditions between the current phase transformations. Here, based on the material restrictions, $\Omega_S = -\varepsilon_L E$ and $\Omega_T \equiv 0$.

In the work presented by Brinson, the author has adapted the transformation equations and transformation stresses to represent the modified internal variables. The author was able to described the analytical model for the detwinning process by adapting the transformation equations presented earlier by Liang. Here, the constitutive model must be divided into three phases, due to the complexity of the shape memory effect: the detwinning process, the stress relaxation and the austenitic transformation. The detwinning process can be estimated by using equation 2.13 combined with equation 2.11, as presented below, with $T > M_s$ and $\sigma_s^{cr} + C_M(T - M_s) < \sigma < \sigma_f^{cr} + C_M(T - M_s)$:

$$\xi_S = \cos\left(\frac{\pi}{\sigma_{\mathrm{s}}^{\mathrm{cr}} - \sigma_{\mathrm{f}}^{\mathrm{cr}}}[\sigma - \sigma_{\mathrm{f}}^{\mathrm{cr}} - C_M(T - M_{\mathrm{s}})]\right)\frac{1-\xi_{S0}}{2} + \frac{1+\xi_{S0}}{2} \tag{2.13}$$

$$\xi_T = \xi_{T0} - \frac{\xi_{T0}}{1-\xi_{S0}}(\xi_S - \xi_{S0}) \tag{2.14}$$

However, for $T < M_{\mathrm{s}}$ and $\sigma_{\mathrm{s}}^{\mathrm{cr}} < \sigma < \sigma_{\mathrm{f}}^{\mathrm{cr}}$:

$$\xi_S = \frac{1-\xi_{S0}}{2}\cos\left[\frac{\pi}{\sigma_{\mathrm{s}}^{\mathrm{cr}} - \sigma_{\mathrm{f}}^{\mathrm{cr}}}(\sigma - \sigma_{\mathrm{f}}^{\mathrm{cr}})\right] + \frac{1+\xi_{S0}}{2} \tag{2.15}$$

$$\xi_T = \xi_{T0} - \frac{\xi_{T0}}{1-\xi_{S0}}(\xi_S - \xi_{S0}) + \Delta_{T\xi} \tag{2.16}$$

where, if $M_{\mathrm{f}} < T < M_{\mathrm{s}}$ and $T < T_0$,

$$\Delta_{T\xi} = \frac{1-\xi_{T0}}{2}\cos(a_M(T - M_{\mathrm{f}})) + \frac{1-\xi_{T0}}{2} \tag{2.17}$$

else, $\Delta_{T\xi} = 0$

Here, the stress relaxation phase is estimated by keeping ξ_S constant at 1 and by reducing the stress back to 0. Lastly, the austenitic phase transformation can be described using equation 2.11 and the following equation, for $T > A_{\mathrm{s}}$ and $C_A(T - A_{\mathrm{f}}) < \sigma < C_A(T - A_{\mathrm{s}})$:

$$\xi = \frac{\xi_0}{2}\left\{\cos\left[a_A\left(T - A_{\mathrm{s}} - \frac{\sigma}{C_A}\right)\right] + 1\right\} \tag{2.18}$$

$$\xi_S = \xi_{S0} - \frac{\xi_{S0}}{\xi_0}(\xi_0 - \xi) \tag{2.19}$$

$$\xi_T = \xi_{T0} - \frac{\xi_{T0}}{\xi_0}(\xi_0 - \xi) \tag{2.20}$$

where M_{s} and A_{s} are the Martensitic and Austenitic transformation start temperatures and similarly, M_{f} and A_{f} are the finish temperatures. While C_M and C_A are the same material properties that tie the internal stresses to a change in transformation temperatures. The details of the constitutive models and the different material constants can be found in work by Brinson (1993). The three phase transformations of the SME, based on the above constitutive equations, can be observed in fig. 2.6.

However, a 3D graph is required to properly display the entire cycle of the shape memory effect as the effect is dependant on the stress and the temperature of the material as shown in fig. 2.7. Here, the material is elongated with the imposition of a stress and the material undergoes the detwinning process where the crystal structures of the material are realigned.

When the stress is removed from the material, the strain is retained up to a maximum of ε_L. As the material is heated to a critical transition temperature, the strain is recovered and the material reverts back to its original shape. Finally, the material is cooled down to revert back to its initial state where the cycle can be repeated.

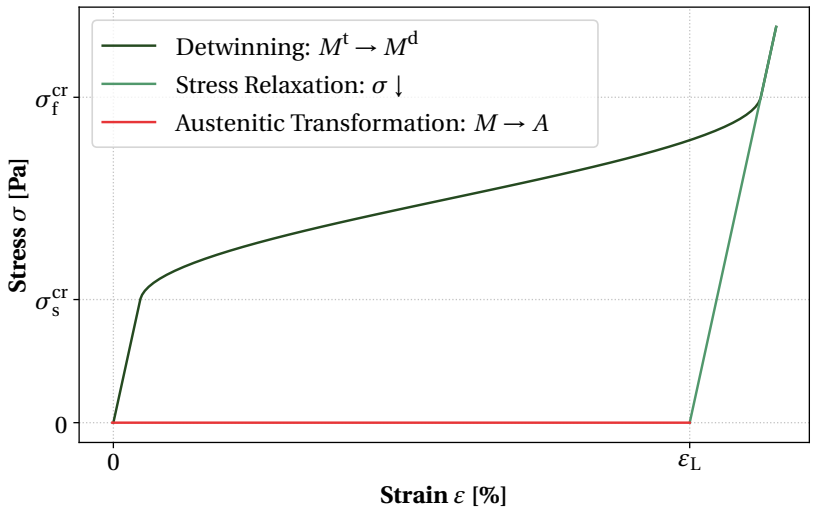

Figure 2.6: The analytical model of the SMA based on the Brinson (1993) constitutive equations. Here, the detwinning of the SMA, represented by the dark green plateau, and the heating of the SMA, represented in red, are shown.

2.3 Finite Element Modelling

The Shape Memory Effect is a complex behaviour that depends on various different material properties and variables. When working with SMA structures that are complex and are actuated in multiple dimensions, the simple one-dimensional constitutive models are no longer feasible. Recent development in modelling of the constitutive models of Shape Memory Alloys has allowed various commercial FEM simulation software to be able to simulate the shape memory effect and superelasticity of the alloy. In this work, *ANSYS, Inc.* was used to simulate the material and predict the effects of applying mechanical and thermal loads to SMA structures as described in ANSYS (2021). The shape memory effect was predicted using a three-dimensional thermomechanical model for stress-induced solid phase changes based on the work by Auricchio (2001) and Souza et al. (1998). The model is able to simulate all of the fundamental properties of shape memory materials in a 3-D stress state within the context of conventional irreversible thermodynamics. The model used to simulate the SME within the FEM software is based on the free energy potential:

$$\Psi(\varepsilon, T, \varepsilon_{tr}) = \frac{1}{2}(\varepsilon - \varepsilon_{tr}) : E : (\varepsilon - \varepsilon_{tr}) + \tau_M(T)||\varepsilon'_{tr}|| + \frac{1}{2}H||\varepsilon'_{tr}||^2 + I_{\varepsilon'_{tr}}(\varepsilon'_{tr}) \tag{2.21}$$

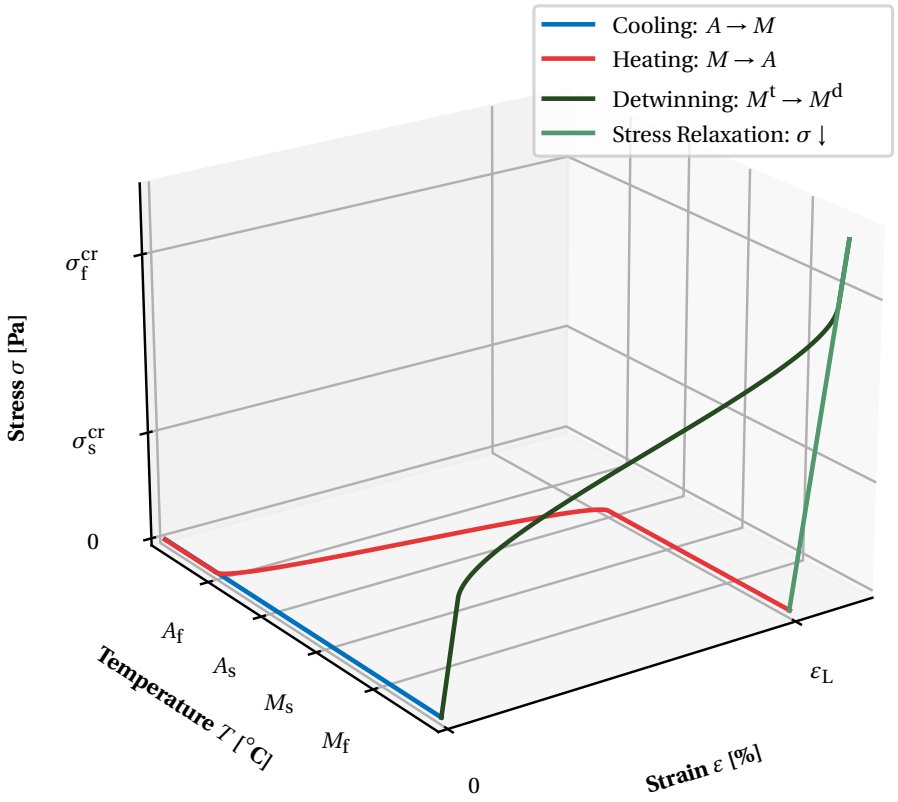

Figure 2.7: The 3D graph showing the Brinson (1993) analytical model of the entire Shape Memory Effect cycle.

where E is the material elastic stiffness tensor, ε is the total strain, ε_{tr} is the total transformation strain, ε'_{tr} is the deviatoric transformation strain, C is the material parameter, $\tau_M(T)$ is a positive monotonically increasing function based on $C(T - T_{ref})$, T is the temperature, T_{ref} is the reference temperature, H is a material parameter related to the hardening of the material during phase transformation and $I_{\varepsilon'_{tr}}(\varepsilon'_{tr})$ is an indicator function that satisfies the constraint on the transformation norm based on Auricchio and Petrini (2002). From this, the stress σ and transformation strain X_{tr} can be deduced as :

$$\sigma = \frac{\delta\Psi}{\delta\varepsilon}, \; X_{tr} \in -\frac{\delta\Psi}{\delta\varepsilon'_{tr}} \tag{2.22}$$

In order to model the shape memory effect of the alloy, a customised material is described by initialising the material data table in *ANSYS*. The shape memory effect option is defined by the density, the Young's modulus in the A phase, the Poisson's ratio and seven material constants as described in table 2.2. These define the stress-strain behaviour of the alloy during the loading and unloading cycles and during thermal loading. These parameters can be obtained from the suppliers or using experimental data from literature as shown in the work by Malagisi

et al. (2017).

Table 2.2: The definitions of the parameters used to define the SME in the commercial FEM software, ANSYS (based on the work by Jaber (2018)).

Parameter		Definition
Density	ρ	SMA density
Young's Modulus	E_A	Ausenite Young's modulus
Poisson's Ratio	θ_A	Austenite Poisson's ratio
Hardening Parameter	H	Slope of $\sigma-\varepsilon$ curve during $A \rightarrow M$
Reference Temperature	T_{ref}	Temperature at which critical stresses are estimated
Elastic Limit	σ_{s}^{AM+}	Critical starting stress for $A \rightarrow M$
Temperature Scaling Parameter	C	Slope of the $\sigma - T$ relationship for both transformations
Maximum transformation strain	ε_{L}	Maximum recoverable strain, $\max(\|\|\varepsilon'_{\text{tr}}\|\|)$
Martensite Modulus	E_M	Martensite Young's modulus
Lode dependency parameter	β	Parameter that determines asymmetrical behaviour between compression and tension

The shape memory effect is defined by the stress-strain curves based on the different mechanical and thermal loading cycles as shown in fig. 2.8. Each parameter defined within the material data within the FEM software has an effect on the curves. The effect of each parameter has been described and explored in the work by Jaber (2018). Furthermore, the various material parameters used in the material data table can be defined by their relationship to the critical transformation stress and temperatures as shown below. The hardening parameter, H, as defined below, defines the change in the slope of the $\sigma-\varepsilon$ curve during the detwinning process.

$$H = \frac{\sigma_{\text{f}}^{AM+} - \sigma_{\text{s}}^{AM+}}{\frac{\sigma_{\text{f}}^{AM+}}{E_M} + \varepsilon_{\text{L}} - \frac{\sigma_{\text{s}}^{AM+}}{E_A}} \tag{2.23}$$

Here, the superscript + and − represent whether the material is loaded in tension or compression, respectively. Furthermore, the superscript MA and AM represent the transformation from the M to the A phase and vice versa. Lastly, the subscript s and f represent the start and finish thresholds, respectively. The temperature scaling parameter is defined in eq. (2.24), and is shown in fig. 2.8 by the relationship between the transformation temperature and stress.

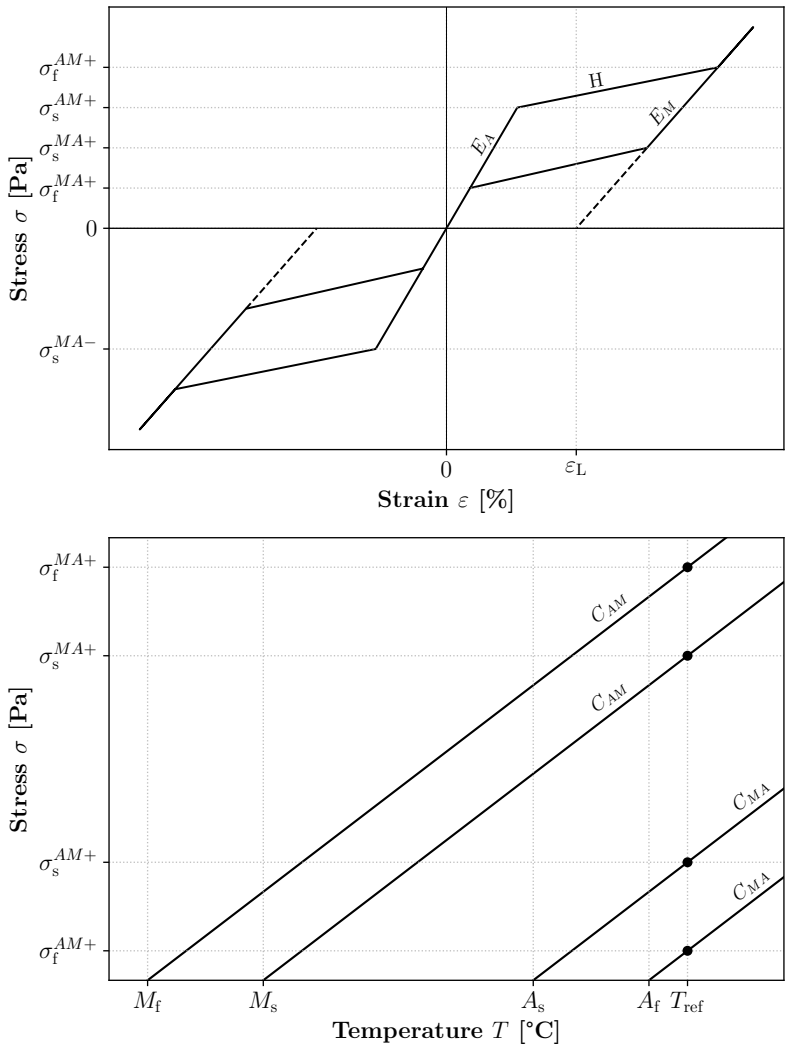

Figure 2.8: A visual representation of the various parameters required to define the Shape Memory Effect within the FEM model based on the work by Jaber (2018).

$$C = C^{AM} = C^{MA} = \frac{\sigma_f^{MA+}}{T_{ref} - A_f} \tag{2.24}$$

In most constitutive models, the SMA behaves symmetrically in tension and compression. However, numerous experimental tests show that there is an asymmetrical behaviour between the two and in this model, the lode dependency parameter, β, as defined below, takes into account this asymmetry.

$$\beta = \frac{|\sigma_s^{AM-}| - \sigma_s^{AM+}}{|\sigma_s^{AM-}| + \sigma_s^{AM+}} \tag{2.25}$$

Using the FEM simulations of the SMA, complex structures composed of the alloy can be used to predict the behaviour of the SME when the thermal load is applied. This strategy can be used to estimate the force requirements when sizing the biasing elements and the stroke output of the overall actuator when activated. However, the computation time of the simulation can be high and thus, using this strategy to optimise designs might not be feasible. Using the one-dimensional analytical models validated by the FEM simulations can be effective in designing SMA actuators in most cases.

2.4 Stroke Estimation of SMA Actuators

As the biasing element plays a major role in the operation of the SMA actuator, the first step in estimating the stroke and force characteristics of the actuator consists of determining the force-displacement profile of the biasing element. In this section, the biasing element is considered to be a linear spring as this is the most common type of SMA actuator implementation. However, this methodology can be applied to any biasing element as soon as its behaviour has been modelled. With the help of eq. (2.26) and the dimensions of the SMA, such as the cross-section area of the SMA, A_{SMA}, and the length of the SMA, L_{SMA}, the stress-strain characteristics of the SMA can be converted into the required force-displacement profile used to compare with the biasing element. In the case of a linear spring with stiffness, K_{BS}, eq. (2.27) can be used to obtain the relevant force-displacement curve of the biasing spring.

$$F = A_{\text{SMA}}\sigma,\ x = L_{\text{SMA}}\varepsilon \tag{2.26}$$

$$\sigma A_{\text{SMA}} = -K_{\text{BS}}\left(L_{\text{SMA}}\varepsilon - x_{\text{off}}\right) \tag{2.27}$$

In fig. 2.9, the schematic of a standard bias-spring SMA actuator shows the simplified operating principle of the actuator. Here, the SMA and the biasing spring are separated by a distance, x_{off}, so as to apply the initial pre-stress to the SMA element. This offset allows the SMA to be biased and detwinned at the lower temperatures. As shown in the diagram, when heated, the SMA contracts to a length, $L_{\text{SMA}} + x_2$, and when cooled, the SMA elongates to a length, $L_{\text{SMA}} + x_1$. Thus, the stroke of the actuator, Δx, can be easily deduce by taking the difference between the two lengths, $x_1 - x_2$, as shown in the figure.

The stroke of the bias-spring SMA actuator can be estimated using the Brinson (1993) model. Firstly, with a known temperature, $T < A_{\text{s}}$, the martensite fraction can be deduced using eq. (2.13) and eq. (2.14). When substituting σ with the bias-spring equation 2.27, a relationship between ξ and ε can be obtained. This relationship, combined with eq. (2.12), the strain, ε, and consequently, the elongation, x, of the SMA can be estimated with respect to its temperature, T. In most cases, however, the cold state exists completely within the detwinned state and the

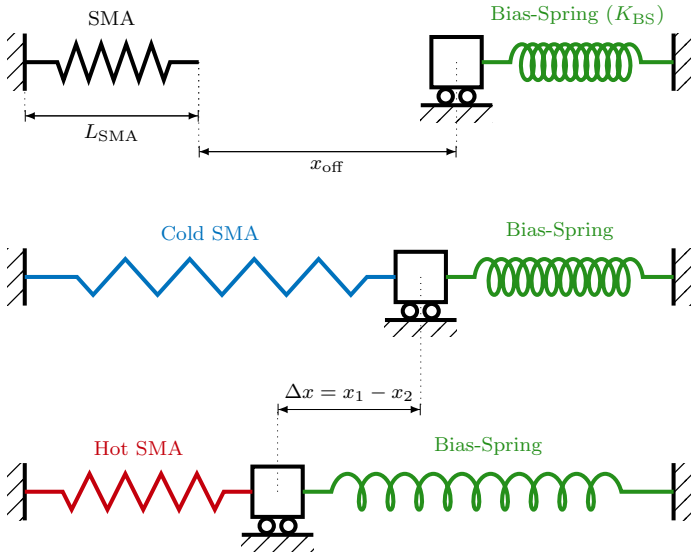

Figure 2.9: A schematic representation of the Bias-spring SMA actuator showing the different variables and the stroke estimation based on the SMA temperature.

hot state exists entirely in the A phase so as to maximise the stroke of the SMA actuator. This consideration can simplify the analytical model.

In the case of the cold state, with $T_1 < M_f$, $\xi_S = 1$ and $\xi_T = 0$, the elongation of the cold bias-spring SMA actuator, x_1 can be estimated as:

$$x_1 = \frac{K_{BS} x_{off} - A_{SMA}(\Omega_S + \Theta(T_1 - T_0))}{\frac{A_{SMA} E_M}{L_{SMA}} + K_{BS}} \tag{2.28}$$

Similarly, in the case of the hot state, where the SMA has been completely transformed into the A phase, with $T_2 < A_f$, $\xi = 0$, the elongation of the hot bias-spring SMA actuator, x_2 can be estimated as:

$$x_2 = \frac{K_{BS} x_{off} - A_{SMA}\Theta(T_1 - T_0)}{\frac{A_{SMA} E_A}{L_{SMA}} + K_{BS}} \tag{2.29}$$

Thus, as stated previously, the stroke of the system can be deduced as $\Delta x = x_1 - x_2$ as shown in fig. 2.10. This graph shows the sizing of an SMA actuator comprised of a 100 μm SMA wire of length 30 mm and a biasing spring with a spring constant of 3.5 N/mm separated by a distance of 6 mm. As presented in the previous equations, the Brinson model has been adapted such that the operating points of the actuator and the stroke can be easily estimated. The material constants, as shown in table 2.3, can be obtained from the supplier or using experimental data from literature such as the work by Elahinia and Ahmadian (2005). The required forces can be easily obtained by using the spring model described in eq. (2.27). This one-dimensional model can be quite effective when sizing actuators powered by sheets or wires. However, when

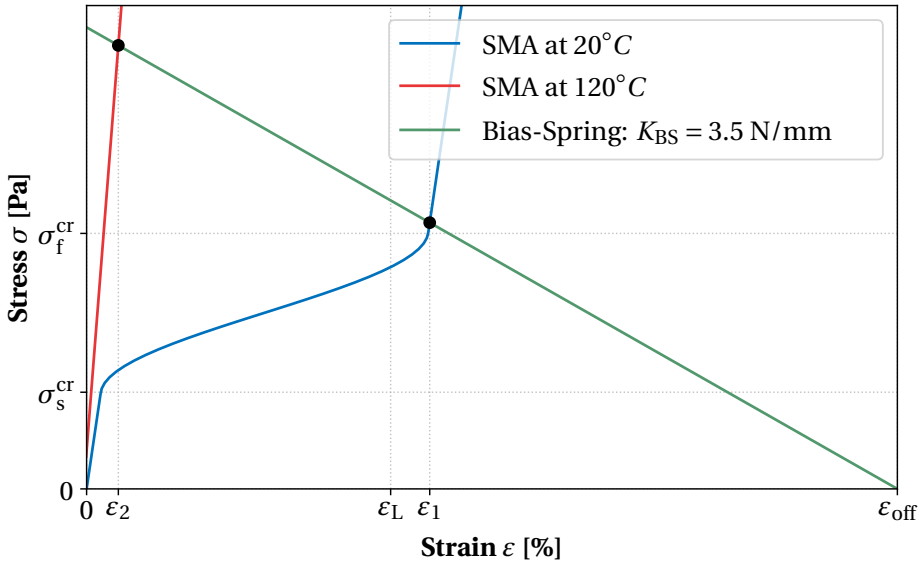

Figure 2.10: A plot showing the stroke estimation of a 100 μm SMA wire actuator using the equations adapted from the Brinson (1993) analytical model. Here, the bias spring is offset from the SMA with a distance of 6 mm and where $\varepsilon_i = x_i / L_{SMA}$

designing actuators with more complex biasing elements or additional mechanical stages, the analytical models of the system can become quite complicated.

2.5 Simplifying the Sizing of the SMA Actuator

Owing to their high power densities, SMA-based actuators are extensively used in mini- and micro-actuators. However, when considered for applications where high-output forces and strokes are required, they are limited. When under tension in the form of SMA wires, this alloy can generate high forces but can only exert it for up to 8% of their length. Thus, in many cases where higher strokes are required, these SMA wires are wound into helical springs which allows them to have high strokes but comes at the cost of their output forces.

As stated previously, the one-dimensional model is quite effective at sizing simple SMA-powered systems. However, when employing SMAs in more complex applications, a simpler methodology has been adopted to size these actuators. When dealing with SMA wires, under uniaxial tension, the highly non-linear Brinson (1993) model is an accurate tool in sizing the actuator. However, when considering an SMA helical spring, the constitutive models appear more linear in its low temperature state as shown in fig. 2.11. Thus, for most design cases, some experimentally-validated assumptions, as stated in the work by Dragoni and Spaggiari (2021), can be made such that the material behaviours can be linearised. Here, the stress-strain curves, as shown in fig. 2.12, can be replaced with straight lines. Here, in this model, the high temperature or Austenitic SMA curve can be replaced with a straight line originating from the

Table 2.3: Some examples of the material properties used in the analytical modelling of the SMA actuator.

Material Property		Value
Martensite Start Temperature	M_s	80 °C
Martensite Finish Temperature	M_f	75 °C
Austenite Start Temperature	A_s	85 °C
Austenite Finish Temperature	A_f	90 °C
Martensitic Young's Modulus	E_M	30 GPa
Austenitic Young's Modulus	E_A	75 GPa
Temperature Scaling Parameter	C_M, C_A	10.3 MPa/°C
Thermoelastic Constant	Θ	0.55 MPa
Maximum Recoverable Strain	ε_L	7.5%
Detwinning Critical Start Stress	σ_f^{cr}	140 MPa
Detwinning Critical Finish Stress	σ_s^{cr}	370 MPa

centre with a slope of E_A while the low temperature or Martensitic SMA curve can be replaced by a straight line with slope of E_M and offset by σ_0.

The A phase of the SMA occurs when the material is heated above its transition temperature, A_f, and reverts back to the M phase when the temperature drops back down below the martensitic transition temperature, M_f. However, as shown in fig. 2.4, there is a relationship between the stress imposed on the alloy and its transition temperatures. This implies that that when sufficiently above a certain critical stress threshold, σ_s^{AM}, the A phase SMA will revert back to the M phase reducing the rigidity of the material. As the SMA actuator operates by the change in material rigidity between the high temperature and low temperature phases, this change in rigidity at the critical stress threshold will cause the actuator to have a reduced stroke. Thus, when designing SMA actuators, this maximum stress or force output must be taken into account using eq. (2.30). In the case where the biasing element exceeds this critical stress, the final stroke of the material is greatly reduced as the material will be operating within its super-elastic region.

$$\sigma_s^{AM} = C_M(T - M_s) \tag{2.30}$$

In this work, SMA helical springs are used due to their availability and their ability to generate large strokes. The material properties were obtained experimentally and by curve-fitting the resulting force-displacement profile. In this case, a PID controller paired with a thermal

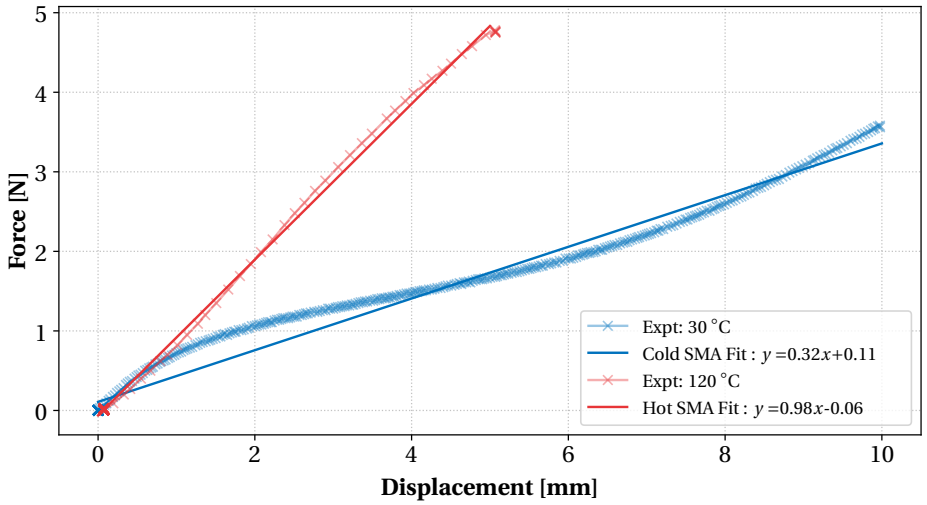

Figure 2.11: Using curve fitting to estimate the simplified material properties of the high temperature and cold temperature SMA helical spring. Here, the spring has a wire diameter of 250 μm, with a mandrel diameter of 0.5 mm and a length of 100 mm.

camera as a feedback is used to maintain the SMA spring at a constant temperature. A pull-tester is used to elongate the spring while measuring the force to obtain the force-displacement profiles at the required constant temperature. These isothermal traction tests are then curve fitted to obtain the material properties in the M and A phases. Finally, these simplified curves can be used to size the SMA-powered actuators.

While the behaviour of the shape memory effect in these springs is still non-linear, the simplified linearised curves can be used to obtain the operating points of SMA actuators as shown in fig. 2.12. These experimental results show that the simplified curves are able to quite accurately depict the force-displacement behaviours of SMA helical springs. In the following chapters, the force-displacement profiles obtained from the experimental results have been used to size the various SMA-based actuators.

This methodology of using the respective hot and cold force-displacement profiles is a useful approach to sizing and characterizing an SMA actuator. However, when multi-output systems are employed and kinematic stages with complex behaviours are integrated, this methodology must be appropriately adapted so as to accurately size the active SMA element and predict the actuator stroke. In the following chapters, this simplified methodology is adapted and employed in the sizing of more complex and integrated SMA-powered actuators.

2.6 Summary and Conclusion

In this chapter, the thermomechanical behaviour referred to as the shape memory effect has been presented and modelled. Various modelling strategies, such as finite element modelling

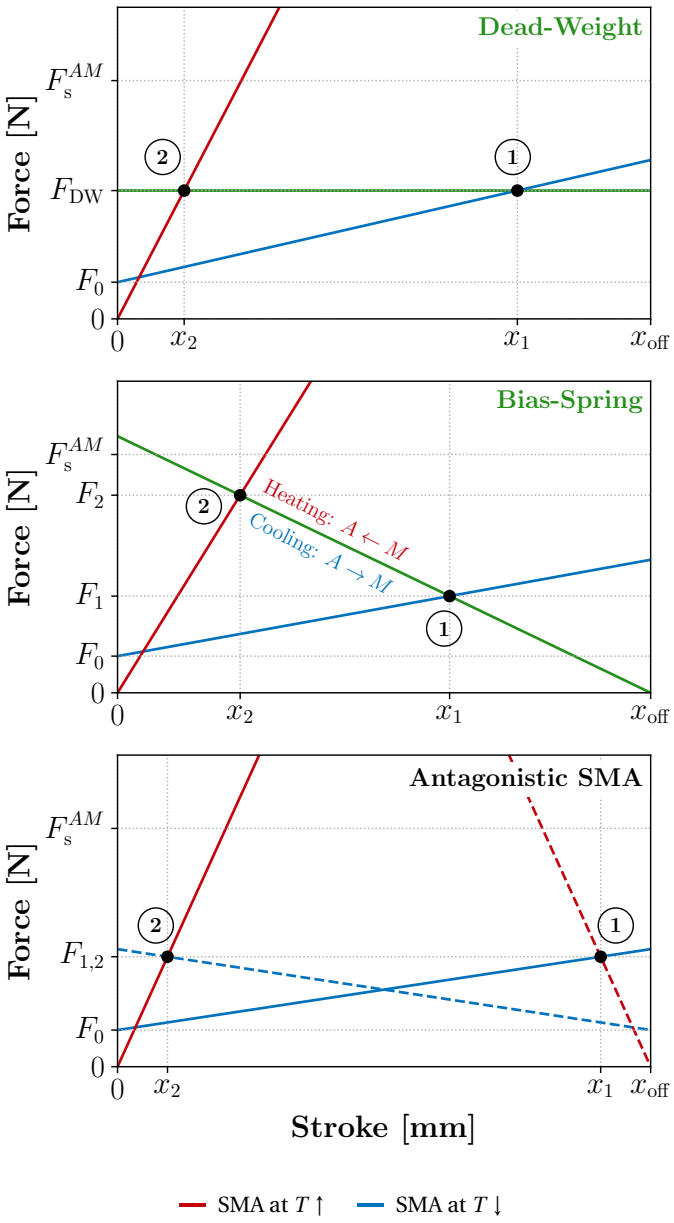

Figure 2.12: The simplified sizing methodology of an SMA actuators. Here, the force-displacement characteristics of the SMA are simplified adapted from the work by Dragoni and Spaggiari (2021).

and analytical modelling, are presented. The models have been used in the scope of predicting the shape memory effect such that actuators powered by these SMAs can be adequately and accurately sized. In the context of traditional SMA actuators, the models have been adapted and described so as to present the traditional design methodology often employed in SMA-based actuators such as the ones presented in chapter 1.

The SME occurs due to various microscopic structure changes that occurs during phase transformations as the alloy is subjected to a thermal load. In the first section, the different phase transformations and crystal structure changes are presented and described. By taking into account the presence of different phases and phase transformations, the requirements and conditions required by the SME cycle is presented and described.

In the context of predicting the SME, the Liang (1990) analytical model is presented. This 1-dimensional phenomenological model has been able to provide some constitutive equations that describes the transformation of the alloy between the high temperature A phase and the low temperature M phase. This model, widely used in traditional SMA actuator design, has been presented in this chapter. However, this model does not take into account the low rigidity and highly elastic nature of the SMA at low temperatures. The Brinson (1993) model, on the other hand, has taken into account the stress induced detwinning process into the phenomenological model and has allowed the model to accurately describe the thermomechanical behaviour of the SMA at low temperatures.

Furthermore, in this chapter, the modelling of SMAs and its shape memory effect using commercial FEM softwares is presented. These softwares make use of the Auricchio (2001) equations to accurately model the 3-dimensional behaviour of the alloy when subjected to thermal and mechanical loading. The FEM models have enabled designers to predict the behaviour of the SMAs in cases with more complex geometries and in scenarios where the 1D Brinson (1993) models are not sufficient. Furthermore, the various material properties required to define the FEM material model has been showcased.

Using the constitutive equations presented in this chapter, the sizing methodology of the SMA actuators are displayed. Using the Brinson (1993) model, the stroke of a commonly used biased-spring SMA actuator is estimated. This adapted model, shown in this chapter, uses the change in rigidity between the two phases of the alloy and the force-displacement profiles of the biasing elements to establish operating points for the actuator based on the temperature of the active element. This methodology allows an accurate sizing of the biasing spring and active SMA element such that the resulting actuator can be designed for any application or scenario. The accurate sizing of the SMA allows employing the smallest and most efficient SMA elements so as to create an actuator that has a compact footprint and a high bandwidth.

In many cases, the highly non-linear nature of the SMA renders the sizing of the SMA actuator quite difficult and computational expensive. Furthermore, in the case of SMA helical springs, the resulting force-displacement curve used in the sizing methodology can be linearised without losing too much accuracy in the stroke estimation. This simplified linear model can be extrapolated to other SMA-based actuators so as to obtain a relatively simple sizing methodology that can be used to estimate in the stroke in the various types of simple SMA actuators.

In the case of SMA-powered actuators where the biasing element or the active element are more complex or perform multiple roles using the same structure, this traditional design

methodology must be adapted. In the following chapters, this work focuses on adapting the traditional design methodology such that the same principle can be implemented in cases where the actuator has been highly integrated. Furthermore, the chapters focus on adapting the methodology such that more complex active and biasing elements can be employed while still being able to accurately size each subsystem.

Publications related to this chapter :

S. Thomas, M. Almanza, and Y. Perriard, *"Design Analysis of a Shape Memory Alloy Bias-Spring Linear Actuator,"* in 2019 12th International Symposium on Linear Drives for Industry Applications (LDIA), Neuchatel, Switzerland, Jul. 2019, pp. 1–5. doi: 10.1109/LDIA.2019.8770987.

3 Development and Modelling of Biased Kinematic Stages for SMA Actuators

3.1 Introduction

In the past few decades, there has been a growing need for miniaturisation. Modern devices have come to require actuators that are compact and lightweight. As mentioned previously, since SMAs have been known to show the highest volumetric work density, they have been increasingly used in applications where compactness and low weight are required.

As previously presented in chapter 1, SMA actuators require an active element, a biasing element and a kinematic stage for motion control. These components, usually as discrete elements, when combined together create an SMA actuator that can preform a specific reversible work, such as gripping as in the work by Lu et al. (2019) or crawling motions as in the work by Yuk et al. (2011). With the objective of miniaturisation, most work has been conducted into rendering these individual components as compact and lightweight as possible as shown in the work by Nespoli et al. (2010). But the fact that these stages are discrete, lowers the overall volumetric work density of the complete actuator. Furthermore, as multiple systems are needed, the actuator also requires various pieces and assembly increasing the complexity and decreasing the compactness.

Recently, there has been a shift in creating novel motion control mechanisms using flexure-based mechanisms. These flexures are multiple compliant elements designed so as to only be compliant in specific degrees of freedom while being rigid in the others. These mechanisms, which can be fabricated using a monolithic piece of material, are lightweight and require virtually no assembly. These flexural stages, when paired with SMAs, have greatly increased the overall work density of the traditional SMA actuators as shown in the work by Yang et al. (2020).

These flexure-based mechanisms are still often integrated into the SMA actuators as discrete mechanisms. In this chapter, the concept of integrating the biasing element as a flexural mechanism is explored. In this case, the kinematic stage and the biasing element are combined and are no longer discrete systems within the mechanism. Some research has been shown

to take into account flexure mechanisms in SMA actuators but they lack a suitable sizing strategy due to the complexity of the shape memory effect and the nonlinear nature of flexures as observed in the work by Scholtes et al. (2021). Thus, in this chapter, this novel design methodology is presented and analysed using an analytical model. The goal of the proposed design methodology where SMAs paired with an integrated biasing kinematic stage, can be adequately sized for the required project specifications.

Furthermore, in this chapter, the design methodology for extending this approach to antagonistic SMA actuators are also presented. When using flexure-based kinematic stage, they present with an inherent stiffness but can also be designed to exhibit interesting mechanical behaviours such as multi-stability. This chapter, will present a design methodology and a sizing strategy that allows antagonistic SMA actuators to be appropriately sized for pairing with complex flexure-based kinematic stages. This design methodologies will be validated using a case study and further extrapolated in the following chapters.

3.2 Adapted Design Concept

As mentioned previously, most SMA actuators are composed of an active element, a biasing element and a kinematic stage charged with converting the linear output of the actuator into a more complex one. In general, these elements are discrete components ranging from SMA coils, passive biasing springs and the kinematic stage comprised of hinges and linear slides. As presented in fig. 3.1, the design methodology consists of integrating the kinematic stage and the biasing element into a single subsystem.

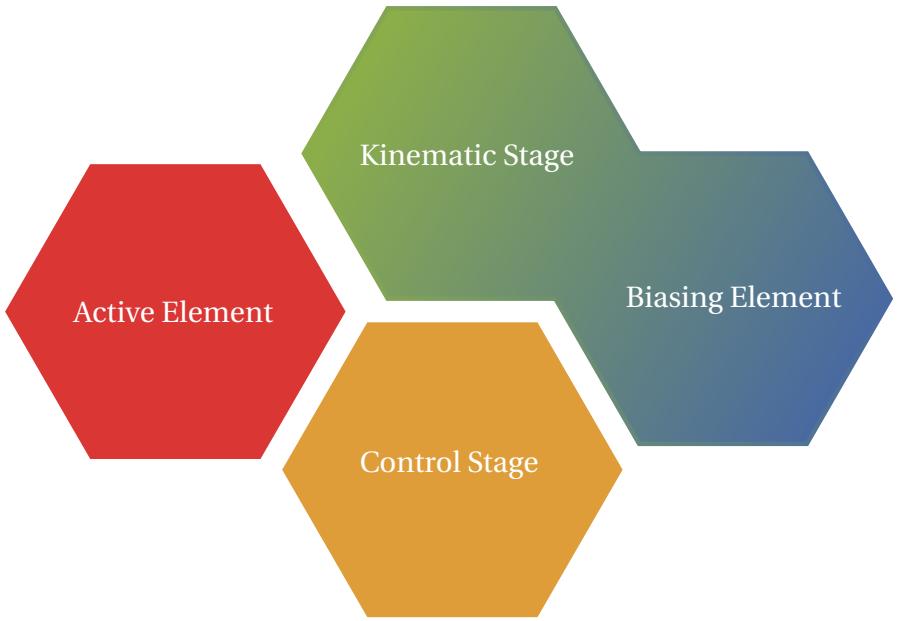

Figure 3.1: Diagram of the adapted building blocks of the SMA actuator.

This integration can be accomplished with the use of flexure-based mechanisms. Generally,

flexures have been used in creating an alternative solution for traditional hinges and linear slides. These flexures are comprised of cantilever beams which allows the mechanism to be compliant in a specific direction while being rigid in the others. As stated earlier, the advantages of such a system is that, when adequately designed, can result in a kinematic stage that is lightweight, lacks any assembly and has high precision.

The main drawback of such a system, compared to traditional bearings, is the inherent stiffness of the mechanism. As these flexures are composed of compliant beams, the rigidity of the beam must be taken into account. In the case of an SMA actuator, this rigidity of the compliant structure can be harnessed as the biasing element. This implies that by pairing the active SMA element with a flexure, the kinematic stage and the biasing element can be combined. This novel approach can be used to create biased SMA actuators that are precise, lightweight and with a limited number of pieces to be assembled.

3.3 Challenges of the Approach

Due to the complex nature of the shape memory effect, the principle challenge when it comes to designing such SMA actuators is the difficulty in sizing the active SMA based on the flexure mechanism. Based on the configuration of the flexural stage, this mechanism can present highly nonlinear behaviour as well. When paired with an SMA wire or coil, this can results in unintended behaviours or secondary operating points.

Recently there has been research such as the work by Maffiodo et al. (2017) that shows the advantages of pairing SMA wires with flexure-based structures. As with this case, the sizing of the SMA element is disregarded and the biasing advantage of the flexure is neglected.

In the case of grippers and mesoscale actuators where the SMA element is passively cooled, the accurate sizing of the SMA is important. In designs, where passive cooling is used, the geometry of the active element is critical as the shape and structure of the active element is directly related to the cooling times. In the case of SMA coils and wires, thinner diameters imply a shorter cooling time. These thinner wires, however, result in smaller forces when heated. This implies that by accurately sizing the SMA element for the biasing flexure, the actuator can be made as thin as possible while still being able to deform the flexure during heating. Thus, by adapting the traditional sizing methodology of bias-spring SMA actuators for flexure-based designs, the SMA actuator can be designed with higher bandwidths.

3.4 Adapting the Simplified Models

In section 2.5, a simplified model of the SMAs is used to size the active element for bias-spring and antagonistic SMA actuators. In the traditional sizing strategy, a simplified linear model of the SMA and the curve of the spring are used to find the operating points of the actuator which is represented by the intersection of the two curves. This simplification allows a relatively

simpler sizing of the components by abstracting the complex nonlinear behaviours of the shape memory effect.

3.4.1 Passive Biasing Compliant Mechanisms

The compliant mechanism, as mentioned previously, acts as the biasing element and as the kinematic stage that produces the desired actuator motion. Here, the basic principle is that the inherent stiffness of the compliant flexure mechanism is harnessed to pre-load the SMA for activation. In this case, at lower temperatures, the SMA is deformed using the energy stored in the compliant mechanism while at higher temperatures, the strain recovered by the shape memory effect is used to deform the compliant mechanism. Based on the design of the compliant mechanism, the SMA actuator can be made to actuate reversibly within a single degree of freedom while being rigid in the others.

In order to size the actuator and its corresponding passive biasing compliant element, an analytical model can be devised and exploited to predict the various operating points of the final SMA actuator. A pseudo-rigid body model (PSBM) based on the work by Henein (2005) can be used to devise the analytical models of the flexures. The flexure hinges are considered to behave like torsional springs with constant angular stiffness, K_θ. The analytical model can be derived by considering the reaction force exerted by the mechanism on the SMA wire or coil when acting as the biasing element.

While a Newtonian approach is possible, the simplest way to compute the force is to consider the elastic potential energy stored in the flexure hinges as the mechanism deforms. This potential energy stored in one torsional spring as a function of the input displacement of the mechanism, x, is given by :

$$U(x) = \frac{1}{2} K_\theta \left(\theta(x) - \theta_0\right)^2 \tag{3.1}$$

where, in the case of a notch flexure hinge, as shown in fig. 3.2, when rotating by an angle of θ, has a stiffness, as described in Henein (2005), equal to:

$$K_\theta = \frac{2Ebe^{2.5}}{9\pi\sqrt{r}} \tag{3.2}$$

Here, E is the Young modulus of the material, and e, b and r the design parameters of the flexure hinge shown in fig. 3.2.

In this approach, the important relationship to obtain is the influence of the contraction of the SMA on the rotation of the hinge, $\theta(x)$. When the flexure-based system is comprised of multiple flexural hinges, the total potential energy can be calculated by the sum of the potential elastic energy of each flexure, $U_{\text{tot}} = \sum U(x)$. The required force to deform the structure can be deduced using :

$$F(\theta(x)) = \|-\nabla U_{\text{tot}}(x)\| = \frac{\partial U_{\text{tot}}(x)}{\partial x} \tag{3.3}$$

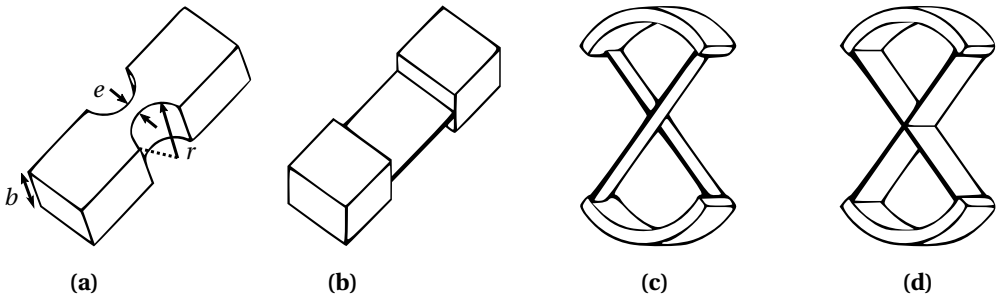

Figure 3.2: The various types of flexure hinges (adapted from Wu et al. (2015)) (a) Notch (b) Leaf spring (c) Cross-strip (d) Cartwheel hinge

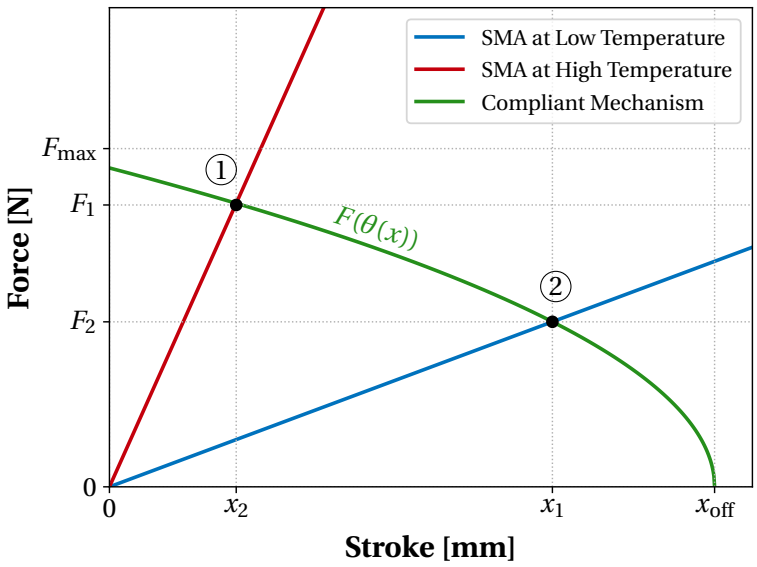

Figure 3.3: The adapted sizing principle of the novel biasing compliant mechanism SMA actuator based on the simplified SMA curves.

As in the case of the traditional SMA sizing methodology, the intersection between the adapted biasing curve and the simplified SMA curves represents the operating points of the SMA actuator, visualised in fig. 3.3 as ① and ②. The stroke of the actuator can be estimated by taking the difference between the x-coordinate of the operating points, $\Delta x = x_1 - x_2$. The variable x_{off} represents the distance by which the SMA element is pre-stretched. This parameter allows the element to work at an operating range with higher forces. But it is important to note that the there is a maximum pull force that the SMA wire or coil can exert, which can often be obtained from the supplier. Thus, the SMA element must be sized such that $F_1 < F_{max}$ so as to obtain the thinnest SMA wire or coil which can still exert enough force to deform the compliant mechanism to the required stroke.

In fig. 3.4, the design methodology for sizing a biased-compliant mechanism SMA actuator is presented. The methodology consists of designing the SMA active element based on the

desired time response (τ) specifications of the application. As explained previously, in the case of passive cooling applications, the wire diameter can be reduced to decrease cooling times and increase τ. Once the diameter of the SMA wire or coil is determined, the biasing element can be designed. In the case of a biasing compliant mechanism, the flexure hinges can be designed based on the desired stroke of the application. As fig. 3.4 details, the operating points must be estimated using the design of the compliant mechanism. The structure and design of the compliant mechanism can be used to determine the relationship between the strain recovered by the SME and rotation of the flexural hinges, $\theta(x)$. This relationship can be used to determine the force-displacement curve of the resulting biasing element using the equation presented in eq. (3.1). Finally, the individual flexural hinges can be adjusted such that the desired stroke, Δx, is obtained and that the maximum pull force of the SMA wire or coil is not exceeded.

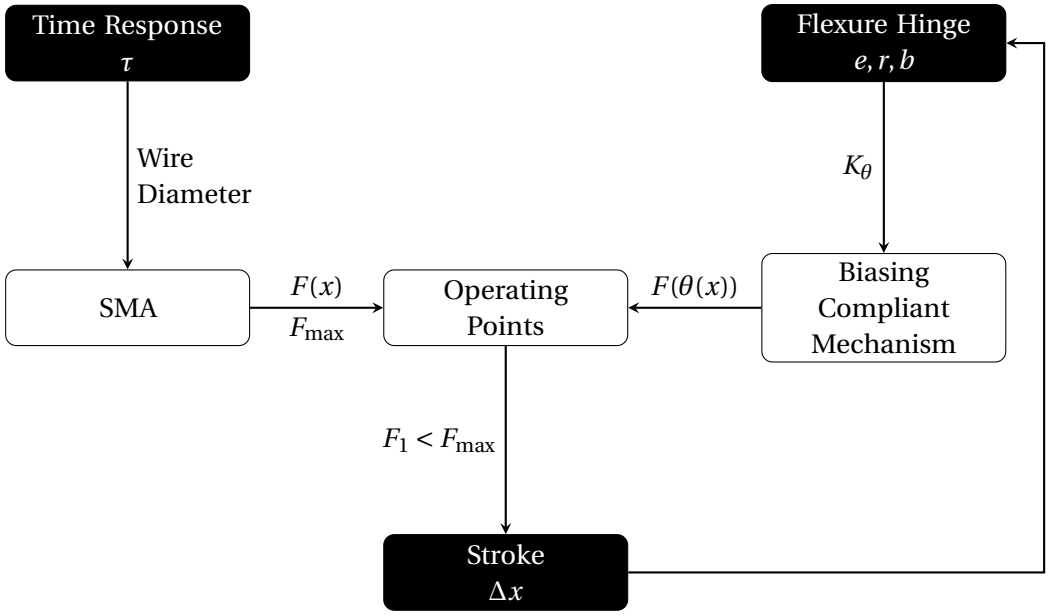

Figure 3.4: Design methodology for sizing biased-compliant mechanism SMA actuators.

Flexure-based hinges, however, exhibit a limited angular stroke. The maximum angle allowed before plastic deformation occurs has to be considered when designing such hinges. This admissible deformation, as described in the work by Henein (2005), can be calculated using :

$$\Delta\theta_{\text{adm}} \cong \frac{3\pi\sigma_{\text{adm}}\sqrt{r}}{4E\sqrt{e}} \tag{3.4}$$

By using the relationship between the input displacement and the hinge rotation, $\theta(x)$, the maximum admission stroke of the compliant mechanism, Δx_{adm}, can be computed. With this theoretical model complete, the entire mechanism can be sized such that the output stroke is maximised while avoiding failures during the deformation of the biasing compliant mechanism.

With $\mathbb{X}_{eq}$ being the set of possible equilibrium positions (see fig. 3.3) and $\mathbb{X}_{el}$ being the set of admissible positions for elastic deformation as defined below :

$$\mathbb{X}_{eq} = \{x \mid x_2 \leqslant x \leqslant x_1\} \tag{3.5}$$

$$\mathbb{X}_{el} = \left\{x \mid x_{off} - \frac{\Delta x_{adm}}{2} \leqslant x \leqslant x_{off} + \frac{\Delta x_{adm}}{2}\right\} \tag{3.6}$$

The set of feasible operating points for the biased-compliant mechanism SMA actuator, $\mathbb{X}_f$, is given by their intersection:

$$\mathbb{X}_f = \mathbb{X}_{eq} \cap \mathbb{X}_{el}. \tag{3.7}$$

Using this principle, if the mechanism is designed such that $\mathbb{X}_{eq} \subseteq \mathbb{X}_{el}$, the safety of the flexure hinges will not depend on precise control of the SMA which can be difficult to achieve. Furthermore, using these principle, various design trade-offs can be deduced, as shown in table 3.1

Table 3.1: The trade-offs observed during the sizing of the biasing compliant mechanism for the SMA actuator with a given SMA wire or coil. Here, S_{mech} and t_{mech} are the surface area and the thickness of the compliant mechanism, respectively.

Parameter	Effects	
$\frac{e}{r} \uparrow$	$\Delta\theta_{adm} \downarrow \Rightarrow \mathbb{X}_{el} \downarrow$	$K_\theta \uparrow \Rightarrow \begin{cases} \mathbb{X}_{eq} \uparrow \\ F_{grip} \downarrow \end{cases}$
$e \uparrow \mid \frac{e}{r}$ fixed	$S_{mech} \uparrow$	
$b \uparrow$	$t_{mech} \uparrow$	
$x_{off} \uparrow$	$\mathbb{X}_{eq} \uparrow$, $\mathbb{X}_{el}$ shifted away from $\mathbb{X}_{eq}$	

In table 3.1, the trade-offs determine how the various parameters of the compliant mechanism and the parameters of the SMA actuator interface affects the final performances of the actuator. By increasing the dimensions of the flexural hinges, the admissible range of operating points increase but comes at the cost of the output force of the actuator. Using these trade-offs, decisions can be made about the biasing complaint mechanism such that the resulting actuator can be sized to the required project specifications. When applying this design methodology, as shown in later sections of this chapter, further trade-offs can appear but the ones present in this table will appear in most applications.

3.4.2 Integration of Compliant Mechanisms in Antagonistic SMA Actuators

The concept of augmenting traditional bias-spring SMA actuators with compliant mechanisms can be extended to Antagonistic SMA actuators. Traditionally, these actuators consist of a pair of active SMA elements where the SMAs are heated and cooled alternately. These actuators

are relatively more complex due to the nonlinear nature of the SME. But, antagonistic SMA actuators have the advantage of an additional degree of freedom during activation. As the first SMA is heated, the antagonistic SMA is deformed and activated. Similarly, only upon heating the antagonistic SMA will the actuator be actuated in the opposite direction.

As with most SMA actuators fabricated using SMA wires or coils, the actuation of the actuator results in a linear motion. In application where complex motions are required, the antagonistic SMA actuator is paired with a kinematic stage that converts the linear movement to the required complex motion. Furthermore, they can be implemented into these antagonistic SMA actuators such that they present different behaviours based on the direction of actuation. As mentioned previously, flexure-based kinematic stages have the advantage of increased precision and reduced weight but presents with an inherent stiffness. Thus, this increased rigidity must be taken into account when sizing the SMA active elements.

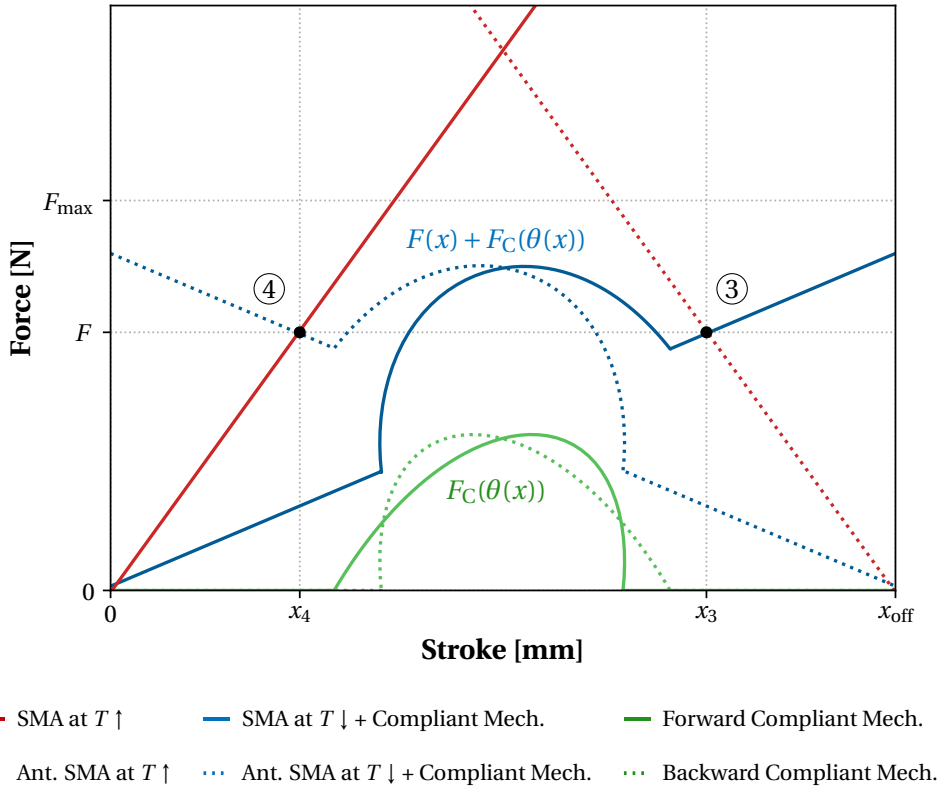

Figure 3.5: The adapted sizing methodology of an antagonistic SMA actuator paired with compliant mechanism using the simplified SMA curves. Here, the compliant mechanism behaves as a bistable element.

In the traditional antagonistic SMA actuator, the first SMA, when heated and returns to its original length, deforms the antagonistic SMA. Thus, in this case, the heated SMA must overcome the rigidity of the cold SMA. The operating points of such a system can be deduced by taking the intersections between the hot and cold SMA curves as shown in section 2.4.

In the case of a compliant mechanism, the system is connected to both SMAs at all times. Thus, the inherent stiffness of the compliant mechanism must be taken into account when actuating both SMAs. Therefore, the force-displacement curve of the compliant mechanism, $F_C(x)$, can be added to the curve of the antagonistic cold SMA, $F(x)$, to obtain the apparent load observed by the heated SMA, as shown in fig. 3.5. The design methodology can thus be adjusted, as shown in fig. 3.6, such that when the SMA elements are sized and operating points are determined, no unintended behaviours occur. It is important to note that due to the complexity of the compliant mechanism curves, these unintended operating points can emerge causing shorter strokes.

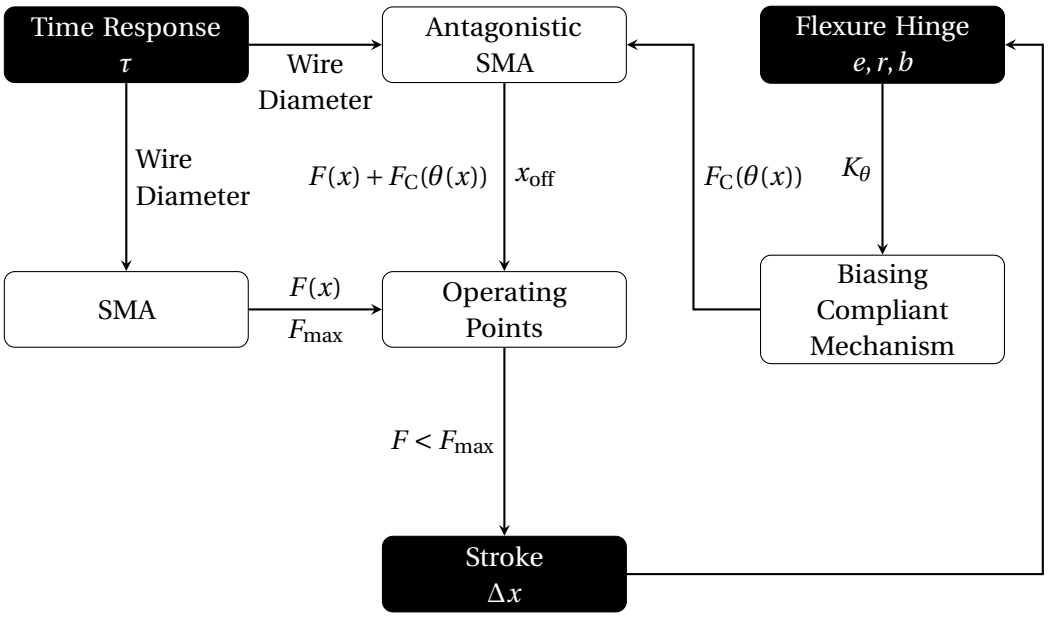

Figure 3.6: Design methodology for sizing antagonistic SMA actuators paired with compliant mechanisms.

In summary, as illustrated in fig. 3.6, the design methodology consists of deriving the force-displacement curves of the SMA elements and the relationship between the input displacement, x, and the hinge rotation, $\theta(x)$. Once these relationships are deduced, the force-displacement relationship of the compliant mechanism, $F_C(\theta(x))$ can be added to the force-displacement curve of the cold antagonistic SMA element. An important parameter to note is the pre-stretched length, x_{off} of the SMAs. With the pre-stretched SMA, when heated, the SMA can exert higher levels of force but could result in forces that exceed F_{max}. Using the two curves, the operating points can be estimated and verified such that the resulting stroke, Δx, fits within the requirements of the application. Furthermore, the geometric parameters of the hinge design of the compliant mechanism can be adjusted such that there are no unintended operating points and that the maximum pull force of the SMA is not exceeded.

Recently, there has been considerable work in developing bistable or multistable actuators. These actuators are able to main a stable position without required any holding energy. This

property could be highly beneficial in applications such as grippers. Here, the gripper can stay in the open or closed position without requiring any additional energy. These bistable systems can be created using flexure-based structures, as shown in the work by Jin Qiu et al. (2004). A axially compressed cantilever beam exhibits bistability and has been implemented in various smart material actuators. In the work by Chouinard and Plante (2012), a dielectric elastomer actuator is paired with a buckled beam to create a compact bistable actuator. Furthermore, in the work by Zhang et al. (2020), a bistable drone-ready gripper is fabricated and is actuated using an electric motor. This principle can be implemented and actuated using SMAs, as shown in the work by Welsch et al. (2018). However, the sizing of such a system are missing due to the complex nature of the bistable mechanism and the nonlinear nature of the SMA. Using the proposed, methodology, as shown in fig. 3.6, the SMA can be sized to present with higher time responses while still able to trigger the bistable positions of the actuator. The accurate sizing of such a bistable SMA actuator is validated later in section 6.2.

3.5 Validation using a Case Study: A Multi-Output SMA Mandrel

3.5.1 Motivation and Background

As previously stated, Shape Memory Alloys exhibit a relatively high volumetric work density. Thus, they are an ideal candidate in creating lightweight actuators for applications where reducing the total weight of the system drastically improves the efficiency such as drone deliveries. Here, any reduced weight increases the total flight time of the drone and thus, makes it the ideal use case of lightweight SMA actuators. In the context of drone deliveries, grippers generally consist of an actuator such as a motor and kinematic stage that converts the motion of the actuator into a gripping motion. In certain scenarios, the required gripping motion can be complex consisting of multiple outputs and radial movements such as the grippers implemented in the work by Lee et al. (2021) and in the work by Singh and Ananthasuresh (2013). In this case study, the goal is to apply the design methodology presented in this chapter to fabricate a drone-ready gripper with an advanced gripping mechanism. Using compliant mechanisms generated by topology optimization, an advanced kinematic stage can be designed to convert the motion of the SMA actuator into a multi-output gripping motion. Based on the design approach, the multi-output SMA gripper is sized and fabricated so as to validate the methodology.

3.5.2 Working Principle of the Gripper

The working principle of the proposed SMA gripper is based on the traditional SMA actuator presented in chapter 2 as adapted by the design methodology described in section 3.4. Here, the gripper consists of a simple SMA coil that acts as the active element and an accompanying compliant structure that behaves as the kinematic stage and as the biasing element.

The active SMA coil is pre-stretched by the biasing element at low temperatures and contracts

when heated above its transition temperature. The biasing element, which also acts as a conversion mechanism to transform the linear actuation of the SMA coil into a gripper movement, exhibits an inherent stiffness due to the fact that it composed of flexure-based hinges. As the SMA cools down, a spring force acts on the coil due to the stiffness of the compliant mechanism. When heating the SMA, the contraction of the coil deforms the compliant biasing element creating the desired gripping motion at the output. By controlling the temperature of the SMA coil, the entire system can be made to grip and release objects.

In this application, the SMA coil is heating using Joule's heating by applying a constant voltage across it. This simple solution makes use of the internal resistance of the SMA coil to exploit the Joule's losses when passing a current through it to raise the temperature of the material. The coil, here, is cooled using passive cooling by simple convection with the surrounding air. This standard solution allows for a simple control system that does not require any external heating system which would add weight to the system. Furthermore, an H-bridge is used to supply the current and control the heating of the SMA coil. Finally, as precise control of the system is required, a hall-effect sensor or any other low profile position sensor can be used to detect the state of the gripper.

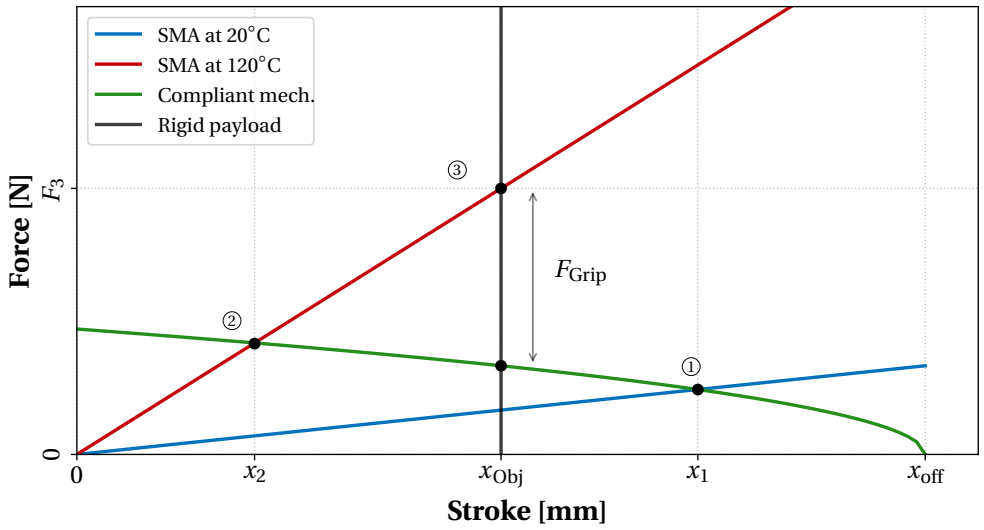

Figure 3.7: The sizing methodology of the biased-compliant SMA gripper based on the proposed designing methodology.

The working principle can be further visualised using the simplified sizing graphs as described in the work by Spaggiari et al. (2013) and as adapted to compliant systems in section 3.4.1. The SMA coil within the gripper operates between the ambient temperature and a temperature above its transition temperature. This behaviour, as mentioned previously, can be simplified into two straight lines based on its temperature. It is important to note that there exists a locus of lines representing the SMA at every temperature in between. Based on the methodology, the operating point of the gripper can be deduced using the intersection of the SMA curves and the characteristic of the designed biasing element. This characteristic will be described and

validated in the following sections. The operating points are labelled in the figure as ① and ②. The maximum possible stroke of the gripper can be estimated by taking the difference between the x-values of the two operating points, $x_1 - x_2$. However, the variable, x_{off}, represents the distance between the SMA and the biasing-element before they are pre-stretched and attached to each other. These operating points described represent the behaviour of the gripper without a payload. In the case a payload, is present, the behaviour of the gripper and the gripping force is dependant on the size of the payload, x_{Obj}. This behaviour of the payload can be simplified as a perfectly rigid object with an infinite stiffness. Thus, the intersection between the force-displacement curve of the payload and the high temperature SMA will deduce the last operating point ③. The gripping force, F_{Grip}, experienced by the payload can be estimated using this last operating point as shown in the figure. Thus, as established by the design methodology presented in chapter 3, the curves of the SMA and the compliant mechanism can be used to estimate the total stroke and gripping force of the system, as represented by $x_1 - x_2$ and F_{Grip} respectively.

3.5.3 Designing the Integrated Biased Kinematic Stage

The main goal of the design presented in this section is to create a multi-output gripper actuated using a single SMA coil. When designing grippers with complex outputs such as the work shown in Zhakypov et al. (2018), multiple active elements are used. The goal of this design is to improve these grippers by implementing an integrated system that can present multi-output gripping motion while only using a single SMA coil as an input. Here, the design is based on the 4-Point Mandrel topology presented in chapter 5. However, here, the structure is used as the passive element as opposed to the active element proposed in the following chapter. Thus, in this gripper design, the 4-prong radial compliant mechanism is used as the passive biasing element and as the kinematic stage. Furthermore, the compliant mechanism is redesigned using flexure-based hinges so as to improve the stroke of the gripper system. Here, as the topology is limited to the 2D plane, the flexural mechanism is further improved by extending the design space to a 2.5D design, which involved stacking 2D structures along the third dimension.

Articulated Parallelogram Core and Analytical Geometry Approach

The algorithmically generated mandrel topology consists of an articulated symmetrical parallelogram (rhombus). The topology can be reduced to four identical triangles joined at one vertex by a pivot as shown in fig. 3.8(a). The kinematics of the design is adapted from the generated one by using hinges instead of distributed deformation. In the figure, the blue arrows represent the input while the black arrows represent the output. The design has been generated such that the SMA coils can be placed at the inputs so as to generate a radial output towards the centre when actuated.

When examining the concept behind the mandrel mechanism, the conclusion can be made

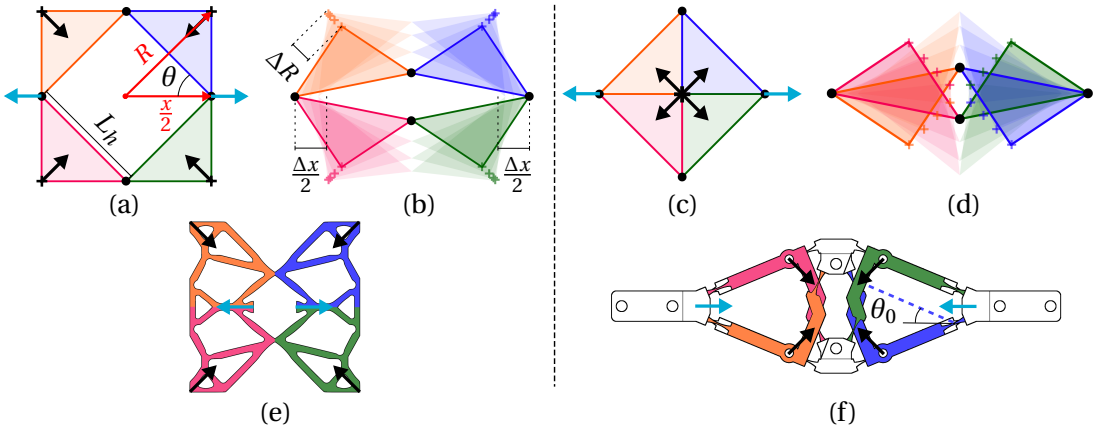

Figure 3.8: Kinematic diagram of proposed design where the black dots represent ideal pivots, the blue and black arrows represent the input and output displacement, respectively. On the left: the outward-triangle configuration with a) the initial position and b) the displaced one. On the right-hand side: the inward-triangle configuration achieving a stroke amplification with c) the initial position and d) the displaced one. e) represents mandrel topology generated with 2D topology optimization which behaves similarly to the outward version. f) shows the 2.5D adaptation of the inward version into a flexure-based mechanism distributed over multiple layers, and with a reversed actuation direction.

that the driving structure consists of four right-angled isosceles triangles which represent the four claws of the mandrel. Furthermore, the pivots, being constrained along the horizontal and vertical axes due to symmetry, force the outputs to move along a 45° path. However, upon careful examination, these constraints can be satisfied in two distinct configurations as shown in fig. 3.8(a) and (c). The four triangles can be position inwardly or outwardly. Due to the inward-facing configuration having overlapping triangles, this topology cannot be generated from a 2D design space. The main advantage of the inward-facing configuration compared to the outward-facing configuration is the stroke amplification of the output vertices based on the stroke of the SMA coil contraction. It is also important to note that the direction of the radial output depends on the direction of the input displacement. Thus, the gripper can be made to open or close when the SMA coil is heated. By attaching the SMA coil to the vertical pivots rather than the horizontal ones, the gripper can be made to be always opened or always closed.

Determining the Relationship between the Hinges and the SMA Stroke

The stroke amplification, γ, of the system is not uniform and is dependant on the position of the mechanism, x. This amplification factor can be described by deriving the output vertex

position, R, with respect to the input vertex position, x, and can be expressed analytically as :

$$\gamma(x) = \frac{\partial R(x)}{\partial x} = \frac{1}{2\sqrt{2}} \left(1 - \text{sign}(\alpha) \frac{\frac{x}{2}}{\sqrt{L_h^2 - \left(\frac{x}{2}\right)^2}} \right) \tag{3.8}$$

where,

$$\begin{aligned} R(x) &= L_h \cos\left(\theta(x) - \alpha\right) \\ &= \frac{1}{\sqrt{2}} \left(\frac{x}{2} + \text{sign}(\alpha) \sqrt{L_h^2 - \left(\frac{x}{2}\right)^2} \right), \end{aligned} \tag{3.9}$$

with,

$$\theta(x) = \arccos\left(\frac{x}{2L_h}\right) \quad \text{and} \quad \alpha = \pm\frac{\pi}{4}. \tag{3.10}$$

Here, L_h represents the length of the hypotenuse of each triangle, θ represents the angle between the horizontal and the hypotenuse, α represents the angle between the hypotenuse and the side of the triangle and can equal a value of $\pm\frac{\pi}{4}$. This angle is defined as positive for the outward-facing configuration and as negative for the inward-facing one. Here, the output stroke is majorly dependant on the sign of the angle α. The outward configuration has a stroke amplification of less than one for almost all possible inputs, implying a stroke reduction. While, on the other hand, the inward configuration has a stroke amplification large than one. In the context of a gripper, the inward version was chosen for its larger output stroke.

Simple Kinematics to a Compliant Mechanism

The kinematic schematic is composed of only simple hinges and rigid links. This makes it the ideal candidate for implementation using flexure-based hinges. In this case, as shown in fig. 3.9, truncated semi-circular flexure hinges were selected for their ability to avoid high localised stress concentration and allow for an acceptable angular stroke as described in the work by Torres Melgarejo et al. (2018).

As stated earlier, the inward-facing triangle configuration was chosen and due to fact that the triangles overlap during actuation, it makes it impossible to be implemented in a 2D design space. Thus, as shown in fig. 3.9, a 2.D design approach was implemented where each overlapping triangle is stacked in the 3$^{\text{rd}}$ dimension. The mechanism is distributed among different superimposed layers linked at the vertices of the triangle to replicated the kinematic schematic. This adaptation to 2.5D design does not impact the functionality of the mechanism as long as the hinges are considered infinitely rigid when bending in any other direction other than the desired one. Here, two layers are implemented to accommodate the four triangles : the L_1 stage comprising of the green and orange triangles, and the L_2 stage comprising of the pink and blue triangles.

In the case of the ideal kinematic schematic, the triangles are attached at a single point to

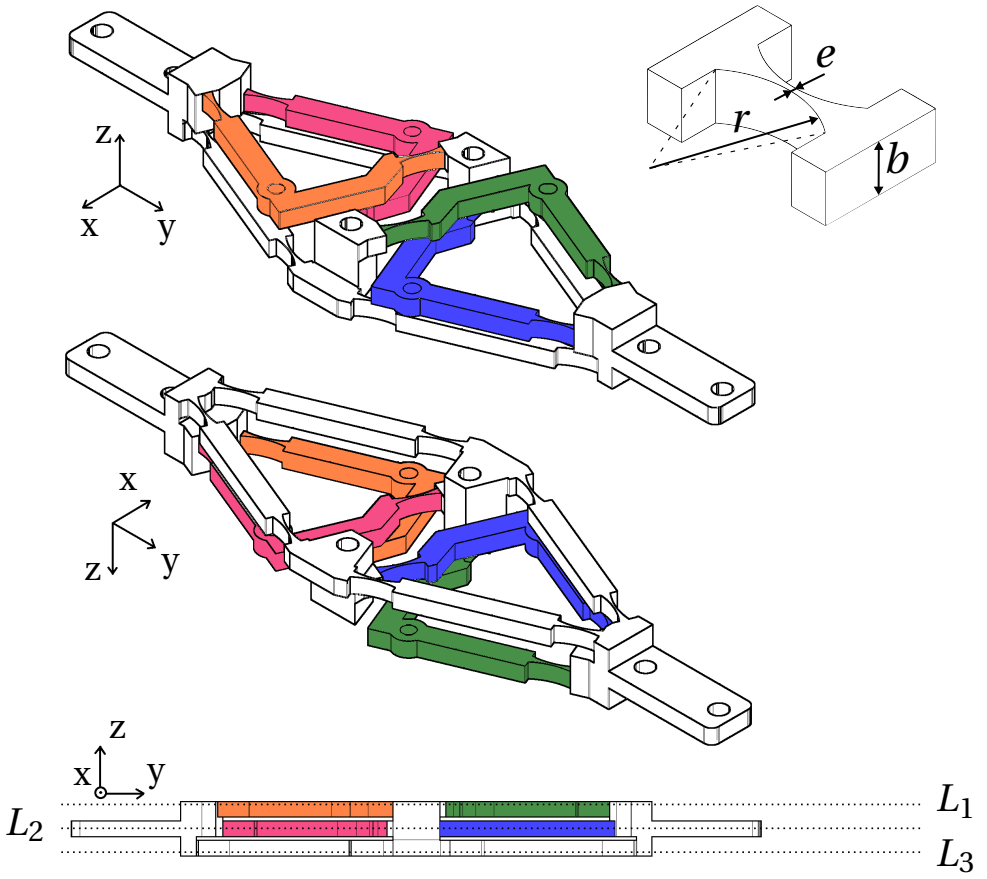

Figure 3.9: Different views of the flexure-based compliant mechanism spreading over multiple stages, and parametrized flexure pivot.

form a parallelogram. However, this is difficult to implement with a flexure-based solution due to the rigid links having a non-null width. This adds unwanted links and hinges to the kinematic chain which results in undesired Degrees of Freedom (DoF). This parasitic DoF is overcome by adding a third DoF-inhibiting stage, L_3, to the 2.5D design as shown in fig. 3.9.

As the goal of this gripper is for drone delivery purposes, another stage, which behaves as the frame of the drone, can be added to the design. For mechanism to behave as intended in the kinematic schematic, the left and right input vertices must be constraint to move along a single line. In this case, for simplicity, this constraint has been implemented using a rail. For a future drone mounted setup, an additional stage can be added to perform this required constraint, showing the advantage of the 2.5D design approach.

Sizing of the Biasing Compliant Mechanism

Based on the proposed design methodology, the goal of the mechanism is to create a kinematic stage that also behaves as the passive biasing element for the SMA coil. The inherent stiffness

of the overall compliant mechanism due to the flexural hinges is harness to pre-stretch the SMA for activation. Thus, in order to size the actuator and the corresponding biasing element, an analytical model of the stiffness must be developed. Using the pseudo-rigid model, as presented in the work by Henein (2005), the flexural hinges can be considered as torsional spring with a constant angular stiffness, K_θ. As detailed in section 3.4.1, the stiffness of the compliant structure requires an expression for the relationship between angular position of the flexural hinge and the contraction of the SMA, $\theta(\Delta x)$. In this case, this relationship can be expressed as :

$$\theta(\Delta x) = \arccos\left(\frac{\Delta x}{2L_h} + \cos(\theta_0)\right), \tag{3.11}$$

with θ_0 being the resting angle at which the mechanism is printer/fabricated as shown in fig. 3.8(f).

As detailed in the methodology, the next step is to calculate the potential energy within the system during deformation. Due to the symmetry of the mechanism, all the hinges store the same potential energy. Here, the L_3 stage has 8 hinges while the stages L_1 and L_2 have 4 hinges each. Thus, the total potential energy of the whole mechanism is :

$$U_{\text{tot}}(\Delta x) = 16 \cdot U(\Delta x) \tag{3.12}$$

The force-displacement characteristic of the mechanism is then given by :

$$\begin{aligned} F(\Delta x) &= \| -\nabla U_{\text{tot}}(\Delta x) \| = \frac{\partial U_{\text{tot}}(\Delta x)}{\partial \Delta x} \\ &= \frac{8K_\theta}{L_h} \frac{(\theta(\Delta x) - \theta_0)}{\sin(\theta(\Delta x))}. \end{aligned} \tag{3.13}$$

The resulting characteristic is plotted as shown in fig. 3.10. Furthermore, the model is validated using experimental results obtained using a pull-tester. As the experimental results follow the model quite closely, it validates the working hypothesis and approximations used during the definition of the analytical model. As the force characteristic flattens unlike a traditional linear spring, the operating points of the actuator will offer higher strokes for a given SMA coil. Furthermore, as the curve also decreases in value near the low-temperature operating point ①, its implies that the gripper can exert higher gripping forces for objects with a larger diameter. This shows that the current force-displacement characteristic of the proposed compliant mechanism is well suited as a biasing element in an SMA actuator. Finally, in the figure, some plastic deformation can be observed as the mechanism was deformed beyond above its admissible range during the test. The flexural hinges exhibit a limited angular stroke which is one of the limitations of such a design. However, the maximal admissible angle before permanent plastic deformation can be estimated using the work by Henein (2005) as :

$$\Delta\theta_{\text{adm}} \cong \frac{3\pi\sigma_{\text{adm}}\sqrt{r}}{4E\sqrt{e}}, \tag{3.14}$$

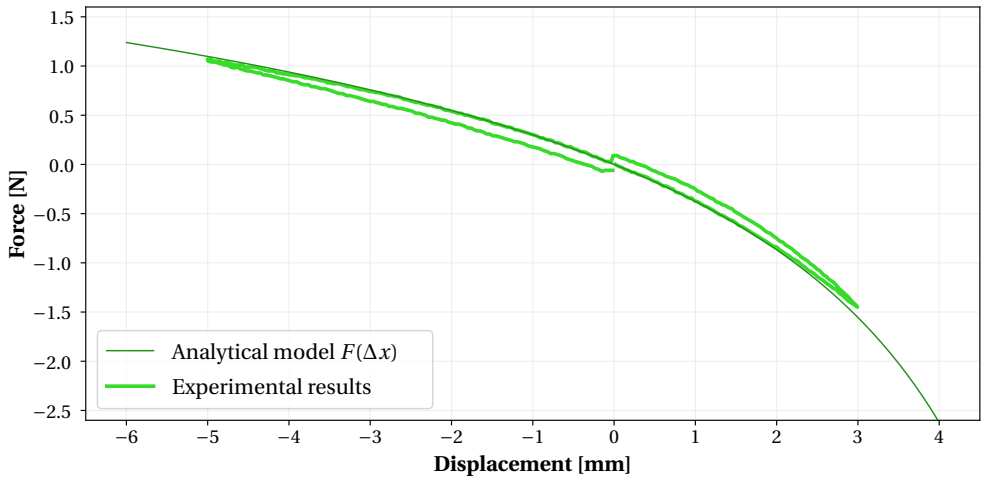

Figure 3.10: Validation of the analytical model of the biasing compliant mechanism using experimental results obtained using a pull-tester. Here, the small discrepency arises due to the creep present in the plastic structure as the mechanism returns to its original shape.

which in this context can be expressed :

$$\begin{aligned} \Delta x_{\text{adm},+} &= 2L_h\left(\cos(\theta_0 + \Delta\theta_{\text{adm}}) - \cos(\theta_0)\right) \\ \Delta x_{\text{adm},-} &= 2L_h\left(\cos(\theta_0 - \Delta\theta_{\text{adm}}) - \cos(\theta_0)\right) \end{aligned} \tag{3.15}$$

If $\mathbb{X}_{\text{eq}} = \{x \mid x_2 \leqslant x \leqslant x_1\}$ is the set of possible operating points (see fig. 3.7) and $\mathbb{X}_{\text{el}} = \{x \mid x_{\text{off}} + \Delta x_{\text{adm},+} \leqslant x \leqslant x_{\text{off}} + \Delta x_{\text{adm},-}\}$ is the set of admissible positions for elastic deformation as portrayed in equation eq. (3.15) and fig. 3.7. Then, based on the design methodology presented in chapter 3, the set of feasible operating points for the actuator $\mathbb{X}_{\text{f}}$ is given by their intersection:

$$\mathbb{X}_{\text{f}} = \mathbb{X}_{\text{eq}} \cap \mathbb{X}_{\text{el}}. \tag{3.16}$$

One of the goals of the sizing methodology for the compliant mechanism is to maximise the output stroke while avoiding permanent deformation during operation. Thus, the compliant mechanism must be sized such that $\mathbb{X}_{\text{eq}} \subseteq \mathbb{X}_{\text{el}}$. This eliminates the need for precise temperature and positional control of the SMA coil during activation to protect the flexural hinges.

In this case, the output stroke of the gripper can be maximised by maximising the size $\mathbb{X}_{\text{f}}$ or by having the operating points be located at positions where the curve of the stroke amplification is high (from eq. eq. (3.8)). A trade-off exists as displacing $\mathbb{X}_{\text{f}}$ for higher stroke amplification tends to reduce the overall size. Based on table 3.1, various additional trade-offs for the proposed mandrel can be observed as summarised in table 3.2.

As seen in the table, an optimal solution can be estimated based on the design parameters. However, in the case of L_h and b, increasing them will always result in an increased stroke

Table 3.2: Additional trade-offs observed when sizing the flexural compliant mechanism actuated by a given SMA wire or coil. Here, S_{mech} and t_{mech} are the surface area and the thickness of the entire compliant mechanism, respectively.

Parameter	Effects
$\frac{e}{r} \uparrow$	$\Delta\theta_{\text{adm}} \downarrow \Rightarrow \mathbb{X}_{\text{el}} \downarrow$
$e \uparrow$ | $\frac{e}{r}$ fixed	$S_{\text{mech}} \uparrow$
$b \uparrow$	$t_{\text{mech}} \uparrow$
	$K_\theta \uparrow \Rightarrow \begin{cases} \mathbb{X}_{\text{eq}} \uparrow \\ F_{\text{grip}} \downarrow \end{cases}$
$x_{\text{off}} \uparrow$	$\mathbb{X}_{\text{eq}} \uparrow$, $\mathbb{X}_{\text{el}}$ shifted away from $\mathbb{X}_{\text{eq}}$
$L_h \uparrow$	$F_{\text{grip}} \uparrow$, $S_{\text{mech}} \uparrow$
$\theta_0 \downarrow$	$\gamma(x) \uparrow$, $F_{\text{grip}} \downarrow$, $\mathbb{X}_{\text{el}} \downarrow$

while increasing the overall size of the mechanism. This shows that there exists a trade-off between the weight/size and the output stroke which will be critical to ascertain based on the gripper specifications.

3.5.4 Implementation and Experimental Results

One of the main advantages of this integrated design is the simplicity of fabrication and assembly. The entire compliant structure is printed from Nylon (PA 2200 Polyamide 12) using selective laser sintering (SLS) as shown in fig. 3.11. As the mechanism consists of stacked layers, the entire structure was printed as a single piece validating the simplicity of the novel design approach.

In fig. 3.12, the validated analytical models are plotted against the force-displacement curves of the SMA coil. This SMA model was estimated using experimental setup where the SMA coil was maintained at a constant temperature using a PID control and a thermal camera, and was then experimentally tested using the pull-tester. With the experimental data, a simplified linear model of the cold and hot SMAs were determined using linear regression. Using these analytical models and the sizing methodology detailed in section 3.4.1, the stroke of the final mandrel gripper can be estimated. In this prototype, the design parameters used are $e = 0.5$ mm, $r = 15$ mm, $b = 4$ mm, $L_h = 42.4$ mm, $x_{\text{off}} = 27.5$ mm and $\theta_0 = \frac{\pi}{8}$. Here, an estimated linear output stroke of up to 4.5 mm is observed for each claw.

The gripping force, however, is dependant on the size of the gripped object. For an object of diameter close to x_1, the gripping force will be maximal. Using a pair of load cells attached to two opposing claws, the gripping force was measured as shown in fig. 3.13. The load cells were placed at different distances from the claws to simulated objects of varying sizes. The results of the gripping force measurements can be seen in fig. 3.14. The gripper shows a force close to constant for large span of SMA temperatures above its transition temperature of 80°C . This

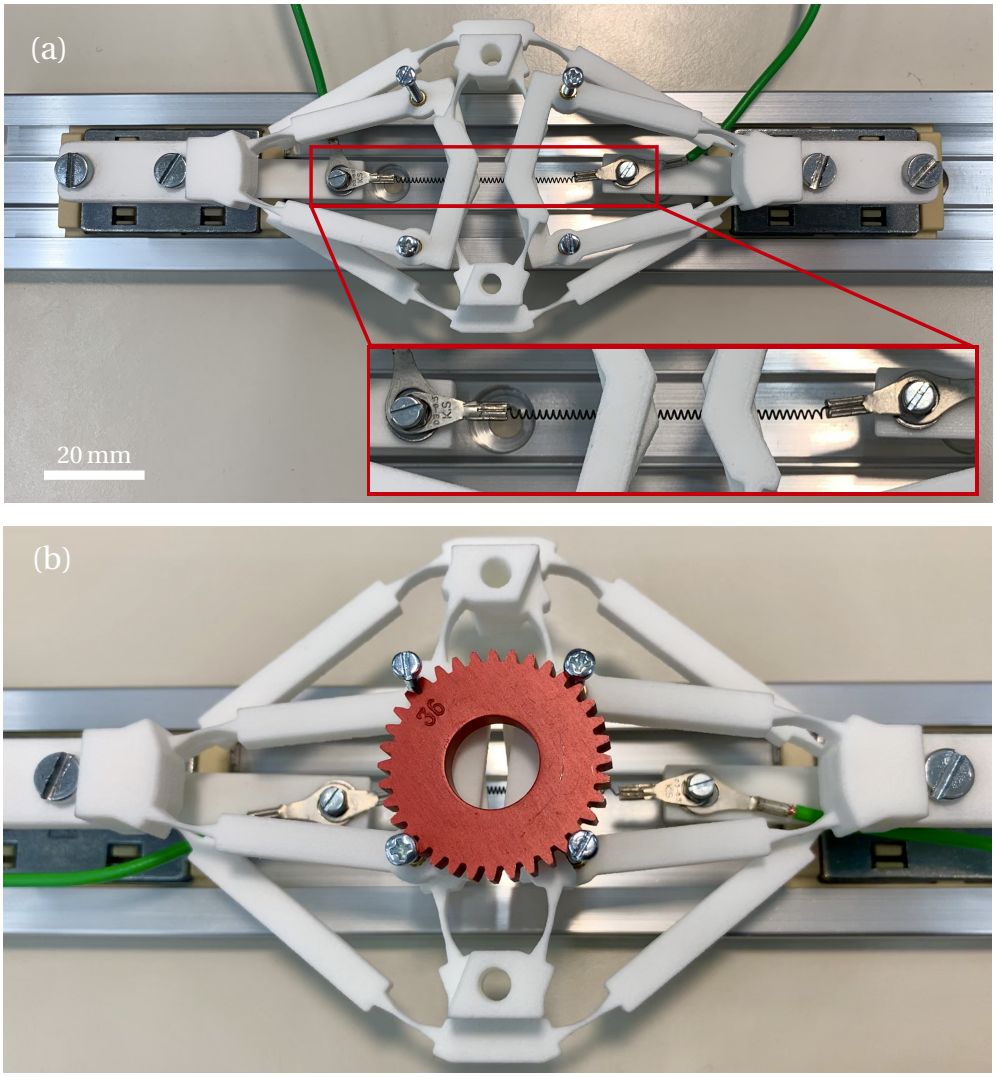

Figure 3.11: The working prototype of the biased-compliant SMA gripper (a) opened configuration with a 0.2mm wire diameter SMA coil (framed in red), (b) closed configuration grasping an object.

constant force behaviour is ideal for a gripper and greatly simplifies the control, preventing any unintended damage to the gripped object. A maximum steady-state force of 1.78 N was measured for the biggest payload size while using the smallest available SMA coil, whose wire diameter is 0.2 mm. While this result is promising, it should be noted that the fabricated prototype is sub-optimal and can be further optimised for greater forces, either by optimising the compliant mechanism or by using thicker SMA coils. Increasing the wire diameter of the SMA coil comes with higher gripping forces but comes at the cost of slower cooling time or increased time delay between the opening and closing sequence of the gripper.

In the end, the final prototype, as seen in fig. 3.11, was measured to weigh only 17 g, which implies that the gripper has a maximum force-density of around 105 N/kg. This shows that

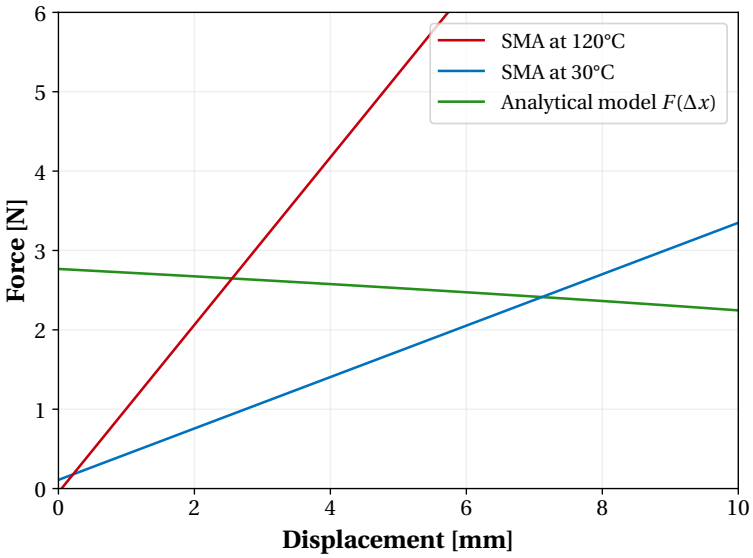

Figure 3.12: The sizing diagram of the SMA mandrel based on the developed analytical model of the compliant mechanism and the models of the SMA coils obtained from experimental results. Here, based on the estimations a maximum stroke of 4.5 mm is observed.

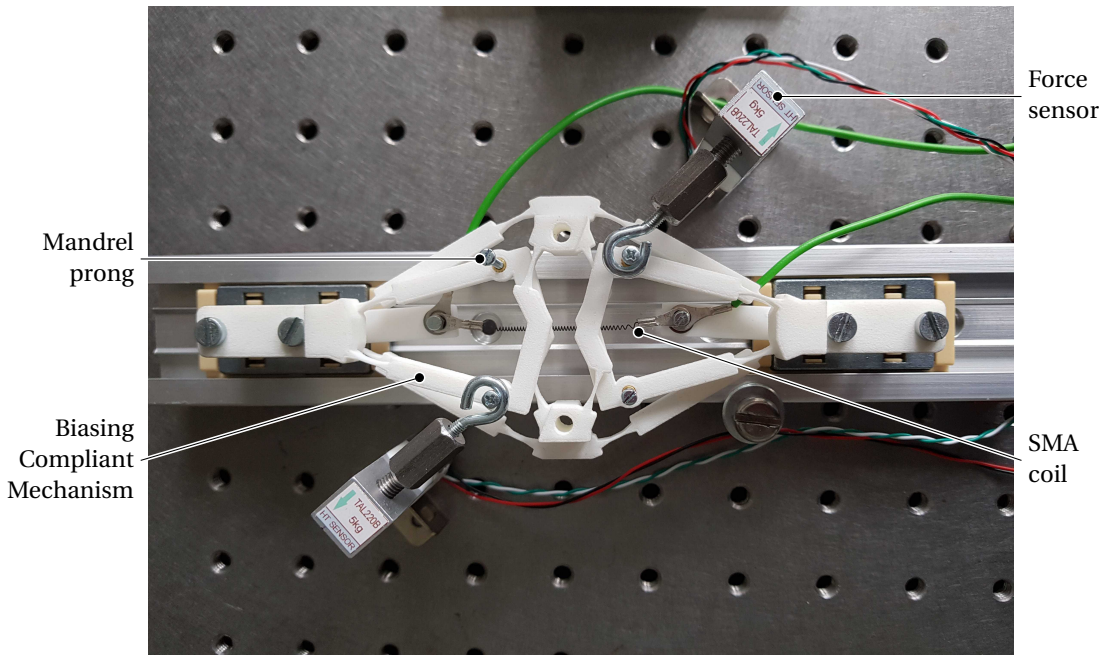

Figure 3.13: The experimental setup, using a pair of force sensors, to measure the gripping force of two opposing jaws.

proposed mandrel gripper can be ideal for lightweight applications such as drone deliveries. Furthermore, this demonstrates the highly integrated nature of the gripper, thus, validating the design methodology presented in chapter 3.

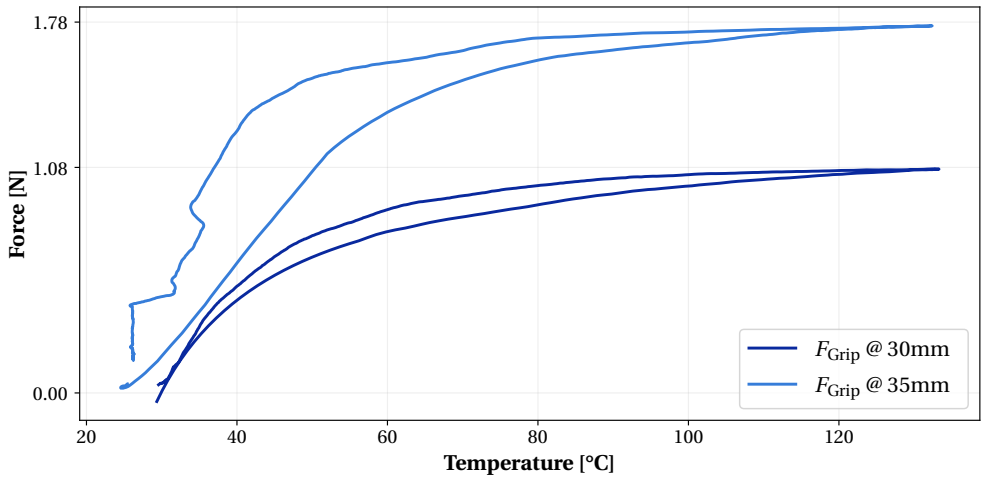

Figure 3.14: Results of the gripping force performed at different object diameters. The temperature and force output were recorded in real-time using a thermal imaging camera and a force sensor, respectively.

3.6 Summary and Conclusion

In this chapter, the traditional sizing methodology has been adapted to fit the case where biasing springs are replaced with passive biasing compliant mechanism. This approach stems from the concept where the traditional SMA actuators consisting of an active element, a biasing element and a kinematic stage is transformed into a more integrated solution where the biasing element and the kinematic stage are combined and fully integrated.

Using pseudo-rigid body models described in the work by Henein (2005), the analytical models of the compliant mechanisms are used to estimate the stroke and behaviour of the novel SMA actuator. Using the simplified SMA curves, these alloys can be sized such that the time response of the SMA actuator is minimized. These simplified curves can be obtained using the models presented in chapter 2 or as in this case, obtained using a linear regression of experimental data.

Furthermore, this novel approach to designing SMA actuators paired with compliant mechanisms has been adapted for antagonistic SMA actuators. By altering the design methodology, the often used antagonistic SMA actuators can be sized such that when paired with compliant mechanisms, the actuator does not present any unintended behaviours and reduces the time response. This methodology will be further validated using case studies in chapter 6.

Most SMA actuators that make use of kinematic stages to convert the linear motion of the actuator into more complex behaviours, also integrate a passive spring in the design. By applying the presented design approach, SMA actuators can be designed such that compliant mechanisms can be used as biasing elements further improving the work density of the actuator. In this chapter, the presented design methodology has been validated using a case

study featuring a 4-prong radial gripper. The methodology proposed a novel way to design compact and integrated SMA actuators. Here, using the proposed approach and techniques, a gripper powered by shape memory alloy coils were conceived and fabricated. The novel methodology also proposed a simplified method with which the SMA and the biasing elements can be sized so as to harness the shape memory effect when a thermal load is applied to the SMA. Finally, the gripper was fabricated using machining techniques that allowed a reduced number of parts and a simplified assembly process, showing one of the key advantages of this proposed integrated approach.

Finally, the four prong mandrel gripper is sized and fabricated. In this prototype, the gripper consists of just an SMA coil and an entirely 3D printed kinematic stage. Based on the design methodology, the kinematic stage is created using compliant flexure-based mechanisms that, while acting as a motion conversion mechanism, also behaves as a biasing spring. The kinematic stage conceived using topology optimization and improved using flexure-based hinges is able to convert the shape memory effect of one SMA coil into a more complex multi-output gripping motion. Based on the design approach presented in this chapter, the compliant mechanism has been sized to optimize the stroke of the SMA actuator while reducing the required SMA coil wire diameter. Using the established and validated analytical models of the kinematic stage and the traditional simplified SMA models, the operating points and the stroke of the gripper, around 4 mm, was estimated. The final prototype of this four prong gripper weighs less than 17 g and is able to exert around 1.78 N of force, which leads to a maximum force-weight density of around 105 N/kg compared to 41 N/kg for conventional DC motor-based gripper as shown in the work by Lee et al. (2021). This shows that by using the proposed design methodology, a lightweight and compact gripper can be fabricated for applications such as drone-deliveries.

Now, with the design methodology for biasing kinematic stages validated, novel SMA actuators can be create with highly integrated and compact features can be designed and sized. This tendency to integrate the different subsystems of the conventional SMA actuator to create actuator with higher work densities and fewer pieces to assemble can be further extrapolated to other subsystems. In the next chapter, a novel approach to integrating the control and the kinematic subsystems of the actuator to create mechanically intelligent SMA actuators is presented.

Publications related to this chapter :

S. Thomas, G. Maquignaz, A. Thabuis, and Y. Perriard, *"A Self-Biasing Shape Memory Alloy Gripper for Lightweight Applications,"* in 2021 IEEE/RSJ International Conference on Intelligent Robots and Systems (IROS 2021), Prague, Czech Republic, 2021, p. 6. (in press)

4 Mechanical Approach to SMA Actuator Control

4.1 Introduction

Shape Memory Alloys, often referred to as artificial muscles, are often used in applications where a compact and lightweight solution is required. When paired with a biasing element such as a spring or compliant mechanism, a lightweight reversible actuator can be fabricated. By heating and cooling the active SMA element, a reversible back and forth motion can be created.

Due to the complex nature of the shape memory effect, sensors or complex control strategies are required for the accurate control of the SMA element, as shown in the work by Narayanan and Elahinia (2016) and Mansour and Kim (2020). The overheating of the SMA can result in the permanent reprogramming of the shape or the destruction of the SMA wire or coil. In the case of smaller, more compact applications, the SMA element used are thin wires or coil. In these cases, using sensors that can measure the temperature can be quite difficult to implement due to the low thermal mass of the SMA element. Recent work such as Sakagami et al. (2019), have implemented sensorless systems where the change in resistivity or inductance is measured as the SMA changes phase to create more compact control solutions. Here, due to the complex nonlinear nature of the shape memory effect, complex control strategies and micro-controllers to efficiently control the SMA and prevent overheating are required.

Often, when considering the volumetric work density of SMA actuators, the electronics, sensors and control strategies are not taken into account. In certain applications, for example untethered crawling robots, the control plays an important role in the final work-weight density of the robot as seen in the work by Yuk et al. (2011). Often, due to the volume and weight restrictions present in the design of mesoscale robotics, the electronics and control systems cannot be integrated into the design and, thus, results in robots that are often tethered and limited in their range as shown in the work by Shi et al. (2019) and Liang et al. (2020). Improvements made in the sensorless and control strategies can, thus, have a major impact in the final dimensions and weight of the SMA actuator.

In this chapter, a novel design concept using mechanical intelligence is presented to further integrate the discrete building blocks present in the traditional SMA actuator. By exploiting the dependence of the mechanical behaviour of the SMA and its temperature, a mechanical intelligent oscillator system can be developed such that the actuator is controlled using a mechanical system rather than using electronics. This design language can be implemented into SMA actuators to create a simple but effective solution to create a sensorless, micro-controller-free control strategy that intrinsically prevents SMA overheating. Furthermore, in this chapter, a crawling robot is conceived using this methodology to validate this novel design approach.

4.2 Design Methodology for the Control System

As mentioned previously, due to the complex behaviour of SMAs, the sensors and control strategies required to actuate an SMA actuator can be cumbersome and reduce the overall work-weight density of the resulting robotic systems. The shape memory effect and the corresponding phase transitions are directly dependant on the temperature of the alloy. By exploiting this mechanical relationship between the temperature of SMA, the control system can be integrated into the kinematic stage, as represented in fig. 4.1.

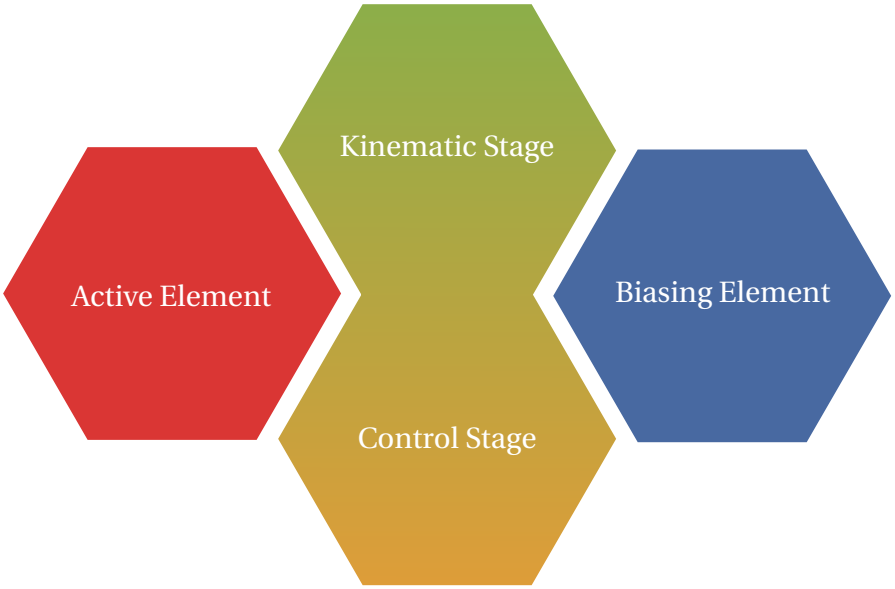

Figure 4.1: Diagram of the adapted building blocks of the SMA actuator.

4.2.1 Working principle

A basic linear SMA actuator consists of an SMA and a biasing spring that when heated and cooled, results in a simple back forth oscillating motion. By accurately controlling the temperature of the SMA above its transition temperature and below a critical overheating temperature,

the SMA can be made to provide a reliable actuation. This reversible actuation results in a back and forth mechanical movement of the biasing spring and the cyclical movement of the kinematic stage, if any. The basic concept of this methodology consists of tying the mechanical behaviour of the actuator into the control.

The SMA element in most cases is heating using Joule's heating by simply passing a current through the SMA and allowing the internal resistance of the SMA element to heat up by Joule's losses as shown in the work by Huang (2002). The cooling of the SMA generally consists of passively extracting the heat from the active element using natural convection with the cooler surrounding air. This simple strategy is often used in the control of SMA actuators due to not requiring any additional mechanisms and thus, does not reduce the work-density of the actuator while keeping the system compact.

Thus, by using the mechanical behaviour of the actuator to cut the current flow across the SMA will immediately cool the active element before it has a chance to overheat. In this manner, the control of the SMA actuator is mechanically controlled by the shape memory effect. Here, as a current is passed through the SMA wire or coil, it heats up the SMA resulting in a strain recovery and the SMA returning to its original length. This change in length, after a certain threshold, can be made to physically cut the electrical contact between the SMA element and the power supply. This cause the immediate cooling of the SMA through heat exchange with the surrounding air. As the SMA cools down, the biasing element will, once again, deform the SMA which will re-establish the electrical contact across the SMA, restarting the oscillating motion. Thus, this design strategy when integrated into the kinematic stage can render the entire SMA actuator compact and electronics-free.

This approach, when properly implemented, can result in an robotic system where a reversible actuation can be observed without the need for any electronics, micro-controllers or sensors, preserving the work-weight density of the system. A mechanical control of the SMA element can result in a system where the SMA element, due to the physical electrical contacts being interrupted, can never overheat.

4.2.2 Implementation

The basic implementation of such as system consists of using a latch system or multi-stable mechanism where after a certain stroke or force threshold results in a snap-through effect that can be exploited to disconnect the electrical contacts across the SMA wire or coil. The rapid bifurcation or spring back from a latch system is used to cut the flow of current across from the SMA and the slow return of the SMA actuator due to cooling can be used to re-establish the electrical connection to create this oscillating effect.

The implementation of this oscillator mechanism in the scope of a simple biased-spring SMA actuator consists of a magnetic or mechanical latch system. A diagram of the working principle of the proof-of-concept can be in fig. 4.2. The latch, here, consists of a magnet mounted on a

leaf spring that is attracted to the end-effector of the bias-spring SMA actuator. The electrical current, in this case, is made to flow across the conductive magnet and into the SMA coil. Thus, only as the the magnet attaches to the end-effector of the SMA actuator will the SMA coil be heated using Joule's losses. Essentially, as the magnet and the SMA coil makes contact, the SMA element is heated and reduces in size due to the shape memory effect. During this phase, the magnet, which is mounted to a leaf spring, experiences a return force, F_S, and will continue to follow the actuator. Once, this force exceeds the attractive magnetic force, F_{mag}, between the magnet and the SMA coil, the latch detaches and immediately returns to its original location. This spring back occurs due to the resting return force of the leaf spring attached to the magnet. This concept can be implement in numerous ways including a mechanical latch mounted on a passive spring. Once this snap-through occurs, the electrical connection and the electrical current across the SMA is cut and will only be re-established when the bias spring of the SMA deforms the SMA coil and extends it back towards the latch as shown in fig. 4.3. In this manner, the oscillating behaviour is observed without any sensors, micro-controllers or electronics.

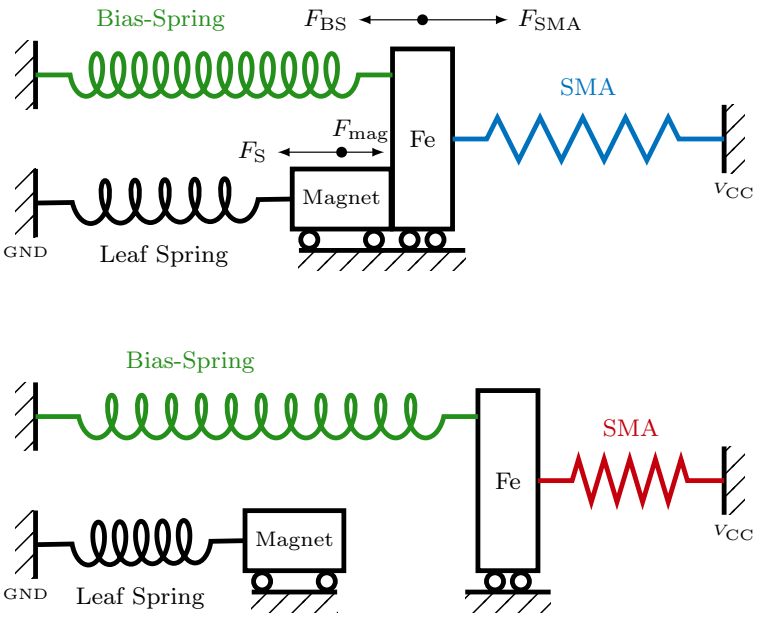

Figure 4.2: Diagram showing the working principle of the magnetic latch system implemented in the SMA oscillator.

As mentioned earlier, using a flexure-based mechanism permits the omission of a dedicated spring in the design. As seen in fig. 4.4, a proof-of-concept of this design methodology is implemented. Here, the linear stage is comprised of two parallel cantilever beams that also behaves as leaf springs. These biasing leaf springs apply a tractional return force on the SMA coil at a lower temperature while also preventing any unwanted degrees of freedom in the other axis. Another leaf spring is used to apply the return spring force required in the magnetic

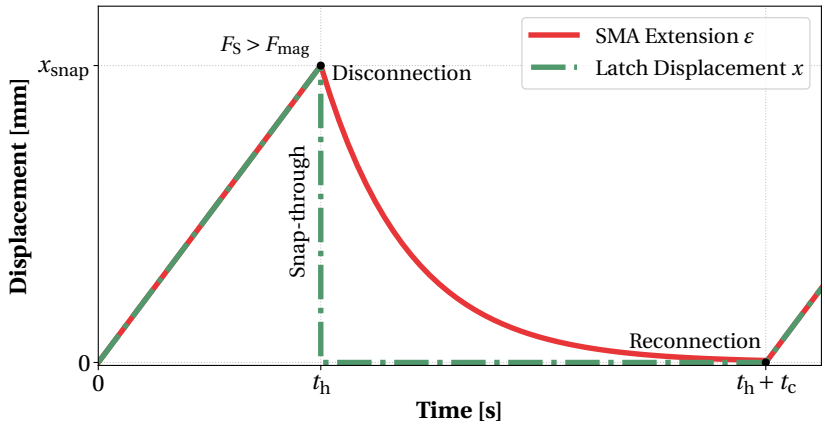

Figure 4.3: A schematic of the working principle of the magnetic latch control system. This diagram can be extended to represent any latch based system where there exists a snap-through at a certain stroke.

latch. Here, the SMA actuator is heated using the magnetic latch system and the snap-through of the latch occurs when the return force of the leaf spring exceeds the attractive force of the magnet, $F_{snap} = F_S > F_{mag}$. Therefore, the required contraction of the SMA coil, ε, can be controlled by sizing the leaf spring associated with the magnet.

$$\varepsilon = \frac{F_{mag}}{K_s} \tag{4.1}$$

where K_s is the rigidity of the leaf spring which depends on the dimensions of the cantilever beams and can be calculated using the analytical model described in the works by Rubbert et al. (2016) and Henein et al. (1998).

Here, in this proof-of-concept, the magnetic latch consists of a small magnet, with an attractive force of 150 g, mounted on a thin leaf spring measuring 500μm × 2.5mm × 30mm. An M2 screw is used to clamp an electrically conductive wire to the magnet and acts as the ground of the electrical circuit. The magnet latches onto another ferromagnetic M2 screw which is mounted to the end-effector of the SMA actuator, as seen in fig. 4.5. The SMA is supplied by *Dynalloy, Inc* (Irvine, CA) and is a 90°C Flexinol® coil with wire diameter of 200 μm and an outer diameter of 1.4 mm. The coil contains around 40 coils and with a solid length of 8 mm. The SMA is mounted on a 3D printed support containing a flexure-based linear stage which supports the free end of the SMA. The linear stage is 3D printed from PLA and consists of 2 parallel leaf springs with dimensions 500 μm x 10 mm x 30 mm.

This basic concept can be implemented in using different methods. The latch system can be replaced by a bistable mechanism and can then be paired with antagonistic SMA actuators. Here, the control system can be linked to the snap-through of the bistable mechanism where each stable position controls the heating of each SMA element. In this way, the first SMA can be heated till the snap-through of the bistable mechanism which will then change the electrical

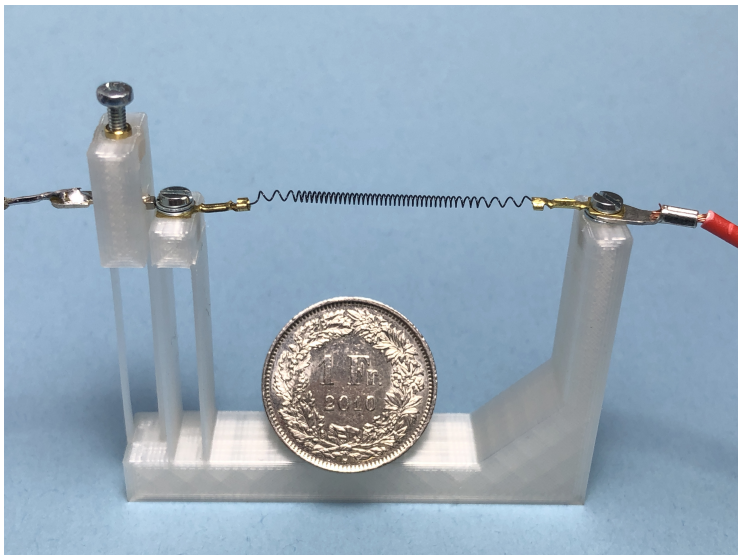

Figure 4.4: The integrated SMA control system implemented using a flexure-based magnetic latch creating an SMA mechanical oscillator.

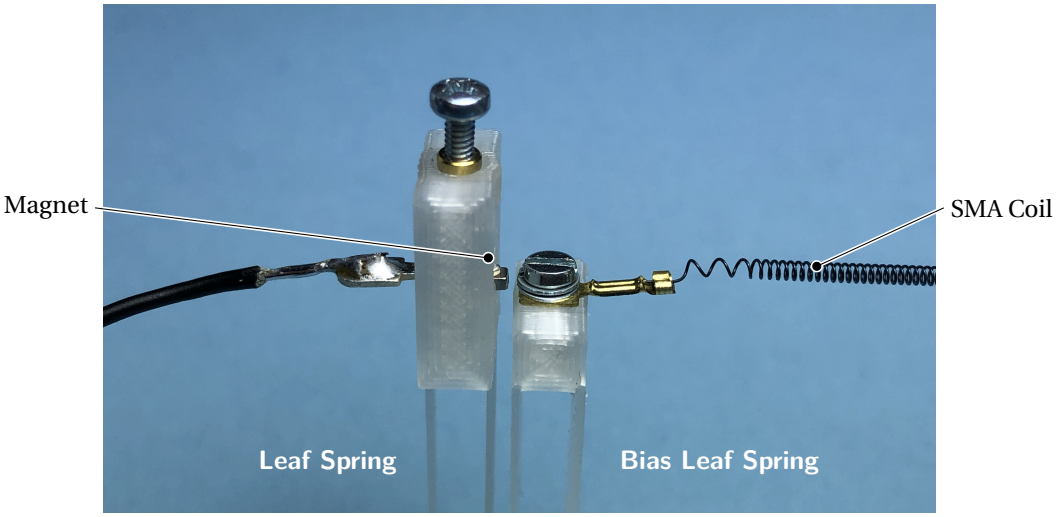

Figure 4.5: The close-up structure of the magnetic latch system that acts as the oscillating electrical contact for the SMA coil. Here, the biasing leaf spring also act as a linear stage for the actuator.

contact across the antagonistic SMA. This concept has been implemented and validated in chapter 6.

4.2.3 Sizing of the oscillator

As mentioned previously, the thermomechanical behaviour of the SME is exploited to create the mechanical control system. The sizing of the oscillator system is, thus, directly, dependant

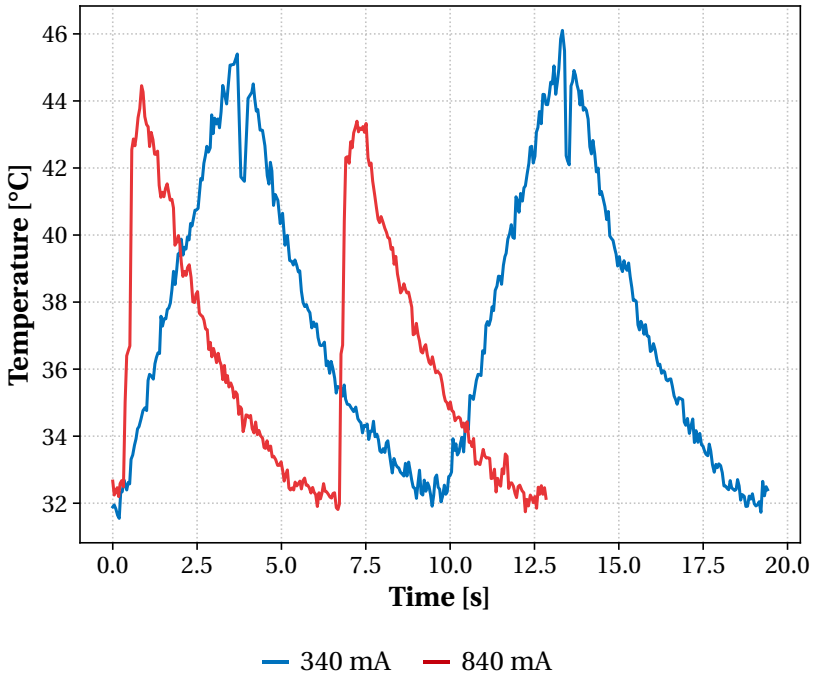

Figure 4.6: Effect of the current on the evolution of the SMA spring's temperature. This shows that the control system averts any risk of overheating.

on the thermal properties of the active element. The rise time or time till the snap-through occurs, depends on the time required to heat the SMA using Joule's heating. This implies that the current supplied across the SMA dictates the rise time of the oscillator. The fall time or time required to re-establish the electrical contact across the SMA depends on the cooling time of the SMA wire or coil. In the case where the SMA is cooled using passive thermal exchange with the surrounding air, the fall time can be controlled by adequately sizing the diameter of the SMA wire or coil. The amplitude of the system, in this case, depends on the latch system and can be sized using the equation 4.1. Furthermore, the stroke of the SMA actuator can be sized using the methods presented in chapter 3 so as to ensure that the actuator is capable of deforming to the levels demanded by the oscillator amplitude. This will ensure that the snap-through of the oscillator occurs before the SMA overheats.

The fall time of the control system can be calculated using a simple thermal model based on the passive cooling of the SMA wire or coil. Here, the time constant, τ_c, of the system in which the thermal exchange of heat from the surface of the SMA to the surround air is used to cool down the SMA can be expressed as :

$$\tau_c = \rho c d/(kH) \tag{4.2}$$

where ρ [kg/m^3] is the density, c [J/(kgK)] is the specific heat capacity, d is the wire diameter, $k = 4$ is the ratio between the surface area of heat exchange, A_S and the volume of the active

element, V, and H [W/(m^{2}K)] is the heat transfer coefficient. The thermal model of the wire can be expressed as :

$$T(t) = T_R + (T_2 - T_R)e^{-t/\tau} \tag{4.3}$$

where T_R is the ambient room temperature and t is time. Thus, the cooling time, t_c, based on the temperature gradient between the SMA and the surrounding air, can be expressed as :

$$t_c = \tau_c \log \frac{T_2 - T_R + \frac{T_2 - T_1}{2}}{T_2 - T_R - \frac{T_2 - T_1}{2}} \tag{4.4}$$

where the subscripts, 1 and 2, represents the operating points of the actuator as shown in chapter 3. The physical properties of the SMA were obtained by consulting the data given by the supplier at *Dynalloy*.

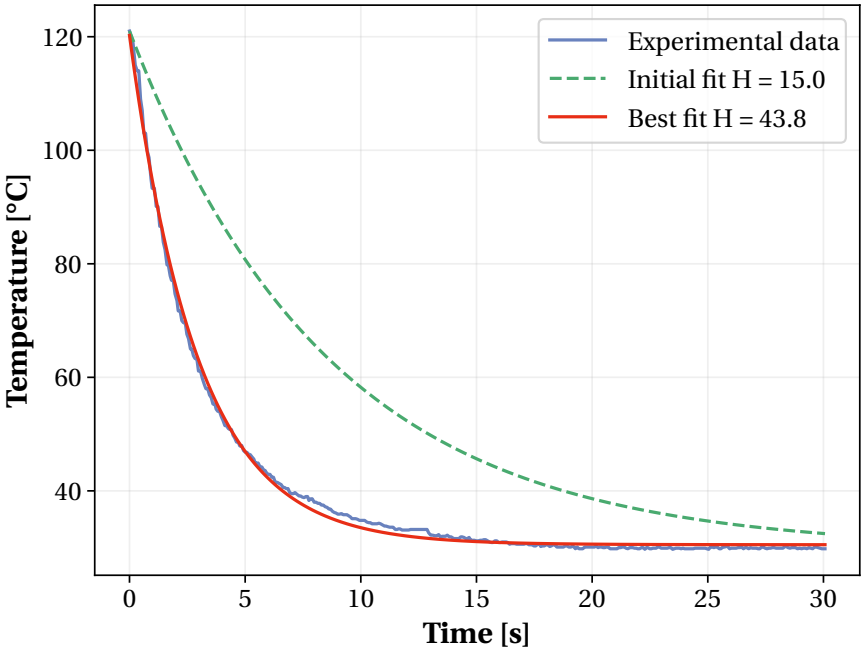

Figure 4.7: Measurement of the heat transfer coefficient, H, using 250 μm wire diameter SMA spring with a mandrel size of 0.5 mm.

Using a thermal camera with an optical zoom that allows for high spatial resolution and using equation 4.3, least-squares minimization is used to fit this thermal model to the cooling time of an SMA coil of 250 μm wire diameter. By doing so, the heat transfer coefficient, H, can be estimated. Using the model and the estimated parameters, the time constant and cooling times of other diameter SMA springs can be extrapolated. By extrapolating the cooling times of different diameter SMA springs, these values can be used to size this oscillator control system for other applications. In fig. 4.8, the cooling based on wire diameter of different SMA springs can be seen. Using these values, the fall time of the oscillator can be estimated for any wire diameter.

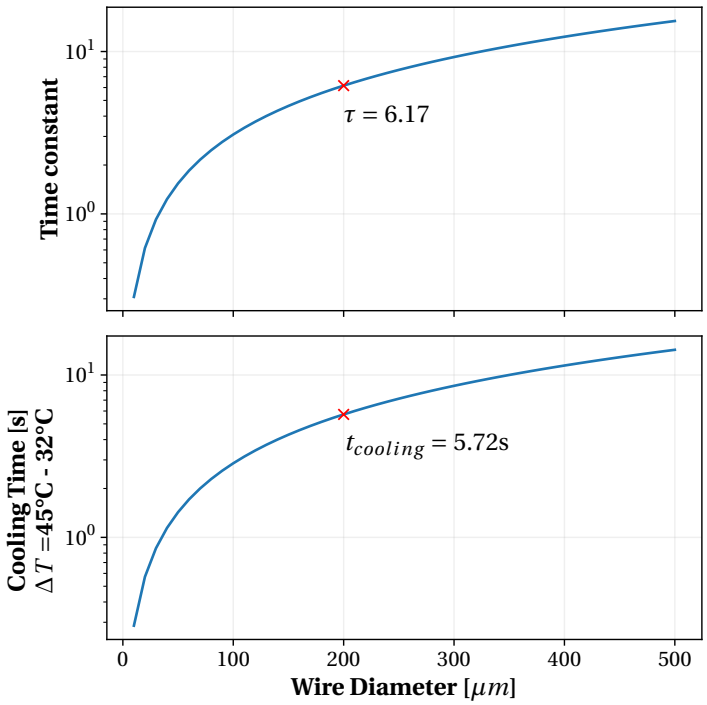

Figure 4.8: Extrapolation of the cooling time based on wire diameter with $H = 43.8$ W/(m^{2}K).

By calculating the time required to the heat the SMA wire using Joule's heating, the rise time of the oscillator, t_h, can be estimated. The known resistance of the SMA wire, R, and the current, I, supplied to the system, which can be easily measured, can be used to calculate the heating time based on the basic laws of electro-thermodynamics. In the case of small currents and a slower rise time, the loss of heat with the surrounding air by convection must be taken into account and can be estimated with the following equation :

$$t_h = \int_{T_1}^{T_2} \frac{\rho V c}{I^2 R - H A_S (T - T_R)} dT \tag{4.5}$$

In this model, the latent heat of transformation is not considered and the resistivity of the SMA is considered to remain constant. These assumptions are not always valid but can still serve as a reasonable approximation of the heating time. The work by Liu et al. (2021) has established an extensive numerical model capable of predicting the heating times quite accurately but requires extensive experimental testing of the material and environmental constants. This complex nature of the heating model makes it difficult to obtain an accurate heating time. Often, this complexity makes it difficult to size the current required to heat the SMA while still preventing the SMA from overheating. Thus, when it comes to accurate control of the SMA, a temperature sensor is required to prevent the destruction of the SMA coil or wire. However, using the proposed integrated control strategy based on mechanical-intelligence, a high current can be supplied to the SMA such that the heating time is drastically reduced and

have the SMA automatically disconnect the contacts so as to ensure the safety of the SMA coil or wire without requiring any sensors.

This control system was supplied with a constant current and left to oscillate for 2 minutes to test the repeatability and consistency of the rise and fall times. The temperature of the SMA coil was measured using a thermal camera with high spatial resolution and the stroke of the SMA actuator was measured using a laser displacement sensor. In fig. 4.6, the temperature and position fluctuations of the oscillator are shown. The rise time of the magnetic latch-based control system when supplied with 340 mA was measured to be 3.8 ± 0.18 s while the rise time when supplied with 840 mA was measured to be 0.64 ± 0.09 s. The cooling time when supplied with 340 mA and 840 mA was found to be 5.71 ± 0.09 s and 5.82 ± 0.2 s, respectively. Thus, the period of the oscillations for the two measurements were found to be 9.60 ± 0.17 s and 6.47 ± 0.22 s which corresponds to a frequency of 0.10 Hz and 0.16 Hz.

The rise time and cooling times of the latch-based control system were measured by detecting the peaks and troughs of the measured signals. The mean and standard deviation of these values were then calculated. Furthermore, the cooling times with respect to the SMA geometry predicted, in fig. 4.8, fits with the measured values, thus, validating the thermal model. Furthermore, with respect to the varying current across the SMA, the cooling time remains relatively constant. This implies that the cooling times can be predicted using the analytical model and the value can be considered to remain constant, even while varying the current. The implication being that the oscillating control system can be sized for a fixed fall time by appropriately sizing the SMA wire dimensions.

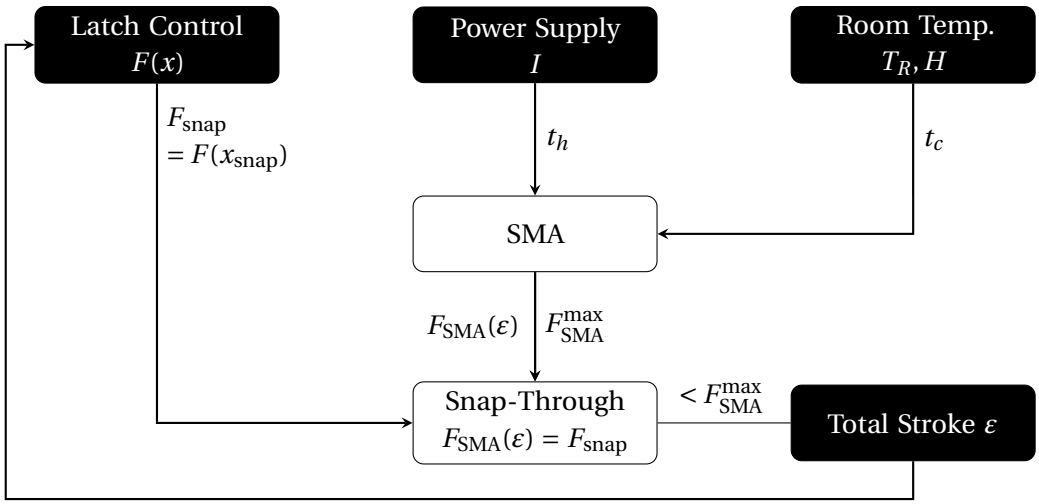

Figure 4.9: The generalised schematic of the mechanically-intelligent control strategy.

This magnetic latch system allowed the bias-spring SMA actuator to be actuated without any sensors or risk of overheating the SMA. The latch enables the SMA to be heated during its entire stroke. Additionally, a system using pogo pins, which are electric contacts consisting of a plunger and a spring mounted inside a barrel, was also tested. This resulted in a behaviour

where the bias-spring SMA actuator oscillated at the tip of the pin. This, unfortunately, showcased the need for a latch system to rapidly bring the electric contact back to the starting position such that the actuator can carry out its entire stroke during the cooling phase as shown in fig. 4.3. A mechanical latch system based on friction and snap-fits can be designed as a simpler alternative. This pogo pin solution had the unexpected effect of allowing the SMA coil to be maintained at a stable temperature. This effect could be potentially used to stabilise an SMA at a fixed temperature based on the stroke of the pogo pin. The behaviour was not further explored in this work. However, as seen in fig. 4.9, a generalised approach to creating the proposed mechanically-intelligent control strategy is described. The basic principle consists of exploiting the snap-through of the latch system. Here, the latch system is sized such that the force required to attain the snap-through is lower than the maximum pull force of the SMA element. This resulting mechanically-intelligent oscillator can be sized and its rise time and fall time can be estimated by using the geometrical dimensions of the active SMA element. Using this principle, the control system of the SMA actuator can be sized so as to allow a cyclical oscillation with a constant stroke and frequency while preventing any chance of SMA overheating. Furthermore, as no sensors or micro-controllers are present, the overall work density of the SMA actuator is conserved.

4.3 Validation of the Approach using a Case Study

As stated previously, the requirement of sensors and complex control strategies in certain applications where compactness and being lightweight are required, pollute the overall work-weight density of the robotic system. In this section, to validate the novel design methodology for mechanically-intelligent control solutions, a lightweight and compact crawling robot powered by shape memory alloys is designed and fabricated. Here, in the creation of an untethered crawling robot, the presence of sensors or micro-controllers will play an important role in the final work density of the system.

In this SMA driven crawling robot, the magnetic latch-based control system is implemented so as to create a small scale robot that can be driven without any sensors or electronics. In this mechanism, the high work density of the SMA is not compromised due to the lack of large biasing-springs and control electronics when compared to examples such as the work by Muralidharan et al. (2021).

4.3.1 Background and Biological Analysis

The mobile robot fabricated using this design approach is inspired by the gait of the inchworm. This insect is not a type of worm but in-fact, a type of caterpillar. These inchworms are known for their peculiar type of locomotion made possible by a looping motion called the two-anchor crawling gait, as described in the work by Wang et al. (2014). Its gait consists of attaching its forelegs and using the muscles located in its abdomen to pull the rest of its body, as demonstrated in Plaut (2015).

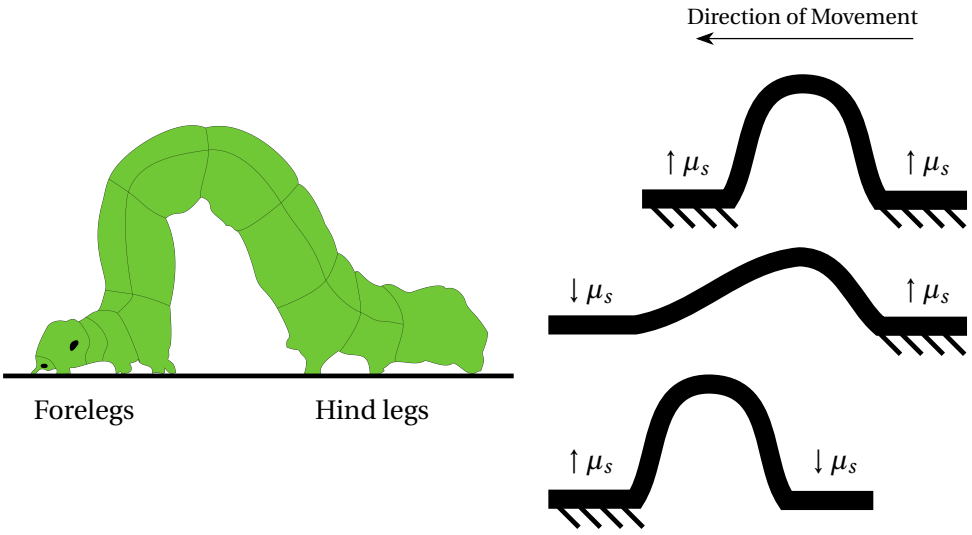

Figure 4.10: The gait analysis of an inchworm showing the change in the coefficient of friction (μ_s) of the insect legs with respect to the ground by either gripping or sliding its legs.

The gait, as seen in fig. 4.10, consists of alternating between gripping or slipping against the ground. Initially, the forelegs are made to slip while the abdominal muscles push against the hing-legs which are now planted firmly on the ground. Nest, the forelegs are made to grip the ground and the abdominal muscles pull the rest of the body while the hind-legs slide across the ground. This pattern is repeating to allow the inchworm to crawl across the surface. The presented mobile robot exploits this gait to create a similar crawling locomotion.

4.3.2 Working principle and Implementation of the Robot

The basic working principle of this mobile robots consists of implementing the design methodology presented in chapter 3 and the magnetic latch-based control system. Here, the linear movement of the SMA oscillator is transformed into a rotation of a pair of legs such that the tips or claws of the leg pulls the body of the insect robot across the ground.

As seen in fig. 4.11, the inchworm robot is entirely 3D printed in a single piece and is powered using an SMA coil. The control system used in this design is based on the approach detailed in section 4.2.2. The legs of the insect robot is attached to the end-effector of the SMA actuator so as to harness the strain recovery when the SMA coil is heated using Joule's heating. Here, as detailed in chapter 3, the biasing element of the SMA actuator consists of a flexure-based cantilever leaf spring. This biasing element also acts as a simple kinematic stage that transforms the SMA linear strain recovery into a rotation of the robot legs.

The insect robot operates in a similar manner to the inchworm presented in section 4.3.1 where the claws alternate between high friction and low friction with respect to the ground. By activating its artificial abdominal muscle consisting of the SMA coil, the insect robot is able to crawl across the ground. Here, the alternating friction that occurs at the claws is due to the

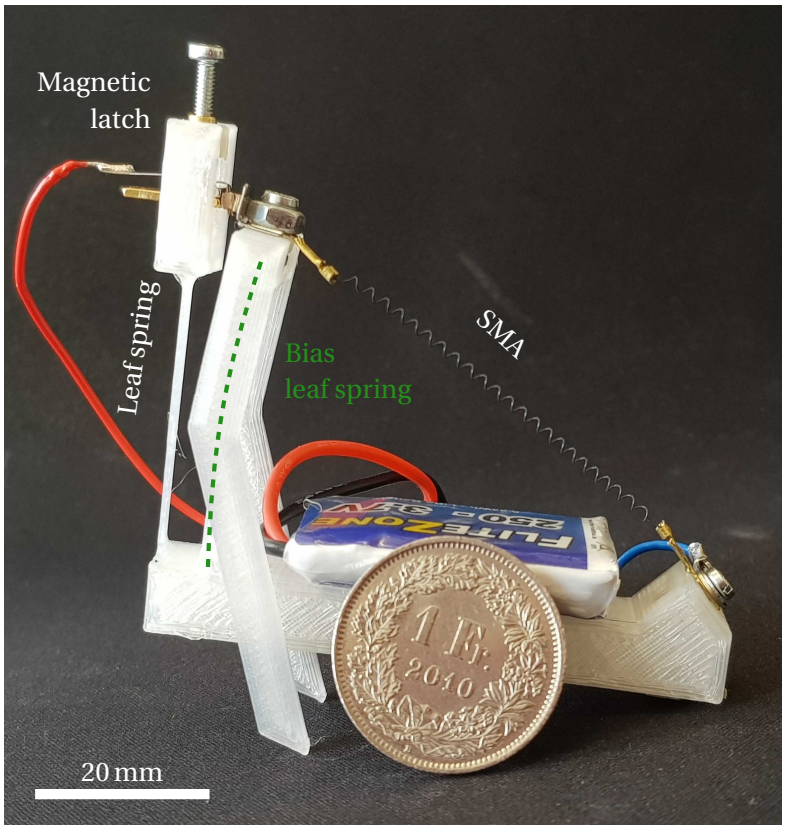

Figure 4.11: The implementation of the insect robot around the mechanical SMA oscillator.

design of the tips of the insect legs. The angle of the legs as the robot moves changes the angle of contact with the ground surface. As the leg tip design is asymmetrical with the direction of movement, the rotation of the legs cause alternating high and low friction. The behaviour is similar to a ratchet system where one degree of freedom is allowed in the forward direction but not in the backward direction. Here, the claw design allows rotation in the clockwise direction but prevents some rotation in the anti-clockwise direction. As the SMA is heated, the insect robot moves its forelegs away from the body. Then, when the SMA coil is stretch by the biasing leaf spring during cooling, the forelegs grip the ground and drags the rest of the body along the ground. By repeatedly heating and cooling the SMA, the insect robot can gradually move across the ground. As detailed in this novel control strategy, the magnetic latch system allows the SMA to oscillate and control the steps of the insect robot without any micro-controllers or electronics.

4.3.3 Analytical model of the Biasing Compliant Mechanism

When sizing the design and SMA of the insect robot, an analytical model of the compliant mechanism is required. This model allows dimensioning the SMA coil such that sufficient stroke is observed during the shape memory effect. Here, the stroke of the SMA actuator or

the contraction of the SMA coil corresponds to the estimated step length of the insect robot.

The crux of the design revolves around the flexure-based biasing element and kinematic stage which, in this design, consists of a simple cantilever leaf spring. This flexural structure converts the linear contraction of the SMA coil into the rotation of the insect legs while also serving as the bias spring for SMA actuator allowing the coil to be stretched during the cooling phase based on the design approach detailed in chapter 3.

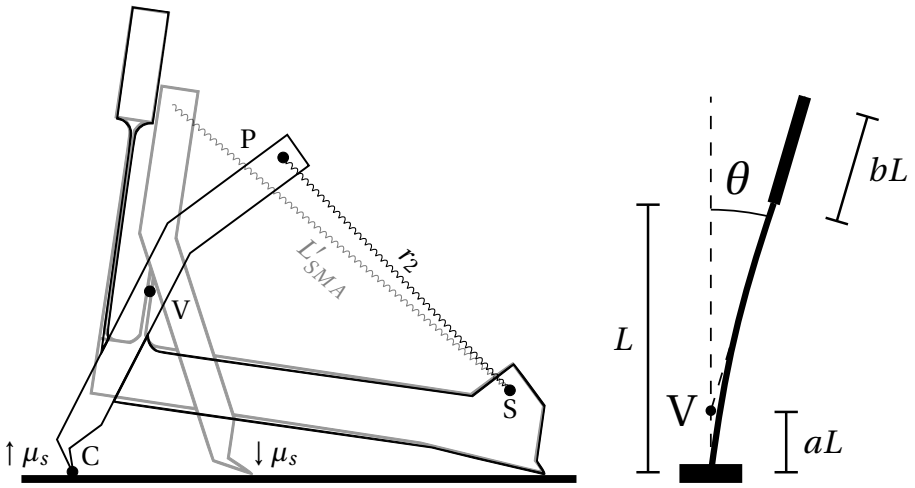

Figure 4.12: The working principle of the insect robot showing the simplification of the cantilever beam to a virtual rigid body pivot. The claw design changes the coefficient of friction (μ_s) of the insect with respect to the ground allowing the robot to crawl.

The pseudo-rigid-body model, as described in the work by Howell et al. (2013), is used to model flexure-based mechanisms such as the cantilever beam as traditional rigid-body mechanisms. Thus, by simplifying the cantilever leaf spring as a virtual pivot, an analytical model can be established to estimate the effect of the SMA coil contraction. In the work by Zhang et al. (2007), the location of the virtual pivot can be estimated with relative accuracy to a point at a distance of aL from the clamped end of the cantilever beam, where L is the length of the beam, bL is the length of the rigid attachment point with the SMA coil and a is:

$$a = \frac{1+3b}{3+6b} \tag{4.6}$$

The pre-stretched SMA coil of length, L'_{SMA}, is attached to the biasing cantilever leaf spring at the free end as shown in fig. 4.12. The position of cantilever tip, $P(x_P, y_P)$, as the SMA coil contracts in length by ε, can be deduced by finding the intersection between the two circles with radii, r_1 and r_2, and with centres at the virtual pivot $V(x_V, y_V)$ and fixed end of the SMA coil $S(x_S, y_S)$, respectively.

$$P(x,y) = \frac{1}{2}\begin{pmatrix} x_V + x_S \\ y_V + y_S \end{pmatrix} + \frac{r_1^2 - r_2^2}{2R^2}\begin{pmatrix} x_S - x_V \\ y_S - y_V \end{pmatrix} \pm \frac{1}{2}\sqrt{2\frac{r_1^2 + r_2^2}{R^2} - \frac{(r_1^2 - r_2^2)^2}{R^4} - 1}\begin{pmatrix} y_S - y_V \\ x_V - x_S \end{pmatrix} \tag{4.7}$$

where R is the Euclidean distance, $|\overline{VS}|$, between the two circle centres, $r_1 = (1 - a + b)L$ and $r_2 = L'_{SMA} - \varepsilon$ representing the current length of the SMA coil.

As the insect legs are attached at the cantilever tip, the claw tips, $C(x_C, y_C)$, of the insect robot can be estimated by using a series of simple translation and rotation transformations from the cantilever tip based on the angles (α) and lengths (L) of the insect leg segments.

$$C(x,y) = \begin{pmatrix} x_P \\ y_P \end{pmatrix} + \sum_{i=1} L_i \begin{pmatrix} \cos(-\frac{\pi}{2} - \theta + \sum_{i=1} \alpha_i) \\ \sin(-\frac{\pi}{2} - \theta + \sum_{i=1} \alpha_i) \end{pmatrix} \tag{4.8}$$

Thus, based on the contraction or strain recovery of the SMA coil (ε), the step length of the insect, ΔC, can be estimated by taking the Euclidean distance between the claw tip location before and after the SMA contraction. The position of the insect robot claw and the step length based on the SMA coil contraction can be seen in fig. 4.13.

4.3.4 Implications of the Prototype

As detailed in the methodology, the analytical model of the inchworm robot that determines the relationship between the contraction of the SMA during actuation and the estimated step length was first estimated. This design was simulated using a commercial finite element modelling (FEM) software which was then used to validate the analytical model, as shown in fig. 4.13. Furthermore, the experimental results obtained from the inchworm prototype were used to validate the model, as shown in the same figure. This comparison shows that the pseudo-rigid body model used to model the design is quite accurate and can thus be used to further optimise the step length in future iterations.

Due to the design being based on flexure-based structure, the inchworm could be fabricated from a single 3D printed piece. The structure was printed from PLA filament using fused deposition fabrication based on the parameters shown in table 4.1. Due to the novel control system based on the magnetic latch, when connecting the robot to a 20 mAh battery, the robot is able to crawl untethered , as shown in fig. 4.14, for an estimated 1.6 min. When allowed to crawl on a flat surface, the average speed of the insect robot was measured to be 1.55 mms^{-1}, as shown in fig. 4.15. The efficiency of the leg design is highly dependant on the surface; smoother surfaces cause the legs to slip and drastically changes the overall efficiency of the design.

Table 4.1: The design parameters of the inchworm robot.

Parameter	Value
SMA dimensions	Coil: ∅1.37 × 12 mm Wire: ∅0.2 mm
Biasing Leaf Spring	30 × 10 × 0.6 mm
Magnet Leaf Spring	30 × 2.5 × 0.6 mm
Magnet force	1 N
Battery Life	1.6 min @ 20 mAh

As stated, the principle advantage to the novel control system approach is the absence of sensors or micro-controllers. Using this methodology, the total weight of the robot including the battery weights 9.7 g. The insect robot is powered using only a single SMA coil. As with most SMA actuators, the coil is heated using Joule's heating by passing a current through it.

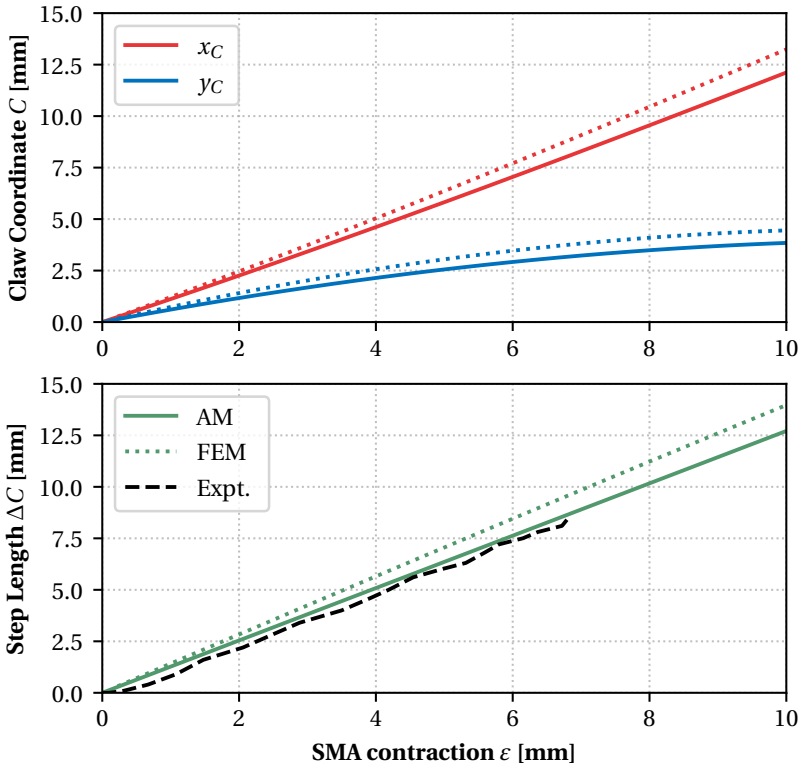

Figure 4.13: Comparison of the leg tip displacement with respect to the contraction of the SMA coil between the analytical model (AM) and Finite Element Model (FEM) simulation. Here, the dotted and filled lines represent the FEM results and analytical model, respectively.

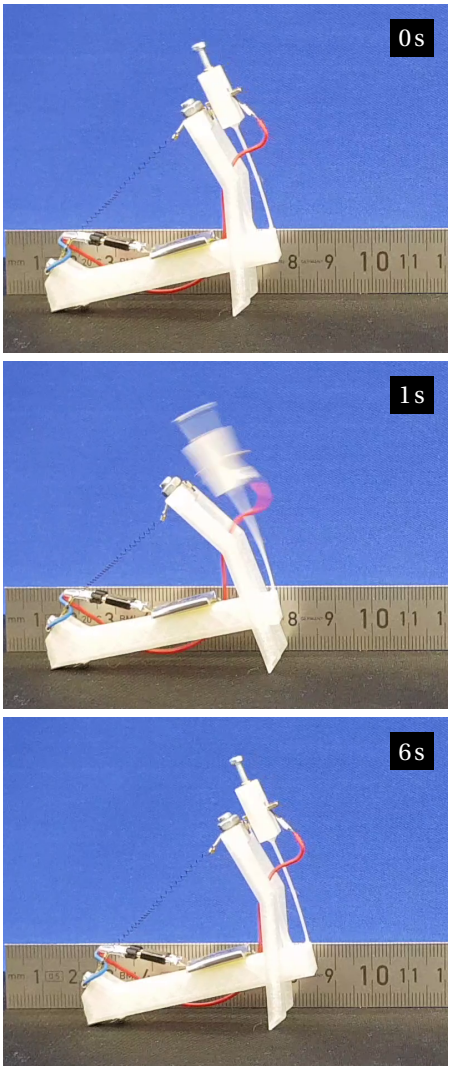

Figure 4.14: The untethered gait of the insect robot with a step length of 8.4 mm. As predicted, the snap-through of the magnetic latch halts the heating of the SMA coil.

Here, the heating consists of passing a 770 mA current for a duration of 750 ms with a power of 1.7 W. As shown in fig. 4.13, the step length of the insect robot was measured to be 8 mm.

Often, in the case of mobile robots, especially bio-inspired robots, the cost of transport (CoT) is calculated to compare the design and implementation. This factor allows the comparison of mobile robots with varying structures, sizes and gaits. It can be calculated using the following equation :

$$\text{CoT} = \frac{E}{mgd} \tag{4.9}$$

where E is the energy required to heat the SMA, m is the total mass of the robot including the battery, g is the acceleration due to gravity and d is the step length of the robot. Using the

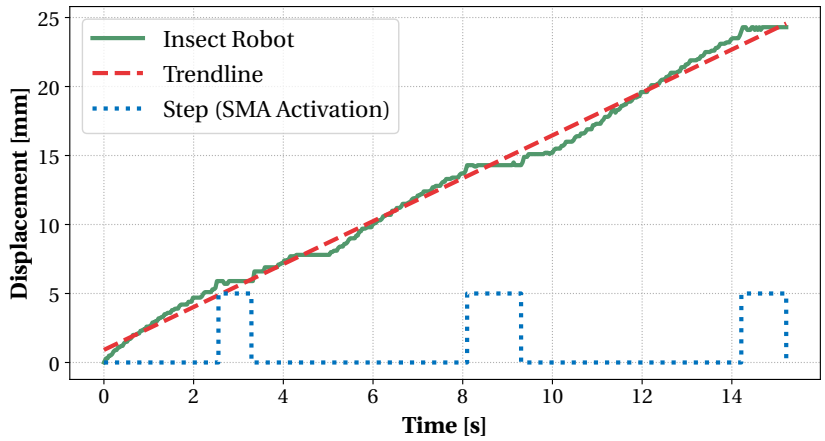

Figure 4.15: The measured gait of the insect robot. The average speed of the robot measured to be 1.55 mms^{-1}. Here, the dotted step line represents the state of the SMA. A high value denotes that the SMA coil is being heated while a low state denotes that the SMA coil is cooling down.

equation, the CoT was calculated to be around 1620 $Jkg^{-1}m^{-1}$. This is comparable to other untethered inchworm robots like in the work by Ji et al. (2019) whose CoT is measured to be 1670 $Jkg^{-1}m^{-1}$. Furthermore, when compared to other SMA powered inchworm robots, as shown in fig. 4.16 and fig. 4.17, this work has performances comparable to its tethered alternatives. In the mesoscale range, this untethered inchworm robot is able to reach higher work densities. This shows the advantage of the proposed design methodology and showcases the advantage of a mechanically intelligent control strategy. The limitations of this robot arise from the inefficiency in the claw design and the dependence on the friction with the ground. The design, while being cheap and easily manufactured using 3D printing, it is limited by the chosen PLA material. The material can be optimised to create thinner leaf springs and the final size of the robot can be greatly reduced. In the future work, the optimisation of the claw design can greatly improve the overall efficiency of the locomotion by preventing slipping.

4.4 Summary and Conclusion

In this chapter, a novel approach to design a mechanically intelligent control system is presented. In this methodology, the control stage of a traditional SMA actuator is integrated into the kinematic stage of the actuator. This results in a control mechanism that uses the thermomechanical behaviour of the SMA such that the system no longer requires any sensors or electronics and is controlled entirely mechanically.

Furthermore, a basic implementation of such a system is presented using a magnetic latch-based system. Using a magnet and flexure-based cantilever leaf springs, a magnetic latch was designed and implemented where after a certain stroke threshold, results in an instantaneous snap-through. This rapid bifurcation is exploited to instantly and mechanically disconnect the

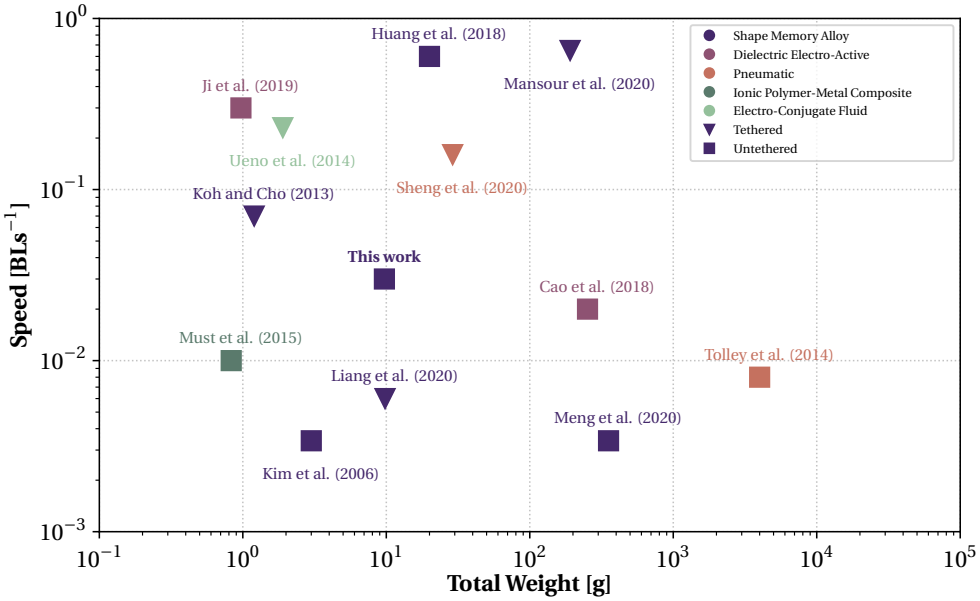

Figure 4.16: The distribution of various different inchworm robots powered by smart materials based on their total weight and speed (in Body Lengths (BL) per second).

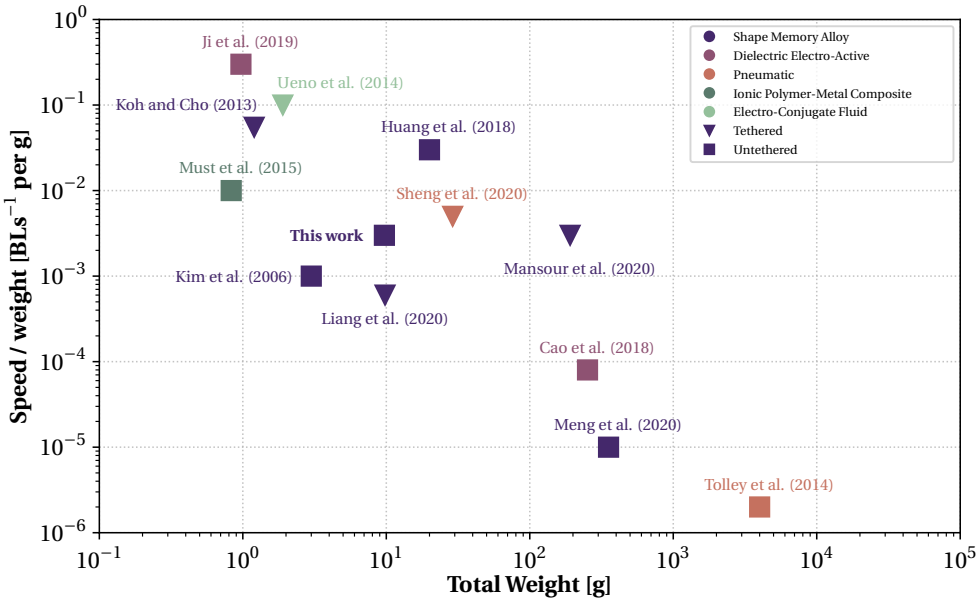

Figure 4.17: The compairson of various different smart material powered inchworm robots with respect to the speed / weight ratio (in Body Lengths (BL) per second per gram).

electrical contact across the SMA and thus, preventing any overheating. This design principle was implemented by fabricating a basic SMA mechanical oscillator that requires no sensors or electronics to oscillate.

Lastly, the design methodology was validated using a case study consisting of an untethered crawling insect robot powered by a single SMA coil. Here, based on the presented design methodology, a biasing flexure-based SMA actuator was modelled and sized to power the crawling robot. Furthermore, the control system presented in this chapter, was implemented using the magnetic latch system so as to create a reversible control scheme for the SMA actuator. The kinematic stage, which acts as the biasing element of the SMA actuator, is exploited within the control system. Based on the results from the locomotion of the untethered insect robot, a regular step size and walking speed is observed while weighing less than 10 g, thus, validating the design approach presenting in this chapter. When compared to similar mesoscale crawling robots, the mechanically intelligent design approach has allowed the speed-weight ratio of the robot to be similar to other tethered alternatives.

Using the methodology presented in this chapter, a novel control system can be designed and sized such that the SMA actuator can be controlled without the need for bulky sensors and micro-controllers and without the risk of overheating the SMA element and greatly increasing the volumetric work density of the actuator.

With the design principles presented in this chapter, the traditional discrete building blocks of an SMA actuator are further integrated. In the follow chapter, the same principle of integration can be extended to create actuators where the active SMA element acts as a kinematic stage. Traditionally, the SMA elements are fabricated and designed using simple geometries such as wires, coils and sheets. By extending the kinematic stages that convert or amplify the of the SMA elements to harness the shape memory effect directly, the work density of the actuator can be further improved. In the next chapter, this design principle will be explored along with tools and strategies to generate such integrated SMA actuators.

Publications related to this chapter :

S. Thomas, P. Germano, T. Martinez, and Y. Perriard, *"An Untethered Mechanically-Intelligent Inchworm Robot Powered by a Shape Memory Alloy Oscillator,"* Sensors and Actuators A: Physical, p. 113115, Oct. 2021, doi: 10.1016/j.sna.2021.113115.

S. Thomas, P. Germano, T. Martinez, and Y. Perriard, *"Control-Free Mechanical Oscillator Powered by Shape Memory Alloys,"* in 2021 IEEE/ASME International Conference on Advanced Intelligent Mechatronics (AIM), Jul. 2021, pp. 1119–1123. doi: 10.1109/AIM46487.2021.9517468.

Table 4.2: Comparison of the proposed mechanically-intelligent inchworm robot with various different smart material based crawling robots based on their speed and weight

Smart Material Technology	Tether	Robot length (BL) [mm]	Speed [mms^{-1}]	Speed [BLs^{-1}]	Total weight [g]	Speed / weight [BLs^{-1} per g]
SMA [This work]	No	60	1.55	0.03	9.7	3×10^{-3}
SMA [Meng et al. (2020)]	No	280	0.95	0.0034	354	1×10^{-5}
SMA [Kim et al. (2006)]	No	50	0.17	0.0034	~3	1×10^{-3}
SMA [Huang et al. (2018)]	No	57	34	0.6	~20	3×10^{-2}
ECF [Ueno et al. (2014)]	Yes	23	5.2	0.23	1.9	1×10^{-1}
SMA [Liang et al. (2020)]	Yes	54	0.34	0.006	9.8	6×10^{-4}
SMA [Mansour et al. (2020)]	Yes	200	130	0.65	191	3×10^{-3}
Pneumatic [Sheng et al. (2020)]	Yes	66	10.5	0.16	29	5×10^{-3}
DEA [Ji et al. (2019)]	No	40	12	0.3	0.97	3×10^{-1}
SMA [Koh and Cho (2013)]	Yes	150	10	0.07	1.2	0.055
DEA [Cao et al. (2018)]	No	200	4	0.02	252.6	8×10^{-5}
Pneumatic actuator [Tolley et al. (2014)]	No	650	5	0.008	~4000	2×10^{-6}
IPMC [Must et al. (2015)]	No	45	0.45	0.01	0.83	1×10^{-2}

5 Generation of Actuators Powered by Compliant SMA Elements

5.1 Introduction

Smart materials, due to their integrated nature of reacting mechanically to a certain type of stimulus, have become an integral part of designing complex actuators. These materials have become an integral part of designing integrated and compact actuators. As presented in chapter 3, integrating the traditional building blocks of the tradition smart actuator can results in more compact designs. The behaviours of smart materials, however, range from simple linear behaviours to highly complex multi-physical behaviours. Thus, designing smart actuators with complex geometries are only feasible with certain types of smart materials.

In the case of shape memory alloys, the shape memory effect is a complex non-linear behaviour that is reliant on multiple kind of physics. This results in active elements present in SMA actuators to often be in the shape of wire, coil or thin sheets. These 1-dimensional structures are the most common type of implementation in SMA actuators due to the fact that their behaviours when heated or cooled are more easily predicted. As stated, in practice, when complex motions are required, the actuator is composed of complex kinematic stages and a simple SMA wire or coil as shown in the work by Singh and Ananthasuresh (2013) and Hwang and Higuchi (2016).

When taking inspiration from other more established smart materials, complex designs that still exhibit the smart behaviours of the material are often generated using algorithm as shown in the work by Ruiz and Sigmund (2018). Topology Optimization (TO) has been essential in designing such complex design that can take simple inputs and transform them into more complex and useful outputs. These compliant mechanisms fabricated from smart materials are compact and lightweight. However, combining this design methodology with SMAs can be quite difficult and computationally expensive to implement due to the highly non-linear nature of the Shape Memory Effect (SME).

In this chapter, a robust design methodology to design compliant SMA structures for powering integrated smart actuator is presented. Furthermore, a qualitative factor is described that

can be used to compare various generated SMA topologies. Using Finite Element Modelling (FEM), the various topologies are simulated and shown to exhibit the shape memory effect.

While the conception of compliant SMA actuators are an attractive solution to creating compact yet complex actuators, the high cost and limited fabrication methods that exist for creating such actuators calls into question the feasibility of such a strategy. Numerous works such as the work by Elahinia et al. (2018) shows the possibility of realising these compliant smart structures and with the advent of these technologies, the proposed design approach can be used to design and generate these novel compliant SMA actuators. In most cases, however, the high cost of fabrication creates a limited implementation of the strategy for a wide range of applications. In this chapter, the design approach to creating compliant SMA smart structures is extended to reduce the fabrication costs by using designs inspired by the art of kirigami.

Kirigami, which is the Japanese art of cutting paper to create intricate structure, can be used to create smart structure from thin sheets of SMA. These structures, using only a limited quantity of SMA, can be cut using a laser cutter or water jet cutting to create deployable structures that deform out of plane to create smart structures that exhibit novel outputs when compared to a simple thin film of SMA. These kirigami structures have been employed in works by Tang et al. (2017) and Shyu et al. (2015) to create stretchable or deployable structures for use in mechanical applications. However, when using the design approach in this chapter, these 2D structures, when fabricated in SMA, can be shown to exhibit the shape memory effect and be used in creating advanced compliant smart actuators.

5.2 Designing Integrated Active Elements

When designing smart actuators that display complex output motions, they generally consist of 1D SMA structures such as wires coupled with complex kinematic stages that transform the simple linear motion into complex ones, as shown in the work by Modabberifar and Spenko (2018) and Maffiodo et al. (2017). By extrapolating the methodology presented in chapter 3, it is conceivable to imagine a scenario where the active SMA elements and the kinematic stages are combined, as shown in fig. 5.1. Here, compliant structures fabricated from a monolithic block of SMA can be used to create compact actuator that no longer require a kinematic stage consisting of multiple pieces.

The challenges posed by this approach consist of the complex nature of the shape memory effect. The behaviour, consisting of highly non-linear behaviour and comprised of multi-physical variables, makes it hard to predict when the complex geometries are heated or cooled. Furthermore, implementing generative algorithms that design these complex geometries, as implemented with other simpler smart materials, is difficult due to the high computational costs required to simulate the shape memory effect.

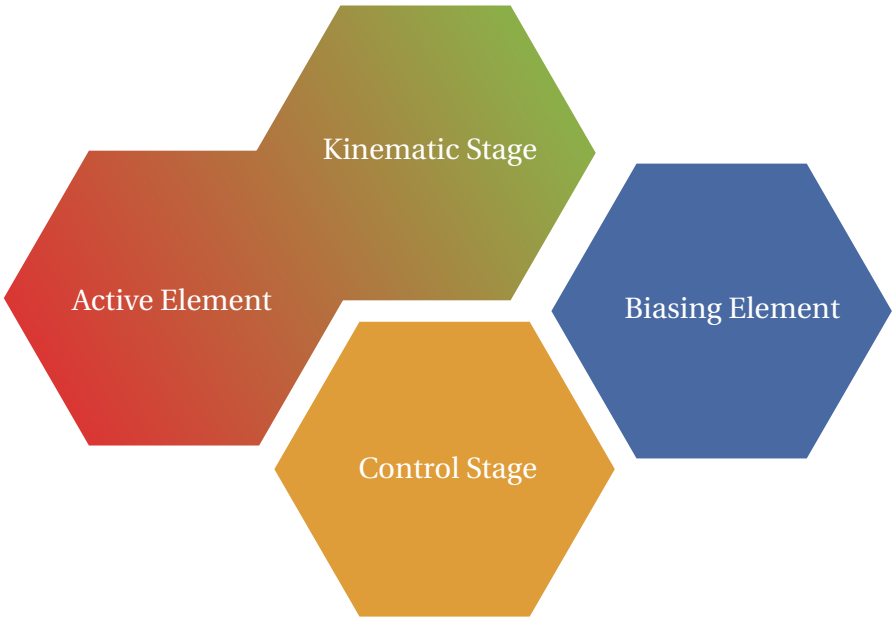

Figure 5.1: Diagram of the adapted building blocks of the SMA actuator based on integrating the active element and the kinematic stage.

5.3 Generation using Topology Optimization

Due to the high computational costs of simulating the shape memory effect, it is quite difficult to generate complex novel geometries even with poor mesh resolution. The basic principle of the proposed approach is to generate novel designs made of SMAs with computer-aided methods such as topology optimisation method (TOM). Here, the crux of the approach consists of abstracting the temperature-dependent effects but appropriately formulate the design problem so as to indirectly take into account the requirements of the shape memory effect.

When purely optimising for strain and assuming a standard elastic material, compliant mechanisms can be designed without considering the nonlinear nature of the material. Here, as mentioned previously, the requirements of the shape memory effect consists of a certain level of deformation during lower temperatures. Thus, the optimisation, when designing the compliant structure that when exposed to a biasing element, prioritises the strain across the entire structure. As long as the material undergoes sufficient deformation, above a critical strain threshold, will exhibit the shape memory effect when heated to higher temperatures. The analysis is executed assuming small and purely elastic deformation to reply on linear finite element analysis so as to significantly reduce the computational time.

5.3.1 Density-Based Topology Optimization

The basic concept being topology optimisation consists of investigating the distribution of material inside a discretised design space while trying to improve a certain specified objective

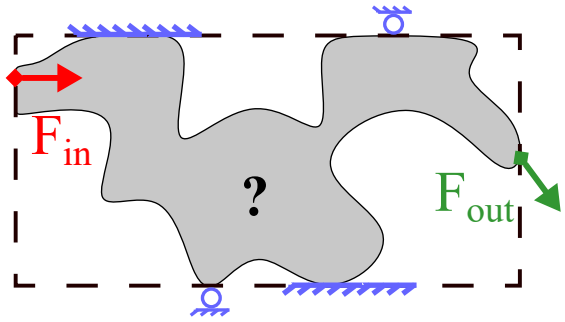

Figure 5.2: Basic design problem for compliant mechanisms.

function. The design variables applied in this density-based approach optimisation are artificial densities ρ that describe the proportion of the material, $0 < \rho_{\min} \leq \rho \leq 1$, an individual domain space is filled with. The lower and upper bounds of density range are considered as *full* materials representing fully empty or fully filled elements, respectively. While the densities within the range are defined as *intermediate* materials. Here, this artificial density variable are made continuous to use a gradient-based solver which has the advantage of lower computational time compared to non-gradient based approaches, as shown in the work by Sigmund (2011). In order to avoid mesh-dependent solutions and checker-board patters, the optimisation is regulated. This is achieved with a density filter that limits the length scale, $r_{\min}$, to a minimum inside the structure, as shown in the work by Bendsøe and Sigmund (2004).

Each iteration of the optimisation consists of the following steps. First, the filtered design variables are mapped to a material property using the Material Interpolation Scheme (MIS). This converts the artificial densities into a usable Young's Modulus. Next, the well-known Solid Isotropic Material Penalisation (SIMP), as shown in eq. (5.1) from the work by Bendsøe and Sigmund (2004), is implemented. This scheme penalises intermediate materials so as to prevent obtaining a geometry that cannot be manufactured. This is done using a penalty facor n which continuously increases throughout the optimisation.

$$\mathrm{E}_e = \mathrm{MIS}(\rho_e) = (\overline{\mathrm{E}} - \underline{\mathrm{E}})\rho_e^n + \underline{\mathrm{E}}, \tag{5.1}$$

with $\underline{\mathrm{E}}$, $\overline{\mathrm{E}}$ the lower and upper bound of $\vec{\mathrm{E}} = [\mathrm{E}, \cdots, \mathrm{E}_{\mathrm{NE}}]^{\mathrm{T}}$ respectively corresponding to the Young's modulus of an "empty" element and a completely filled one. NE is the number of elements inside the domain. When the material properties of each element are known, the *Stiffness matrix* K of the corresponding structure is constructed. Next, Finite Element Analysis (FEA) is performed to estimate the displacement U of each node under imposed external loads F so as to solve the linear elasticity equation: KU = F. The chosen objective function with its associated sensitivity (gradient of the objective function with respect to the design variable) is evaluated using these, aforementioned, displacements. For the following iteration, the sensitivities can, then, be used by the solver to update the design variables. In this case, the Optimality Criteria (OC) scheme from the work by Bendsøe and Sigmund (2004) is used as the solver.

One of the main advantages to this approach to designing compliant SMA elements is the fact that various Open-Source academic codes are available for implementing this structural topology optimisation as shown in the work by Zhu et al. (2020) and Talischi et al. (2012). Due to ignoring the thermal dependencies of the shape memory effect, the resulting FEA used is similar to that of traditional compliant mechanisms and can thus be easily extended to such generative algorithms by simply changing the objective functions and associated sensitivity.

5.3.2 Topology Optimization of Compliant Mechanisms

The basic principle behind designing a compliant mechanism, as illustrated in fig. 5.2, can be formulated as : "Under an external input force and certain boundary conditions, what is the distribution of material defining the compliant mechanism that transforms the input load to a specific output one?"

At the input and output points, artificial springs are added to simulate the input work and resistance to the output displacement of the workpiece, respectively, as shown in the work by Alonso et al. (2014). In the final geometry, these springs are removed and are only present during the design process. Regarding the objective function that governs the final design of the compliant mechanism, a formulation that can be extended to Multi-Input Multi-Outputs (MIMO), is implemented based on various strain energies as shown in the work by Alonso et al. (2014).

An objective function based upon the mutual strain energy between the input and output is chosen. This permits to distribute the strain throughout the structure and avoid to have only *de facto* (single point) hinges responsible for the compliant behaviour. Ideally, the maximum volume of the structure should be deformed to harvest as maximum work, when the alloy is heated and experiences the shape memory effect. Here, the objective function is built using three different types of strain energies. First, there is the input strain energy S_{in}, that is present when only an input load F_{in} is applied and result in some nodal displacements U_{in}. Similarly, the output strain energy S_{out}, is present when only a dummy unit load F_{out} is applied at the output port resulting in nodal displacements U_{out}. Finally, the Mutual Potential Energy (MPE) or mutual strain energy S_{mut} can be built with the two previous nodal displacements. The objective function is chosen as a ratio of these three energies due to its non-dimensional aspect and due to the fact that the desired input and output displacements are indirectly accounted for. Here, since the problem is formulated as a minimisation, a minus signed is placed before the chosen ratio to maximise the MPE as follows :

$$\gamma = -\frac{S_{mut}}{S_{in} + S_{out}} = -\frac{{U_{out}}^{T} K U_{int}}{\frac{1}{2}{U_{out}}^{T} K U_{out} + \frac{1}{2}{U_{in}}^{T} K U_{in}}. \tag{5.2}$$

Lastly, two separate FEAs are performed to evaluate the chosen objective: $KU_{in} = F_{in}$ and $KU_{out} = F_{out}$.

The current objective governing the design of the generated compliant mechanisms made of *conventional* linear material, can be extended to generating design for mechanisms made from SMAs. This is due to the fact that, as previously mentioned, the algorithm tends to distribute the strain throughout the structure which will indirectly allow a large portion of the material to be activated if made from SMA. The optimisation problem, as formulated in eq. (5.3), consists of the minimisation of the objective function γ subject to the limitation of the infill Vol^* of the design domain's volume, with V_e the volume of element e.

$$\begin{aligned} \min_{\vec{\rho}}: \quad & \gamma(\vec{\mathrm{U}_{\mathrm{in}}}, \vec{\mathrm{U}_{\mathrm{out}}}, \vec{\mathrm{E}}) \\ \text{s.t.}: \quad & \mathrm{KU}_{\mathrm{in}} = \mathrm{F}_{\mathrm{in}} \\ & \mathrm{KU}_{\mathrm{out}} = \mathrm{F}_{\mathrm{out}} \\ & \mathrm{Vol} < \mathrm{Vol}^*, \text{ with } \mathrm{Vol} = (\sum_{e=1}^{\mathrm{NE}} \rho_e \cdot V_e)/(\sum_{e=1}^{\mathrm{NE}} V_e) \\ & \vec{\mathrm{E}} = \mathrm{MIS}(\vec{\rho}) \quad 0 < \rho_{\min} \leqslant \rho \leqslant 1. \end{aligned} \tag{5.3}$$

In fig. 5.3, the basic design problem is displayed using the common force inverter scenario. Due to the symmetry of the problem, the domain space can be restricted to half the surface while adding rolling supports at the symmetry axis. In fig. 5.4, the evolution of the optimisation can be observed. Here the domain space is uniformly initialised with intermediate materials such that the volume limitation is satisfied so as to have the design converge to a solution that is only composed of full materials.

5.4 Testing using Benchmark problems

Before designing complex multi-output compliant SMA elements, the shape memory effect of the generated geometries must be validated. In this regard, a common practice is to use some traditional benchmark problems. The problems, while being simple problems, can be used to validate the generated designs using a commercially available Finite Element Modelling (FEM) software such as ANSYS®. Using an FEM, the shape memory effect of the generated topologies can be simulated, verifying the efficiency of the algorithm for designing compliant SMA mechanisms.

The proposed design method is applied to three benchmark problems : an inverter, a crimper, and a gripper. They are all fixed at their bottom and top left corners (which corresponds to ideal pivots) but each have their own input and output forces. The design problems and the resulting geometries are shown in fig. 5.3, fig. 5.5, and fig. 5.6. This half domain space has been discretised into 10^4 elements and the design variables are initialised uniformly with a volume fraction constraint of 30%. The stiffness of each artificial spring is equal to 0.1 and the input forces are equal to 1. When run on a Windows workstation with an Intel i7 3.6 GHz, 8-core

processor and 32 GB of memory, the complete process takes less than 1 minute to converge to solution. It is important to note that the computational time would have been significantly higher if a non-linear and multi-physic analysis was executed. Due to the short computational time, this design method can be extended to 3-Dimensional problems.

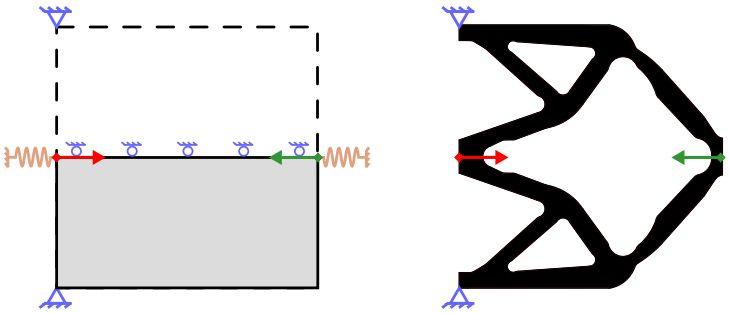

Figure 5.3: Inverter: Design problem (left), Interpolated final topology (right). Input force is shown in red while the output force is shown green.

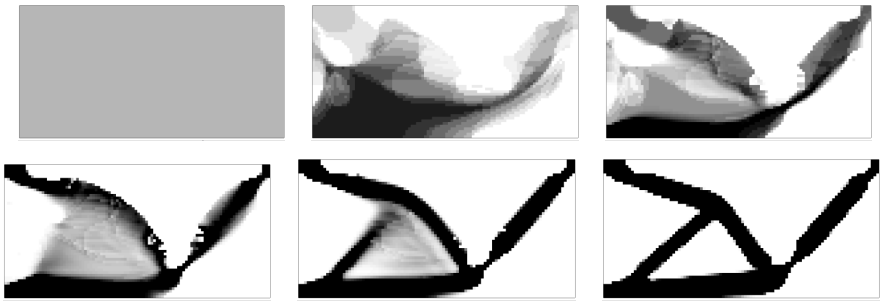

Figure 5.4: Evolution of the inverter design throughout the optimization. The grayscale represent the value of the filtered artificial density.

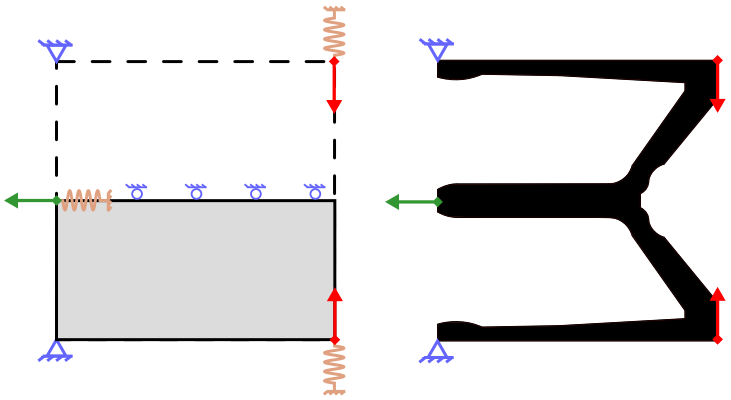

Figure 5.5: Crimper: Design problem (left), Interpolated final topology (right). Input force is shown in red while the output force is shown green.

Here, in the hopes of validating the shape memory effect, a four time-step simulation is constructed. The four different simulated steps can be seen in fig. 5.7. Here, the figures represent the results of the FEM simulation for each benchmark problem. The simulation

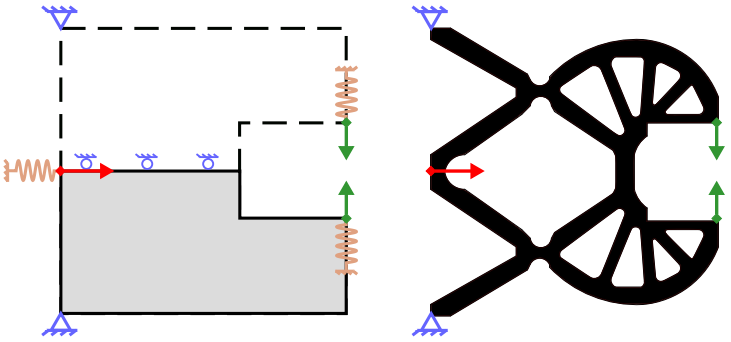

Figure 5.6: Gripper: Design problem (left), Interpolated final topology (right). Input force is shown in red while the output force is shown green.

consists of first applying an input displacement which generates a displacement at the output, $\varepsilon_{\text{loaded}}$. If the entire structure is sufficiently strained to undergo the detwinning process, as explained in chapter 2, the structure will keep its deformed shape when the input displacement constraint is released. However, as some areas of the compliant structure does not undergo detwinning, a portion of the strain will be lost when the constraint is released. Thus, the observed strain at the output will decrease to $\varepsilon_{\text{free}}$. During the third time step, the structure is heated to activate the shape memory effect and force the structure to revert back to its original shape where all the strain is recovered. Finally, the structure is allowed to cool down and return the material back to its martensitic phase.

5.4.1 A Qualitative Measure of the SME

Since the topologies generated by the algorithm are widely different consisting of varying inputs, outputs and geometries, a measure by which the results can be compared is required. The final goal, being to integrate these compliant mechanisms as the active element in a biased-spring SMA actuator, the measure should represent the degree to which work has been stored by the biasing element. This measurement factor could be formulated as a measure of the relative quantity of material activate (or detwinned) by the biasing element. This implies that the larger the value of the factor is, the more optimal the biased-actuator will perform.

The amount of detwinned material in the geometry can be roughly estimated using the principle that the deformed material behaves plastically. In other words, it is the volume of the material that is able to retain its shape after the load has been released. This factor, as described in eq. (5.4), is expressed as the strain retention factor and is defined as the amount of strain observed in the topology after the deformation load is released. This factor will vary between 0 implying non of the material has been activated and the topology retains completely back to its original shape when the load is released and 1 for a perfectly detwinned material where the entirety of the strain is retained and can only be reverted back to its original shape

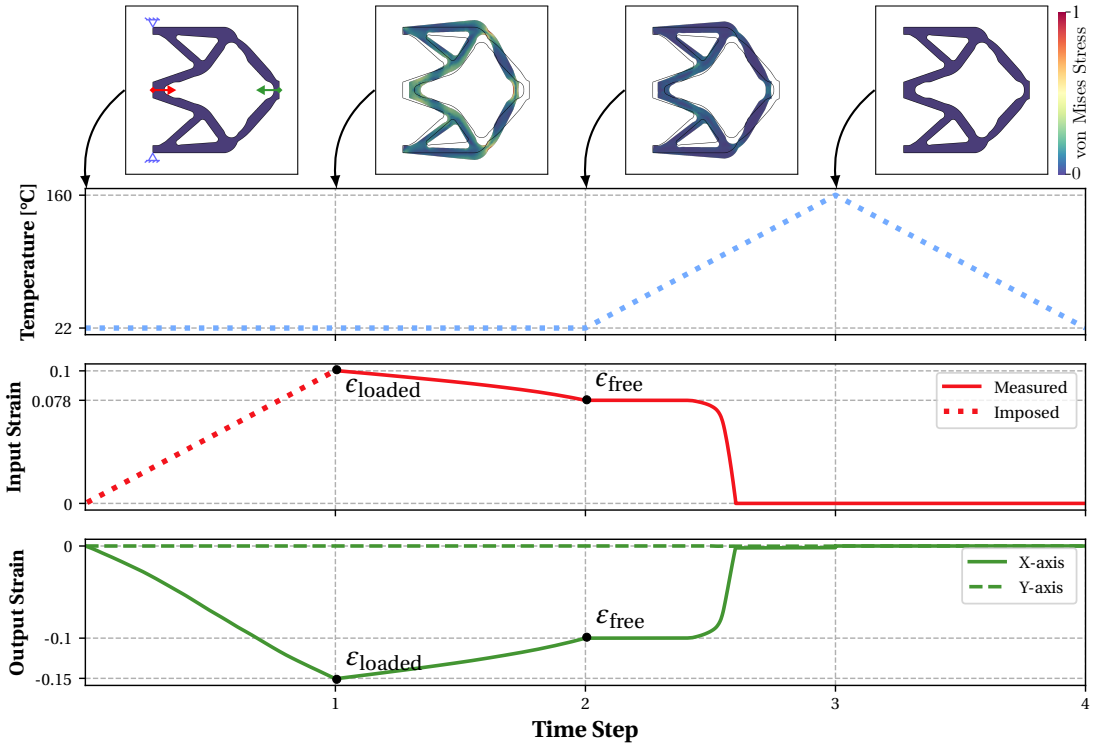

Figure 5.7: Results of the shape memory effect simulation of the Inverter design. Here, the displacements are calculated relatively to the design domain size L. The displacements observed between time steps 1 and 2 show a strain retention of $\alpha_\epsilon = 77.6\%$ confirming the presence of the shape memory effect.

when heated. This strain retention factor can be calculated using :

$$\alpha_\epsilon = 1 - \frac{\epsilon_{\text{loaded}} - \epsilon_{\text{free}}}{\epsilon_{\text{loaded}}}, \tag{5.4}$$

with ϵ_{loaded} and ϵ_{free} representing the domain space normalised input displacement at time step 1 and 2 respectively. It is important to note that this factor can never be equal to 1 as there is some natural elastic spring back of the material even when fully detwinned and thus, is only a qualitative measure of the shape memory capabilities of the topology. It is still an effective way to compare the different topologies presented using the benchmark problems. The FEM results of the strain retention of each benchmark problem can be seen in table 5.1. This principle can be further extended to more complex designs where goal is to create compliant SMA structures that can have multiple outputs using just a single input biasing element which will be presented in future sections.

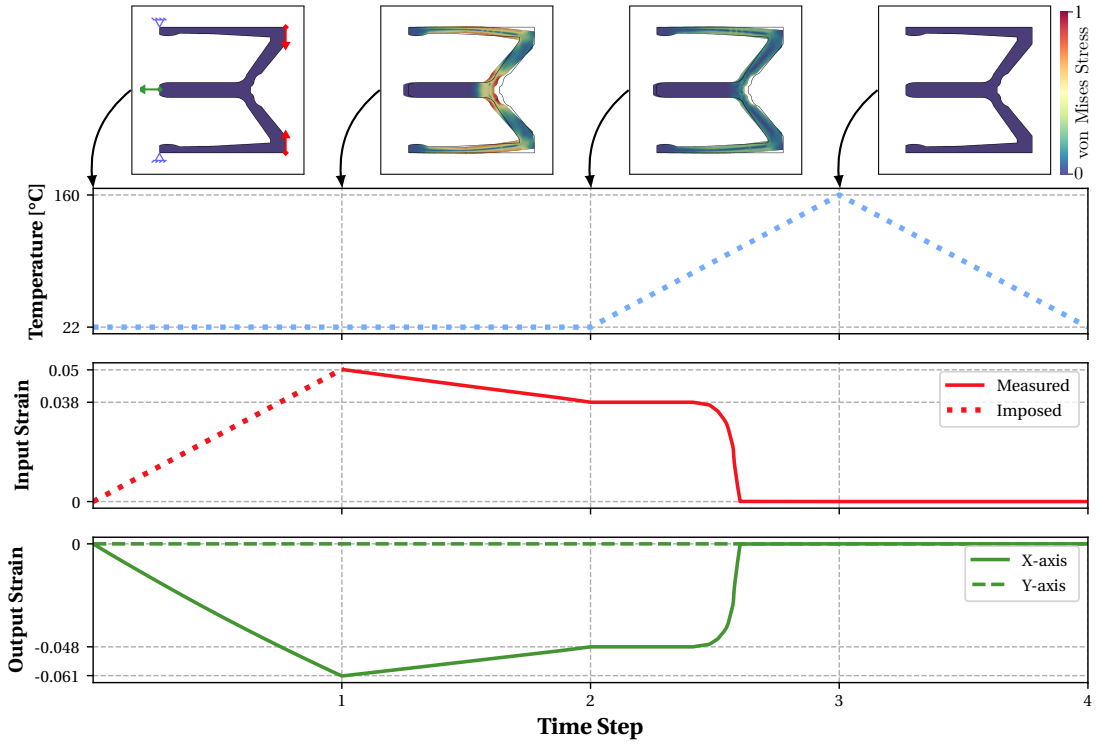

Figure 5.8: Results of the shape memory effect simulation of the Crimper design showing a strain retention of $\alpha_\epsilon = 75.2\%$.

Table 5.1: The simulation results of the strain retention factor for each of the benchmark problems: $\mathscr{I}$ Inverter; $\mathscr{C}$ Crimper; $\mathscr{G}$ Gripper

	$\varepsilon^x_{\text{loaded}}$	$\varepsilon^y_{\text{loaded}}$	$\varepsilon^x_{\text{free}}$	$\varepsilon^y_{\text{free}}$	α^x_ϵ	α^y_ϵ
$\mathscr{I}$	0.149	-	0.103	-	**77.6%**	-
$\mathscr{C}$	−0.061	-	−0.048	-	-	**75.2%**
$\mathscr{G}$	0.015	−0.085	0	−0.065	**77.6%**	-

5.4.2 Experimental Validation of the Methodology

In the previous section, three benchmark problems were used to validate the presence of the shape memory effect of topologically optimised compliant structures made from SMAs. Furthermore, a qualitative measure was formulated so as to compare and assess the degree to which these compliant structures would be ideal in creating biased-spring SMA actuators. However, to truly verify the presence of the shape memory effect, an experimental prototype can be fabricated.

For an accurate comparison between the FEM results and the experimental data, a prototype of a benchmark problem is conceived. For the sake of simplicity, the inverter problem is chosen

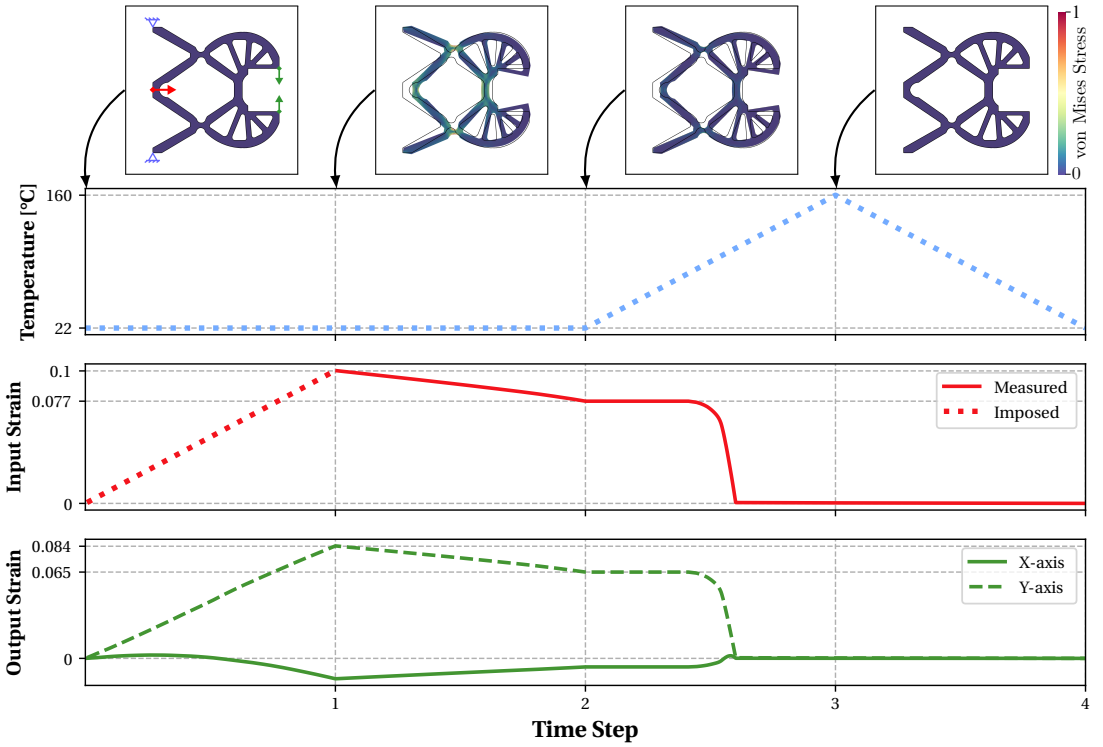

Figure 5.9: Results of the shape memory effect simulation of the Inverter design showing a strain retention of $\alpha_\epsilon = 77.6\%$.

due to the fact that there is only one input and output. When designing the inverter, ideal pivots are used. However when creating the experimental prototype, these ideal pivots are changed to a more realistic solution involving mounting holes. Based on these new boundary conditions, the inverter problem is redesigned using the proposed topology optimisation algorithm.

When fabricating the prototype, the cost of machining a monolithic block of NiTiNOL was deemed unfeasible. With the advent of additive manufacturing of NiTiNOL as portrayed in the work by Sabahi et al. (2020), the creation of such compliant mechanisms has become cheaper and more feasible. However, in this case, as the topology generative is 2-Dimensional, the inverter prototype was fabricated by laser cutting thin sheets of NiTiNOL (55.8 wt. % Ni). This laser cut inverter structure was then sandwiched between two PMMA sheets to prevent any unwanted buckling in the third dimension, as shown in fig. 5.10. This ensures that the deformations observed within the structure resembles the simulation.

The advantages of such a implementation, to test the validity of the design methodology, include the reduced cost of the prototype and more importantly, ensuring that the stress and strain distribution within the 2D structure is identical to the simulated 3D structure. This implies that the output displacement of the inverter prototype will closely resemble that of the simulated structure. The main disadvantage of this implement comes from the

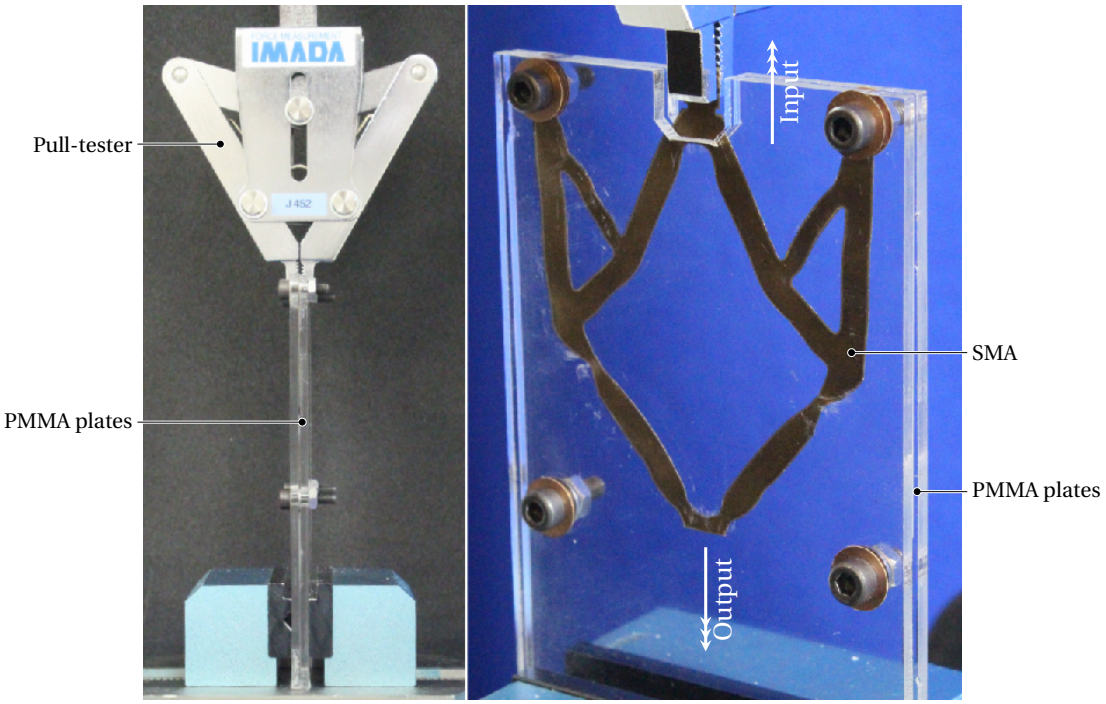

Figure 5.10: The experimental setup of the laser-cut inverter prototype. The prototype is fabricated from a thin SMA sheet and is sandwiched between PMMA sheets to prevent buckling. The input load is applied with the help of the pull-tester while the input displacement and force are measured. The output displacement is recorded and measured using a camera.

fact that the PMMA sheets cause lots of friction with the compliant structure. This implies that force requirements at the input will be higher than expect. As we sandwich the PMMA sheets more tightly around the compliant structure, the output displacements will be more accurate while increase the friction and force requirements to create the aforementioned output displacement. Thus, a trade-off is present but the strain retention factor, as described in eq. (5.4), is only dependent on the the displacement and not the force requirements. Thus, the prototype was fabricated to maximise the input and output fidelity rather than the force requirement. Here, a pull-tester is used to measure the displacement of the input and the force requirements.

The goal of this section is to experimentally validate the proposed design methodology. The prototype of the compliant SMA benchmark problem was realised and must be compared to the results of the simulation. As described before, the strain retention factor was developed to compare the various generated topologies and to have a qualitative analysis of the structure to be used as a bias-spring SMA actuator. Thus, this factor can also be used to compare the experimental prototype of the modified inverter mechanism and its corresponding FEM simulation.

In fig. 5.11, the pull-tester results can be seen. The strain retention is measured by applying an initial strain to the input of the prototype using the pull-tester. By then reversing the direction

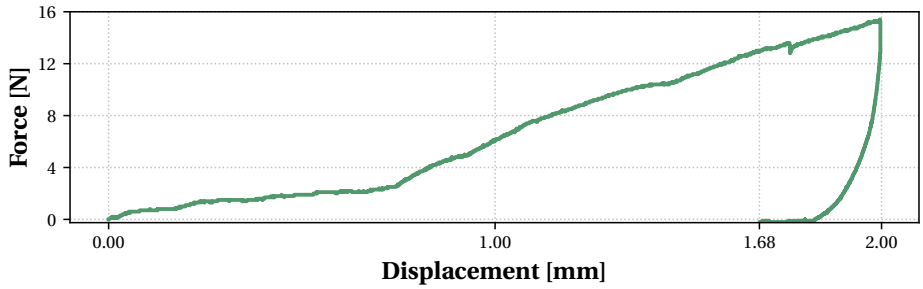

Figure 5.11: The experimental results of the inverter prototype are obtained using a pull-tester and a strain retention of 84.3% is observed.

of the pull-tester and measuring the reaction force, the point at which the reaction force descends below 0 N will define the strain that is retained by the structure after the initial load is released. We assume that as the pull-tester observes a value below −0.2 N, the structure has overcome the internal friction with the PMMA sheets and is now bending the input of the prototype rather than returning to its original shape. Based on the values observed using the pull-tester, a strain retention of 84.2% is measured as shown in table 5.2. When comparing to the results of the simulation of the same modified inverter topology of 78.9%, the shape memory effect capabilities of topologies generated by this design approach is validated. The difference in the strain retention between the experimental and FEM results can be accounted by the friction present in the physical implementation.

Table 5.2: Comparison between the FEM and experimental results of the modified inverter benchmark problem.

	x_{loaded} [mm]	x_{free} [mm]	α_ϵ [%]
FEM	2.0	1.58	78.9
Expt.	2.0	1.68	84.3

5.5 Proposed Induction Heating Strategy

Due to the complex geometries of the generated topologies, simply passing a current through the structure by attaching electrode to the ends is no longer possible. In the case of inverter prototype, electrodes must be attached at multiple points so as to allow current to flow through all the areas of the geometry.

Various works have been established where surface mounted coils have been installed to function as a heating coil that raise the temperature of the SMA structures for localised heating, as shown in the work by Paik et al. (2010). This can be quite cumbersome due to possible risks of delamination while the SMA contracts and dilates during actuation. Another option would be to use hot air as a medium to increase the temperature of the SMA structure,

perhaps with tools such as hot air guns. These external heating structure drastically reduce the work density of the resulting actuator and are thus, rarely used in small and compact applications.

Due to the complex geometry of the inverter prototype, the current paths for Joule's heating are no longer unique, nor trivial anymore. Here, in this case, multiple electrodes with multiple external wires are required to heat the structure. Thus, here, the proposed heating solution consists of a contactless, wireless strategy where a current is induced within the SMA structures using external induction coils.

5.5.1 Magnetic Induction Heating

The basic working principle of the proposed heating methodology and its application in the inverter mechanism can be seen in fig. 5.12. By passing an alternating current at a high frequency through the primary coil and generates a magnetic field. When any electric conductor, the SMA structure in this case, is placed inside the generated magnetic field, a secondary electric current, I_{induced}, is induced inside the structure. This induced current will generate Joule's losses, P_{Joules}, heating the SMA :

$$P_{\text{Joules}} = R_{\text{SMA}} \cdot I_{\text{induced}}^2 = \frac{V_{\text{emf}}^2}{R_{\text{SMA}}}. \tag{5.5}$$

The magnitude of the current is based on the electromotive force, V_{emf}, generated by the primary coil, and the effective resistance, R_{SMA}, of the path taken by the induced current. The coupling between the primary coil and the SMA piece, as described in eq. (5.6), dictates the electromotive force.

$$V_{\text{emf}}^2 = \left(-\frac{\mathrm{d}\Psi}{\mathrm{dt}} \right)^2 = \left(-2\pi f L \cdot I_{\text{prim}} \right)^2 \tag{5.6}$$

where Ψ is the total flux linkage between the primary and SMA side, f is the working frequency, I_{prim} is the *RMS* value of the primary current and L is the mutual inductance between the primary coil and the SMA structure. As a voltage source is used to power the system, the input current is maximised and the resistance of the primary coil is minimised. This is further increased by creating a resonating circuit where a capacitor is connected to the primary coil.

When designing the heating solution for maximum induced current, as shown in eq. (5.6), a large working frequency is desired. However, when working with alternating currents at high frequencies, undesirable effects such as skin and proximity effects, arise which increase the resistance of the primary coil. Furthermore, the parasitic capacitance of the impedance of the coil will take over above a certain critical frequency, cancelling the inductive effect. By limiting the working frequency, a favourable balance between the losses at the primary coil and the induced current at the resonant value can be maintained. The mutual inductance between the primary coil and the SMA structure can be maximised for a large area of influence and a large number of turns. However, the area of influence cannot be increased as it is constrained by the shape of the generated SMA topology while the number of turns is limited by the associated

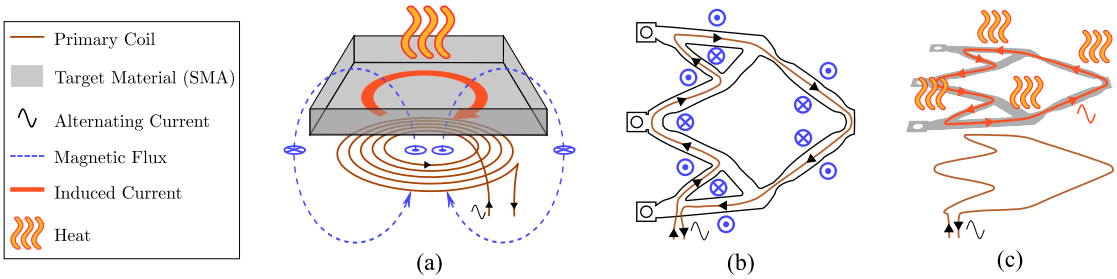

Figure 5.12: Working principle of the induction heating strategy - (a) General principle, (b) 2D view of the coil designed for the deformed inverter, with the direction of the generated magnetic flux normal to the plane, (c) 3D view of the induction system for the inverter problem.

increase in resistance which in turn reduces the magnitude of the input current. Thus, based on the application, the sizing of the primary coil comes with various trade-offs.

5.5.2 Fabrication and Results of Primary Coil

Due to the complex shape of the generated SMA topologies, the shape of the primary coil must be designed so as to induce a current path across the deformed regions of the compliant mechanism. Currently, the fabrication of the primary coil is performed by hand using nails and a wooden plate. The nails are used to create the shape based on the desired current path and a wire is wound around the nails to fabricate the coil. Once constructed, varnish is used to maintain the shape of the primary coil when the nails are removed. As shown in fig. 5.13, two types of primary coils are constructed using 25 turns a standard monolithic wire with a copper diameter of 0.30mm, and another composed of 15 turns of a Litz wire composed of 300 strands with a diameter of 0.040mm each. As shown in fig. 5.13, the resistance of tbe wire increases significantly with the frequency due to the skin and proximity effects. This implies that a thinner effective cross-section is preferred, as in the case of the Litz wire.

As mentioned previously, the working frequency plays an important role in this proposed heating system. A trade-off is present where a higher value increases the heating but also increase the parasitic capacitance of the coil, limiting the impedance above a critical frequency, $f_c^{\text{mono}} = 17\text{MHz}$ and $f_c^{\text{litz}} = 41\text{MHz}$ for the coil made of monolithic and Litz wire, respectively. As shown, despite the lower inductance of the Litz coil, better heating performance is achieved due to the working frequency and higher primary current when compared to the monolithic wire.

Here a working frequency of around 4 Mhz has been chosen so as to ensure that it sits safely below the critical frequency. At this frequency, the inductance of the coil is $L = 7.4\ \mu\text{H}$ and its resistance $R = 0.4\ \Omega$. A capacitor of $C = 230$ pF is attached in series with the primary coil to create an LC circuit with a resonating frequency $f = (2\pi\sqrt{LC})^{-1} = 3.86$ MHz. Here, the input source is constructed using a half-bridge inverter based on GaN transistors (EPC9024). With the Litz coil, a primary current of $I = 1.5$ A is generated at the working frequency while dissi-

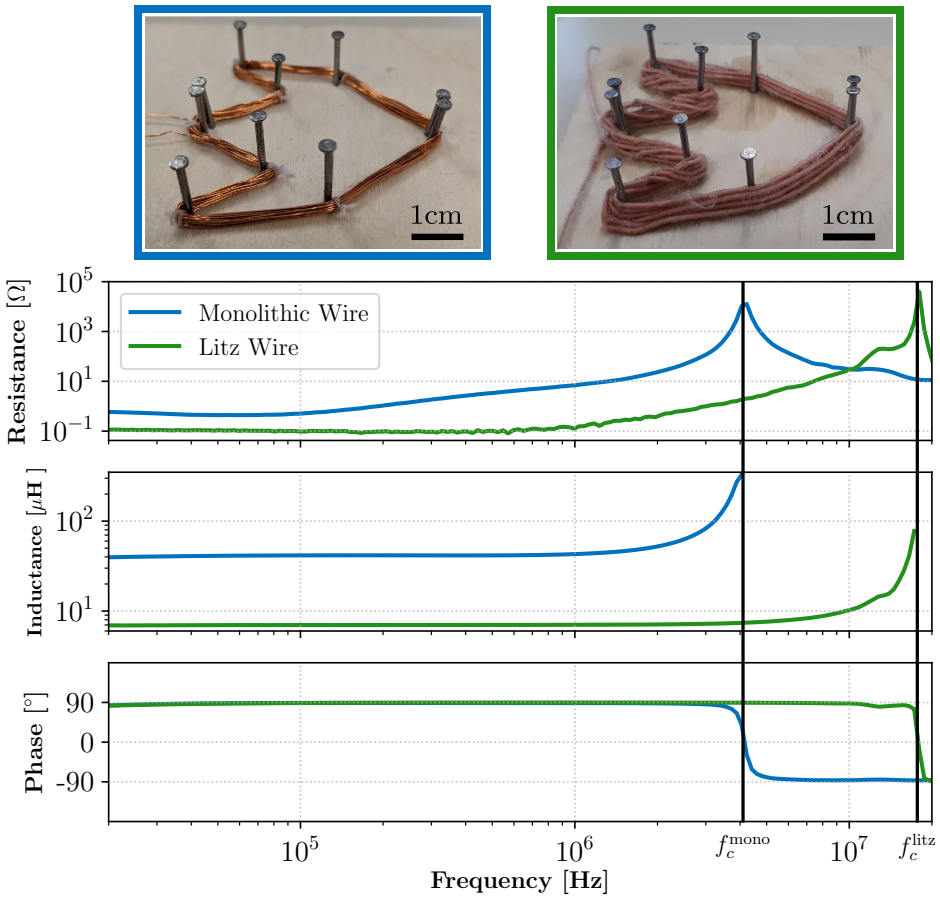

Figure 5.13: A comparison of primary coils with different wire types. As the impedance becomes mainly capacitive over its critical frequency, the inductance's values after f_c^{mono} = 17MHz and f_c^{litz} = 41MHz are removed for the monolithic and Litz wire respectively.

pating 0.9 W of heat. This increased temperature is negligible and implies a stable operation. However, the coil made from the monolithic wire would result in higher temperatures at the primary resulting in a change in resistance and inductance values.

The fig. 5.14 illustrates the implementation of the contactless inductive heating system for the compliant SMA prototype as well as the temperature distribution across the SMA structure using the FLUKE® Ti25 thermal camera. A glass plate is placed between primary coil and the SMA to avoid any heating through convection. Using the proposed heating system, the SMA inverter prototype was heated above 120°C validating the system as an active heating system. Furthermore, as the structure reverts back to its original shape, this further validates the presence of the shape memory effect.

In this implementation of the prototype, the penetration depth does not limit the excitation frequency as the structure is composed of a thin film of SMA. In the case of a working frequency of 10 MHz, the penetration depth is larger than the 100 μm thick SMA sheet. However, in a

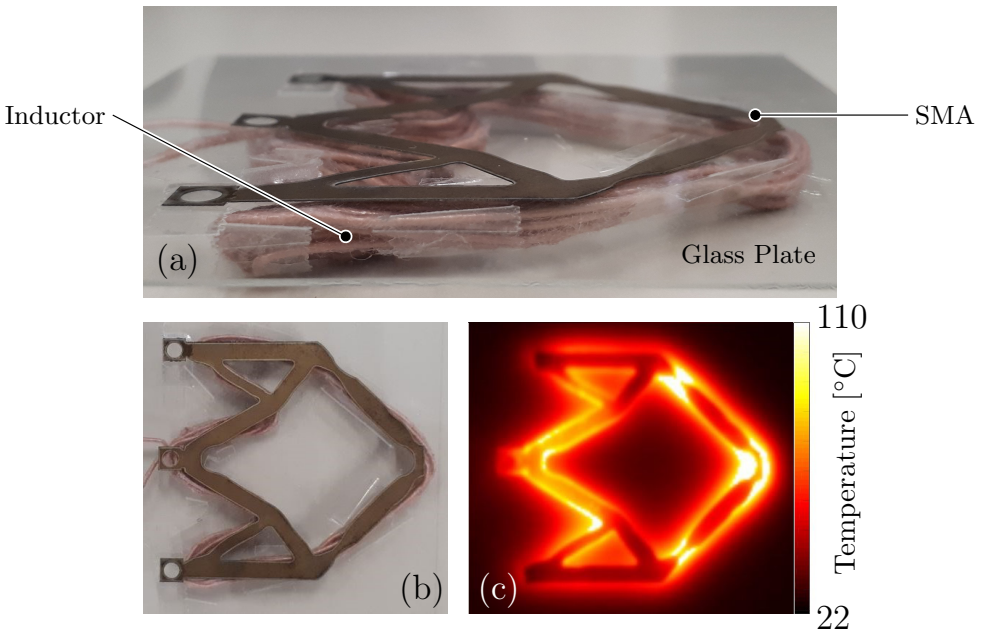

Figure 5.14: Implementation of induction heating system. When activated, it resulted in the heating of the SMA structure, reverting the deformed structure back to its original shape.

real world application where the compliant structure is created from a thick monolithic block of SMA or 3D printed, the penetration depth would be an additional parameter to account for when sizing the input frequency.

5.6 Designing Multi-Output Compliant SMA Actuators

The proposed design methodology consisting of using topology optimisation to design compliant SMA mechanisms was validated using a FEM simulations and experimental results using standard benchmark problems. Furthermore, as the generative design algorithm used made abstraction of the shape memory effect, the designs of the compliant mechanisms were generated with a relatively low computational time. Due to the cost of NiTiNOL and advanced manufacturing techniques, prototype of the proposed design could not be fabricated but advanced additive manufacturing methods that avoid waste of material such subtractive methods such as machining has become possible as shown in the work by Alagha et al. (2021) and Zhu et al. (2021). With these techniques, complex compliant SMA actuators could be fabricated in the near future. Thus, the proposed design methodology could be a great tool in creating novel biased-spring SMA actuators.

5.6.1 Generated Multi-Output SMA Actuators

In this section, various novel multi-output actuators fabricated from compliant SMA topologies are generated based on the proposed design methodology. These topologies were, similar to the benchmark problems in section 5.4, simulated and their corresponding strain retention factors were measured, as shown in fig. 5.16. The *rhombus* structure is a multi-directional mechanism where the axes move in opposing directions. They elongate in the y-axis and contract in the x-axis. The other structures, named the 8-*point mandrel*, the 4-*point mandrel* × and the 4-*point mandrel* +, perform as outer-mandrels for gripping objects. The evolution of the topology during the generative optimisation process for the 4-*point mandrel* × is shown in fig. 5.15. In a similar way to the benchmark problems, these topologies are generated while making abstraction of the shape memory effect and while neglecting the nonlinear nature of the alloy so as to drastically reduce the computational time, which took less than 2 min per design.

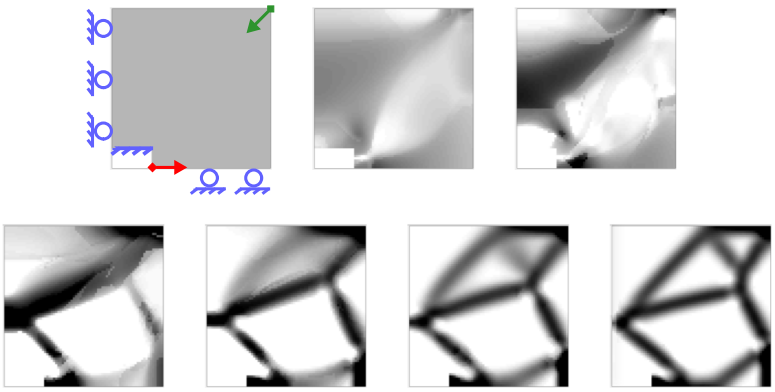

Figure 5.15: 4-point Mandrel × : Evolution throughout the optimization. The grayscale represents the value of the filtered artificial density. The input force is shown in red and the output force in green.

Using the FEM simulation of these multi-output compliant mechanisms and the strain retention factor, the presence of the shape memory effect within the generated topologies is validated. A fixed input strain of 10% is applied at each input, where the bias-spring is attached, to have comparable results for each design. The results of the FEM simulation of the design are presented in table 5.3. The obtained strain retention factor for each actuator topology shows that the majority fo the strain applied by the biasing spring is retained and will be recovered when heated using the proposed induction heating methodology. This implies that this design methodology could be an attractive tool for designing novel multi-output biased-spring SMA actuators.

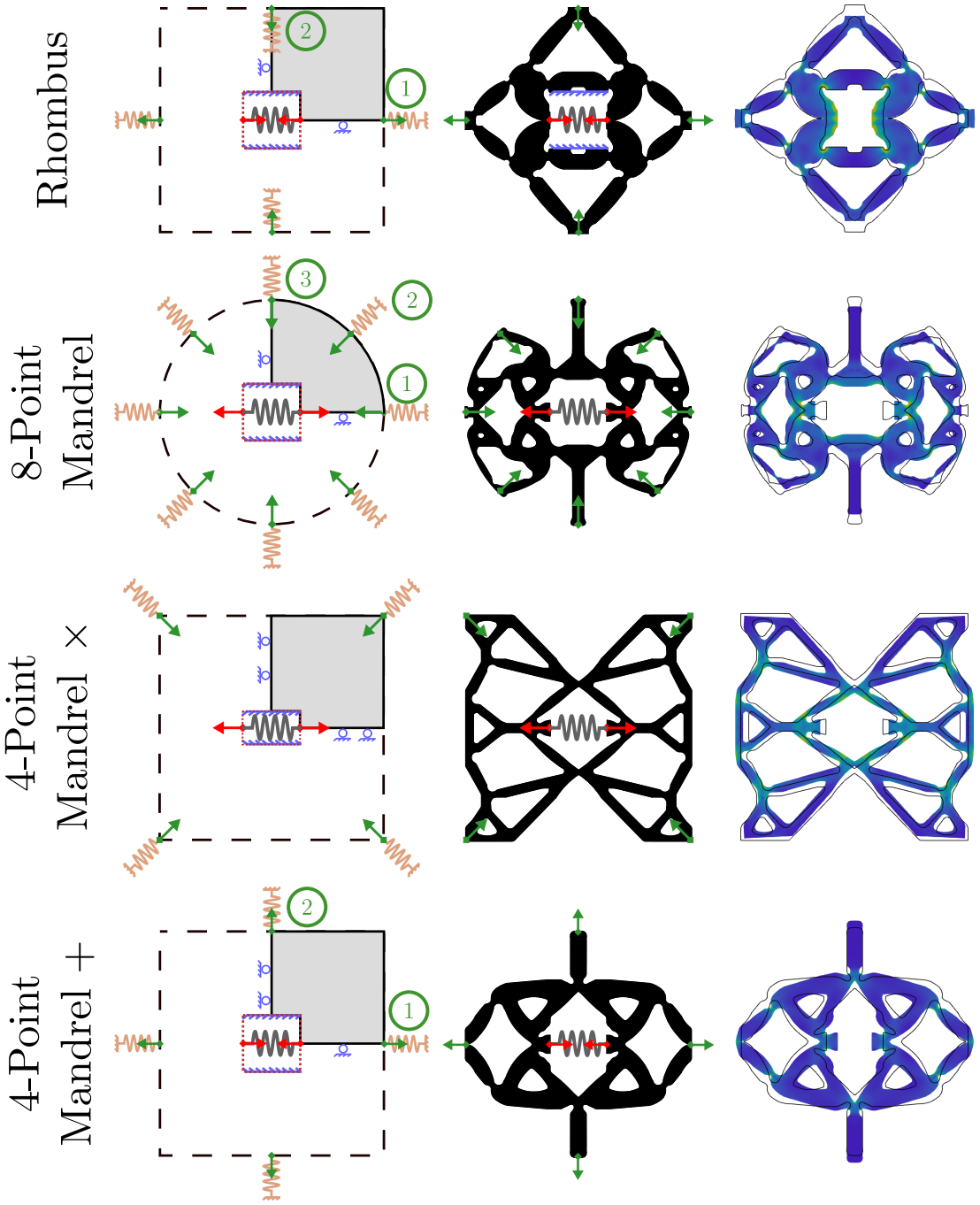

Figure 5.16: Using the novel design methodology, multi-output bias-spring SMA actuators are generated making use of compliant SMA structures, shown with normalised stress distribution in the deformed state. The input forces are shown in red and the output forces in green. The artificial springs present in the topology optimisation are shown in brown while the bias-springs of the actuators are shown in grey.

Table 5.3: Results of the strain retention factor for each of the generated multi-output compliant SMA structures.

	$\varepsilon^x_{\text{loaded}}$	$\varepsilon^y_{\text{loaded}}$	$\varepsilon^x_{\text{free}}$	$\varepsilon^y_{\text{free}}$	α^x_ϵ
Rhombus	①: 0.051 ②: 0	①: 0 ②: 0.062	①: 0.042 ②: 0	①: 0 ②: 0.045	**67.9%**
8-Point Mandrel	①: -0.057 ②: -0.057 ③: 0	①: 0 ②: -0.05 ③: -0.085	①: 0.037 ②: -0.038 ③: 0	①: 0 ②: -0.034 ③: -0.058	**74.7%**
4-Point Mandrel ×	-0.029	-0.022	-0.023	-0.017	**81.4%**
4-Point Mandrel +	①: 0.051 ②: 0	①: 0 ②: 0.062	①: 0.042 ②: 0	①: 0 ②: 0.045	**68%**

5.7 Kirigami inspired Compliant SMA Actuators

Using topology optimization, various compliant SMA actuators can be designed with the intent to combine the functions of the kinematic stage and the active element. However, due to the current limitations of fabrication and its costs, the feasibility of such an actuator, in the current sense, is unlikely. As additive manufacturing of SMAs becomes more accessible, the advantages of designing compliant SMA structures such as increasing the overall work density of the actuator, will become more apparent and attractive.

Kirigami, the Japanese art of cutting paper to create intricate structure, has gained traction in various engineering fields to create stretchable structure as shown in the work by Tang et al. (2017). While designing 3D compliant structure made of SMA is expensive, this kirigami approach can be extended to SMAs to create compliant structures that when cut in a specific manner, can exhibit surprising mechanical behaviours.

When designing actuators, a key detail to keep in mind is the life cycle of the device. In common industrial applications, the number of cycles to fatigue of traditional grippers can exceed 10^6 cycles. In the case of SMA actuators, this number is much lower and is directly related to the structural fatigue of the material. The determining factors regarding the fatigue life of SMAs are the strain amplitude and the type of strain applied to the material. The work

by Runciman et al. (2011) looks at the fatigue lifetime of NiTiNOL based on different loading conditions, such as torsion, tension and bending. They conclude that SMAs tend to have a much longer life cycle when loading under torsion or bending when compared to tension. The results show that with a fixed strain amplitude of 1%, in tension, the number of cycles to failure is less than 10^3 whereas in bending or torsion, the number of cycles to failure is around 10^5.

The availability of NiTiNOL in different geometries such as springs, wires and sheets, has allowed the creation of multiple classes of SMA actuators that exploit their respective advantages. As mentioned in previous sections, the simplest approach would be to use the alloy in the shape of a wire paired with a biasing spring to drive an actuator where the stress and strain of the material corresponds directly to the stroke and force output of the actuator. In these cases, SMA wires are elongated under pure traction and are then heated to recover the strain and provide the force output as shown in the works by Kyung et al. (2008), Welsch et al. (2018), Haibin et al. (2018), and Andrianesis and Tzes (2015). Here, the stroke of the actuator can not exceed 1% without compromising its fatigue life. Thus, in cases where a larger stroke is required, the geometry of the wire is adapted to form a spring which can provide stroke above 100% as implemented in the works by Ikuta (1990) and Zhakypov et al. (2018). Here, the material no longer deforms in traction but rather in torsion, thereby increasing its fatigue life but while compromising the force output. This implies that there is a trade-off to be made between the force output, and the stroke and fatigue life.

Since SMAs are available in the form of sheets which can be machined using laser cutters into complex geometries, different kinds of SMA actuator systems exploit the longer fatigue life of SMAs in flexion to create novel grippers as shown in the works by Kohl et al. (2002), Benard et al. (1998), Zhakypov et al. (2018). The major advantage to using sheets instead of wires is the fact that they provide a much higher force output. The difference in force output between sheets and wires can be reduced by placing multiple wires in parallel to generate forces in the same order of magnitude as sheets. Thus in applications, where a higher force output is required, the use of SMA sheets or multiple wires in parallel can be a viable solution.

When working with thin wires, placing them in parallel to augment the overall force output also increases the complexity of the system greatly. The manufacturing and assembly of such a system can be difficult. Furthermore, it is also impossible to uniformly deform all the wires equally, resulting in some wires being inactive during the shape memory effect. Thus, in cases where a higher force output is required, the design space can become limited to just using sheets. For maximum force output, the sheet can be elongated in pure traction but only up to about 1%. In applications where a large stroke and force output is required, the SMA sheets in its original state is no longer viable. Traditionally, this limitation is overcome by adding a kinematic stage to amplify the stroke of the SMA actuator but comes with the cost of reduced overall work density of the final actuator.

In this section, a novel approach will look at a new kirigami-based approach to designing SMA

sheets in order to obtain an actuator that can provide higher force output while being able to also provide high strokes. Kirigami is a variation of origami that involves the cutting of the substrate to create different shapes and behaviours. The pattern presented in this paper is based on the work by Shyu et al. (2015) where a nanocomposite substrate is patterned to create a stretchable element. This approach allows an SMA sheet to reach strains over 100% without losing its capacity to deliver a high force output.

5.7.1 Proposed Patterns

The pattern plays the most important role when creating a kirigami-inspired SMA actuator. The pattern when cut into the SMA sheet creates a meta-material that alters the mechanical properties from the original material. Based on the pattern used, various different behaviours such as stroke amplification or movement conversion can be imparted into the sheet. In this work, as seen in fig. 5.17, two patterns are explored. The Ω-pattern, taken from the work by Shyu et al. (2015), provides an amplification of the stroke while also deforming the SMA in flexion which is favourable for the overall fatigue of the material. The second pattern consists of the Lotus-pattern which allows the material to rotate around its centre. Furthermore, if fabricated using SMA and actuated, this pattern can be used to an active smart pivot.

(a) Ω-pattern (b) Lotus-pattern

Figure 5.17: The proposed kirigami patterns for the SMA actuator where (a) allows for a large stroke linear elongation while (b) allows a rotation around its centre.

These patterned structures make use of out-of-plane deformation to create the desired mechanical properties such as stroke amplification. These highly stretchable sheets, when exposed to an imposed force or moment, make use of the out-of-plane deformation of each individual pattern to elongate beyond the capabilities of the material on its own. Due to the fact that these deformations are irregular and can be sophistic to predict, an FEM model where the large deformations of the individual patterns are simulated can be an essential tool in determining the resulting behaviour of the metamaterial. In fig. 5.18, the proposed kirigami-inspired patterns are simulated showing their highly extensible nature and their respective out-of-plane deformations.

The FEM simulation was constructed such that rolling supports are placed on the sides to

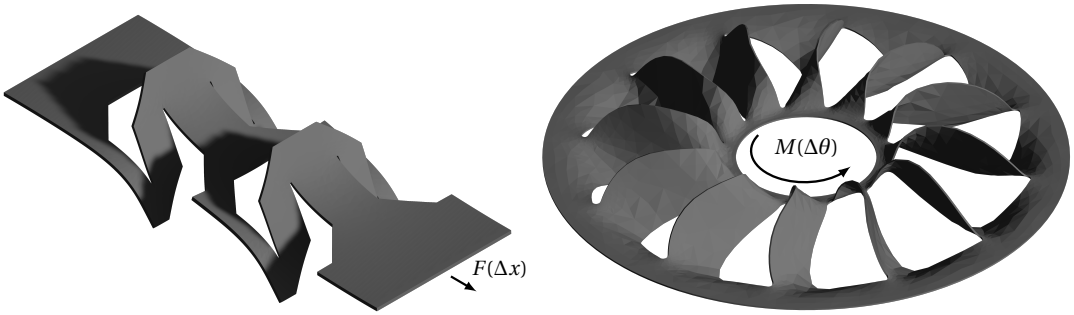

Figure 5.18: The out-of-plane deformation of the Ω-pattern and the Lotus-pattern using an FEM model.

simulate the adjacent patterns. In the case the Ω-pattern, one end of the pattern is fixed while an elongation is applied at the opposite end while measuring the reaction force of the pattern. Similarly, in the Lotus-pattern, the outer circumference is fixed while a rotation is applied on the inside circumference and the reaction moment is measured. The primary goal of simulated these proposed patterns is to establish a force-elongation profile so as to determine the rigidity of the metamaterial.

As seen in the work by Shyu et al. (2015) and the work by Firouzeh and Paik (2015), the force-displacement characteristics of the patterns are highly non-linear. However, the characteristic shows two distinct regions which can be simplified linearly. Initially, the metamaterial is highly rigid and requires a large force to create some deformation. This behaviour can be explained by the buckling load required to create the out-of-plane deformation. Initially, the individual beams present in the patterns are compressed axially as the structure is force to elongate. As soon as the buckling load is reached, these beams will buckle and deviate from the plane create a slight deformation. This deviation allows each beam to deform from the plane which drastically reduces the stiffness of the metamaterial creating the second region of rigidity. This principle can be also extended to other kirigami-inspired patterns such as the lotus-pattern and other out-of-plane deforming patterns presented in Shyu et al. (2015). In the case of the Ω-pattern, the individual beams, post-buckling, are deformed in flexion and undergoes large deformations. The deflection and deformations of the individual patterns can be used to deduce the rigidity of the final resulting metamaterial.

The design of a basic SMA actuator consists of estimating the output stroke of the actuator based on the force-displacement curves of the SMA and the biasing element as shown in the work by Dragoni and Spaggiari (2021). By establishing the aforementioned force-displacement curves of the SMA kirigami-patterns and the biasing element, the intersection of these curves represent the operating points of the actuator. However, due to the highly complex multi-physic behaviour of the shape memory effect, these alloys are often simplified and represented as having two separate force-displacement curves: the high temperature and low temperature states as described in chapter 2. The intersection of these curves will, thus, represent the operating points of the actuator before and after actuation and can then be used to obtain the

final stroke of the actuator. It is, therefore, quite pertinent to elaborate the force-displacement curves of the biasing element and the active SMA element as shown later in fig. 5.22.

5.7.2 Case Study: Modelling of the Ω-Pattern

In this section, the active SMA element of the actuator consists of a thin sheet of SMA. As shown in the work by Morikawa et al. (2018), thin sheets of metal when machined with repeated kirigami-inspired patterns can result in structures that can provide higher strokes and create stretchable structures. In this approach, by making use of this concept, an SMA structure can be created such that higher actuation strokes can be achieved when compared to an actuator made from just the thin sheet. Here, in this section, the Ω-pattern presented in the work by Shyu et al. (2015) as illustrated in fig. 5.17a, is used to create the kirigami-inspired SMA element. This pattern, in the original study, has not been fully studied but presents a valuable resource when created an SMA actuator due to the fact that the pattern allows the stretching of the sheet using out-of-plane flexion. As mentioned earlier, flexural stress in SMAs results in better fatigue life and thus, is advantageous when fabricating an actuator and thus, makes it an ideal pattern for creating a long lasting large displacement linear actuator.

The Ω-pattern has been parametrised as shown in fig. 5.19. The stretchable nature of the patterned sheet changes its mechanical properties when compared to the sheet on its own. Thus, based on these parameters, the stiffness of this resulting metamaterial is sized in this section. The stiffness of the structure can be estimated by calculating the resulting elongation based on the imposed force at one of the extremities. Here, the Young's modulus of the base material is considered linear whereas in the case of an active SMA element, this assumption can be consequential but nevertheless the resulting study can prove to be useful in determining the effects of the various parameters.

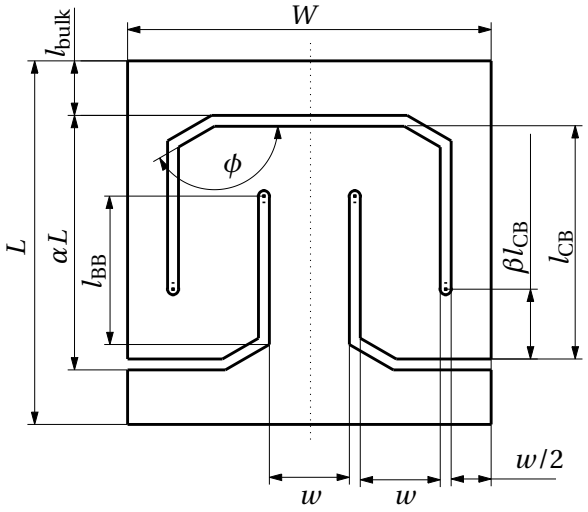

Figure 5.19: Parametrisation of the Ω-pattern with the thickness of the sheet denoted by t.

Simplifying the Out-of-plane Deformation

The stretchability or stroke amplification of this 2D structure is due to the out-of-plane deformation of the generated beams in the pattern as shown in fig. 5.20. This out-of-plane deflection causes a displacement of the extremities resulting in an increased effective length of the structure which can be viewed as an elongation of the metamaterial. As seen in the figure, the pattern can be reduced to two buckling beams coupled by an undeformed beam. These deflected beams, referred to as the buckling beam, is denoted with the subscript BB. While the rigid beam is referred to as the coupling beam and is denoted with the subscript CB as shown in fig. 5.19.

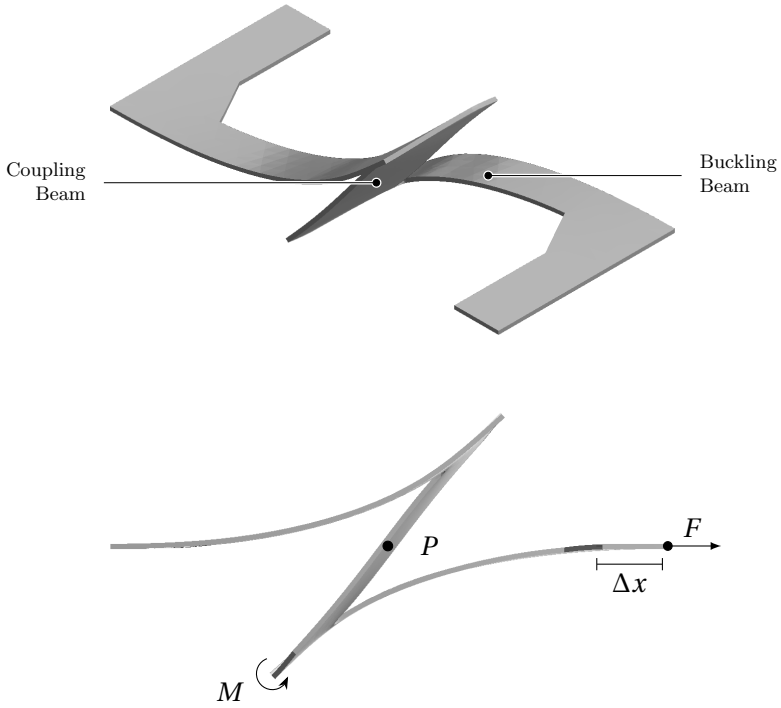

Figure 5.20: A visualisation of the out-of-plane deformation of the Ω-pattern based on the FEM model. Here, only half the pattern is simulated to reduce the computational time of the FEM simulation.

When examining the deformation behaviour in fig. 5.20, as the force is applied to one end, the initial deformation occurs when the buckling beams approach a critical load and buckles out-of-plane. This critical load can be calculated by using the Euler's critical load as given by (5.7), with the column effective length factor $K = 2$.

$$P_{\text{cr}} = \frac{\pi^2 E I_{\text{BB}}}{K l_{\text{BB}}} \tag{5.7}$$

Once the beams buckle, the deflection of the beams continues as the coupling beam applies a moment, M, around its centre, as denoted by P in fig. 5.20. Thus, the buckling beam

is deflected out-of-plane due to this applied moment caused by the imposed force at the extremities. This deflection can thus be calculated using (5.8).

$$\theta = \frac{M l_{CB}}{E I_{BB}} \tag{5.8}$$

with $M = F l_{CB}/2$ as the coupling beam rotates around the pivot P located at half its length, F denotes the applied force at the extremity of the pattern and EI denotes the flexural rigidity of the beam. This deflection of the buckling beam can be converted to a translation of the ends of the beams using (5.9).

$$\Delta x = \frac{l_{CB}}{2}(1 - \cos\theta) \tag{5.9}$$

Estimating the Apparent Young's Modulus

As previously stated, by machining specific patterns into a sheet of material, the resulting structure exhibits mechanical properties different to the material on its own. Thus, this resulting structure can be viewed as a new metamaterial with an apparent stiffness and Young's modulus.

The resulting virtual rigidity of the metamaterial can be estimated by measuring the slope of the force-displacement curves. Thus, the apparent stiffness of the Ω-pattern can be estimated using the above equations as follows :

$$k_\Omega = \frac{\partial}{\partial x}(F + P_{cr}) \tag{5.10}$$

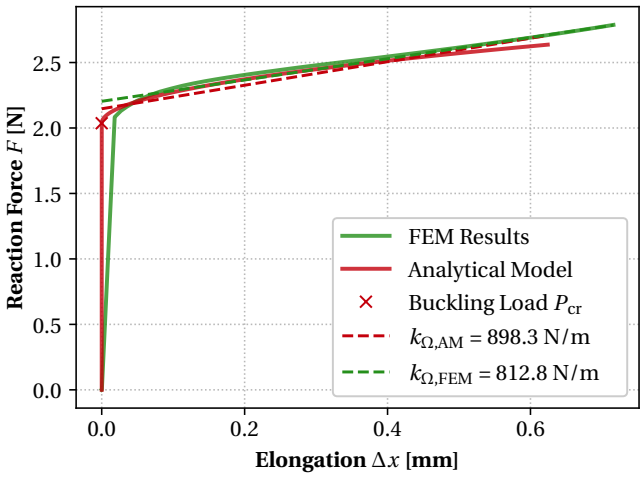

Figure 5.21: Comparison of the analytical model and the FEM results of the Ω-pattern. The stiffness of the metamaterial is calculated using an exponentially weighted linear regression. Here, the dimensions of the pattern are based on the values shown in table 5.4.

The analytical model of the pattern is validated using a finite element method (FEM) simulation. As shown in fig. 5.20, only half the pattern is simulated due to the symmetry of the pattern and to cut down on the computational cost of the simulation. Here, in the FEM simulation, one end of the sheet is fixed while a displacement is imposed on the opposite end of the pattern to observe and measure the reaction force required for the displacement. The resulting apparent stiffness of the pattern can be estimated by using an exponentially weighted linear regression fit. The weighted regression allows the fit to ignore the initial buckling load and obtain the slope of the linear section of the force-displacement curve after the initial buckling condition.

The comparison between the analytical model and the FEM results can be seen in fig. 5.21. Based on the figure, the results of the FEM simulation are quite similar to the analytical model, showing that the approximations made during the description of the model are valid. Here, the parameters and dimensions used in the simulation of the pattern can be seen in table 5.4 which are also the same values used in the analytical model during the comparison.

Table 5.4: The dimensions of the simulated Ω-pattern.

Parameter	Value	Parameter	Value
W	5 mm	l_{BB}	4.7 mm
L	10 mm	ϕ	120°
α	0.8	w	1.1 mm
l_{CB}	6.3 mm	t	100 μm
β	0.27	l_{bulk}	1 mm
Material	CuBe (TM08)	E	1.25 GPa

The apparent Young's modulus of the metamaterial, E_Ω, can be calculated using the rigidity and the geometrical dimensions of the sheet where the force, F, can be transformed into stress using $\sigma = F/W \cdot t$ and the elongation, Δx, can be transformed into strain using $\varepsilon = \Delta x/L$. Thus, using these equations and the analytical model of the Ω-pattern, this virtual Young's modulus can be easily sized for the required specifications of the use case scenario.

5.7.3 Implementation of a Kirigami-inspired Linear Actuator

As previously mentioned, a basic SMA actuator consists of the active SMA element, the biasing element and the kinematic stage. In this section, however, the active element is based on the proposed kirigami-inspired SMA element. The goal of the kirigami structure is to modify the mechanical properties of the SMA sheet such that the stroke amplification can be implemented. In this section, a prototype is fabricated using the kirigami-inspired SMA actuator paired with a flexure-based biasing element. As shown in chapter 4, a flexure-based linear stage has been used to constrain the movement of the SMA element such that the actuator has a linear stroke and does not result in any undesired buckling. As the flexure-based linear guide presents with an inherent stiffness, this structure is used as a biasing spring for the activation of the active SMA element. Essentially, the flexure allows the subsystem to function

as both the kinematic stage and as the biasing element preventing the degradation of the work density of the active material. Furthermore, the kirigami-based actuator allows for a stroke amplification of the SMA element without requiring an additional kinematic stage.

The design of a basic SMA linear actuator consists of estimating the output stroke of the actuator based on the force-displacement curves of the SMA and the biasing element as presented in chapter 3. As stated in the sizing methodology, the force-displacement curves of the kirigami-inspired SMA element can be used to determine the operating points of the actuator and estimate the final stroke. In fig. 5.22, the schematic of the sizing methodology when considering the highly non-linear SMA kirigami structure and the flexure-based biasing element.

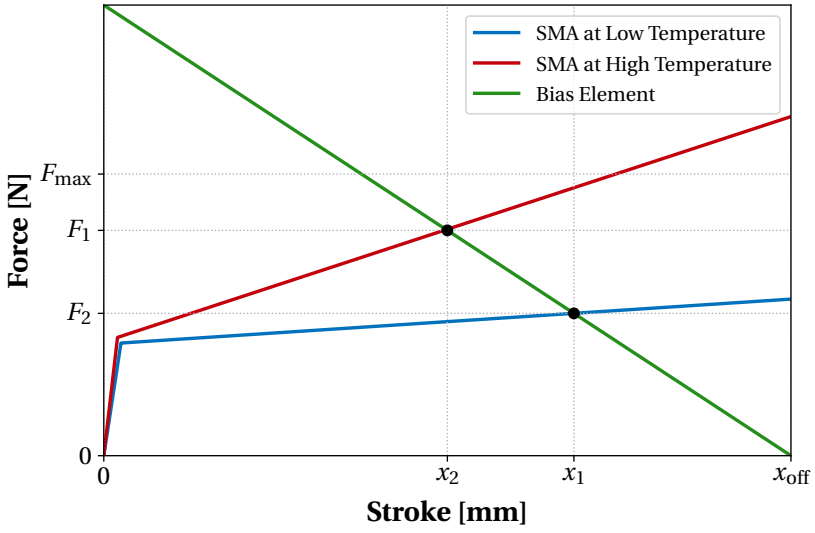

Figure 5.22: A schematic of the working principle and sizing methodology of the kirigami-inspired SMA actuator.

The kirigami-inspired SMA element can be easily fabricated by using a thin sheet of the alloy and cutting the desired pattern using laser cutting or water-jet cutting. The SMA sheet has been purchased from Memry Corporation and is composed of NiTiNOL. The primary advantage to this methodology consists in the fact that based on the pattern imbued into the sheet, various novel mechanical properties can be imparted into the material, in this case, stroke amplification. Using the Ω-pattern, compared to a simple rectangular sheet of the material, the structure can be made to reach elongations up to 100% as opposed to the traditional 4 - 8%. This stroke amplification can be achieved using multiple springs arranged in parallel, but with the proposed kirigami pattern, the same amplification can be achieved with a single piece and reduced assembly. Furthermore, as the pattern consists of beams that deform out-of-plane in flexion, the fatigue life of the material is conserved compared to if the sheet were elongated in pure traction.

The rigidity of the resulting metamaterial produced from a passive material such as Copper

Berryllium can be determined using the analytical model of the Ω-pattern, as confirmed in fig. 5.21. When building the kirigami-based active SMA element for the actuator, however, the analytical model must be updated for the shape memory effect's non-linear behavior, and only then can it be used to establish the actuator. The prototype in this section makes use of the flexure-based biasing element whose stiffness can be sized using the work by Henein et al. (1998).

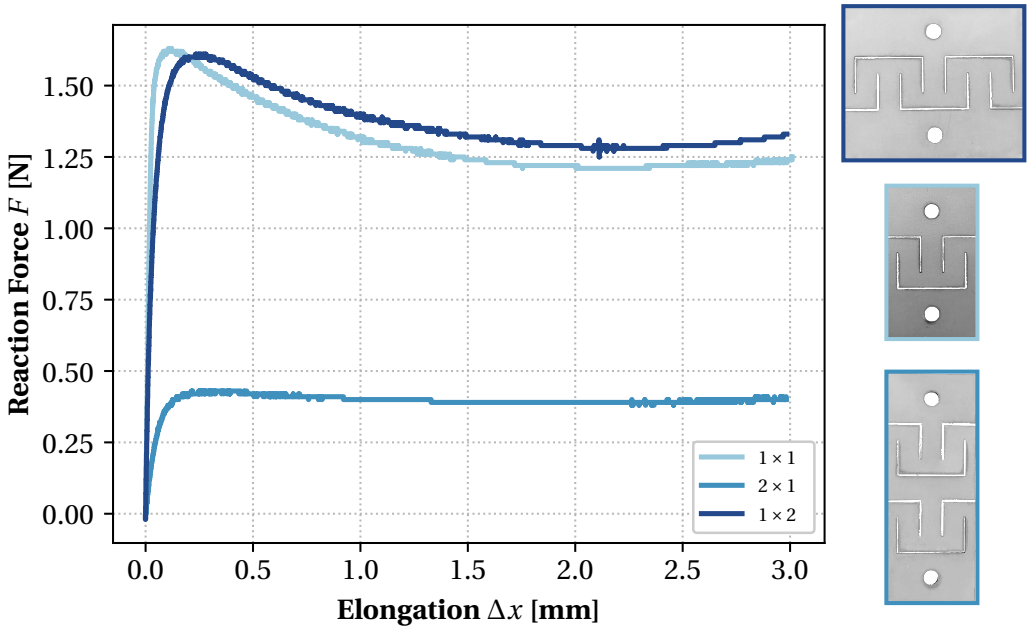

Figure 5.23: Results of the pull-tester of the single Ω-pattern sample cut from a 100 μm NiTiNOL sheet showing the force-displacement curve of the metamaterial.

In order to understand the effects of using an active non-linear material such as the SMA on the properties of the metamaterial, a single Ω-pattern is cut in a small sheet of the SMA as opposed to the passive linear material. As plotted in fig. 5.23, the results of the pull-tester can be seen and the mechanical behaviour of the single (1 × 1) unit pattern test is observed. Here, one can deduce that the highly non-linear behaviour of the SMA active material has a large effect on the properties of the resulting metamaterial. This highly extensible nature of the pattern is attractive for large stroke linear applications. This non-linearity in the metamaterial force-displacement curve can be attributed to the non-linear nature of the SMA at low temperatures. In order to further understand the effects of the kirigami patterns on the metamaterial, the metamaterials containing the unit pattern in series (2 × 1) and parallel (1 × 2) are tested and whose force-displacement curves are shown fig. 5.23. As one can see from the experimental results obtained from the pull-tester, adding patterns in series or in parallel can be exploited to vary the stiffness of the resulting metamaterial and can be used to size the active material based on the requirements of the actuator.

The kirigami SMA actuator is fabricated by laser cutting the repeating Ω-pattern into the 100

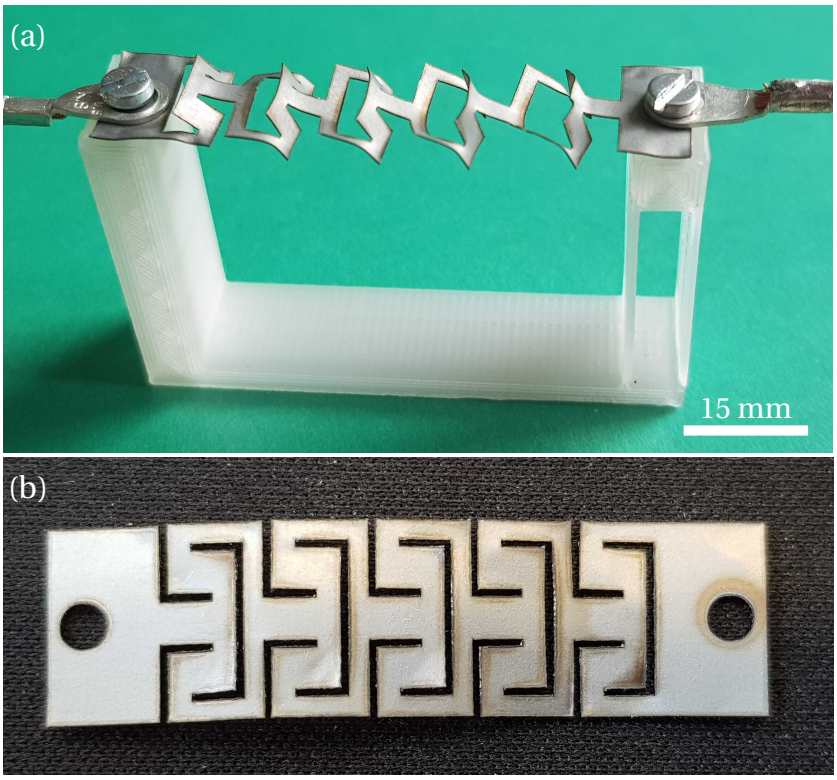

Figure 5.24: A linear actuator powered by a kirigami-inspired SMA active element. Here, using flexure-based structures, the final dimensions and complexity of the system has been further optimised.

μm thin NiTiNOL sheet. Using 5 patterns arranged in series, the structure is conceived to have increased output strokes. The kirigami structure can extend by 20 mm displacement an elongation up to 60%. As observed in fig. 5.24, pairing this active metamaterial with the linear stage flexure, a lightweight compliant linear actuator is designed and fabricated using 3D printing. The actuator is actuated by simply passing a current across the ends of the SMA element. The internal resistance of the kirigami-based metamaterial allows Joule's losses to raise the temperature and activate the shape memory effect. As the material cools down passively, the biasing flexure spring deforms the metamaterial back to its deformed state.

This proof-of-concept prototype is able to produce large strokes due to the mechanical properties of the proposed kirigami SMA structure as opposed to a simple SMA sheet. As detailed in chapter 3, this large stroke linear actuator is paired with a flexure-based biasing element allowing the structure to be lightweight and compact. With a 9.6 mm wide SMA sheet, the final prototype is able to produce pulling forces equivalent to multiple springs attached in parallel with considerably less complexity and assembly time. The kirigami-inspired SMA linear actuator, fabricated from the 100 μm SMA sheet, is able to produce strokes up to 5 mm and apply a pulling force of 2.1 N as opposed to the 0.4 N of pull-force for a 200 μm diameter SMA spring. This shows the advantage of this proposed methodology and shows the possibility

of preventing the work density deterioration of the SMA actuator.

5.8 Summary and Conclusion

In this chapter, a design methodology, consisting of integrating the kinematic stage and active element to create a compact SMA actuator, is proposed. Using topology optimization and a novel approach to generate topologies while making abstraction of the shape memory effect is detailed. By implementing such a generative algorithm, the computational time to design novel topologies has been drastically reduced. This has the implication to extending such a design algorithm to 3D structures.

The design approach using topology optimisation was tested using benchmark problems with a standard input and output parameters to create various topologies that can be fabricated from SMAs. The presence of the shape memory effect and the feasibility of the topologies to be used in SMA actuators was validated using a FEM simulation and an experimental prototype. Furthermore, a qualitative measure called the strain retention factor was proposed as a means to compare the various topologies that can be generated using such an approach.

As these novel structures can be complex, the heating of such geometries using simple Joule's heating is no longer trivial. A novel heating solution was proposed and fabricated so as to activate the shape memory effect of the fabricated topologies. Furthermore, using this design approach and generative design algorithm, various multi-output biased-spring SMA actuators, that can be actuated using only a single biasing spring, were proposed.

These SMA structures were designed within a 2D space with the intention of fabricating the structure from a 3D monolithic block of SMA. As the design algorithm was implemented with a volume constraint to preserve material, fabricating the structure with subtractive methods such as machining will result in large amounts of wasted material. However, due to the current cost limitations of additive manufacturing processes that exist for SMA, the feasibility of such a compliant SMA structure is limited.

Lastly, the same methodology where structures composed of complex patterns that exhibit surprising mechanical behaviours, can be be seen in kirigami-inspired mechanisms. By extending this same design principle to SMA actuators, patterns can be cut into thin SMA sheets such that useful mechanical properties such as a rotational stroke or stroke amplification can be imparted into the actuator without the need for cumbersome external kinematic stages. In this chapter, a proof-of-concept kirigami-inspired SMA linear actuator was designed and sized based on the proposed methodology. This prototype was able to produce forces up to 2.1 N and strokes up to 5 mm. When compared to similar SMA springs that are able to produce similar levels of elongation, multiple springs in parallel are required to reach the same levels of force shown in this proof-of-concept. This shows the potential of SMA actuators designed using the proposed strategy in maintaining the high work density of the alloy.

Using this design principle, compliant SMA active elements can be designed and fabricated so as to appropriate the functions of the kinematic stage within the SMA actuator. This allows for the creation of compact SMA actuators that retain their high work energy density while still displaying the complex output and mechanical behaviours required by the application specifications.

Using these proposed design methodologies, in the next chapter, the work aims to validate the methodology using a case study. In the following chapter, a bistable SMA-powered robotic gripper is designed using the novel methodologies such that a compact and lightweight gripper is fabricated while sizing the SMA elements to optimize for the fastest time responses.

Publications related to this chapter :

S. Thomas, A. Thabuis, T. Martinez, P. Germano, and Y. Perriard, *"Designing compliant mechanisms composed of shape memory alloy and actuated by induction heating,"* Smart Mater. Struct., Aug. 2021, doi: 10.1088/1361-665X/ac1b15.

S. Thomas, A. Thabuis, T. Martinez, and Y. Perriard, *"Shape Memory Effect of Benchmark Compliant Mechanisms Designed With Topology Optimization,"* in 2020 IEEE/ASME International Conference on Advanced Intelligent Mechatronics (AIM), Jul. 2020, pp. 571–576. doi: 10.1109/AIM43001.2020.9158984.

S. Thomas, A. Thabuis, T. Martinez, and Y. Perriard, *"Multi-Output Compliant Shape Memory Alloy Bias-Spring Actuators,"* in 2020 IEEE/ASME International Conference on Advanced Intelligent Mechatronics (AIM), Jul. 2020, pp. 795–800. doi: 10.1109/AIM43001.2020.9158997.

S. Thomas, M. Ghorbani, G. Lang, T. Martinez and Y. Perriard, *"Modelling and Fabrication of a Kirigami-Inspired Shape Memory Alloy Actuator,"* in 2021 International Conference on Electrical Machines and Systems (ICEMS), Gyeongju, Oct. 2021, (in press).

S. Thomas, P. Peralta, R. Mottet, M. Lehmann, Y. Civet, and Y. Perriard, *"Analysis and Reduction of Time Response in Thermally Activated Shape Memory Alloys,"* in 2018 21st International Conference on Electrical Machines and Systems (ICEMS), Oct. 2018, pp. 1783–1788. doi: 10.23919/ICEMS.2018.8549332.

6 Validation using a Novel SMA Gripper System

6.1 Introduction

In chapter 1, by exploring the different domains in which SMA actuators are used, the various design criteria and priorities were outlined. By comparing the various design strategies of SMA actuators in their respective applications, the miniaturisation and integration of SMA actuators was deemed to be critical in designing robotic systems powered by smart materials. In the previous chapters, various design methodologies were presented to further integrate the different subsystems present in a conventional SMA actuator. This strategy was explored in order to create miniature robotic systems powered by SMA actuators. In this chapter, the goal is to explore the design methodology presented earlier so as to implement and validate them using a case study.

Here, in this work, the presented design methodologies are implemented in tandem to design and size a novel robotic system powered by an SMA actuator. The sizing methodology and design parameters of conventional SMA actuators were adapted and is used in this chapter to create a more compact and integrated solution so as to miniaturise the final prototype. As stated previously, in this final chapter, the novel design methodologies are validated using a case study. This case study employs the strategies and analytical models described and defined in the previous chapters to adequately size a compact and lightweight gripper. By creating such a work dense SMA powered gripper, the different models are validated while also validating the basic premise of the described methodologies.

As mentioned previously, the primary advantage of SMAs being their relatively high work density when compared to other smart materials, they can be exploited to create powerful actuators for applications where low weight and compactness are required. In this context, a common application for SMAs are in actuators used to power grippers for drones or pick and place machine as shown in the works by Lu et al. (2019), Lee et al. (2019) and Modabberifar and Spenko (2018). Their lightweight nature makes them ideal for drone-based applications and the active nature of the material makes them ideal for clean-room applications as opposed to traditional pneumatic solutions. Here, the primary criteria to take into account are the

overall dimensions, weight and time responses of the gripper. When designing SMA grippers, the main drawback is the large cooling time required resulting in a poor bandwidth. In the case where passive cooling is employed, this drawback is further pronounced and can only be limited by the optimal design of the SMA geometry. Using the design methodology presented earlier, the force and stroke requirements of the application can be taken in account such that the sizing of the SMA actuator can result in a gripper that is still highly integrated while retaining a reasonably fast time response.

In the context of pick and place machines or bistable grippers in general, the primary focus of the design centres around the rigid volume and weight constraints. Furthermore, the bandwidth of the resulting gripper, in certain use cases, can impose a rigid constraint as well. Here, the bistable gripper is designed and sized, using the proposed integrated design methodology, such that the resulting gripper remains within a small foot print and uses the thinnest SMA coils so as to retain an efficient time response with respect to the resulting gripping force. By creating such a bistable gripper, where a compact and integrated solution is obtained while also obtaining a reasonably fast time response, the design methodologies can be validated.

6.2 A Case Study of an SMA-Powered Bistable Gripper

The core ideology behind SMA actuators has been to create miniature and compact systems that could potentially replace the current traditional solutions. In this work, the basic concept has been to discover methods by which the high work dense nature of SMAs can be conserved when designing actuators.

This section has been primarily motivated by the need to replace traditional pneumatic pick and place grippers that require large compressors to operate. These conventional pneumatic grippers, as they operate using compressed air and are a source of dust, are incompatible with clean-room applications. These pneumatic grippers are bistable grippers that fit within a small footprint with the disadvantage of requiring a wired connection to a large air compressor. The motivation behind this section is to replace such a gripper and create a compact and lightweight solution that can be compatible with clean-room applications.

Recently, SMAs have been paired with bistable elements to create actuator as shown in the work by Meng et al. (2020) and Scholtes et al. (2020). A simple but effective way to create a bistable element is to axially compress a beam such that they buckled. This buckled beam, which can be easily fabricated in varying dimensions, now can exist in two stable positions. The main advantage to using a bistable system is the fact that they require no additional energy to remain in these stable positions. They only require power when switching from one stable configuration to another. Thus, this behaviour can be further advantageous for designing grippers that often tend to remain in an open or closed position for extended periods of time such as drone-deliveries as shown in the work by Zhang et al. (2020). As stated in previous examples, a fully compliant system can reduce the assembly complexity and weight while also

preserving the life cycle if properly designed. Furthermore, a compliant bistable SMA-driven gripper can be the ideal candidate to replace the current pneumatic solution for clean-room pick and place applications.

When compared to other bistable SMA-powered systems as shown in the work by Scholtes et al. (2021), this work presents a novel decoupled compliant system accompanied with a simplified sizing methodology. The bistable element prevents the gripper from requiring any energy while grasping whereas the SMA element allows the gripper to achieve high forces without increasing the weight of the system. However, the main drawback of the system consists of the long cooling time required by the SMA elements. In this work and what is often lacking in similar proposed designs, the analytical models and sizing methodology are implemented and validated such that the geometry of the SMA element is optimised so as to reduce the passive cooling time and enable the gripper to have a higher bandwidth.

6.3 Working Principle and Operation

In this design, the basic concept consists of combining antagonistic SMAs with a bistable compliant mechanism based on the proposed design methodology as described in section 3.4.2. Using a buckled beam, a simple bistable compliant mechanism can be designed such that no energy is required to remain in the open or closed position of the gripper. As previously stated, the behaviour of SMAs are difficult to model accurately and predicting the shape memory effect can be quite difficult. Similarly, multistable mechanisms with snap-through behaviours are incredibly difficult to model mathematically and therefore, a system pairing both SMAs and buckled beam are used but are, often, not adequately sized. Commonly, as displayed in the works by Scholtes et al. (2021) and Welsch et al. (2018), the authors present a similar mechanism but lack the methodology to appropriately size the SMA. The SMAs used in such systems are often oversized and present with higher cooling times degrading the time response and work density. However, in this work, using the proposed design methodology, the SMA buckled beam bistable gripper will be sized using the simplified models so as to create a gripper with reduced cooling times.

The basic principle of the presented gripper consists of using a pair of SMAs as external triggers to switch the buckled beam from one of its stable configurations to the other. In fig. 6.1, a simple diagram of the system can be observed. Here, as mentioned, the buckled beam which is axially compressed exhibits the bistability and behaves as the compliant bistable mechanism. The buckled beam is mounted at both ends using two supporting pivots and the snap-through is triggered by heating one of the two SMA coils. The initially straight beam, which can be fabricated as such, is buckled by bringing together the support pivots. Here, one of the pivots is considered the input pivot and connected to the pair of SMA coils. The remaining pivot is considered the output and is connect to the jaws of the gripper.

The SMA coils, when heated, will contract and revert back to their original size. The input pivot is adapted to host a lever arm. As the SMA coils are allowed to contract, being attached

to the lever arm, will cause the rotation of the input pivot. Here, the integrated lever arm acts converts the linear contraction of the SMA into the rotation of the input pivot. The lever arm can be sized to increase or decrease the force and stroke output of the SMA coil with respect to the input pivot. This rotation of the input pivot will, after a certain angular stroke, triggers the rapid snap-through of the buckled beam switching it to its alternate stable position. Similarly, by heating the antagonistic SMA, the buckled beam can be made to switch back to its original stable position. Thus, by alternately heating either of the two SMAs, the compliant system can be made to switch back and forth between its two stable positions. As the SMA cools down, the complaint system requires no additional energy from the SMA coils to remain in the stable configurations and only requires energy when forcing the snap-through to occur.

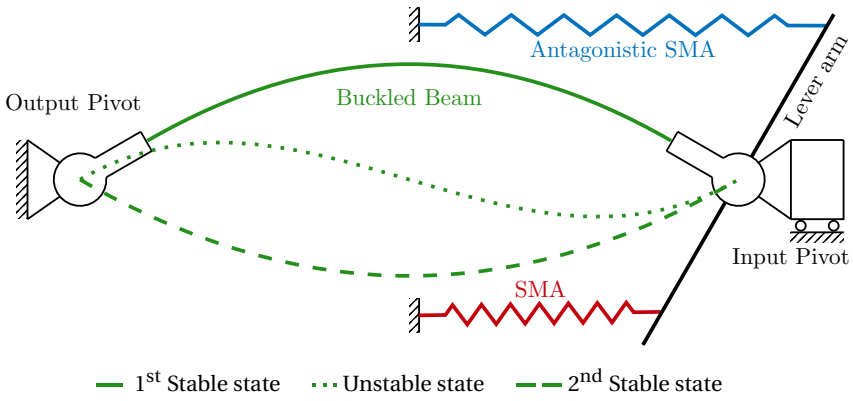

Figure 6.1: The schematic of the bistable SMA actuator composed on a buckled beam and a pair of SMA coils.

Compared to other bistable SMA actuators such as the work by Scholtes et al. (2021), the real advantage of the proposed kinematic stage, using a buckled beam supported by pivots, is that the gripping output is independent of the actuation input up to the point of snap-through. This decoupling of the input and output stage prevents the actuation of the SMA from applying unnecessary forces on the grasped object. From the stable to unstable position of the buckled beam, the input lever makes a near full stroke while the output pivot barely rotates. As soon as the unstable position is exceeded, rapid snap-through occurs and the output pivot switches instantaneously to the other stable stage, allowing for a rapid grasping or releasing motion.

Finally, in regards to the control of such a system, the SMAs are heated by passing a current across them to generate heat using Joule's losses. The internal resistance of the SMA coil is used to reach the transformation temperature of the SMA and generate the forces require to switch the bistable element. However, as the SMA coils are heated, there runs a risk of overheating and destroying the SMA. In conventional SMA actuators, a temperature sensor is used to control the heating of the SMA and prevent any unwanted damage to the actuator. This additional sensor, when combined with the micro-controller required to process the control logic, results in a significant addition to the overall weight and footprint to the system, degrading the work density of the material. Furthermore, in the case of sub-millimetre thin

SMA wires or coils, temperature sensors are difficult and expensive to integrate within the system. However, based on the design methodology presented in chapter 4, the kinematic stage of the actuator and the control can be integrated to create a mechanically-intelligent control system that can prevent the overheating of the SMA without any additional sensors or micro-controllers. In this proposed mechanism, the bistable element is used to trigger the electrical connection across the SMA. As the first SMA coil heats up, this triggers the buckled beam to snap and cut the electrical connection across this first SMA and establish the connection across the second antagonistic SMA. This prevents the SMA from overheating while also creating a control system that can mechanically choose the appropriate SMA coil to heat for activation. This mechanically-intelligent design, as proposed in the earlier chapter, allows a more compact and integrated footprint for the final design of the gripper prototype.

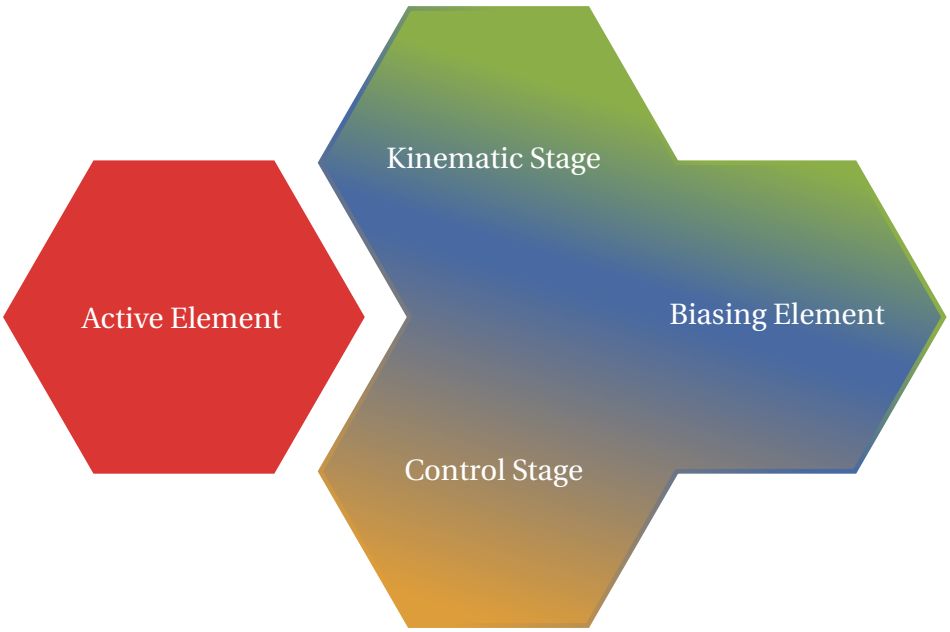

Figure 6.2: Diagram of the adapted building blocks of the bistable SMA-powered robotic gripper.

As shown in fig. 6.2, the different design methodologies presented in this work are combined to create a more highly integrated SMA actuator that reduces the overall footprint of the system while allowing for a relatively fast time response. Here, the kinematic stage, as proposed in chapter 3, acts as a biasing element and transforms the behaviour of the antagonistic SMA actuator into a bistable motion with rapid activation while also, as proposed in chapter 4, acts as the control strategy for the mechanical intelligence of the actuator. This allows the integration of the kinematic stage into the core of the SMA actuator where this motion conversion stage, which acts as the gripping mechanism, is an integral part of the SMA actuator.

6.4 Design of the Bistable Kinematic Stage

The next step, as proposed by the design methodology, consists of defining the relationship between the contraction of the SMA and the kinematic stage. In this section, the analytical model of the snap-through behaviour of the proposed bistable buckled beam is described and this model can then be used to design and size the buckled beam and the SMA coils so as to create a rapidly switching gripper with any required force and stroke specifications. This section is a result of the collaboration with Loic Tissot-Daguette (Instant-Lab, EPFL).

6.4.1 Analytical Model of the Buckled Beam

A beam theory model is proposed in this section to size the bistable buckled beam mechanism for the kinematic stage. In fig. 6.3, a schematic view of the buckled beam is shown. The initially flat beam buckles when compressed by a distance of Δl by the preloading stage attached to the input pivot. The SMA is considered to apply an input torque of M_{in} at the input pivot. As the final prototype of the kinematic stage is composed completely of flexure-based mechanisms, the pivots also present with an inherent angular stiffness, K_{in} and K_{out} at the input and output pivot, respectively. This stiffness must be taken into account when sizing the SMA element for the actuator. The buckled beam has a flexural rigidity of EI and an initial length before compression of L. As the flexure-based pivots are not ideal, the extremities of the beam start at a distance of p from the centre of rotation of the pivots as shown in fig. 6.3.

Based on the hypothesis described in the work by Tissot-Daguette et al. (2021) and the Euler-Bernoulli beam theory, the beam deflection can be described using the following equation:

$$y(x) = \left(A \sin kx + B(\cos kx - 1) + C\frac{x}{l} \right) l\theta_{\text{in}} \tag{6.1}$$

with $k = \sqrt{P/(EI)}$. The boundary conditions and the consequent analytical model of the buckled beam system, as developed by Loic Tissot-Daguette, has been illustrated in detail in appendix A.

The input moment required by the bistable mechanism, to be supplied by the SMA coils, can be described as seen in the following eq. (6.2).

$$\begin{aligned} M_{\text{in}} &\cong M_l + K_{\text{in}}\theta_{\text{in}} + Vp - Pp\theta_{\text{in}} \\ &= \frac{EI}{l}\left((kl)^2 \left(\overline{p}\,(C-1) - A\sin kl - B\cos kl \right) + \varepsilon_l \right) \theta_{\text{in}} \end{aligned} \tag{6.2}$$

where $\varepsilon_l = K_{\text{in}}/(EI/l)$. Here, the input angle can be expressed as :

$$\theta_{\text{in}} = \pm\sqrt{\frac{\Delta l}{l}}\sqrt{\frac{1}{H}} \tag{6.3}$$

where, the deflections parameters, A, B, C, Δl, and H, are defined in appendix A. Using

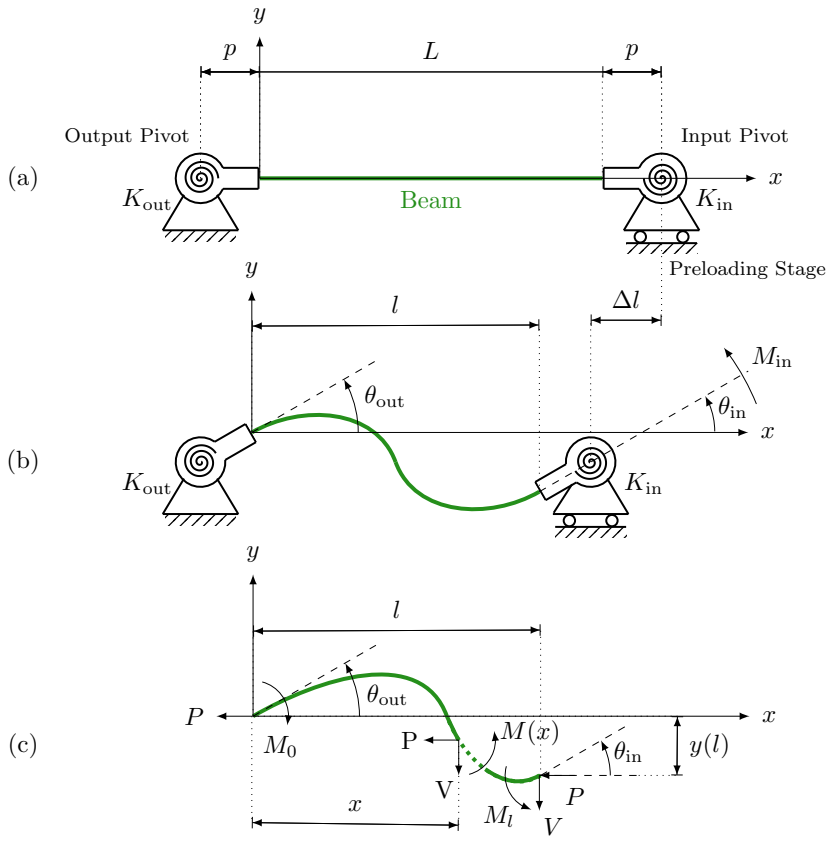

Figure 6.3: The diagram of the bistable mechanism (a) As-fabricated, (b) buckled and (c) free-body diagram of the buckling beam. (Illustration by Loic Tissot-Daguette)

these equations, the moment and angular stroke requirements of the bistable element can be estimated as shown in fig. 6.5. These values can then be utilised in sizing the bistable element so as to fit the requirements of the project specifications while also verifying that the SMA active element can sufficiently provide the required moment and stroke to trigger the snap-through of the buckled beam.

6.4.2 Design and Fabrication of Kinematic Stage

With the help of this analytical model, a flexure-based kinematic stage can be designed and sized accordingly. In this case, cross-spring pivots, as shown in fig. 6.4, are used for the input and output pivots that mount the buckled beam. Based on the work by Henein (2005), their angular stiffness can be estimated using the equation below

$$K_p = \frac{2Ebh_p^3}{3L_p}, \tag{6.4}$$

where h_p and L_p are the thickness and the total diagonal length of the cross blades, respectively. The interface between the SMA coils and the kinematic stage consists of a lever arm that can be sized to adapt the force and stroke requirements of the SMA so as to trigger the snap-through of the buckled beam. The preloading screw, as observed in fig. 6.4 (b), is used to displace the preloading stage by Δl so as to cause the buckling of the initially straight beam. This buckling creates the bistability observed within the kinematic stage. In this gripper, the jaws are designed to move towards the centre symmetrically in a parallel motion. This jaw guidance mechanism, linked to the output pivot, is comprised of a reverse motion linkage of lever length, r, and two linear stages to ensure that the jaws move is opposite directions with the same amplitude, x_{out}, when the gripper is triggered to open. The angular stiffness, K_{out} of the jaw guidance mechanism perceived at the output pivot was estimated using FEM simulations for small values of the output angle, θ_{out}. As the gripper is triggered to close, x_{out} drops to zero and θ_{out} is approximated to zero. Due to the reaction torque experience by the output pivot coming from the buckled beam, a gripping force, F_{out}, is applied by each jaw onto the payload. These jaws can be interchanged to accommodate differing sizes and types of payload, allowing the gripper to be used in a wide variety of scenarios.

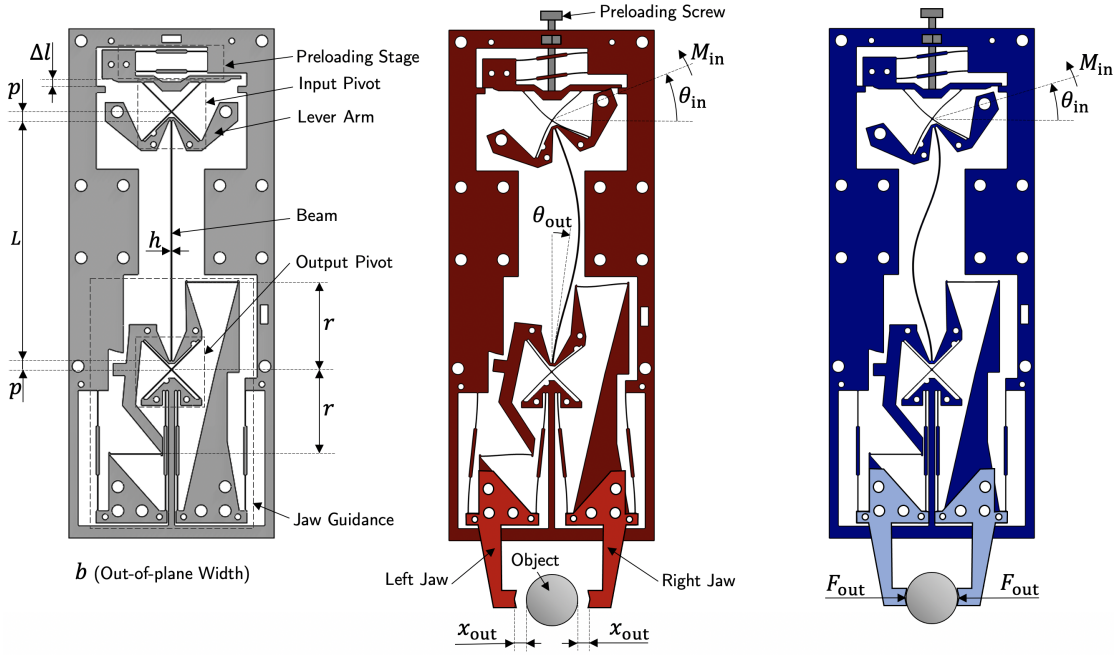

Figure 6.4: (a) Schematic view of the bistable mechanism as fabricated. Gripper with mounted jaws and the beam preloaded, (b) in open stable equilibrium and (c) in closed unstable equilibrium. (Designed and illustrated by Loic Tissot-Daguette)

The gripping requirements of the gripper, as deduced by Loic Tissot-Daguette, can be estimated using the following equations, as shown in fig. 6.5.

$$x_{\text{out}} \cong r\theta_{\text{out}} = (Akl + C)\, r\theta_{\text{in}} \tag{6.5}$$

$$F_{\text{out}} = \frac{M_0 - V\,p}{2r} = -\frac{EI}{l}\frac{\left(B + C\overline{p}\right)(kl)^2}{2r}\theta_{\text{in}} \tag{6.6}$$

where K_{out} tends to infinity when F_{out} is calculated as the object is considered to be infinitely rigid. In this case, the specifications of the gripper are sized with a jaw stroke, x_{out}, of 1.5 mm and a gripping force, F_{out}, of 1 N.

The flexure-based kinematic stage was fabricated from *Bohler K390* steel due to its high yield strength to Young's modulus ratio (σ_y/E). The prototype of the mechanism was fabricated using wire-cut electrical discharge machining (EDM) which allows a minimal thickness of 50 μm for the blades with a tolerance of a few μm. The design parameters of the fabricated prototype can be found in table 6.1.

Table 6.1: A summary of the design parameters for the flexure-based bistable mechanism.

	Parameter	Value
Material (Böhler K390)	E	220 GPa
	σ_y	2300 MPa
Structure Width	b	10 mm
Preloading Stage	Δl	1.25 mm
Buckled Beam	h	150 μm
	L	40 mm
	p	2 mm
Input Pivot	h_p	60 μm
	L_p	11.2 mm
	$K_{\text{in}} = K_p$	28.3 Nmm/rad
Jaw Guidance	r	14 mm
	K_{out}	205 Nmm/rad
Relative Stiffness	ε_0	12.8
	ε_l	1.77

6.4.3 Testing and Validation of the Kinematic Stage

For the validation of the bistable mechanism and the analytical model, a finite element method (FEM) 2D static study was implemented, with the efforts of Loic Tissot-Daguette, using the commercial software, *Comsol Multiphysics 5.4*. The material was, first, verified to determine whether the compliant structure can withstand the internal stresses during its maximal deformation. This determines the maximal admissible deformation to verify if the material is sufficient. Numerical simulations of the force-displacement characteristics of the mechanism were established to verify the analytical model as shown in fig. 6.5. As the numerical results fit the analytical model quite well, its implies that this model can be used to adequately size the SMA actuator as described in the sizing methodology proposed in

chapter 3.

Furthermore, a test bench was constructed to validate the analytical model with experimental results. The test bench consists of a manual micrometer linear stage to push the input lever arm, θ_{in} and measure the required force using the *Kistler Model 9207* force sensor for the input torque, M_{in}. Lastly, another force sensor is placed between the two jaws to measure the gripping force, F_{out}.

The experimental results of the mechanical behaviour of the gripper are portrayed in fig. 6.5. Based on the equations 6.2-6.6, the analytical model is traced out with the parameter kl ranging from 1.4π (near stable position) to 2.4π (near unstable position) for the opening sequence and from 1.3π (near stable position) to 2.2π (near unstable position) for the closing sequence. Here, l is approximated as $L-\Delta l$. The FEM results are also presented in the same figure to display the minor discrepancies present between the analytical, numerical model and experimental results.

As shown in fig. 6.5, the gripper is in its stable states when the input lever angle is at $-20°$ and at $21°$, which corresponds to its open and closed positions, respectively. The snap-through occurs when the lever angle exceeds the unstable position which corresponds to $-16°$ when the gripper is open and $17°$ when the gripper is closed. As the snap-through occurs, a rapid change between the open and closed gripper positions are observed. Furthermore, the high hysteresis of the bistable mechanism helps keep the gripper in a fixed state against any external perturbations such as accelerations and shocks to the gripper frame.

The output force and displacements also always stay positive. This implies that the gripper will continuously apply a gripping force during the opening transition and will always be open for the closing transition. However, during these transitions the output force and displacement increase by nearly 50%.

6.5 Sizing of the Actuator using the Proposed Methodology

The goal of this section is to validate the sizing methodology presented in section 3.4.2 by sizing the SMA coils for the proposed bistable gripper. The sizing of the SMA coils is a critical part in designing this proposed bistable gripper as the active element must have sufficient pull force to switch the bistable element while not being too rigid to overwrite the required bistability. In this design, the SMA coils are heated using Joule's heating and cooled passively. This implies that the cooling time of the SMA coil is directly and principally determined by the wire thickness of the coil. The thinnest wire diameter provided by the supplier was 200 μm and thus, the sizing methodology was applied to size the mechanism to work with such a thin SMA coil. Furthermore, by utilising the thinnest SMA coil available, the time between opening and closing sequences is minimised.

As mentioned in fig. 6.4, a lever arm is used to convert the linear motion of the SMA actuator

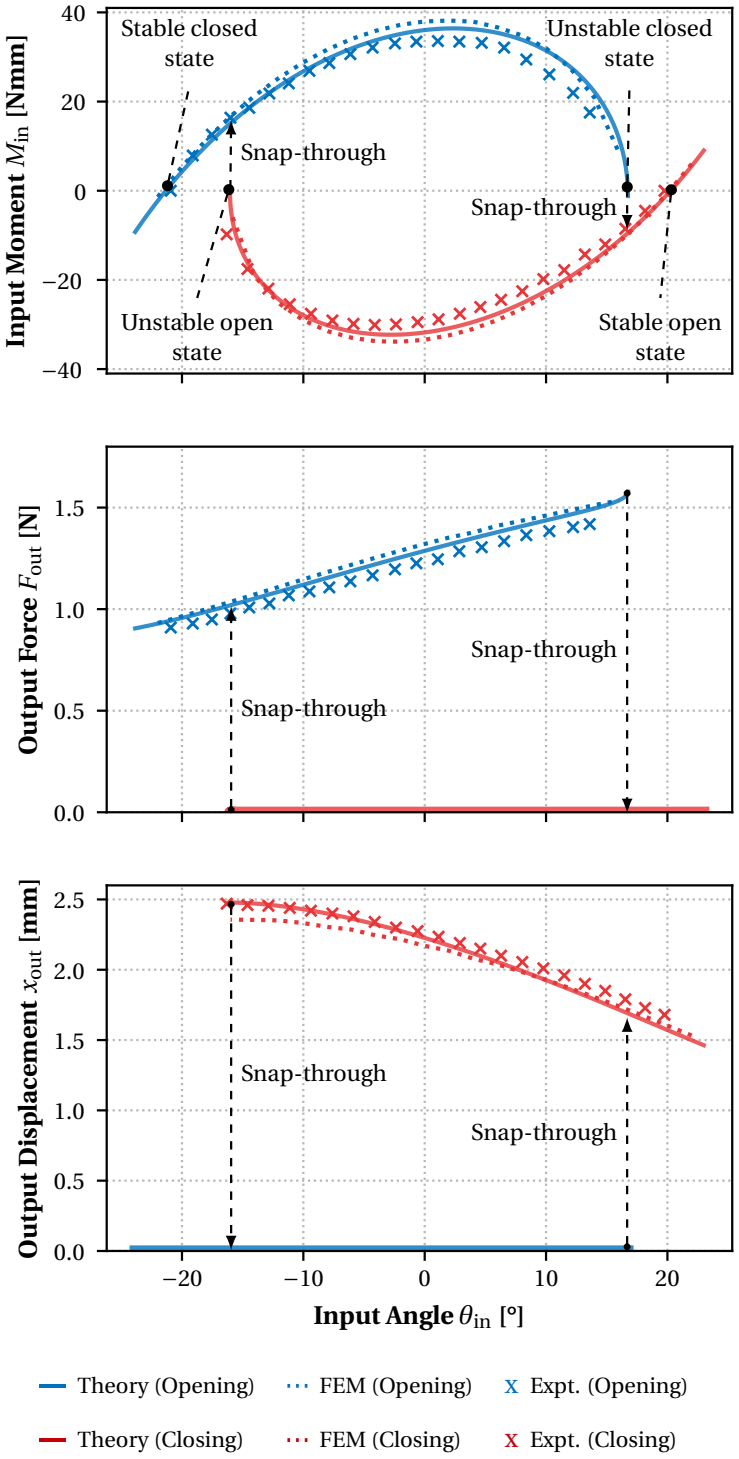

Figure 6.5: Validation of the analytical model of the bistable mechanism against the finite element model and experimental results. (Data courtesy of Loic Tissot-Daguette)

to a rotational output of the input pivot of the kinematic stage. By increasing the length of this lever arm, the required force to switch the stable state of the buckled beam within the kinematic stage can be controlled. However, increasing the lever arm length also increases the required stroke to trigger the snap-through.

Using the simplified sizing methodology presented in chapter 3, the operating points of the SMA actuator are determine by estimating the intersection between the force-displacement curve of the SMA and the kinematic stage. As the SMA is activated, the coil must overcome the switching requirements of the bistable mechanism as well as the detwinning requirements of the antagonistic SMA. In this case, the analytical model of the buckled beam developed in the previous sections is added to the curve of the antagonistic SMA to determine the biasing curve. The operating points are, thus, estimated by obtaining the intersection between the high temperature SMA curve and the combined buckled beam and cold temperature antagonistic SMA curve as shown in fig. 6.6 as ① and ②. It is important to note that both SMA must be cool to re-initiate the switching sequence to prevent both SMAs applying a pulling force on the kinematic stage at the same time. This operating point where both SMAs are cooled is represented in the figure as ①′.

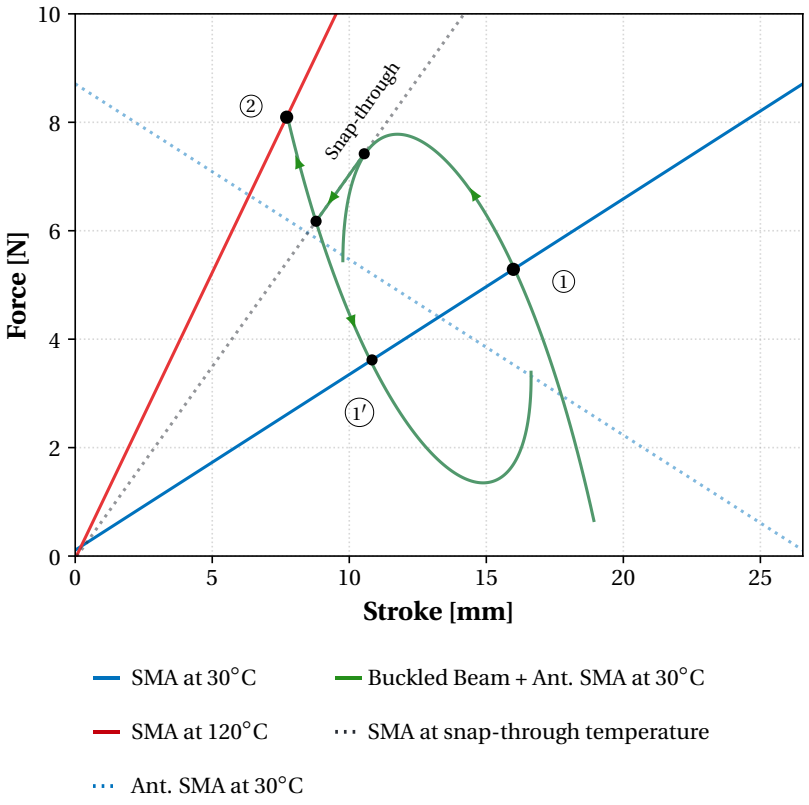

Figure 6.6: An estimation of the operating points of the bistable mechanism based on the adapted sizing methodology. Here, the lever arm is assumed to have a length of 12 mm and the SMA coils are pre-stretched by 7.5 mm when attached to the lever.

As stated earlier, an important parameter in sizing the SMA actuator is the length of the lever arm which can be used to adapt the switching requirements of the buckled beam. The linear SMA model, obtained using a pull-tester while maintaining the coil at a fixed temperature using a PID controller and a thermal camera as a feedback loop, can be used to determine the capabilities of the SMA coil. By sizing the lever arm, the curve of the bistable kinematic stage can be transformed such that the resulting force-displacement curve only intersects the SMA curve at two points preventing any undesired operating points. Furthermore, another important parameter to consider in the sizing strategy is the initial preloading deformation of the SMA coil. By adjusting this parameter, the SMA can be preloaded to recover more strain when heating but this comes at the cost of increased restoring force for the detwinning of the antagonistic SMA which is added to the force requirements of the activated SMA. This parameter can be visualised in fig. 6.6 as a shift in the SMA curve along the x-axis. The final sizing parameters of the lever arm and the SMA are summarized in table 6.2.

Table 6.2: The design parameters of the SMA actuator. The SMA coils were supplied by *Dynalloy, Inc.*

Parameter	Value
SMA dimensions	Coil: ∅1.37 × 12 mm Wire: ∅0.2 mm
Transition temperature	90 °C
Lever arm	12 mm
SMA prestretch	7.5 mm
Cooling time	2.83 s

The implementation of the lever arm and the SMA pre-stretching mechanism can be seen in fig. 6.7. This interface between the SMA coils and the bistable kinematic stage, shown in white, is fabricated from polyoxymethylene (POM) using laser cutting. This interface acts as a thermally and electrically insulated layer. Here, the interface consists of two parallel leaf spring stages that allow the preloading of the SMA using a screw and a trapped nut. This interface is constructed as a layer which can be mounted on top of the kinematic stage. Making use of this 2.5D design, an additional interface layer can be mounted on the opposing side to double the amount of SMAs coils, effectively doubling the pulling force of the SMA actuator without increasing the cooling time.

As previously stated, the main advantage to the proposed sizing methodology is the ability to adequately size the SMA elements based on the require force-displacement requirements of the bistable kinematic stage. This allows the gripper to employ the thinnest SMA coils and thus, when passively cooled, results in the shortest cooling time. As presented in section 4.2.3, the cooling time of the SMA can be estimated using a simple thermal model. As shown in the model, the cooling time can be further optimised by increasing the thermal gradient between

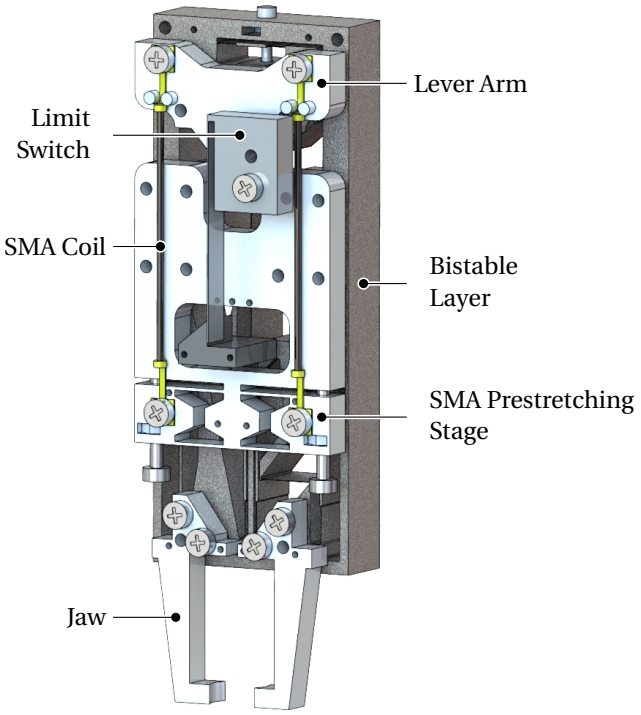

Figure 6.7: The assembly of the bistable gripper. Here, in white, the interface layer between the SMA actuator and the bistable mechanism can be seen.

the SMA and the ambient temperature. Thus, by employing SMA coils with high transition temperature, the cooling time can be further reduced. Additionally, as shown in the sizing of the SMA, the antagonistic cold SMA provides some additional force requirements when triggering the system. Thus, using the sizing methodology, the temperature of the antagonistic cold SMA can be sized such that the system operates at a temperature above ambient, further increasing the bandwidth of the gripper. It is important to note, however, that the temperature of the antagonistic SMA must be below M_f. In the case of the proposed bistable SMA gripper, using 200 μm SMA coils and a transition temperature of 90 °C, a cooling time of 2.83 s was obtained.

6.6 Actuation using the Mechanically-Intelligent Control Strategy

As explained previously, the principle behind the operating of the gripper consists of alternately heating the SMA coils by passing a current through them and cooling the coils passively by heat exchange with the surrounding air. Here, the basic working principle of the control is to heat the first SMA coil till the buckled beam switches and then leave sufficient time to cool the coil. Once, the temperature of the coil decreases sufficiently, the opposing antagonistic SMA is heated.

Thus, the heating and cooling time of the SMA coils are critical parameters to consider when implementing the control. By reducing these parameters, the time required between the opening and closing sequences can be minimised, implying that the time response of the gripper can be increased. Based on the methodology of an integrated control scheme presented in chapter 4, the mechanical behaviour of the SMA and the kinematic stage is exploited to control the SMA and prevent any overheating. In this design, the bistability of the buckled beam is used to cut the current flow across the corresponding SMA to prevent overheating. The electrical contact across the SMA is implemented using a limit switch. This Honeywell SX, 5A, 1CO, 0.2N limit switch is used to pass a current across the coils as it is rated for high current. Furthermore, the limit switch, activated by the buckled beam snap-through, is used to detect the state of the output pivot and cut the electrical contacts across the SMA coils, as shown in fig. 6.7 and fig. 6.10.

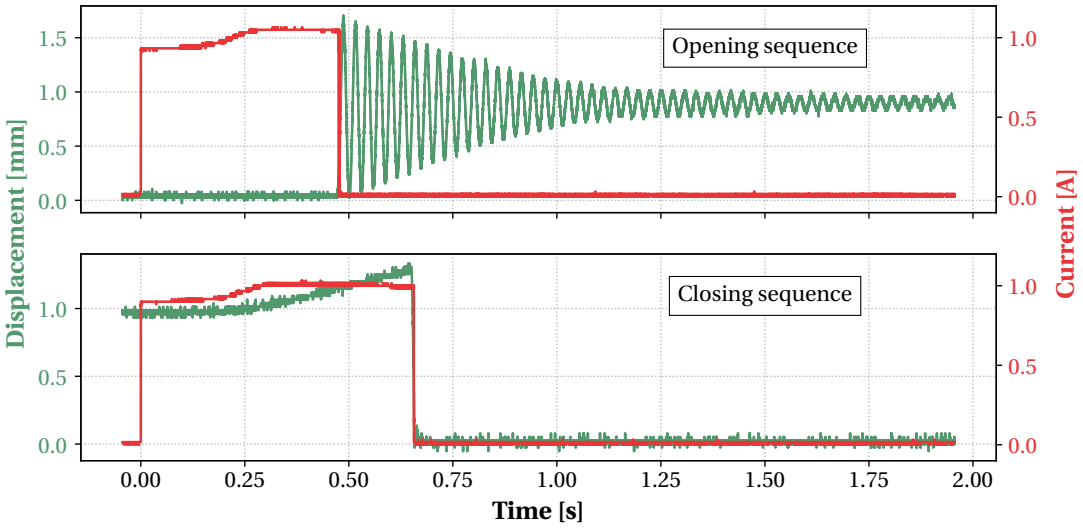

Figure 6.8: The jaw position and SMA current readings during the opening and closing sequences of the gripper showing that the current across the SMA is instantly cut when the gripper switches between its stable positions.

The basic strategy consists of heating the SMA by passing the current through the limit switch and into the SMA. The SMA coil is supplied with a pulse of high current which is automatically cut when the buckled beam switches and activates the limit switch as shown in fig. 6.8. Similarly, another pulse of current is sent across the antagonistic SMA. This ensures that the absolute minimum energy is used to heat the SMA and the minimum heating time is obtained. The width of the pulse can be increased to accommodate the cooling time as once the limit switch is activated, no more current is physically allowed to flow through the SMA coil. Therefore, this strategy requires no control logic for the activation of the gripper. Ideally, due to the conductive nature of the kinematic stage, the limit switch mechanism could be implemented within the kinematic stage to further integrate the solution. In this case, using a small form factor limit switch reduced the complexity of the design while still fitting withing

the imposed volume constraints.

As previously mentioned, the activation of the gripper is controlled by supplying one of the SMA coils with a pulse of current so as to heat the alloy. An H-bridge circuit is used to supply the current to either of the two SMA coils to activate the gripper in the required direction. A current pulse of 3 s is supplied to each SMA through the limit switch such that the required cooling time is also taken into account. The wiring of the gripper can be seen in fig. 6.9.

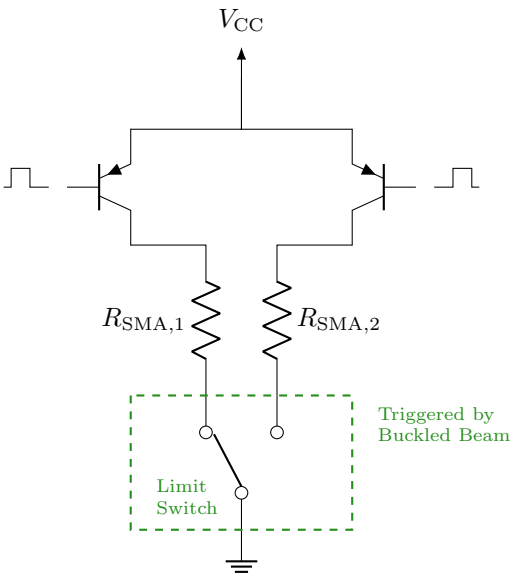

Figure 6.9: The electrical circuit diagram of the bistable SMA gripper based on the proposed control strategy.

The measurements presented in fig. 6.8 shows that by using the limit switch design, the gripper switches state and cuts the current across the SMA immediately ensuring that the minimum heating time is obtained and preventing any overheating of the SMA coil. The figure shows the opening and closing sequence of the gripper as the current passes through the coils. The gripper switches very quickly between states, thanks to the buckled beam snap-through. However, it can be observed that the jaws vibrate after the gripper opening around the stable open position. This is due to the fact that the compliant gripper dissipates the energy of the closed to open snap-through very gradually. A damping mechanism could be added to the gripper output to decrease the jaw vibration. During actuation testing, the buckled beam was not fully preloaded showing that the gripper stroke can be adjusted. Similarly, adjusting the preload should allow adapting the gripping force to a given application.

6.7 Specifications of the Final Prototype

Based on the design methodology, the final prototype consists of a flexure-based bistable mechanism that acts as the kinematic stage for the SMA actuator. As mentioned previously,

this stage was fabricated using electrical discharge machining from a monolithic block of *Bohler K390* steel, as shown in fig. 6.10. As the entire stage is created from a monolithic block, the system consists of only a single piece and thus, does not require any complex micro-assembly, displaying one of the key advantages of the use of flexure-based structures and this design methodology.

The SMA elements are integrated into the kinematic stage using a 2.5D design where an interface layer is used to actuate the input pivot of the kinematic stage. Using the design methodology, the pair of SMA coils, arranged in an antagonistic manner, is sized such that the thinnest SMA coils are used so as to keep the cooling time below 3 s. The design methodology takes into account the inherent stiffness of the bistable structure and sizes the SMAs such that there are no unintended operating points during the activation and snap-through of the gripper system. The final gripper has a stroke of 2.5 mm per jaw and has a gripping force of around 1.4 N.

Furthermore, the bistable mechanism and the thermoelastic behaviour of the SMA is exploited to create the mechanically-intelligent control strategy based on the proposed design methodology. In the final prototype, the current flowing the limit switch and into the SMA is controlled by the state of the buckled beam. The kinematic stage is able to cut the current across the SMA in less than 10 ms. Thus, with the use of these proposed design methodologies, the entire kinematic stage with the integrated SMA actuator fits within a volume constraint of $110 \times 34 \times 26$ mm.

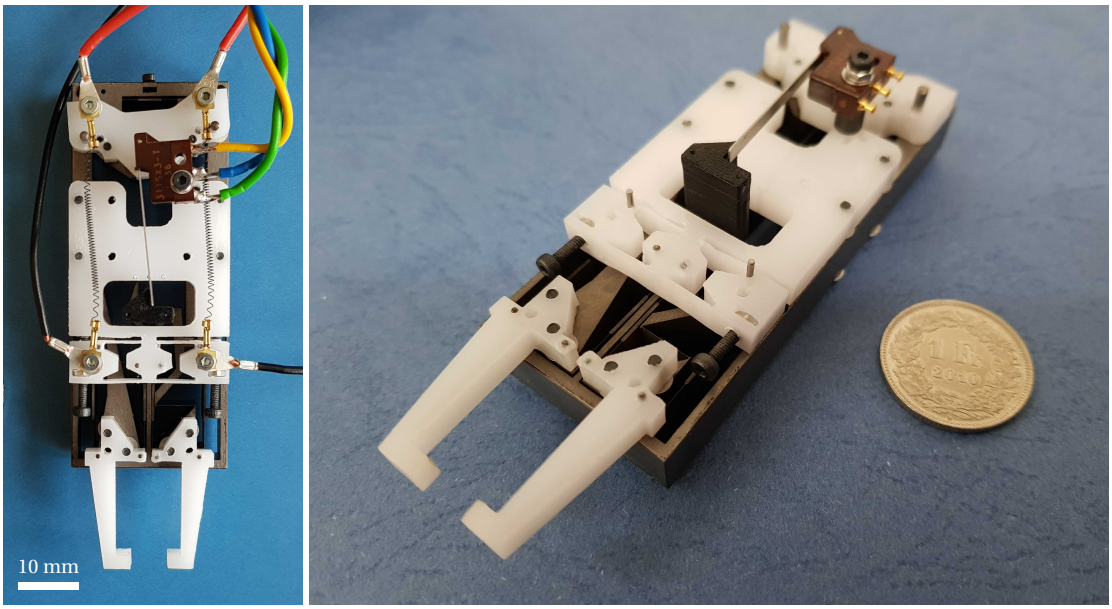

Figure 6.10: The fabricated prototype of the bistable gripper with the wiring circuit presented on the left.

6.7.1 Comparison of the Proposed Gripper

Due to the complex nature of the bistable mechanism, the literature on bistable grippers powered by smart materials is limited. However, a comparison of the proposed gripper with other bistable grippers shows the innovative aspects and the advantages of the design methodology. In most cases, as shown in the work by Zhang et al. (2020) and Scholtes et al. (2021), the bistable gripper requires no holding energy but however also does not provide any gripping force. As the stable state exists at 0 N, the gripping force depends on the size of the object and in the case of the aforementioned works, the grasped object is retained only using friction. In the case of bistable grippers using other smart materials, as shown in table 6.3, they often provide lower gripping force. The proposed gripper is able to provide a constant gripping force and stroke and has been sized to show comparable bandwidth. Thus, it is clear to see the primary advantages of the proposed methodology. Additionally, the presented gripper, when compared to other works, is able to produce fixed gripping forces and strokes while also using a compliant structure to provide a parallel gripping motion, compact footprint and a decoupled input-output actuation. Furthermore, the sizing strategy can be adapted to fit the various specifications of the application and the grasped object.

Table 6.3: Comparison of the proposed bistable gripper against other smart material powered bistable grippers.

	Material	Total Weight [g]	Gripping Force [N]	Bandwidth [Hz]	Switching Force [N]	Stroke [mm]
This work	SMA	135	1.4	0.33	7.8	5
Scholtes et al. (2021)	SMA	150	-	0.75	-	3
Zhang et al. (2020)	DC Motor	8	0	0.5	0.4	20
Wang et al. (2018)	DEA	-	0	-	0.05	5.65
Liu et al. (2017)	PZT	-	0.6	-	0.15	0.2
Lerner et al. (2020)	SMP	6.8	0.2	0.008	0.5	25

6.8 Summary and Conclusion

In this chapter, the design methodology presented in this work was validated using a case study. The described methodology proposed novel ways to design actuators that were compact and integrated. Using the various strategies proposed in the previous chapters, a gripper powered by shape memory alloys is designed and sized such that the resulting gripper presents with a relatively high time response while maintaining a low footprint. Furthermore, using the

simplified sizing methodology presented in this work has been implemented in this chapter to create a gripper with reduced cooling times and faster time responses. The methodology allowed the conception of a gripper that can be fabricated and assembled with a reduced number of parts, showing one of the primary advantages of the proposed design methodology.

In this final case study, a bistable SMA-powered gripper was designed and experimentally validated. Here, the prototype of the gripper consists of a bistable kinematic stage paired with an antagonistic SMA actuator. Furthermore, the kinematic stage and the shape memory effect has been exploited to create an integrated mechanical control that is able to perfectly control the temperature of the SMA coils without any micro-controllers or control logic. The bistable kinematic stage was conceived using flexure-based hinges and sized using the proposed methodology from chapter 3. Here, using the validated analytical models of the bistable element, the operating points of the final gripper were estimated and the final behaviour was verified to not present any unexpected operating points. Using the sizing methodology, the SMA coils and the kinematic stage were sized such that the thinnest wires could be used so as to increase the overall time response of the gripper. The prototype, while being able to apply a constant gripping force, could easily be adjusted to show different types of gripping behaviours and be made to grasp various sizes of objects which showcases one of the key advantages when compared to other bistable gripper solutions. Furthermore, by using the integrated mechanical control strategy as presented in chapter 4, this case study was able to validate the proposed approach. Here, using the bistable element to mechanically control the electrical contacts across the SMA coils, the gripper is able to be actuated without the use of temperature sensors or complex control schemes. Finally, the entire prototype, which fits in a foot print of $110 \times 34 \times 26$ mm, exhibits a stroke and gripping force of 2.5 mm and 1.4 N, showing the strength of the design strategy in creating compact actuators for application such as industrial pick-and-place grippers. Furthermore, using the novel sizing strategy, the bandwidth of the gripper was optimised such that the cooling time required by the SMA coils is as low as 2.8 s.

As seen with the illustration in fig. 6.2, the gripper, while being already highly integrated, there is still room to create a system that can incorporate all the subsystems of the actuator. Currently, the gripper is lightweight and compact and the use of SMA coils as the active element has allowed the gripper to have a short cooling time while being able to attain large strokes. The high elongation of the SMA coil allows it to adequately supply the required angular stroke of the bistable mechanism. However, a lever arm is still required to convert the linear movement into a rotational one. In future work, with the goal of further integration, a kirigami-inspired SMA structure, as shown in section 5.7, can be designed to provide a rotational output and be directly integrated into the kinematic stage. Furthermore, using the proposed sizing methodology, the SMA structure and the kinematic stage can be sized such that the resulting gripper has the required stroke, force output and bandwidth of the application specifications.

The gripper, presented in this chapter, is powered using shape memory alloys and are designed

using the different design methodologies presented in this work. These gripper, which can be used in industrial or drone related application, can be further optimised for their specific use cases but can also serve as an example for designing future grippers with differing specifications. Furthermore, future work could include using kirigami inspired SMA elements, to remove the need for a lever arm and further reduce the footprint and assembly time of the proposed gripper.

Publications related to this chapter :

S. Thomas, L. Tissot-Daguette, et al., *"Microgripper Device"*, European Patent Application, 21150579.7 - 1016

S. Thomas, L. Tissot-Daguette, T. Martinez, C. Baur, and Y. Perriard, *"Design and Modelling of a Flexure-based Bistable Gripper Powered by Shape Memory Alloys,"* Sensors and Actuators A: Physical, p. 8, 2022. (pending)

S. Thomas, P. Peralta, R. Mottet, M. Lehmann, Y. Civet, and Y. Perriard, *"Analysis and Reduction of Time Response in Thermally Activated Shape Memory Alloys,"* in 2018 21st International Conference on Electrical Machines and Systems (ICEMS), Oct. 2018, p. 7. doi: 10.23919/ICEMS.2018.8549332.

Conclusion and Contributions

In this thesis, the goal of the work was to develop and demonstrate an novel approach to designing highly integrate and energy dense SMA-powered actuators. Initially, the research objective focused on the traditional methodologies and models when designing and sizing SMA actuators. Furthermore, the common types of implementations of such actuator were considered and their sizing methodologies were studied to deduce the various areas in which the work densities could be improved. This objective led to the development of a systematic design strategy that allowed creating integrated SMA-based actuators that improved the overall work density by transforming traditionally discrete subsystems into integrated multifunctional ones. Additionally, the traditional analytical and sizing models were adjusted to create an adapted sizing methodology so as to create actuators for any application.

In this work, multiple case studies were presented that were designed and fabricated based on the proposed integrated SMA actuator design methodology. These include :

- A multi-output lightweight gripper ideal for drone-based applications. This system consists of a compliant kinematic stage that also behaves as a biasing element for the SMA actuator and displays a high force-weight density.
- A highly lightweight untethered mechanically-controlled SMA inchworm robot that is able to produce a constant gait without the use of any sensors or control electronics.
- A simple kirigami-inspired linear actuator that behaves as a proof-of-concept for a high force-high stroke output actuator. This actuator manages to remain lightweight, compact and retain its high energy work density.
- A bistable gripper powered by a pair of antagonistic SMA helical springs capable of providing a gripping force without the need for any additional energy.

Contribution Statement

This thesis aimed to contribute and explore the answers to the following key research questions:

How can the work density degradation of SMAs be prevented when designing actuators? In this work, various SMA-based actuators were studied from the major domains in which SMAs are employed. This study showed the key design considerations and criteria used in the design of SMA-powered actuators, the major one being the work density. This study also showed that in most cases, the traditional approach consists of creating an actuator where the key subsystems are discrete and lack integration. This results in the degradation of the work density as passive materials are added to the actuator without adding to the work output. This works answers the research question by proposing a holistic design methodology where the key subsystems present within an SMA actuator are integrated where the novel subsystems become multifunctional. In this thesis, a design methodology is presented to create SMA-based actuators that employ this holistic approach. This integration strategy has been employed on the various key elements of the SMA actuator such as the biasing element, kinematic and control stage. In each case, a case study is presented that makes use of this novel approach in the hopes to validate the design and sizing methodology. Furthermore, the key findings of this research question has led to numerous scientific publications and has contributed to the field by presenting novel techniques in designing SMA-powered actuators.

How can the traditional sizing methodology be adapted for integrated SMA actuators? This work demonstrates that by taking a holistic approach to creating SMA actuators can be beneficial when considering the work density of the resulting system. However, due to the multi-physical nature of the SME and the complex kinematic stages required, sizing such systems can be difficult. This works presents the traditional sizing methodology employed in SMA actuator designs and adapts the models such that they can be implemented in the proposed integrated SMA actuators. This sizing methodology allows the actuator to be designed in such a way that the least amount of the active material is required to drive the system. In most cases and in the case of the actuators presented in this work, the active SMA material is cooled passively using heat transfer with the surrounding air. Thus, the bandwidth of the resulting actuator depends directly on the cooling time required to return the SMA material back to the M phase. Thus, the sizing methodology presented and validated using various case studies, in this thesis, has allowed the actuator to be sized so as to maximize the bandwidth. Furthermore, the various adapted sizing methodologies have been described in the context of different SMA-powered actuators and published in various scientific publications.

Can a generative design approach be used to create and validate compliant SMA structures? The aforementioned integrated subsystem approach, in this work, was extended to other areas of the SMA actuator. Creating or generating compliant SMA actuators is proposed as a way to combine the functionality of the active material and the kinematic stage into one subsystem so as to further improve the work density of the final system. However, due to the complex nature of the SME creating complex geometries and predicting the resulting behaviour once heated can be difficult and computational expensive. Often, when a large design space is present with multiple variables, topology optimization can be used to algorithmically generate complex

structures. In this work, topology optimization was presented and adapted to produce multi-output complaint SMA structures that can be be algorithmically generated with a relatively low computational cost. Furthermore, this work describes and validates a qualitative factor that can be used to test the efficiency of the generated design within the context of an SMA actuator. This simple algorithm was validated experimentally and has been published in a research publication so as to allow the creation of future 3D printed multi-output SMA actuators.

Future Implications

This work has established a methodology that allows future engineers to create highly integrated and work dense SMA-powered actuators. With the advent of 3D printing technology and additive manufacturing of Ni-Ti based alloys, complex SMA structures can be fabricated and have already begun to show up on the forefront of research. Using the methodology and generative algorithms presented in this work, future researchers can exploit the approach to create multi-output and compact SMA-powered actuators capable of performing complex tasks.

Furthermore, the use of compliant structures paired with SMAs has been shown in this work to allow the creation of complex, yet, lightweight actuators. In future work, this design approach can be used to design and size lightweight actuators for various applications based on the required project specifications. In this work, the identified subsystems present in a traditional SMA-based actuator have been integrated so as create multi-functional elements and thus, reduce the overall work density degradation. This concept can be however extended to further incorporate the actuator into the entire robotic system for a greater holistic approach. In the case of a drone-ready gripper, the entire actuator can be integrated within the frame of the drone to further improve the work density of the system and render the robotic system even more lightweight or compact. Additionally, active cooling as a relevant subsystem in the actuator design has not been taken into account and can be another avenue of integration that can be considered to further extend this work while also increasing the bandwidth of the resulting actuator.

Lastly, in this work, the control strategy used for the proposed SMA-powered systems were simple without the use of any sensors. Furthermore, a mechanical control strategy was proposed that removed the need for control electronics or sensor further increasing the work density of the system. However, in future work, the sensorless control of the SMA element could be taken into account to allow the more complex SMA structures to also benefit from the removed sensors within the system, thereby, preventing work density degradation. Further developments in SMA manufacturing technologies can be harnessed with the use of the proposed design methodologies to create highly integrated, compact and lightweight actuators.

A Analytical Modelling of Buckled Beam Mechanism

The bistable mechanism consists of an initially flat beam which, when compressed by a distance Δl, buckles and forms a structure that exists in two stable positions. In the case of the actuator, which consists of a pair of SMA coils and the buckled beam itself, is considered to require an input torque M_{in} at the input pivot to switch between its two stable states.

As the entire kinematic stage is comprised of flexure-based mechanisms, as shown in fig. 6.4, the pivots that support the buckled beam present with an inherent angular stiffness, K_{in} and K_{out} at the input and output pivot, respectively. The buckled beam is considered to have a flexural rigidity of EI and an initial length before compression of L. The distance between the centre of the flexural pivots and the beam is considered to be offset by a distance of p, as shown in fig. 6.3.

Based on the hypothesis described in the work by Tissot-Daguette et al. (2021) and the Euler-Bernoulli beam theory, the beam deflection can be described using the following equation:

$$y(x) = \left(A \sin kx + B(\cos kx - 1) + C\frac{x}{l}\right) l\theta_{\text{in}} \tag{A.1}$$

with $k = \sqrt{P/(EI)}$ and the boundary conditions of the supported beam are as follows

$$y(0) = 0$$

$$y'(0) \cong \theta_{\text{out}}$$

$$M_0 \cong K_{\text{out}}\theta_{\text{out}} + Vp - Pp\theta_{\text{out}}$$

$$y(l) \cong -p(\theta_{\text{out}} + \theta_{\text{in}})$$

$$y'(l) \cong \theta_{\text{in}}$$

Furthermore, the deflection parameters of eq. (A.1) are given by

$$A = \frac{(1+2\overline{p})kl + \varepsilon_0\left(\overline{p}\sin kl - \frac{\cos kl-1}{kl}\right)}{kl\left(kl\cos kl - \sin kl - \left(\overline{p}^2+\overline{p}\right)(kl)^2\sin kl + \varepsilon_0\left(\sin kl + 2\frac{\cos kl-1}{kl}\right)\right)} \tag{A.2}$$

$$B = \frac{\overline{p}(1+2\overline{p})(kl)^2 + \varepsilon_0\left(\overline{p}(\cos kl-1) + \frac{\sin kl}{kl} - 1\right)}{kl\left(kl\cos kl - \sin kl - \left(\overline{p}^2+\overline{p}\right)(kl)^2\sin kl + \varepsilon_0\left(\sin kl + 2\frac{\cos kl-1}{kl}\right)\right)} \tag{A.3}$$

$$C = \frac{\overline{p}^2(kl)^2\sin kl - 2\overline{p}kl\cos kl - \sin kl - \varepsilon_0\left(\overline{p}\sin kl - \frac{\cos kl-1}{kl}\right)}{kl\cos kl - \sin kl - \left(\overline{p}^2+\overline{p}\right)(kl)^2\sin kl + \varepsilon_0\left(\sin kl + 2\frac{\cos kl-1}{kl}\right)} \tag{A.4}$$

where $\overline{p} = p/l$ and $\varepsilon_0 = K_{\text{out}}/(EI/l)$. When considering the beam's arc length as constant, the end-shorting, Δl, can be approximated using the following expression

$$\Delta l \cong \frac{p}{2}(\theta_{\text{in}}^2 + \theta_{\text{out}}^2) + \int_0^l \frac{y'(x)^2}{2}dx = Hl\theta_{\text{in}}^2 \tag{A.5}$$

Here, the coefficient H is expressed as

$$\begin{aligned} H = {} & \frac{\left(A^2+B^2\right)(kl)^2}{4} + \frac{\left(A^2-B^2\right)kl\sin 2kl}{8} + \frac{ABkl(\cos 2kl - 1)}{4} \\ & + AC\sin kl + BC(\cos kl - 1) + \frac{C^2}{2} + \frac{\overline{p}}{2}\left((Akl+C)^2+1\right) \end{aligned} \tag{A.6}$$

By rearranging eq. (A.5), the input angle can be expressed as

$$\theta_{\text{in}} = \pm\sqrt{\frac{\Delta l}{l}}\sqrt{\frac{1}{H}} \tag{A.7}$$

Finally, the input moment can be described as the following eq. (A.8)

$$\begin{aligned} M_{\text{in}} &\cong M_l + K_{\text{in}}\theta_{\text{in}} + Vp - Pp\theta_{\text{in}} \\ &= \frac{EI}{l}\left((kl)^2\left(\overline{p}(C-1) - A\sin kl - B\cos kl\right) + \varepsilon_l\right)\theta_{\text{in}} \end{aligned} \tag{A.8}$$

where $\varepsilon_l = K_{\text{in}}/(EI/l)$. These equations, as developed by Loic Tissot-Daguette, are used to obtain the moment and angular stroke requirements of the bistable element when sizing the SMA elements for the bistable gripper.

Bibliography

Abdul Kadir, M. R., Dewi, D. E. O., Jamaludin, M. N., Nafea, M., and Mohamed Ali, M. S. (2019). A multi-segmented shape memory alloy-based actuator system for endoscopic applications. *Sensors and Actuators A: Physical*, 296:92–100.

Alagha, A. N., Hussain, S., and Zaki, W. (2021). Additive manufacturing of shape memory alloys: A review with emphasis on powder bed systems. *Materials & Design*, 204:109654.

Alonso, C., Ansola, R., and Querin, O. M. (2014). Topology synthesis of Multi-Input–Multi-Output compliant mechanisms. *Advances in Engineering Software*, 76:125–132.

Andrianesis, K. and Tzes, A. (2015). Development and Control of a Multifunctional Prosthetic Hand with Shape Memory Alloy Actuators. *Journal of Intelligent & Robotic Systems*, 78(2):257–289.

ANSYS (2021). Nonlinear Material Properties. In *Material Reference*, page 215. ANSYS, Inc., Canonsburg, PA, release 2021 r2 edition.

Auricchio, F. (2001). A robust integration-algorithm for a finite-strain shape-memory-alloy superelastic model. *International Journal of Plasticity*, 17(7):971–990.

Auricchio, F. and Petrini, L. (2002). Improvements and algorithmical considerations on a recent three-dimensional model describing stress-induced solid phase transformations. *International Journal for Numerical Methods in Engineering*, 55(11):1255–1284.

Bellini, A., Colli, M., and Dragoni, E. (2009). Mechatronic Design of a Shape Memory Alloy Actuator for Automotive Tumble Flaps: A Case Study. *IEEE Transactions on Industrial Electronics*, 56(7):2644–2656.

Bellouard, Y. (2008). Shape memory alloys for microsystems: A review from a material research perspective. *Materials Science and Engineering: A*, 481-482:582–589.

Benafan, O., Moholt, M. R., Bass, M., Mabe, J. H., Nicholson, D. E., and Calkins, F. T. (2019). Recent Advancements in Rotary Shape Memory Alloy Actuators for Aeronautics. *Shape Memory and Superelasticity*, 5(4):415–428.

Benard, W. L., Kahn, H., Heuer, A. H., and Huff, M. A. (1998). Thin-film shape-memory alloy actuated micropumps. *Journal of Microelectromechanical Systems*, 7(2):245–251.

Bendsøe, M. P. and Sigmund, O. (2004). *Topology Optimization: Theory, Methods, and Applications*. Springer Berlin Heidelberg, Berlin, Heidelberg.

Brinson, L. (1993). One-Dimensional Constitutive Behavior of Shape Memory Alloys: Thermomechanical Derivation with Non-Constant Material Functions and Redefined Martensite Internal Variable. *Journal of Intelligent Material Systems and Structures*, 4(2):229–242.

Cao, J., Qin, L., Liu, J., Ren, Q., Foo, C. C., Wang, H., Lee, H. P., and Zhu, J. (2018). Untethered soft robot capable of stable locomotion using soft electrostatic actuators. *Extreme Mechanics Letters*, 21:9–16.

Chang, L. C. and Read, T. A. (1951). Plastic Deformation and Diffusionless Phase Changes in Metals — the Gold-Cadmium Beta Phase. *JOM*, 3(1):47–52.

Chen, Y., Zhao, H., Mao, J., Chirarattananon, P., Helbling, E. F., Hyun, N.-s. P., Clarke, D. R., and Wood, R. J. (2019). Controlled flight of a microrobot powered by soft artificial muscles. *Nature*, 575(7782):324–329.

Chouinard, P. and Plante, J. (2012). Bistable Antagonistic Dielectric Elastomer Actuators for Binary Robotics and Mechatronics. *IEEE/ASME Transactions on Mechatronics*, 17(5):857–865.

Dragoni, E. and Spaggiari, A. (2021). Design and development of advanced SMA actuators. In *Shape Memory Alloy Engineering For Aerospace, Structural, and Biomedical Applications*, pages 413–453. Butterworth-Heinemann, second edition.

Duerig, T. and Pelton, A. (1994). Ti-Ni shape memory alloys. In *Materials properties handbook: titanium alloys*, pages 1035–1048. ASM International, Materials Park, OH.

Elahinia, M., Moghaddam, N. S., Amerinatanzi, A., Saedi, S., Toker, G. P., Karaca, H., Bigelow, G. S., and Benafan, O. (2018). Additive manufacturing of NiTiHf high temperature shape memory alloy. *Scripta Materialia*, 145:90–94.

Elahinia, M. H. and Ahmadian, M. (2005). An enhanced SMA phenomenological model: I. The shortcomings of the existing models. *Smart Materials and Structures*, 14(6):1297.

Faran, E. and Shilo, D. (2016). Ferromagnetic Shape Memory Alloys—Challenges, Applications, and Experimental Characterization. *Experimental Techniques*, 40(3):1005–1031.

Firouzeh, A. and Paik, J. (2015). The Design and Modeling of a Novel Resistive Stretch Sensor With Tunable Sensitivity. *IEEE Sensors Journal*, 15(11):6390–6398.

Haibin, Y., Cheng, K., Junfeng, L., and Guilin, Y. (2018). Modeling of grasping force for a soft robotic gripper with variable stiffness. *Mechanism and Machine Theory*, 128:254–274.

He, X. M. and Rong, L. J. (2004). DSC analysis of reverse martensitic transformation in deformed Ti–Ni–Nb shape memory alloy. *Scripta Materialia*, 51(1):7–11.

Henein, S. (2005). *Conception des structures articulées à guidages flexibles de haute précision*. PhD thesis, EPFL, Lausanne. Publisher: Lausanne, EPFL.

Henein, S., Bottinelli, S., and Clavel, R. (1998). Parallel spring stages with flexures of micrometric cross sections. In *Microrobotics and Microsystem Fabrication*, volume 3202, pages 209–220. International Society for Optics and Photonics.

Howell, L. L., Magleby, S. P., and Olsen, B. M., editors (2013). *Handbook of compliant mechanisms*. John Wiley & Sons, Inc, Chichester, West Sussex, United Kingdom ; Hoboken.

Huang, W. (2002). On the selection of shape memory alloys for actuators. *Materials & Design*, 23(1):11–19.

Huang, X., Kumar, K., Jawed, M. K., Nasab, A. M., Ye, Z., Shan, W., and Majidi, C. (2018). Chasing biomimetic locomotion speeds: Creating untethered soft robots with shape memory alloy actuators. *Science Robotics*, 3(25). Publisher: Science Robotics Section: Focus.

Huang, X., Kumar, K., Jawed, M. K., Nasab, A. M., Ye, Z., Shan, W., and Majidi, C. (2019). Highly Dynamic Shape Memory Alloy Actuator for Fast Moving Soft Robots. *Advanced Materials Technologies*, 4(4):1800540.

Hwang, D. and Higuchi, T. (2016). A Planar Wobble Motor With a XY Compliant Mechanism Driven by Shape Memory Alloy. *IEEE/ASME Transactions on Mechatronics*, 21(1):302–315.

Ikuta, K. (1990). Micro/miniature shape memory alloy actuator. In , *IEEE International Conference on Robotics and Automation Proceedings*, pages 2156–2161 vol.3.

Jaber, M. B. (2018). Ansys parameters for shape memory alloys (Aurricchio Model). https://www.researchgate.net/publication/323883785.

Ji, X., Liu, X., Cacucciolo, V., Imboden, M., Civet, Y., El Haitami, A., Cantin, S., Perriard, Y., and Shea, H. (2019). An autonomous untethered fast soft robotic insect driven by low-voltage dielectric elastomer actuators. *Science Robotics*, 4(37):eaaz6451.

Jin Qiu, Lang, J. H., and Slocum, A. H. (2004). A curved-beam bistable mechanism. *Journal of Microelectromechanical Systems*, 13(2):137–146.

Kim, B., Lee, M. G., Lee, Y. P., Kim, Y., and Lee, G. (2006). An earthworm-like micro robot using shape memory alloy actuator. *Sensors and Actuators A: Physical*, 125(2):429–437.

Koh, J.-S. and Cho, K.-J. (2013). Omega-Shaped Inchworm-Inspired Crawling Robot With Large-Index-and-Pitch (LIP) SMA Spring Actuators. *IEEE/ASME Transactions on Mechatronics*, 18(2):419–429.

Kohl, M., Krevet, B., and Just, E. (2002). SMA microgripper system. *Sensors and Actuators A: Physical*, 97-98:646–652.

Kyung, J. H., Ko, B. G., Ha, Y. H., and Chung, G. J. (2008). Design of a microgripper for micromanipulation of microcomponents using SMA wires and flexible hinges. *Sensors and Actuators A: Physical*, 141(1):144–150.

Lee, J.-H., Chung, Y. S., and Rodrigue, H. (2019). Long Shape Memory Alloy Tendon-based Soft Robotic Actuators and Implementation as a Soft Gripper. *Scientific Reports*, 9(1):1–12.

Lee, L. Y., Syadiqeen, O. A., Tan, C. P., and Nurzaman, S. G. (2021). Closed-Structure Compliant Gripper With Morphologically Optimized Multi-Material Fingertips for Aerial Grasping. *IEEE Robotics and Automation Letters*, 6(2):887–894.

Lerner, E., Zhang, H., and Zhao, J. (2020). Design and Experimentation of a Variable Stiffness Bistable Gripper. In *2020 IEEE/RSJ International Conference on Intelligent Robots and Systems (IROS)*, pages 9925–9931, Las Vegas, NV, USA. IEEE. ISSN: 2153-0866.

Liang, C. (1990). *The constitutive modeling of shape memory alloys*. Dissertation, Virginia Polytechnic Institute and State University, Blacksburg, Virginia.

Liang, C., Wang, Y., Yao, T., and Zhu, B. (2020). A shape memory alloy–actuated soft crawling robot based on adaptive differential friction and enhanced antagonistic configuration. *Journal of Intelligent Material Systems and Structures*, 31(16):1920–1934. Publisher: SAGE Publications Ltd STM.

Liu, X., Liu, H., and Tan, J. (2019). Mesoscale Shape Memory Alloy Actuator for Visual Clarity of Surgical Cameras in Minimally Invasive Robotic Surgery. *IEEE Transactions on Medical Robotics and Bionics*, 1(3):135–144.

Liu, X., Liu, H., and Tan, J. (2021). Actuation Frequency Modeling and Prediction for Shape Memory Alloy Actuators. *IEEE/ASME Transactions on Mechatronics*, 26(3):1536–1546.

Liu, Y., Zhang, Y., and Xu, Q. (2017). Design and Control of a Novel Compliant Constant-Force Gripper Based on Buckled Fixed-Guided Beams. *IEEE/ASME Transactions on Mechatronics*, 22(1):476–486.

Lu, Y., Xie, Z., Wang, J., Yue, H., Wu, M., and Liu, Y. (2019). A novel design of a parallel gripper actuated by a large-stroke shape memory alloy actuator. *International Journal of Mechanical Sciences*, 159:74–80.

Maffiodo, D., Raparelli, T., and Department of Mechanical and Aerospace Engineering, Politecnico di Torino (2017). Three-Fingered Gripper with Flexure Hinges Actuated by Shape Memory Alloy Wires. *International Journal of Automation Technology*, 11(3):355–360.

Malagisi, S., Marfia, S., and Sacco, E. (2017). Coupled normal-shear stress models for SMA response. *Computers & Structures*, 193:73–86.

Mansour, N. A., Jang, T., Baek, H., Shin, B., Ryu, B., and Kim, Y. (2020). Compliant closed-chain rolling robot using modular unidirectional SMA actuators. *Sensors and Actuators A: Physical*, 310:112024.

Mansour, N. A. and Kim, Y. (2020). ANFIS-Based System Identification and Control of a Compliant Shape Memory Alloy (SMA) Rotating Actuator. In *IEEE Robotics & Automation Magazine*, volume 16, pages 81–94, Boston, MA.

Meng, L., Kang, R., Gan, D., Chen, G., Chen, L., Branson, D. T., and Dai, J. S. (2020). A Mechanically Intelligent Crawling Robot Driven by Shape Memory Alloy and Compliant Bistable Mechanism. *Journal of Mechanisms and Robotics*, 12(061005).

Modabberifar, M. and Spenko, M. (2018). A shape memory alloy-actuated gecko-inspired robotic gripper. *Sensors and Actuators A: Physical*, 276:76–82.

Mohd Jani, J., Leary, M., and Subic, A. (2017). Designing shape memory alloy linear actuators: A review. *Journal of Intelligent Material Systems and Structures*, 28(13):1699–1718.

Mohd Jani, J., Leary, M., Subic, A., and Gibson, M. A. (2014). A review of shape memory alloy research, applications and opportunities. *Materials & Design (1980-2015)*, 56:1078–1113.

Morikawa, Y., Yamagiwa, S., Sawahata, H., Numano, R., Koida, K., Ishida, M., and Kawano, T. (2018). Ultrastretchable Kirigami Bioprobes. *Advanced Healthcare Materials*, 7(3):1701100.

Motzki, P., Kunze, J., York, A., and Seelecke, S. (2016). Energy-efficient SMA Vacuum Gripper System. In *15th International Conference on New Actuators*.

Muralidharan, M., Brolin, A., Mithun, R., Patil, R., and Palani, I. A. (2021). Investigations on Bending Characteristics of Soft Mesh Structure using Shape Memory Alloy Spring Towards Bio-Inspired Robotic Applications. *Iranian Journal of Science and Technology, Transactions of Mechanical Engineering*, 45(4):927–937.

Must, I., Kaasik, F., Põldsalu, I., Mihkels, L., Johanson, U., Punning, A., and Aabloo, A. (2015). Ionic and Capacitive Artificial Muscle for Biomimetic Soft Robotics. *Advanced Engineering Materials*, 17(1):84–94.

Narayanan, P. and Elahinia, M. (2016). Control of a shape memory alloy–actuated rotary manipulator using an artificial neural network–based self-sensing technique. *Journal of Intelligent Material Systems and Structures*, 27(14):1885–1894.

Nespoli, A., Besseghini, S., Pittaccio, S., Villa, E., and Viscuso, S. (2010). The high potential of shape memory alloys in developing miniature mechanical devices: A review on shape memory alloy mini-actuators. *Sensors and Actuators A: Physical*, 158(1):149–160.

Otsuka, K. and Shimizu, K. (1986). Pseudoelasticity and shape memory effects in alloys. *International Metals Reviews*, 31(1):93–114.

Paik, J. K., Hawkes, E., and Wood, R. J. (2010). A novel low-profile shape memory alloy torsional actuator. *Smart Materials and Structures*, 19(12):125014.

Plaut, R. H. (2015). Mathematical model of inchworm locomotion. *International Journal of Non-Linear Mechanics*, 76:56–63.

Preumont, A. (2006). *Mechatronics: dynamics of electromechanical and piezoelectric systems*. Number v. 136 in Solid mechanics and its applications. Springer, Dordrecht.

Rao, A., Srinivasa, A. R., and Reddy, J. N. (2015). *Design of Shape Memory Alloy (SMA) Actuators*. SpringerBriefs in Applied Sciences and Technology. Springer International Publishing, Cham.

Ricciardi, M. R. and Antonucci, V. (2021). Chapter 5 - Experimental characterization of shape memory alloys. In Concilio, A., Antonucci, V., Auricchio, F., Lecce, L., and Sacco, E., editors, *Shape Memory Alloy Engineering (Second Edition)*, pages 141–164. Butterworth-Heinemann, Boston.

Rodrigue, H., Wang, W., Kim, D.-R., and Ahn, S.-H. (2017). Curved shape memory alloy-based soft actuators and application to soft gripper. *Composite Structures*, 176:398–406.

Roshan, U., Amarasinghe, R., and Dayananda, N. (2018). Design and Fabrication of a Minimally Invasive Surgical Device with Customized Shape Memory Alloy Spring Actuator. *Journal of Robotics, Networking and Artificial Life*, 5(3):194–198. Publisher: Atlantis Press.

Rubbert, L., Bitterli, R., Ferrier, N., Fifanski, S., Vardi, I., and Henein, S. (2016). Isotropic springs based on parallel flexure stages. *Precision Engineering*, 43:132–145.

Ruiz, D. and Sigmund, O. (2018). Optimal design of robust piezoelectric microgrippers undergoing large displacements. *Structural and Multidisciplinary Optimization*, 57(1):71–82.

Runciman, A., Xu, D., Pelton, A. R., and Ritchie, R. O. (2011). An equivalent strain/Coffin–Manson approach to multiaxial fatigue and life prediction in superelastic Nitinol medical devices. *Biomaterials*, 32(22):4987–4993.

Sabahi, N., Chen, W., Wang, C.-H., Kruzic, J. J., and Li, X. (2020). A Review on Additive Manufacturing of Shape-Memory Materials for Biomedical Applications. *The Journal of The Minerals, Metals & Materials Society (TMS)*, 72(3):1229–1253. Company: Springer Distributor: Springer Institution: Springer Label: Springer Number: 3 Publisher: Springer US.

Sakagami, T., Seki, K., and Iwasaki, M. (2019). Sensorless Position Control Based on Resistance and Heat Transfer Models in Shape Memory Alloy Actuators. In *2019 IEEE/ASME International Conference on Advanced Intelligent Mechatronics (AIM)*, pages 217–222. ISSN: 2159-6255.

Scholtes, D., Seelecke, S., and Motzki, P. (2021). Development of a Bistable SMA Actuated Industrial Gripper Based on a Compliant Design. In *ACTUATOR; International Conference and Exhibition on New Actuator Systems and Applications 2021*, pages 1–4.

Scholtes, D., Seelecke, S., Rizzello, G., and Motzki, P. (2020). Design of a Compliant Industrial Gripper Driven by a Bistable Shape Memory Alloy Actuator. American Society of Mechanical Engineers Digital Collection.

Sheng, X., Xu, H., Zhang, N., Ding, N., Zhu, X., and Gu, G. (2020). Multi-material 3D printing of caterpillar-inspired soft crawling robots with the pneumatically bellow-type body and anisotropic friction feet. *Sensors and Actuators A: Physical*, 316:112398.

Shi, Z., Pan, J., Tian, J., Huang, H., Jiang, Y., and Zeng, S. (2019). An Inchworm-inspired Crawling Robot. *Journal of Bionic Engineering*, 16(4):582–592.

Shintake, J., Rosset, S., Schubert, B., Floreano, D., and Shea, H. (2016). Versatile Soft Grippers with Intrinsic Electroadhesion Based on Multifunctional Polymer Actuators. *Advanced Materials*, 28(2):231–238.

Shyu, T. C., Damasceno, P. F., Dodd, P. M., Lamoureux, A., Xu, L., Shlian, M., Shtein, M., Glotzer, S. C., and Kotov, N. A. (2015). A kirigami approach to engineering elasticity in nanocomposites through patterned defects. *Nature Materials*, 14(8):785–789.

Sigmund, O. (2011). On the usefulness of non-gradient approaches in topology optimization. *Structural and Multidisciplinary Optimization*, 43(5):589–596.

Singh, P. and Ananthasuresh, G. K. (2013). A Compact and Compliant External Pipe-Crawling Robot. *IEEE Transactions on Robotics*, 29(1):251–260.

Soother, D. K., Daudpoto, J., and Chowdhry, B. S. (2020). Challenges for practical applications of shape memory alloy actuators. *Materials Research Express*, 7(7):073001.

Souza, A. C., Mamiya, E. N., and Zouain, N. (1998). Three-dimensional model for solids undergoing stress-induced phase transformations. *European Journal of Mechanics - A/Solids*, 17(5):789–806.

Spaggiari, A., Spinella, I., and Dragoni, E. (2013). Design equations for binary shape memory actuators under arbitrary external forces. *Journal of Intelligent Material Systems and Structures*, 24(6):682–694. Publisher: SAGE Publications Ltd STM.

Sreekumar, M., Nagarajan, T., Singaperumal, M., Zoppi, M., and Molfino, R. (2007). Critical review of current trends in shape memory alloy actuators for intelligent robots. *Industrial Robot: An International Journal*, 34(4):285–294. Publisher: Emerald Group Publishing Limited.

Sreetharan, P. S., Whitney, J. P., Strauss, M. D., and Wood, R. J. (2012). Monolithic fabrication of millimeter-scale machines. *Journal of Micromechanics and Microengineering*, 22(5):055027. Publisher: IOP Publishing.

Talischi, C., Paulino, G. H., Pereira, A., and Menezes, I. F. M. (2012). PolyTop: a Matlab implementation of a general topology optimization framework using unstructured polygonal finite element meshes. *Structural and Multidisciplinary Optimization*, 45(3):329–357.

Tang, Y., Lin, G., Yang, S., Yi, Y. K., Kamien, R. D., and Yin, J. (2017). Programmable Kiri-Kirigami Metamaterials. *Advanced Materials*, 29(10):1604262.

Tissot-Daguette, L., Smreczak, M., Baur, C., and Henein, S. (2021). Load cell with adjustable stiffness based on a preloaded t-shaped flexure pivot. *euspen's 21st International Conference and Exhibition*.

Tolley, M. T., Shepherd, R. F., Mosadegh, B., Galloway, K. C., Wehner, M., Karpelson, M., Wood, R. J., and Whitesides, G. M. (2014). A Resilient, Untethered Soft Robot. *Soft Robotics*, 1(3):213–223. Publisher: Mary Ann Liebert, Inc., publishers.

Torres Melgarejo, M. A., Darnieder, M., Linß, S., Zentner, L., Fröhlich, T., and Theska, R. (2018). On Modeling the Bending Stiffness of Thin Semi-Circular Flexure Hinges for Precision Applications. *Actuators*, 7(4):86. Number: 4 Publisher: Multidisciplinary Digital Publishing Institute.

Ueno, S., Takemura, K., Yokota, S., and Edamura, K. (2014). Micro inchworm robot using electro-conjugate fluid. *Sensors and Actuators A: Physical*, 216:36–42.

Wang, N., Cui, C., Chen, B., and Zhang, X. (2018). Design and Analysis of Bistable Dielectric Elastomer Actuator with Buckling Beam. In *2018 International Conference on Manipulation, Automation and Robotics at Small Scales (MARSS)*, pages 1–6, Nagoya, Japan. IEEE.

Wang, W., Lee, J.-Y., Rodrigue, H., Song, S.-H., Chu, W.-S., and Ahn, S.-H. (2014). Locomotion of inchworm-inspired robot made of smart soft composite (SSC). *Bioinspiration & Biomimetics*, 9(4):046006. Publisher: IOP Publishing.

Wayman, C. and Duerig, T. (1990). An introduction to martensite and shape memory. In Duerig, T. W., Melton, K. N., Stöckel, D., and Wayman, C. M., editors, *Engineering Aspects of Shape Memory Alloys*, pages 3–20. Butterworth-Heinemann.

Welsch, F., Kirsch, S.-M., Motzki, P., Schmidt, M., and Seelecke, S. (2018). Vacuum Gripper System Based on Bistable SMA Actuation. In *Volume 1: Development and Characterization of Multifunctional Materials; Modeling, Simulation, and Control of Adaptive Systems; Integrated System Design and Implementation*, page V001T04A014, San Antonio, Texas, USA. ASME.

Williams, E. A., Shaw, G., and Elahinia, M. (2010). Control of an automotive shape memory alloy mirror actuator. *Mechatronics*, 20(5):527–534.

Wu, J., Cai, S., Cui, J., and Tan, J. (2015). A generalized analytical compliance model for cartwheel flexure hinges. *Review of Scientific Instruments*, 86(10):105003.

Yang, X., Chang, L., and Pérez-Arancibia, N. O. (2020). An 88-milligram insect-scale autonomous crawling robot driven by a catalytic artificial muscle. *Science Robotics*, 5(45). Publisher: Science Robotics Section: Research Article.

Yoo, Y.-I., Kim, Y.-J., Shin, D.-K., and Lee, J.-J. (2015). Development of martensite transformation kinetics of NiTi shape memory alloys under compression. *International Journal of Solids and Structures*, 64-65:51–61.

Yuk, H., Kim, D., Lee, H., Jo, S., and Shin, J. H. (2011). Shape memory alloy-based small crawling robots inspired by C. elegans. *Bioinspiration & Biomimetics*, 6(4):046002.

Zhakypov, Z., Heremans, F., Billard, A., and Paik, J. (2018). An Origami-Inspired Reconfigurable Suction Gripper for Picking Objects With Variable Shape and Size. *IEEE Robotics and Automation Letters*, 3(4):2894–2901.

Zhang, H., Lerner, E., Cheng, B., and Zhao, J. (2020). Compliant Bistable Grippers Enable Passive Perching for Micro Aerial Vehicles. *IEEE/ASME Transactions on Mechatronics*, pages 1–1.

Zhang, X. M., Liu, A. Q., Lu, C., and Tang, D. Y. (2007). A Real Pivot Structure for MEMS Tunable Lasers. *Journal of Microelectromechanical Systems*, 16(2):269–278.

Zhu, B., Zhang, X., Zhang, H., Liang, J., Zang, H., Li, H., and Wang, R. (2020). Design of compliant mechanisms using continuum topology optimization: A review. *Mechanism and Machine Theory*, 143:103622.

Zhu, J.-N., Borisov, E., Liang, X., Farber, E., Hermans, M. J. M., and Popovich, V. A. (2021). Predictive analytical modelling and experimental validation of processing maps in additive manufacturing of nitinol alloys. *Additive Manufacturing*, 38:101802.

Sean Thomas

Lausanne, Switzerland
+41 79 780 4134
seanthomas0409@gmail.com
sean-thomas.org

About

Technology and engineering have always been my passion. During my **PhD**, I have learned that the best way to apply my creativity is in **research**. Being at the forefront of technology and innovation is the ideal way to keep my creative juices flowing.

Education

September 2017 - January 2022	**PhD in Robotics, Control and Intelligent Systems (Integrated Actuators Laboratory)** Synthesis of Novel Integrated Actuators Powered by Shape Memory Alloys Director : Prof. Yves Perriard
September 2012 - March 2017	**Master & Bachelor of Science in Robotics and Autonomous Systems** Polytechnic program with an emphasis on micro-engineering, robotics, autonomous control systems and sensors.

Publications

S. Thomas, L. Tissot-Daguette, et al., *"Microgripper Device"*, European Patent Application, 21150579.7 - 1016

S. Thomas, P. Germano, T. Martinez, and Y. Perriard, *"An untethered mechanically-intelligent inchworm robot powered by a shape memory alloy oscillator,"* Sensors and Actuators A: Physical, Dec. 2021

S. Thomas, G. Maquignaz, A. Thabuis, and Y. Perriard, *"A Self-Biasing Shape Memory Alloy Gripper for Lightweight Applications,"* in 2021 IEEE/RSJ International Conference on Intelligent Robots and Systems (IROS 2021), Sep. 2021

S. Thomas, A. Thabuis, T. Martinez, P. Germano, and Y. Perriard, *"Designing compliant mechanisms composed of shape memory alloy and actuated by induction heating,"* Smart Mater. Struct., Aug. 2021

S. Thomas, P. Germano, T. Martinez, and Y. Perriard, *"Control-Free Mechanical Oscillator Powered by Shape Memory Alloys,"* in 2021 IEEE/ASME International Conference on Advanced Intelligent Mechatronics (AIM), Jul. 2021

P. Peralta, **S. Thomas**, and Y. Perriard, *"Characterization and Verification of Eddy-Current Position Sensing for Magnetic Levitation,"* IEEE Transactions on Industry Applications, 2021

S. Thomas, A. Thabuis, T. Martinez, and Y. Perriard, *"Shape Memory Effect of Benchmark Compliant Mechanisms Designed With Topology Optimization,"* in 2020 IEEE/ASME International Conference on Advanced Intelligent Mechatronics (AIM), Jul. 2020

S. Thomas, A. Thabuis, T. Martinez, and Y. Perriard, *"Multi-Output Compliant Shape Memory Alloy Bias-Spring Actuators,"* in 2020 IEEE/ASME International Conference on Advanced Intelligent Mechatronics (AIM), Jul. 2020

P. Peralta, **S. Thomas**, and Y. Perriard, *"Integrated, Eddy-Current-Based Sensing of Rotor Position for Magnetic Levitation,"* in 2020 IEEE Energy Conversion Congress and Exposition (ECCE), Oct. 2020

S. Thomas, M. Almanza, and Y. Perriard, *"Design Analysis of a Shape Memory Alloy Bias-Spring Linear Actuator,"* in 2019 12th International Symposium on Linear Drives for Industry Applications (LDIA), Jul. 2019

S. Thomas, P. Peralta, R. Mottet, M. Lehmann, Y. Civet, and Y. Perriard, *"Analysis and Reduction of Time Response in Thermally Activated Shape Memory Alloys,"* in 2018 21st International Conference on Electrical Machines and Systems (ICEMS), Oct. 2018

S. Thomas, M. Almanza, Y. Civet, and Y. Perriard, *"Actuation Displacement Analysis of a Self-Switching Shape Memory Alloy Buckled Beam,"* in 2018 21st International Conference on Electrical Machines and Systems (ICEMS), Oct. 2018

S. Thomas, L. Tissot-Daguette, T. Martinez, C. Baur, and Y. Perriard, *"Design and Modelling of a Flexure-based Bistable Gripper Powered by Shape Memory Alloys,"* Sensors and Actuators A: Physical, 2022 (pending)

Experience

October 2016 - March 2017	**Master Thesis at Human Robotics Group, Imperial College London** - Development of Single-Joint Neuromechanics device Supervisors : Prof. Etienne Burdet; Prof. Hannes Bleuler; Dr. Mohamed Bouri; Dr. Hsien Yung Huang
July 2016 - October 2016	**Onward** - Human Rehabilitation Robot, R&D engineer internship Supervisors: Dr. Joachim v. Zitzewitz; Dr. Urs Keller
July 2015 - March 2016	**G-Lab, EPFL** - Sensor Design of Body Weight Support Robot for Rodent Rehabilitation Supervisors: Prof. Gregoire Courtine; Dr. Joachim v. Zitzewitz

Skills

Python, C++, Objective C, Javascript, Java, HTML CSS, Matlab, 3D CAD, Finite Element Modelling, 3D Printing, Optimisation, LabView, Sensor Design, Modelling, Actuator Design, Latex